INVESTIGATION OF THE STRUCTURAL, MULTIFERROIC, AND DIELECTRIC PROPERTIES OF MODIFIED $BaTiO_3$

Ph.D. Thesis

By

MANEESHA. P

DISCIPLINE OF PHYSICS

INDIAN INSTITUTE OF TECHNOLOGY INDORE

NOVEMBER 2025

INVESTIGATION OF THE STRUCTURAL, MULTIFERROIC, AND DIELECTRIC PROPERTIES OF MODIFIED $BaTiO_3$

A THESIS

Submitted in partial fulfilment of the requirements for the award of the degree
of
DOCTOR OF PHILOSOPHY

by
MANEESHA. P

DISCIPLINE OF PHYSICS
INDIAN INSTITUTE OF TECHNOLOGY INDORE
November 2025

INDIAN INSTITUTE OF TECHNOLOGY INDORE

I hereby certify that the work which is being presented in the thesis entitled **INVESTIGATION OF THE STRUCTURAL, MULTIFERROIC, AND DIELECTRIC PROPERTIES OF MODIFIED $BaTiO_3$** in the partial fulfilment of the requirements for the award of the degree of **DOCTOR OF PHILOSOPHY** and submitted in the **DEPARTMENT OF PHYSICS, Indian Institute of Technology Indore**, is an authentic record of my work carried out during the period from December 2020 to November 2025 under the supervision of Prof. Somaditya Sen, Professor, Department of Physics, IIT Indore.

The matter presented in this thesis has not been submitted by me for the award of any other degree of this or any other institute.

01.12.2025

MANEESHA. P

This is to certify that the above statement made by the candidate is correct to the best of my/our knowledge.

01.12.2025

Prof. SOMADITYA SEN

ACKNOWLEDGEMENTS

This PhD thesis is a result of the invaluable guidance and encouragement of many people. Throughout this arduous journey towards a doctoral degree, many individuals and institutions supported me, and I was able to secure the prestigious Prime Minister's Research Fellowship (PMRF) to pursue my PhD. At this moment of accomplishment, I would like to remember and acknowledge all those great humans in this journey.

I am extremely grateful to my principal supervisor, Prof. Somaditya Sen, for giving me this opportunity to work on many scientific projects in our lab and mentoring me throughout my PhD journey. The support and encouragement he has given me for obtaining the PMRF and for publishing numerous journal publications and book chapters within four years of completing my PhD were invaluable to my entire career. I am always grateful for the faith he has in me and the fatherly affection he has showered on me. On a personal level, he always stood with me in many difficulties I faced in my life and helped me to the utmost he could. The extensive, insightful scientific discussions, constructive criticisms, and advice he has given are a great asset to my thesis.

I would like to thank my PSPC members, Prof. Krushna R. Mavani, and Dr. Saptarshi Ghosh, for evaluating and giving their valuable comments to improve my research work. The guidance and encouragement they have provided when I approached them for different projects related to their area of field was invaluable, and always thankful to them. The crucial comments and hard questions incentivised me to widen my research work and shape my final dissertation.

I take this opportunity to express my gratitude to Prof. Preeti Bhobe (HoD, Physics) for her help and support in completing my PhD. I am also grateful to all the faculty and students of the Department of Physics, IIT Indore, whom I came across during my PhD journey.

I had the honour of working with some of the leading scientists in their respective areas of research. I want to especially thank my notable collaborators which include Dr. Indraneel Bhaumik (RRCAT, Indore), Abdelkrim Mekki, Khalil Harrabi (KFUPM, Saudi Arabia for XPS measurement and TEM measurement), Dr. V. Raghavendra Reddy, Meenal Dhanetwal (UGC-DAE Indore for ferroelectric PUND measurement), Arjun Pathak (SUNY Buffalo, USA for magnetic measurements), Dr. Rajashri Urkude, Dr. Biplab Ghosh (RRCAT Indore for EXAFS measurement), Dr. Soma Banik, Kiran Baraik (RRCAT Indore for PES measurement), Department of Physics, Thapar University for magnetoelectric measurement. Dr. Mayanak. K. Gupta, Dr. Mittal (BARC, Mumbai for theoretical calculation.

Sophisticated Instrumentation Center (SIC), IIT Indore, is acknowledged for providing a valuable experimentation facility. I thank all my collaborators in other labs at IITI for providing an experimental facility at their laboratories for my thesis. I sincerely want to thank all staff members of IITI Indore for providing all comfort and convenience.

I want to express my sincere gratitude towards Prof. Ashutosh Mishra, Prof. Choyal, and other faculty members in Devi Ahilya Viswa Vidyalaya (DAVV) for providing me with a Teaching Assistantship during my PMRF tenure. I am thankful to all students in DAVV for helping me to widen my knowledge and improve my teaching skills.

Lab members are always crucial to maintaining a proper research environment during the PhD period. I am extremely blessed to have the best lab members in SMART LAB. I am always grateful for the guidance provided by Dr. E.G. Rini during the early stages of my PhD journey. I am extending my gratitude to Dr. Prasanth Kumar and Mukul Kumar. I want to thank Dr. Koyal Suman Samantaray and Suresh Chandra Baral for being with me when I struggled during the initial periods of my PhD. I am blessed to have helpful and supportive juniors like a family, and I would like to

thank all my juniors, Poonam Singh, Rakhi Saha, Manju Kumari, Tabinda Nabi, and Mohammed Vasim. I want to thank Dilip Sasmal and Prithwiraj Ganguly for the many insightful discussions. I am thankful to some of the MSc students who have passed out from the SMART lab, Sayak Dutta, Kailash Dukhiya, Karthik, and Prashanth, who later turned out to be my brothers. I also remember Dr. Muthukrishnan and Dr. Ankur for the help they have provided during a short period in the lab. I thank some of the special enthusiastic interns in the lab with whom I had a really great time in the LAB. I would also like to thank Prof. Sen's family members, Soma Sen, Srishti Sen, Sagnika Sen, and Dadi for treating me as their family member.

I acknowledge UGC for providing JRF fellowship, MHRD for providing PMRF fellowship, and IITI for providing institute fellowship to complete my PhD thesis. Besides this, several people have knowingly and unknowingly helped me in the successful completion of my thesis, to whom I want to show my respect.

The constant support of my parents throughout my educational career made me pursue higher studies. Their unconditional love, patience, and belief in me always encourage me to dream and work hard for great achievements. The mental support given by my sister, brother, father-in-law, mother-in-law, and other family members is sincerely acknowledged at this moment. I also remember and am grateful to all my teachers throughout my educational journey.

Two people who are with me always in all my ups and downs, and they give me support when I fail, stand with me when I am alone, make me laugh when I am sad, motivate me when I am depressed, pull me back to reality when I am overwhelmed, are my partner, Deepak P, and my son, Thanay P. This thesis would not have been possible without these two people who are close to my heart.

Maneesha. P

Dedicated to

MY PARENTS

VELAYUDHAN. P & GEETHA. C

MY PARTNER & MY SON

DEEPAK. P & THANAY. P

SYNOPSIS

Magnetoelectric (ME) and multiferroic materials are essential for developing next-generation, novel, multifunctional devices. Hence, these are high-priority ferroic research materials. To date, extensive research has been conducted on magnetic and electric ordering and their coupling. Various materials and coupling mechanisms have been explored for ME coupling [1-2]. $BaTiO_3$ (BTO) is a well-known ferroelectric (FE) material. BTO can be chemically modified to impart ferromagnetism (FM) to the crystal structure and develop magnetoelectric properties in the material. Transition metal (TM) doping at the Ti site is an effective method to achieve BTO-based magnetoelectric materials [3,4]. Some examples of the solid solutions of BTO with magnetic (ABO_3) perovskite materials that demonstrate ME coupling are $BaTiO_3$-$BiFeO_3$ [5], $BaTiO_3$–$La_{0.7}Ba_{0.3}MnO_3$ [6], Mn- and Co-modified $BaTiO_3$–$BiFeO_3$ [7], etc. Apart from doping magnetic ions and solid solutions, composites with ferromagnetic materials [8], core-shell structures with magnetic materials [9], and heterojunction thin films of BTO with ferromagnetic films [10] facilitate ME coupling. Excellent ME coupling was observed in most of these materials, prompting exploration of their physical properties and utilisation in industrial applications.

Compared with a composite or heterostructure material, a single-phase compound can show intrinsic ME behaviour. Unfortunately, no single-phase ME material that meets room temperature applications has been discovered yet. The most severe weaknesses of single-phase ME materials are linked not only to their operational temperatures (mostly well below room temperature) but also to the magnitudes of the order parameters. The introduction of a new ferroic order in a single-phase ferroic material leads to the decrease of the existing ferroic order in the material. Their extremely low switchable polarisation (usually in the order of magnitude of nC/ cm^2) can be useful for fast switching applications. The

development of single-phase multiferroic materials is constrained by factors such as different symmetry breaking and different physical requirements of magnetism and ferroelectricity owing to ferroic ordering at extremely low temperatures. However, composite materials show enhanced coupling through the contribution of different strong ferroic orders from different phases in the material. In ME composites, ME coupling takes place as FE and magnetic domains are coupled through their secondary (ferro/magneto) elastic domains because of electrostriction and magnetostriction.

Doping with a TM ion (Fe, Mn, Co, Ni) at the Ti-site can induce magnetism in BTO, but it will diminish the ferroelectricity in BTO. Simultaneous substitution with suitable elements at the Ba-site can retain the FE of the structure. Those modifications of BTO can show magnetic orderings while retaining the FE, leading to multiferroicity and magnetoelectric coupling. The FM exchange mechanism is induced by the TM ion in the Ti site, and the appropriate doping in the A site stabilises the tetragonal structure and favours ferroelectricity. Hence, this thesis work modifies the $BaTiO_3$ by doping the A site and B site with suitable elements to investigate a structure correlated multiferroicity and probable magnetoelectric coupling in these materials. The structure correlated dielectric and transport properties were also investigated in detail. This research work investigated two series of samples of La and Fe doped BTO; $Ba_{(1-x)}La_{(x)}Ti_{(1-y)}Fe_{(y)}O_3$(x=y=0, 0.01, 0.03, 0.06), Ca and Mn doped BTO; $Ba_{(1-x)}Ca_{(x)}Ti_{(1-y)}Mn_{(y)}O_3$ (x=y=0, 0.03, 0.06, 0.09) for the multiferroic applications. The oxidation state and valence state studies and the corresponding changes in the band gap and dielectric and electrical transport properties are studied further to correlate all the properties exhibited by this material. A theoretical investigation of the density of states and electron localisation function is further studied to connect with the experimental results.

Sol-gel prepared series of samples $Ba_{(1-x)}Ca_{(x)}Ti_{(1-y)}Mn_{(y)}O3$ (x=y=0,0.03,0.06,0.09), has been prepared through sol–gel synthesis.

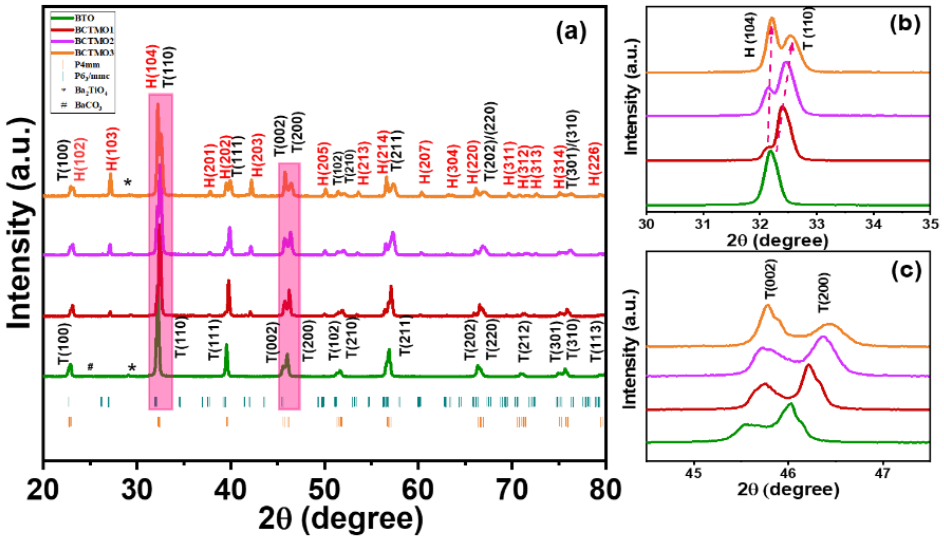

Figure 1 *:(a) XRD data of all samples with the CIF file of the P4mm and P63/mmc space groups. (b) Zoomed-in image of the variation in the intensity of the hexagonal peak H(104) and tetragonal peak T(110) with composition. (c) Zoomed-in image of the splitting of tetragonal T(002) and T(200) peaks.*

XRD and Raman spectroscopy reveal characteristic peaks corresponding to a dual phase of ferroelectric tetragonal *P4mm* and ferromagnetic hexagonal *P6₃/mmc* $BaTiO_3$. A reduced O–Ti–O angle may be a consequence of an increased hybridisation of the 2p–3d orbitals in the x = 0.03 sample compared with the other samples, which may correlate with the enhanced ferromagnetic double exchange interaction. The intensity variation of the characteristics of the hexagonal peaks indicates an increase in the hexagonal phase with doping in the samples. XRD of all the samples with changes in the hexagonal peak (104), tetragonal peak (110), (002), and (200) are shown in Figure 1.

The multiple oxidation states of Mn^{3+}, Mn^{4+}, Ti^{3+}, $Ti^{4+,}$ and the corresponding changes in the amount of oxygen vacancies are the reasons for the ferromagnetism. Deconvoluted XPS spectra of the x=0.03 sample are shown in Figure 2.

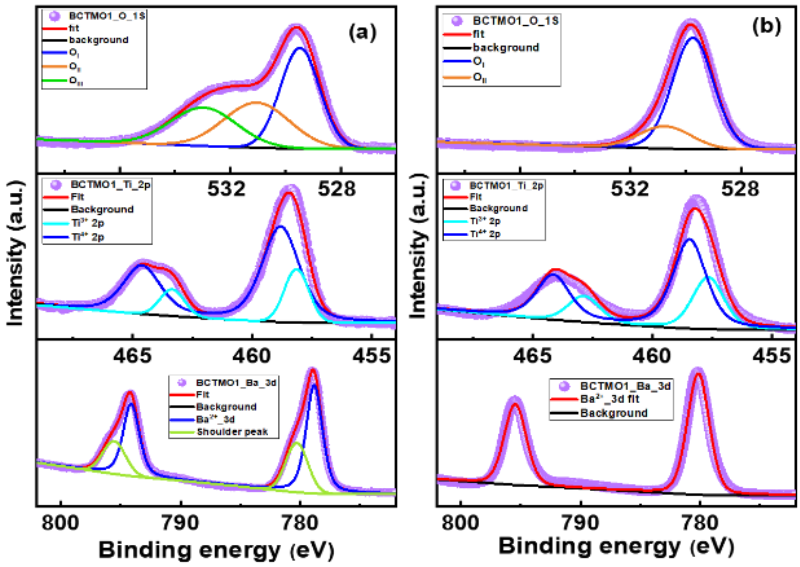

***Figure 2**: Deconvoluted XPS spectra of the BCTMO1 sample. (a) Ba 3d, Ti 2p, and O 1s data before etching. (b) Ba 3d, Ti 2p, and O 1s data after etching.*

Hexagonal emergence in Ca and Mn-modified $BaTiO_3$ has been investigated through TEM, and two types of lattice planes corresponding to the tetragonal and hexagonal lattices have been observed [Figure 3].

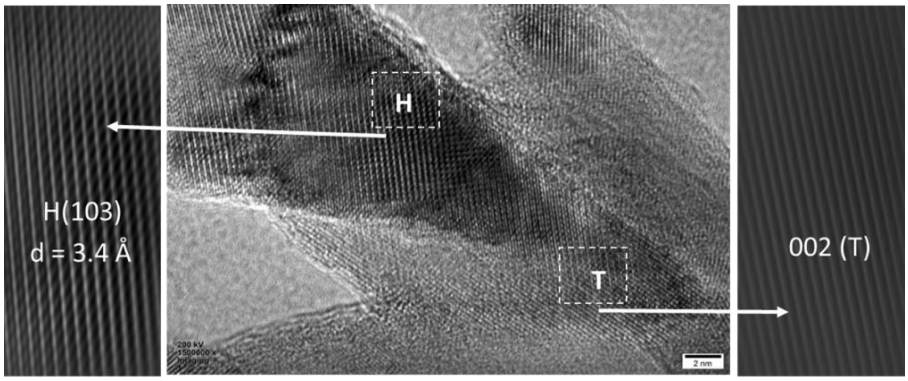

***Figure 3**: TEM Image of X=0.03 sample*

The ferroelectric hysteresis shows a saturated P–E loop for x = 0 and a lossy unsaturated pinched P–E loops for doped samples. M–H loops indicate diamagnetism for x=0, weak ferromagnetic hysteresis in a paramagnetic background for x=0.03, and paramagnetic behaviour for the other samples. The coexistence of ferroelectricity and ferromagnetism in x=0.03 leads to multiferroicity and magnetoelectric coupling. Induced polarisation with an applied magnetic field shows a linear response,

indicating direct ME coupling in this material [Figure 4]. The applied magnetic field shows a linear response, indicating direct ME coupling in this material [Figure 4].

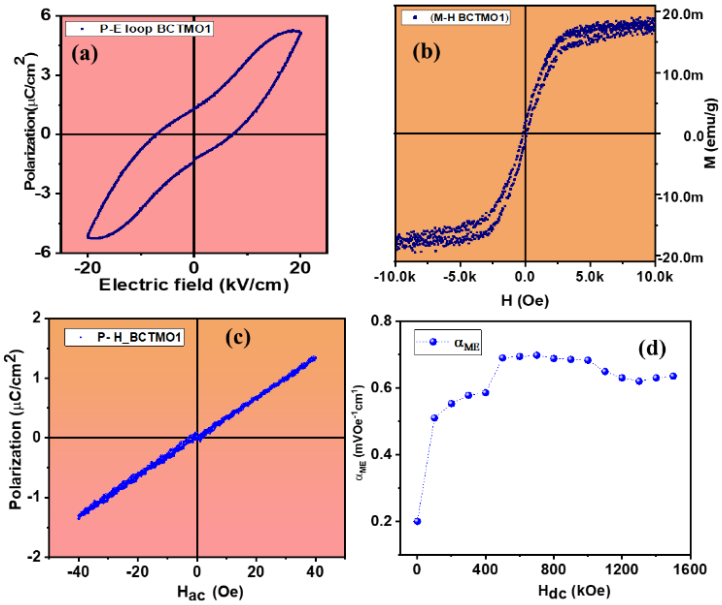

Figure 4: *(a) P–E hysteresis of BCTMO1. (b) M–Hysteresis of BCTMO1. (c) Polarisation with an AC magnetic field with a bias DC magnetic field of 600 Oe. (d) Variation in* a_{ME} *with a DC magnetic field at a constant AC magnetic field of 5 Oe.*

A weak magnetoelectric coupling coefficient of α_{ME} ~0.704 mVcm^{-1}Oe^{-1} was obtained for a DC magnetic field of 800 Oe and an AC magnetic field of 40 Oe. Hence, $Ba_{(0.97)}Ca_{(0.03)}Ti_{(0.97)}Mn_{(0.03)}O_3$ is a magnetoelectrically coupled material. This ME coupling is absent for higher percentages of doping. The P-E, M-H, and P-H curve and the value of α_{ME} with applied dc magnetic field for a constant ac magnetic field is given in Figure 9.

$Ba_{(1-x)}Ca_{(x)}Ti_{(1-y)}Mn_{(y)}O_3$ (x=y=0, 0.03, 0.06, 0.09) samples have been investigated for structural polymorphism, band gap tuning, and dielectric anomalies. UV-DRS shows a reduction in band gap, E_g from 3.2 to 2.05 eV and a highest Urbach energy, E_U for the x=0.03 sample [Figure 5(a)]. The Valence band edge in PES is observed to be shifted towards E_F due to the presence of in-gap states [Figure 5(b)]. XANES analysis confirms the

presence of Ti^{3+}, Ti^{4+}, $Mn^{3+}$and Mn^{4+} oxidation states and the structural transformation to a centrosymmetric structure. EXAFS analysis indicates the local structural modification and bond length variations near the Mn and Ti sites with doping [Figure 6 (a), (b)].

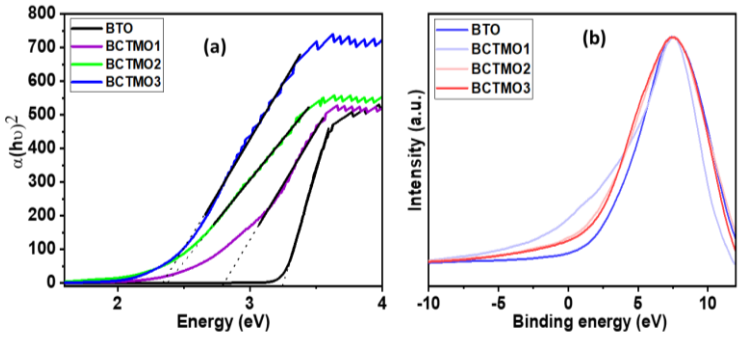

Figure 5: *Tauc plot of all samples from UV-DRS, (b) VB spectra of all samples from PES.*

These electronic modifications are supported by the DOS and ELF theoretical calculations. Density of states calculations reveal a shift of VB and CB with doping in the tetragonal lattice and formation of defect states with doping in the hexagonal lattice. Electron localisation function calculations indicate the lattice contraction with Ca doping in both tetragonal and hexagonal lattices; however, a lattice expansion is observed with Mn doping in the tetragonal lattice and hexagonal lattice [Fig. 6 (c),d].

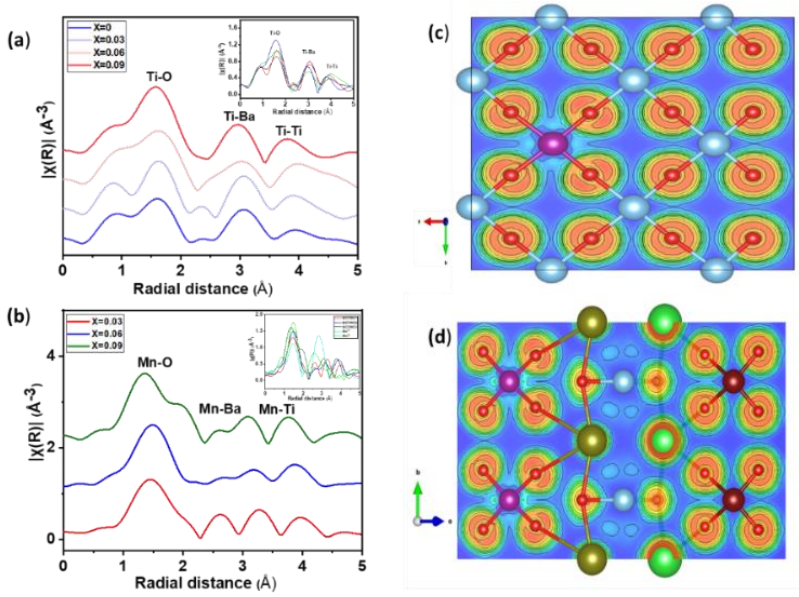

Figure 6: *(a), (b)EXAFS plot, (c), (d)ELF calculation of tetragonal and hexagonal lattice for x=0.03.*

Dielectric studies show a decrease in the permittivity [Figure 7(a)] and an increase in tanδ corresponding to the decrease in tetragonality and increase of the hexagonal phase. A sharp tetragonal to cubic phase transition in BTO transforms to diffuse behaviour with Ca and Mn doping. The diffuse nature corresponds to the Polar nano Regions (PNRs) formed by the destruction of the long-range ferroelectric order. For x=0.09, the major hexagonal phase sample shows an abnormal shoulder feature [Figure 7(b)] before phase transition that may correspond to the ordering of the PNRs in the hexagonal phase or core-shell structure formation of the strong ferroelectric lattice and the weak ferroelectric doped lattice.

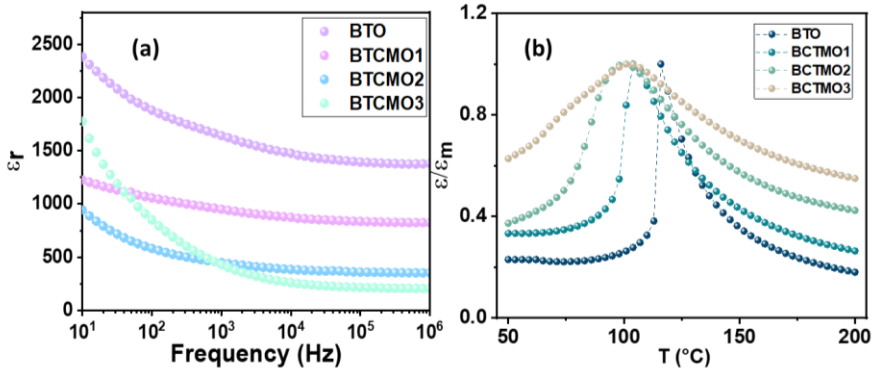

Figure 7: *(a) RT permittivity plot with frequency for all samples, (b) Variation of phase transition behaviour from sharp transition for x=0 to diffuse behaviour with doping.*

Sol-gel prepared $Ba_{(1-x)}La_{(x)}Ti_{(1-y)}Fe_{(y)}O_3$ revealed a pure tetragonal *P4mm* phase for x = 0 and 0.01, while a mixed tetragonal and cubic *Pm-3 m* phase for 0.03 and 0.06. The structural modifications are studied by Rietveld refinement of the XRD data. The obtained lattice parameters are shown in Figure 8. Raman studies confirm the observations obtained through XRD regarding the tetragonal to cubic transformation and the bond length variations. From XPS analysis, the presence of multiple oxidation states, $Ti^{3+,}$ and Fe^{2+} is observed that resulting in O_v in the material. The grain size was observed to decrease from 2.89 µm to 1.38 µm from

FESEM studies. EPR studies show signals corresponding to defect complexes, which can contribute to the conductivity and magnetic ordering.

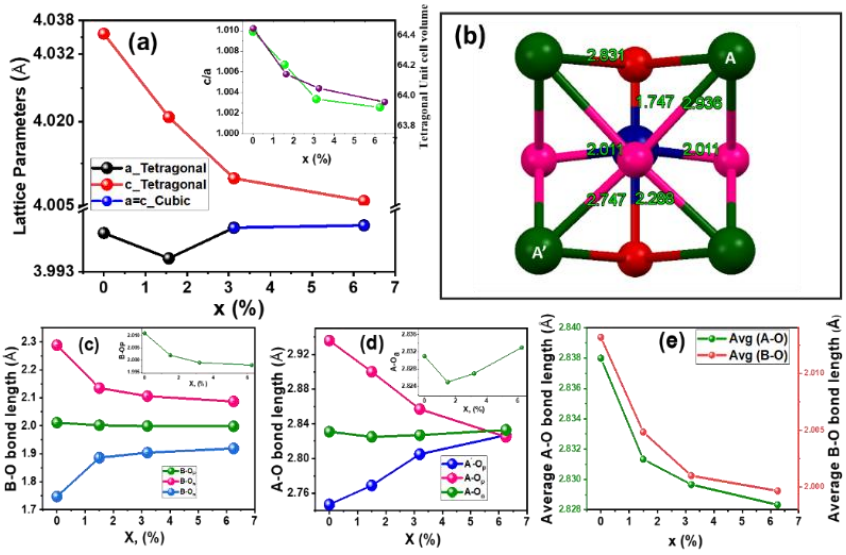

Figure 8: *(a) Variation of a, b, and c lattice parameters for the tetragonal and cubic phase (inset) variation of c/a and unit cell volume with composition (b) Schematic of the tetragonal P4mm structure. (c) Variation of avg. A-O and B-O bond length (d). Variation of three B-O bond lengths (e). Variation of three A-O bond lengths.*

Ferroelectricity was observed in the single-phase samples up to x = 0.01. For x >0.01, the samples become lossy ferroelectrics due to the high conduction losses. Along with the ferroelectric ordering, a ferromagnetic component was also observed in the single-phase samples.

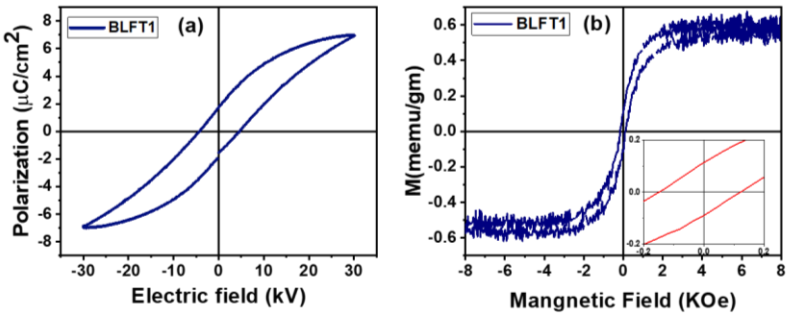

Figure 9: *(a) P-E loop (b) M-H loop of the x=0.015 sample*

The ferromagnetism arises from the F center exchange mediated by Bound Magnetic Polarons. However, for the higher substitution (x>0.01),

both orderings are compromised and lose the multiferroicity. The proper P-E loop and M-H loop of the x=0.01 sample are shown in Figure 9.

The coupling of the ferroelectric and ferromagnetic orders was revealed from magnetodielectric property measurements. The magnetocapacitance percentage value 2.7% is the highest for x = 0.01 at 1 T and 10 kHz. This is an indication of magnetoelectric coupling, and can be correlated with the structural variations and associated ferroelectric and magnetic properties. Variation of permittivity and MC% with magnetic field is shown in Figure 10.

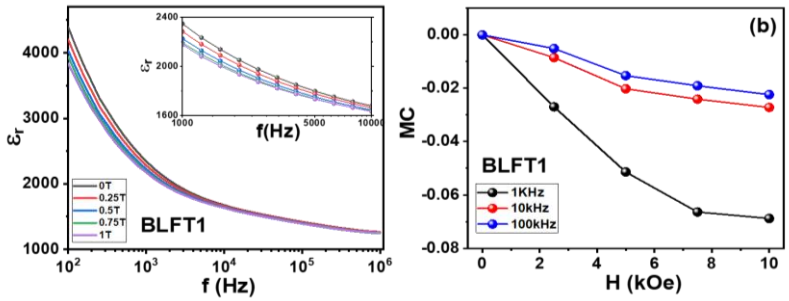

Figure 10: *Variation of (a) permittivity, (b) Variation of magneto capacitance with magnetic field for different frequencies for x=0.01 sample.*

La and Fe modification in BTO revealed band gap tuning from the UV region (3.25 eV in BTO) to the visible region (2.54 eV in BLFT3) [Figure 11 (a)], which can be correlated to an increase of lattice distortion and disorder in these samples. Theoretical calculations reveal shifts in the valence band maxima and conduction band minima, along with the formation of defect states inside the bandgap with La/Fe doping [Figure 11 (b& c)].

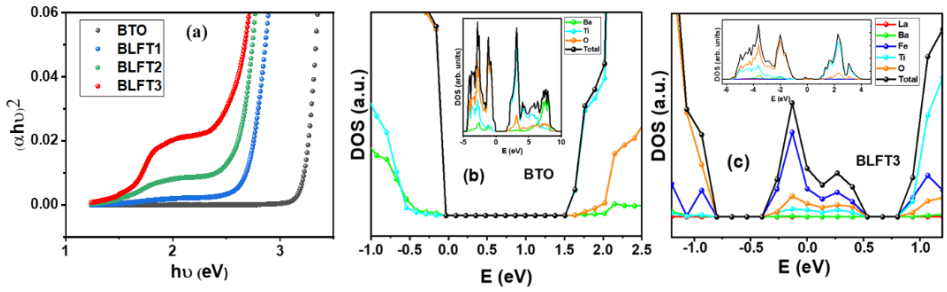

Figure 11: *(a) UV-Vis absorption spectra of all samples, DOS of (a) BTO and (b) BLFT3 corresponding to Ba 5p states, La 5d states, Ti 3d states, Fe 3d states, O 2p states.*

The electronic states are modified due to such defect states and correlated structural distortions/disorders, which increase the Urbach energy (E_U).

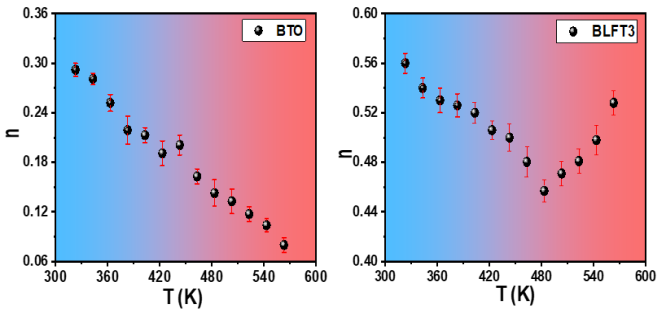

Figure 12: *Variation of frequency exponent 'n' of Johnscher's power law with temperature.*

Such electronic modifications were justified by transportation measurement using dielectric properties, AC conductivity, and impedance spectroscopy. A theoretical assessment of the modifications was estimated using electron localisation function calculations, revealing a more distorted lattice for the doped samples, suggesting localisation of the electrons. An experimental verification of the localisation was estimated using different transportation models. The variation of Johnsher's power law exponent with temperature revealed the presence of correlated Barrier Hopping (CBH) in BTO and Overlapping Large Polaron Tunnelling (OLPT) for the La/Fe-modified BLFT samples [Figure 12]. With doping, the local structural deformations and the polaron formations lead the transportation towards a hopping to tunnelling process. The defects induce band gap tuning, and the associated polaron-induced conduction mechanism makes these samples suitable for optoelectronic applications.

A comprehensive structural investigation of the La/Fe-doped $BaTiO_3$ and Ca/Mn-doped $BaTiO_3$ for dielectric, multiferroic, and magnetoelectric applications has been conducted, along with the thorough experimental, theoretical, and characterisation techniques in this research work. A room temperature ME coupling is reported for 3% Ca and Mn-doped $BaTiO_3$. The thesis provides information regarding the band gap tuning of $BaTiO_3$ with suitable B-site doping with transition metal ions.

Depending on the structural variations, the magnetic and electric properties will change, which can be controlled with the A-site and B-site substitution.

References

[1] N. Pereira, A. C. Lima, S. Lanceros-Mendez and P. Martins, Magnetoelectrics: Three Centuries of Research Heading Towards the 4.0 Industrial Revolution, Materials, 2020, 13(18), 18, DOI: 10.3390/ma13184033.

[2] R. Gupta and R. K. Kotnala, A review on current status and mechanisms of room-temperature magnetoelectric coupling in multiferroics for device applications, J. Mater. Sci., 2022, 57, 12710–12737, DOI: 10.1007/s10853-022-07377-4.

[3] T.Costanzo, J. McCracken, A. Rotaru, and G. Caruntu, Quasi Monodisperse Transition-Metal-Doped BaTiO3 (M = Cr, Mn, Fe, Co) Colloidal Nanocrystals with Multiferroic Properties, ACS Appl. Nano Mater., 2018, 1(9), 4863–4874, DOI: 10.1021/ acsanm.8b01036.

[4] Y.-H. Lin, J. Yuan, S. Zhang, Y. Zhang, J. Liu, Y. Wang, and C. W. Nan, Multiferroic behaviour observed in highly oriented Mn-doped BaTiO3 thin films, Appl. Phys. Lett., 2009, 95(3), 033105, DOI: 10.1063/1.3182793.

[5] S.-C.Yang, A.Kumar, V.PetkovandS.Priya, Room-temperature magnetoelectric coupling in single-phase BaTiO3–BiFeO3 system, J. Appl. Phys., 2013, 113(14), 144101, DOI: 10.1063/ 1.4799591.

[6] S. Sahoo, S. Das, P. K. Mahapatra and R. N. P. Choudhary, Fabrication and characterisation of LaFeO3–BaTiO3 electro ceramics, Mater. Chem. Phys., 2018, 216, 158–169, DOI: 10.1016/j.matchemphys.2018.05.032.

[7] Q. Fu, L. Zhou, D. Zhou, L. Miao, C. Chen and F. Xue, Large magneto-electric effects in hexagonal La0.7Ba0.3MnO3 BaTiO3 solid solutions and magneto-electric coupling mechanism discussion, J. Appl. Phys., 2014, 116(13), 134103, DOI: 10.1063/1.4897200.

[8] M.Naveed-Ul-Haq, V. V.V.Shvartsman, S.Salamon, H.Wende, H. Trivedi, A. Mumtaz, and D. C. Lupascu, A new (Ba, Ca) (Ti, Zr) O3-based multiferroic composite with large magnetoelectric effect, Sci. Rep., 2016, 6(1), 32164, DOI: 10.1038/srep32164.

[9] W. Liu, H. Zhao, C. Zhang, S. Xu, and F. Zhang, In situ activation of flexible magnetoelectric membrane enhances bone defect repair, Nat. Commun., 2023, 14(1), 4091, DOI: 10.1038/s41467-023-39744-3.

[10] C. Liu, W. Wan, S. Gong, H. Zhang, and W. Guo, Multiple magnetoelectric coupling effects in BaTiO3/Sr2CoMoO6 heterostructures, Sci. Rep., 2017, 7(1), 3856, DOI: 10.1038/ s41598-017-03876-6

. LIST OF PUBLICATIONS

List of publications from PhD thesis work

1. **P Maneesha**, Koyal Suman Samantaray, Suresh Chandra Baral, Grace Brzykcy, Indranil Bhaumik, Abdelkrim Mekki, Arjun K. Pathak, Somaditya Sen, Effect of oxygen vacancies and cationic valence state on multiferroicity and magnetodielectric coupling in (1-x)$BaTiO_3$.(x)$LaFeO_3$ solid solution**,** Journal of Alloys and Compounds, 2024, https://doi.org/10.1016/j.jallcom.2023.172587.

2. **P Maneesha**, KS Samantaray, SC Baral, R Mittal, MK Gupta, S Sen, Defect/disorder correlated modification of transport properties from hopping to tunnelling processes in $BaTiO_3$–$LaFeO_3$ solid solution, Journal of Applied Physics,2024, https://doi.org/10.1063/5.0195109.

3. **P Maneesha**, Koyal Suman Samantaray, Rakhi Saha, Tabinda Nabi, Rajashri Urkude, Biplab Ghosh, Arjun K. Pathak, Indranil Bhaumik, Abdelkrim Mekki, Khalil Harrabi, Somaditya Sen, Room temperature Multiferroicity and Magnetoelectric coupling in Ca/Mn modified $BaTiO_3$, Journal of Materials Chemistry C, 2025, https://doi.org/10.1039/D5TC00873E.

4. **P Maneesha,** Dilip Sasmal, Rakhi Saha, Kiran Baraik, Soma Banik, R. Mittal, Mayanak K. Gupta, Abdelkrim Mekki, Khalil Harrabi, Somaditya Sen Hexagonal polymorphism induced band gap modifications and dielectric anomalies in Ca/Mn modified $BaTiO_3$, https://doi.org/10.48550/arXiv.2511.17940.

List of publications during PhD

1. **P Maneesha**, S C Baral, E.G. Rini, and Somaditya Sen, An overview of the structural correlation of magnetic and electrical properties of Pr_2NiMnO_6 Double perovskite, Progress in Solid State Chemistry, 2023, https://doi.org/10.1016/j.progsolidstchem.2023.100402.

2. S C Baral, **P Maneesha**, Prashant Kumar Mishra, Pravarthana Dhanapal, Somaditya Sen, Rapid photocatalytic degradation of organic pollutants by Al^{3+} doped CuO powders under low power visible light and natural sunlight, Optical materials, 2024, https://doi.org/10.1016/j.optmat.2023.114653.

3. S C Baral, **P Maneesha**, EG Rini, S Sen, Recent advances in La_2NiMnO_6 double perovskites for various applications; challenges and opportunities, Progress in Solid State Chemistry, 2023, https://doi.org/10.1016/j.progsolidstchem.2023.100429.

4. S C Baral, **P Maneesha**, S Datta, K Dukiya, D Sasmal, KS Samantaray, Ssen, Enhanced photocatalytic degradation of organic pollutants in water using copper oxide (CuO) nanosheets for environmental application, JCIS Open, 2024, https://doi.org/10.1016/j.jciso.2024.100102.

5. K S Samantaray, **P Maneesha**, I Bhaumik, S Sen, Understanding the depolarization phenomena in (1-x) $Na_{0.5}Bi_{0.5}TiO_3$.(x) $Ba_{0.85}Ca_{0.15}Ti_{0.90}Zr_{0.10}O_3$ solid solutions using in-situ temperature-dependent Raman spectroscopy, Journal of Physics: Condensed Matter, 2024, https://doi.org/10.1088/1361-648X/ad475e.

6. K S Samantaray, **P Maneesha**, R Saha, K Harrabi, A Mekki, S Sen, Composition and electric field driven studies on modified NBT-based lead-free ceramics, Materials Science and Engineering: B, 2024, https://doi.org/10.1016/j.mseb.2023.117140.

7. K S Samantaray, Ruhul Amin, **P Maneesha**, Indranil Bhaumik, Somaditya Sen, Effect of electrical poling on the structural, vibrational, and electrical properties of (0.94) ($Na_{0.5}Bi_{0.5}TiO_3$)-(0.06-x)$CaTiO_3$-(x)($BaTiO_3$) lead-free ceramics, Journal of Alloys and Compounds, 2023, https://doi.org/10.1016/j.ceramint.2023.01.018.

8. Prithwiraj Ganguly, Vince Kamboj, **P Maneesha**, Somaditya Sen, A novel method of finding the dielectric constant of ceramic materials in microwave range with Dielectric Resonator Antenna setup using the $HEM_{11\delta}$ mode, Ceramics International, 2024, https://doi.org/10.1016/j.ceramint.2024.11.313.

9. K S Samantaray, Dilip Sasmal, **P Maneesha**, Somaditya Sen, R3c to P4bm Phase Transition Assisted Small to Large Polaron Crossover in Sodium Bismuth Titanate-Based Ferroelectrics, Journal of Applied Physics, 2024, https://doi.org/10.1063/5.0224323.

10. K S Samantaray, Sourabh Kumar, **P Maneesha**, Dilip Sasmal, Suresh Chandra Baral, BR Krupa, Arup Dasgupta, K Harrabi, A Mekki, Somaditya Sen, Contribution of piezoelectric effect on piezo-phototronic coupling in ferroelectrics: A theory-assisted experimental approach on NBT, The Journal of Chemical Physics, 2024, https://doi.org/10.1063/5.0227731.

11. Rakhi Saha, Koyal Suman Samantaray, **P Maneesha**, Suresh Chandra Baral, Sachindra Nath Sarangi, Rajashri Urkude, Biplab Ghosh, R. Mittal, Mayanak K Gupta, Abdelkrim Mekki, Khalil Harrabi, Somaditya Sen Effect of V^{5+}/V^{4+} substitution on structural and magnetic orderings of $SrFeO_{3-\delta}$ Ceramics International, 2025, https://doi.org/10.1016/j.ceramint.2025.06.220.

12. Prithwiraj Ganguly, Prashant Joshi, Maneesha Puthiyoth, Dilip Sasmal, Somaditya Sen, Estimating the Diffuseness for the Non-Relaxor Type Ferroelectric to Paraelectric Phase Transition in $BaTiO_3$, Physical Review B Letters, 2025, https://doi.org/10.1103/2sks-sgwy.

List of book chapters published during PhD

1. **P Maneesha**[†]**,** Koyal Suman Samantaray[†], Somaditya Sen, Chapter 3: Spectral interpretation, X-Ray, Photoelectron Spectroscopy: Principles, Techniques and Applications, Nova Science Publishers, 2023, eBook ISBN: 979-8-89113-180-4.
   [†]Equal contribution.

2. Suresh Chandra Baral[†], **P Maneesha**[†], Srishti Sen, Sagnika Sen, and Somaditya Sen, Chapter-1: An Introduction to the metal oxides, Optical Properties of Metal Oxide Nanostructures, Springer, eBook ISBN -978-981-99-5640-1.
   [†]Equal contribution.

3. Sayak Datta, **P Maneesha**, Prashant Kumar Mishra, Somaditya Sen, Chapter 7, Role of Defects in Metal Oxide Nanostructures, Optical Properties of Metal Oxide Nanostructures, Springer, 2023, eBook ISBN - 978-981-99-5640-1.

4. Suresh Chandra Baral[†], **P Maneesha**[†]**,** Ananya T. J, Srishti Sen, Sagnika Sen, Somaditya Sen, and E. G. Rini, Chapter 11, Rare earth manganites and related multiferroicity, CRC Press, Emerging Applications of Low Dimensional Magnets, 2022, eBook ISBN9781003196952.
   [†]Equal contribution.

5. **P Maneesha**[†]**,** Suresh Chandra Baral[†], E. G. Rini and Somaditya Sen, Chapter 11: Nanomagnetic materials; Structural and Magnetic Properties, CRC Press- Fundamentals of Low Dimensional Magnets, 2022, eBook ISBN9781003197492.
   [†]Equal contribution.

List of conferences & workshop presentations/attended during PhD

Oral presentations

1. CANDEE 2024, IIITM, Gwalior, December 03-05, 2024, **Best Oral presentation Award.**
2. RAM 2024 Bikaner, Rajasthan, November 15-16, 2024, **Oral presentation.**
3. 5th Virtual Conference on Materials Science and Engineering held during September 26-29, 2023, **Oral presentation.**
4. International conference on frontiers of material science (FOMS-19), material science organised by Department of Physics, St. Joseph's College, Devagiri (Autonomous) – December 2019, **Oral presentation.**

Poster presentations

5. E-MRS Fall meeting-2024, Warsaw University, Poland, September 16-19, 2024, **Poster Presentation.**
6. 68^{th} DAE Solid State Physics Symposium 2024**,** BARC, December 18-22, 2024, **Poster Presentation.**
7. 34th AGM of MRSI and 5th Indian Material Conclave, IIT BHU, December 12-16, 2024, **Poster Presentation.**

Workshops

8. School on Fundamental Crystallography and Workshop on Rietveld Refinement Analysis (SFCWRRA-2023), NIT Rourkela, 10-15 July 2024.
9. Participation in QIP course organised by Department of MEMS, IIT Indore, Material characterisation techniques – March 2021.
10. Participation in QIP course organised by the Department of Physics, IIT Indore, Synthesis and characterisation of thin films – March 2022.

TABLE OF CONTENTS

FIGURES

LIST OF TABLES

NOMENCLATURE

ACRONYMS

1. Chapter 1: Introduction

1.1. Introduction and Background

1.2. Perovskite Oxide

1.2.1. Distorted Perovskite oxide

1.2.2. Tolerance factor

1.2.3. Jahn-Teller distortion

1.2.4. Deviation from the ideal chemical composition

1.2.5. Influence of external factors

1.3. Crystal structure and Phase transitions of $BaTiO_3$

1.3.1. Order of Phase Transition

1.3.2. Hexagonal Polymorph of perovskite $BaTiO_3$

1.4. Ferroelectricity

1.5. Dielectric Properties

1.5.1. Polarisation Mechanisms in dielectric material

1.5.2. Temperature-dependent dielectric and phase transitions

1.5.3. Normal phase transition and Diffuse Phase transition

1.5.4. AC conductivity studies

1.5.5. Impedance and Modulus formalism

1.6. Literature Survey on the structural and functional properties of modified $BaTiO_3$

1.6.1. A site and B site doping in $BaTiO_3$

1.6.2. Multiferroicity in modified BTO

1.6.3. Magnetoelectric Coupling in modified BTO
1.6.4. Dielectric Properties in modified BTO
1.6.5. Theoretical studies on band structure and electron localisation of modified BTO
1.7. Applications of modified BTO
1.8. Objective of the Present Work
1.9. Thesis Outline

2. Chapter 2: Experimental methods and characterisation techniques

2.1. Sample Synthesis
2.1.1. Sol-Gel synthesis of $BaTiO_3$
2.1.2. Sintering of pellets
2.1.3. La and Fe doped $BaTiO_3$ sample preparation
2.1.4. Ca and Mn doped $BaTiO_3$ sample preparation
2.2. Characterisation Techniques
2.2.1. X-Ray Diffraction (XRD)
2.2.1.1. Rietveld Refinement
2.2.2. Raman Spectroscopy
2.2.3. UV-Visible Diffuse Reflectance Spectroscopy (UV-Vis DRS)
2.2.4. X-Ray Photoelectron Spectroscopy (XPS) for core level studies
2.2.5. Photo Electron Spectroscopy (PES) for valence band studies
2.2.6. X-Ray Absorption Spectroscopy (XAS)
2.2.7. Field Emission Scanning Electron Microscope (FE-SEM)
2.2.8. High Resolution Transmission Electron Microscope (HR-TEM)
2.2.9. Electron Paramagnetic Resonance Spectroscopy (EPRS)
2.3. Experimental techniques

2.3.1.1. Ferroelectric measurementsPositive Up Negative Down measurement (PUND)
2.3.2. Magnetic measurements
2.3.3. Dielectric measurements
2.3.4. Magnetodielectric Measurements
2.3.5. Magnetoelectric Measurements
2.4. Theoretical Density of States and Electron Localisation Function Calculations.

3. Chapter 3: Room temperature multiferroicity and magnetoelectric coupling in Ca/Mn-modified $BaTiO_3$
3.1. Introduction
3.2. Results and Discussions
3.2.1. XRD analysis
3.2.2. Raman Analysis
3.2.3. XPS analysis
3.2.4. Magnetic studies
3.2.5. Ferroelectric studies
3.2.5.1. PUND studies
3.2.6. TEM Analysis
3.2.7. Magnetoelectric coupling studies
3.3. Conclusions

4. Chapter 4: Hexagonal polymorphism induced structural disorder and dielectric anomalies of Ca/Mn modified $BaTiO_3$
4.1. Introduction
4.2. Results and Discussions
4.2.1. XAS Analysis
4.2.2. Optical band gap studies using UV-DRS

4.2.3. Valence Band studies using Photo Emission Spectroscopy
4.2.4. Theoretical Calculations
4.2.4.1. Density of States Calculation
4.2.4.2. Electron Localisation Calculation
4.2.5. Dielectric Properties
4.3. Conclusions

5. Chapter 5: Effect of oxygen vacancies and cationic valence state on multiferroicity and magnetodielectric coupling in La and Fe modified $BaTiO_3$

5.1. Introduction
5.2. Results and discussions
5.2.1. XRD Analysis
5.2.2. Raman analysis
5.2.3. FE-SEM analysis
5.2.4. XPS analysis
5.2.5. Electron Paramagnetic Resonance Spectroscopy
5.2.6. Ferroelectric studies
5.2.7. Magnetic studies
5.2.8. Multiferroicity and Magnetodielectric studies
5.3. Conclusions

6. Chapter 6: Defects induced band gap modification and Dielectric properties of La and Fe doped $BaTiO_3$

6.1. Introduction
6.2. Results and Discussions
6.2.1. Optical band gap studies UV-DRS absorption spectroscopy
6.2.2. Theoretical Density of States calculation
6.2.3. Electron localisation function calculation
6.2.4. Dielectric properties

6.2.5. AC conductivity studies

6.2.6. Impedance and modulus analysis

6.3. Conclusions

7. Chapter 7: Conclusions and Scope for Future Work

8. APPENDIX: Additional research works

8.1. **Appendix A:** Magnetoelectric Ca/Mn modified $BaTiO_3$ for Dielectric Resonator Antenna Application

8.2. **Appendix B:** $BaTiO_3$ and $CaMnO_3$ epitaxial film through Pulsed Laser Deposition

9. REFERENCES

LIST OF FIGURES

Figure 1.1: Two types of arrangement of ABO_3 perovskite structure (a) B site ion at the center of the unit cell, (b) A site ion at the center of the unit cell.

Figure 1.2: Degenerate d orbitals and the crystal field splitting of the orbitals into e_g and t_{2g} states.

Figure 1.3: Possible titanium ion positions, compatible with the Oh symmetry in the paraelectric phase: (a) static Ti at the ideal position in the center of the unit cell; (b) Ti disordered among eight off-center displacements along the eight <111> directions. Ti shifts are shown greatly exaggerated. (c) The assignment of off-center positions. n_i is the probability of and the Ti ion in the i^{th} off-center site.

Figure 1.4: (a) Variation of free energy density with temperature and polarisation. Arrows in wells indicate spontaneous polarisation states, (b) Variation of spontaneous polarisation with temperature, and (c) Variation of reciprocal dielectric constant with temperature for a first-order ferroelectric phase transition **(i)** First order transition **(ii)** Second order transition.

Figure 1.5: Schematic of the Hexagonal unit cell with Ti-O lattice and Ba-O lattice.

Figure 1.6: P-E hysteresis loop of ferroelectric.

Figure 1.7: Different polarisation mechanisms corresponding to the different frequency ranges.

Figure 1.8: Phase transition obtained in dielectric permittivity in $BaTiO_3$ [1].

Figure 1.9: Dielectric constant versus temperature showing (a) sharp phase transition, (b) diffused phase transition.

Figure 1.10: Relationship between multiferroic and magnetoelectric materials. Illustrates the requirements to achieve both in a material.

Figure 1.11: Schematic illustrating different types of coupling present in materials interconnection between Piezoelectricity, magnetoelectric coupling, and magnetostriction.

Figure 2.1: Schematic of the Sol-Gel process.

Figure 2.2: Flow chart of the different information obtained from the powder diffraction.

Figure 2.3: Schematic of the Bragg equation.

Figure 2.4: Schematic of the X-Ray generation and the characteristic radiations generated.

Figure 2.5: Schematic diagram of the Bragg Brentano geometry.

Figure 2.6: Flow chart of steps in the process of structural analysis from Powder Diffraction Data.

Figure 2.7: Picture of Bruker D2 Phaser XRD.

Figure 2.8: (a) Schematic of the different lines in Raman scattering, (b) Energy excitation diagram of different Raman lines.

Figure 2.9: Block diagram of the instrumentation of the Raman spectrometer.

Figure 2.10: Photo of LabRAM Raman spectrometer.

Figure 2.11: Schematic of the specular reflection and Diffuse reflectance.

Figure 2.12: Schematic of the instrumentation of the UV-DRS.

Figure 2.13: Shimadzu UV-Vis DRS spectrophotometer.

Figure 2.14: Schematic diagram illustrating the XPS equation that includes X-ray energy (hν), binding energy (B.E.), and the kinetic energy measured (K.E). The sample's work function is represented by φ_S and spectrometer work function (φ_{Sp}).

Figure 2.15: Schematic of the XPS instrumentation.

Figure 2.16: Instrumentation of the PES in Beamline 10, Indus II synchrotron facility.

Figure 2.17: Schematic of the X-Ray absorption and the scattering of the outgoing photoelectron wave.

Figure 2.18: Different regions of XAS spectra.

Figure 2.19: Block diagram of the EXAFS measurement setup in Indus BL 9 synchrotron radiation facility.

Figure 2.20: EXAFS measurement instrumentation in Beamline 9, Indus II synchrotron radiation facility.

Figure 2.21: Schematic of the different kinds of radiation emitted when high-energy electrons impinge on the sample.

Figure 2.22: Block diagram of the FE-SEM.

Figure 2.23: Photo of FE-SEM Instrument.

Figure 2.24: Block diagram of the TEM instrument.

Figure 2.25: Photo of TEM Instrument.

Figure 2.26: Principle of EPR spectroscopy for the detection of unpaired electrons and energy levels in a magnetic field.

Figure 2.27: Block diagram of EPR spectrometer.

Figure 2.28: EPR spectrometer.

Figure 2.29: Block diagram of Sawyer tower circuit for ferroelectric hysteresis measurement.

Figure 2.30: Experimental setup for P-E loop measurement.

Figure 2.31: PUND measurement setup.

Figure 2.32: (a) Dynacool 9T PPMS setup (b) sample holder.

Figure 2.33: Block diagram of LCR meter setup.

Figure 2.34: Dielectric measurement setup.

Figure 2.35: Block diagram of magnetodielectric setup.

Figure 2.36: Magneto dielectric measurement setup.

Figure 2.37: Block diagram of Magnetoelectric measurement setup.

Figure 2.38: Magnetoelectric measurement setup (1), (2), (3), (4), (5), (6).

Figure 3.1 (a) XRD data of all samples with the CIF file of the P4mm and $P6_3/mmc$ space groups. (b) Zoomed-in image of the variation in the intensity of the hexagonal peak H(104) and tetragonal peak T(110) with composition. (c) Zoomed-in image of the splitting of tetragonal T(002) and T(200) peaks.

Figure 3.1_1: Refinement plots of all the samples, the inset shows the zoomed image of the fitting of H(104) and T(110) peaks.

Figure 3.2: (a) Rietveld refinement of the BCTMO1 sample with the P4mm and $P6_3/mmc$ space groups. Inset: (a1) Zoomed-in image of the T(110) and H(104) peaks of the refinement using both phases. (b) Variation in the phase percentage of the tetragonal and hexagonal phases with composition.

(c) Schematic of the crystal structure of tetragonal P4mm and hexagonal $P6_3/mmc$ using VESTA software.

Figure 3.3: (a) Schematic of the P4mm structure and different types of Ti–O and Ba–O bonds. (b)Schematic of the $P6_3/mmc$ structure. (b1) Schematic of the Ti and O lattice in the $P6_3/mmc$ structure with two types of Ti–O bonds. (b2) Schematic of the Ba and O lattice in the $P6_3/mmc$ structure with two types of Ba–O bonds.

Figure 3.3_1: Variation of Ti-Ti separation in octahedral dimer in hexagonal $BaTiO_3$ with Mn doping.

Figure 3.4: (a) Displacement of Ti2 atoms in the opposite direction from the centrosymmetric position of the Ti_2O_9 dimers. (b) Displacement of consecutive Ba atoms in the opposite direction from the Ba–O plane along the c direction (represented by blue arrows) and the b direction (represented by black arrows).

Figure 3.5: (a) Variation in tetragonal and hexagonal lattice parameters with composition. (b) Variation in the average Ba/Ca–O and Ti/Mn–O bond lengths with composition. (c) Variation in the tetragonal and hexagonal volumes and the tetragonal c/a ratio with composition. (d) Variation in the tetragonal and hexagonal Ti–O–Ti bond angles with composition.

Figure 3.6: (a) Raman spectra of all samples. (b) Zoomed image of the variation in the 305 cm^{-1} tetragonal mode. (c) Zoomed image of the variation in the 635 cm^{-1} hexagonal mode and 720 cm^{-1} tetragonal mode. (d) Variation in the intensity of the 305 cm^{-1} and 635 cm^{-1} modes with composition. (e) Variation in the Raman shift of the 305 cm^{-1} and 635 cm^{-1} modes with composition.

Figure 3.7: Deconvoluted XPS spectra of the BCTMO1 sample (a) Ba 3d, Ti 2p, and O 1s data before etching. (b) Ba 3d, Ti 2p, and O 1s data after etching.

Figure 3.8: Deconvoluted XPS spectra of the BCTMO1 sample (a) Ca 2p and Mn 2p data before etching. (b) Ca 2p and Mn 2p data after etching.

Figure 3.9: Fractional variation in f_{OII}, f_{3+} (a) before etching and (b) after etching [inset shows the individual variation of the fractional area of f_{Ti3+}, f_{Mn3+}].

Figure 3.10_1: Deconvoluted XPS spectra of all the samples, (a) Ba 3d before etching, (b) Ba 3d after etching.

Figure 3.10_2: Deconvoluted XPS spectra of all the samples, (a) Ca 2p before etching, (b) Ca 2p after etching.

Figure 3.10_3: Deconvoluted XPS spectra of all the samples, (a) Ti 2p before etching, (b) Ti 2p after etching.

Figure 3.10_4: Deconvoluted XPS spectra of all the samples, (a) Mn 2p before etching, (b) Mn 2p after etching.

Figure 3.10_5: Deconvoluted XPS spectra of all the samples, (a) O 1s before etching, (b) O 1s after etching.

Figure 3.11: M–H loop of (a) BTO, (a1) Diamagnetic subtracted M–H loop of BTO, (a2) Zoomed-in plot of the diamagnetic subtracted M–H loop of BTO, (b) M–H loop of BCTMO1. (a1) Paramagnetic subtracted M– H loop of BCTMO1, (a2) Zoomed-in plot of the paramagnetic subtracted M–H loop of BCTMO1, (c) M–H loop of BCTMO2. (d) M–H loop of BCTMO3.

Figure 3.12: M–H loop of BTO (after diamagnetic subtraction), BCTMO1 (after paramagnetic subtraction), BCTMO2, and BCTMO3; the inset shows the zoomed image of the M–H loop.

Figure 3.13: (a) Room temperature P–E loop of all the samples, (b) Comparison of the room temperature P–E loop of all the samples, [Inset: zoomed-in image showing the variation in the Pr value of all the samples, (c) Variation in P_m and P_r obtained from the unsaturated P–E loop.

Figure 3.14: PUND measurement of all doped samples at 1.5 kV.

Figure 3.15: x=0 →(a) TEM image of tetragonal lattice, (b) background subtracted lattice plane image of (a), SAED pattern of (a), x=0.03→ (a) TEM image of hexagonal and tetragonal lattice, (b), (c), (d) background subtracted lattice plane image of selected region. x=0.06→ (a) TEM image of hexagonal and tetragonal lattice, (b), (c), (d) background-subtracted lattice plane image of selected region. x=0.09→ (a) TEM image of hexagonal and tetragonal lattice, (b), (c), (d), (e) background-subtracted lattice plane image of selected region, (f) SAED pattern corresponding to the hexagonal region.

Figure 3.16: (a) P–E hysteresis of BCTMO1, (b) M–Hysteresis of BCTMO1, (c) Polarisation with an AC magnetic field with a bias DC magnetic field of 600 Oe, (d) Variation in α_{ME} with a DC magnetic field at a constant AC magnetic field of 5 Oe.

Figure 4.1: (a) XANES data of the Ti K-edge with the absorption peak E and all the pre-edge features marked as A, B, C, and D. (b) Variation in the features with samples. Inset (b1) is the

zoomed-in image of absorption peak E. Inset (b2) is the zoomed-in image of the pre-edge feature C. Inset (b3) is the zoomed-in image of the pre-edge feature B.

Figure 4.2: Deconvoluted XANES spectra of the Ti edge of all samples.

Figure 4.3: (a) Schematic of the displacement of Ti from the centrosymmetric position in the P4mm tetragonal structure of $BaTiO_3$. (b) Variation in Ti displacement from the centrosymmetric position of BaTiO3 (P4mm) and variation in the intensity of the Ti pre-edge feature B with composition.

Figure 4.4: (a) XANES data of the Mn K edge. (b) Variation in the features with samples. Inset (b1) shows the zoomed-in images of the absorption peak. Inset (b2) shows the zoomed-in image of the pre-edge feature.

Figure 4.5: Fourier transformed EXAFS spectra of (a)Ti edge, (b) Mn edge.

Figure 4.6: (a) UV-DRS tauc plot of all samples, (b) Variation of E_g and E_U with substitution.

Figure 4.7: (a)VB spectra of different samples, (b) Deconvoluted VB spectra.

Figure 4.8: Variation of the normalised area of IGS of peaks D and E with substitution.

Figure 4.9: DOS plot of (a) x=0 tetragonal, (b) x=0.125 Ca and Mn doped tetragonal, (c) DOS plot of x=0 hexagonal BTO, (a) DOS plot of x=0.125 Ca and Mn doped hexagonal BTO.

Figure 4.10: (a) (001) plane of Ca doped Ba-O lattice and Mn doped Ti-O lattice in tetragonal $BaTiO_3$ for x=0.125, (b) Replacement of dimer Ti atoms by Mn atoms in (-101) plane hexagonal

lattice and that of (001) plane is shown in for x=0.125, (c) The replacement of centrosymmetric octahedral Ti atoms in the hexagonal lattice by Mn atom in the (-101) plane and (001) plane for x=0.125.

Figure 4.11: FESEM micrographs of all samples.

Figure 4.12: (a)RT permittivity variation with frequency, (b) RT tanδ variation with frequency.

Figure 4.13: Temperature-dependent permittivity variation showing ferroelectric to paraelectric phase transition.

Figure 4.14: Comparison of the phase transition from a sharp nature to a diffuse nature with doping.

Figure 4.15: 1/ε v/s T plot of all samples.

Figure 4.16: ln $(1/\varepsilon - 1/\varepsilon_m)$ vs ln(T-Tm) plots for all samples.

Figure 4.17: dε/sT v/s T plots of all samples.

Figure 4.18: (a) Diffuse phase transition in x=0.09 sample, (b) dε/dT variation with temperature.

Figure 5.1: (a) XRD pattern of all the prepared samples, (b) Shift of 101/110 peak, (c) Splitting of 002/200 peak.

Figure 5.2: Rietveld refinement plot of samples. The inset shows the zoomed image of the 101/110 peak and 002/200 mode.

Figure 5.3: The schematic of the off-centering of the Ti cation and O anion.

Figure 5.4: (a) Variation of a,b, and c lattice parameters for the tetragonal and cubic phase (inset) variation of c/a and unit cell volume with composition (b) Schematic of the

tetragonal P4mm structure. (c) Variation of avg. A-O and B-O bond length (d). Variation of three B-O bond lengths (e) Variation of three A-O bond lengths.

Figure 5.5: Schematic of the variation of (1) 180^0 O_p-B-O_p and A_1-O_a-A_3 bond angles. (2) two types of 90^0 bond angle A_1-O_p-A_2 and A1′-Op-A2′, for all samples. (3a) BTO to represent the bond angles. (3b) O_p-B-O_p and A_1-O_a-A_3, A1-Op-A2′, Oa-B-Oa bond angle with composition. (3c) Plot of A_1-O_p-A_2, A_1′-O_p-A_2′, B-Oa-A, B-Op-A bond angles with composition. (3d) Plot of the displacement of the B ion and the average. An ion with a composition.

Figure 5.6: Area fraction calculated from Ti^{3+}, O_v, and Fe^{2+}.

Figure 5.7: (a) Raman spectrum of all samples, (b) Zoomed image of the disorder phonon mode at 770 $cm^{-1,}$ (c) Correlation of c/a ratio with intensity variation of 305 cm^{-1} with composition, (d) Correlation of the variation of B-O bond length and Raman shift of 305 cm^{-1} with composition.

Figure 5.8: Surface morphology of sintered pellets for (a)BTO, (b)BLFT1, (c)BLFT2, (d)BLFT3 (e) BLFT4 compositions, and the inset shows the grain size distribution curves for the respective compositions. (f) Variation of grain size with composition.

Figure 5.9: La 3d core level XPS spectra of all samples.

Figure 5.10: Fe 2p core level XPS spectra of all samples and f_{Fe}^{2+} with composition.

Figure 5.11: Ti 2p core level XPS spectra of all samples and f_{Ti}^{3+} with composition.

Figure 5.12: Ba 3d core level XPS spectra of all samples and $f_{Ba\text{-}shoulder}$ with composition.

Figure 5.13: O 1s core level XPS spectra of all samples and f_{Ov} with composition.

Figure 5.14: P-E loop of the samples at 30 kV and Variation of P_r and P_s with composition and correlation of variation of P_r and P_s with c/a ratio.

Figure 5.15: EPR signals of (a) BTO, (b)BLFT1, the derivative of the EPR signal (c) BTO, (d) BLFT1.

Figure 5.16: (a) M-H loop of the samples at 60 kOe [Inset: Zoomed M-H loop at 6 kOe shows small opening] (b)Diamagnetic and paramagnetic subtracted M-H loop.

Figure 5.17: (a)Schematic of the BMP in BTO, (b) Schematic of BMP in BLFT.

Figure 5.18: (a) Comparison of the M-H curve of all the samples together, (b)Variation in the M_s and M_R value with composition, (c) Variation of Ti-O-Ti bond angle with composition.

Figure 5.19: Variation of ε_r with frequency for all the samples under different magnetic fields from 0 T to 1 T.

Figure 5.20: Variation of MC% of all samples with magnetic field at (a)-(e)1kHZ, 10kHZ, 100 kHz, (f) Comparison of MC% for all the samples at 1 kHz.

Figure 5.21: Variation of M_r, M_s, and MC% at a magnetic field of 1 T and an electric field of 10 kHz for all compositions.

Figure 6.1: (a) UV-visible tauc plot of the samples, (b) enlarged view of the pre absorption edge, (c) Variation of E_g and E_U with composition.

Figure 6.2: DOS of Ba 5p states, La 5d states, Ti 3d states, Fe 3d states, O 2p states. (a) BTO and (b) BLFT3.

Figure 6.3: Schematic of the electron density plots of the (a) Ba-O layer in the a–b plane of BTO. (b) Ba-O layer in the a–b plane for La atoms doped in the Ba site. (c) Ti-O layer in the a–b plane of BTO. (d) Ti-O layer in the a–b plane of Fe atoms doped in the Ti site.

Figure 6.4: Room temperature (a) dielectric permittivity and (b) loss tangent with frequency.

Figure 6.5: Variation of dielectric permittivity with temperature and tanδ in the temperature range 50 ^{0}C to 200 ^{0}C. [Solid circles represent permittivity, and a hollow star indicates tanδ].

Figure 6.6: Fitted AC conductivity plots with Johnscher's double power law.

Figure 6.7: n−T plots of all samples.

Figure 6.8: Fitted 6/(1-n) v/s T plots of all samples

Figure 6.9: Plots of Z′ and M′ with frequency.

Figure 6.10: (a) Variation of Z″ with frequency, (b) Variation of M″ with frequency.

Figure 6.11: Combined plots of the imaginary part of impedance Z″ and the imaginary part of modulus M″.

LIST OF TABLES

Table 2.1: Laser sources of Raman spectroscopy with wavelength.

Table 3.1: Magnetic measurement results.

Table 3.2: PUND measurement results of the BCTMO samples with unsaturated P-E loops.

Table 3.3: Maximum polarisation, Saturation magnetisation, and magnetoelectric coupling values reported for single chemical phase bulk material at room temperature.

Table 4.1: Obtained values of E_g and E_U from UV-DRS.

Table 5.1: Variation of unit cell parameters, phase fraction, and unit cell volume with doping.

Table 5.2: Maximum magnetocapacitance (%) values were collected from literature data and compared with the present system.

Table 6.1: Fitted values of 6/(1-n) v/s T plots.

NOMENCLATURE

g	Lande's g-factor
H_c	Coercivity
T_c	Curie temperature
h	Planck's constant
K_B	Boltzmann constant
M_R	Remnant Magnetisation
M_S	Saturation Magnetisation
P_r	Remnant Polarisation
P_s	Saturation Polarisation
μ_B	Bohr Magneton
t	Goldschmidt's tolerance factor
Å	Angstrom
λ	Wavelength
μ	Micro
m	Milli
σ	Sigma
~	Tilde
χ	Chi
ω	Omega
eV	Electron volt
Oe	Oersted

emu	Electromagnetic unit
cm	Centimetre
nm	Nanometer
a.u.	Arbitrary unit
T	Tesla
G	Guass
k	Kilo
hkl	Miller Indices
°	Degree
°C	Degree Centigrade
>	Greater than
<	Less than
≥	Greater than or equal to
≤	Less than or equal to
E_g	Band gap
E_U	Urbach energy

ACRONYMS

$BaTiO_3$	BTO
$Ba_{(1-x)}La_{(x)}Ti_{(1-y)}Fe_{(y)}O_3$	BLFT
$Ba_{(1-x)}Ca_{(x)}Ti_{(1-y)}Mn_{(y)}O_3$	BCTMO
Bound Magnetic Polarons	BMP
Charge-coupled device	CCD
Conduction Band minimum	CBM
Diffuse Reflectance Spectroscopy	DRS
Diffused Phase transition	DPT
Density Of States	DOS
Extended X Ray Absorption Fine Structure	EXAFS
Electron Localisation Function	ELF
In Gap State	IGS
Ferromagnetism	FM
Ferroelectric	FE
Field Emission Scanning Electron Microscopy	FESEM
Full Width at Half Maxima	FWHM
High Resolution Transmission Electron Microscope	HRTEM
Localised Vibrational Modes	LVM
Magnetoelectric coupling	MEC
Magnetocapacitance effect	MCE
Magnetodielectric effect	MDE

Oxygen Vacancies	O_v
Pseudo Jahn-Teller effect	PJTE
Photo Electron Spectroscopy	PES
Positive Up Negative Down	PUND
Polar Nano Region	PNR
Physical Property Measurement System	PPMS
Room Temperature	RT
Temperature Dependent	TD
Transition Metal	TM
Urbach Energy	E_U
Valence Band maximum	VBM
Vibrating Sample Magnetometer	VSM
X-ray Diffraction	XRD
X-Ray Photo Electron Spectroscopy	XPS
X Ray Absorption Spectra	XAS
X Ray Absorption Near-Edge Spectrum	XANES
Near-Edge Absorptivity Ratio	NEAR

CHAPTER 1
INTRODUCTION

In this chapter, a brief description of the structure and functional properties of $BaTiO_3$ has been discussed. A literature survey on the multifunctional properties of $BaTiO_3$ is illustrated. The chapter is concluded with motivation and an outline of the thesis and the questions that the present thesis seeks to answer.

1.1 Introduction and Background

Barium Titanate, $BaTiO_3$ (BTO), has been of practical interest for more than 60 years because of its attractive properties. It has a chemically and mechanically stable crystal structure and ferroelectricity at and above room temperature, an easy synthesis process in the form of ceramic polycrystalline samples. The high dielectric constant and low loss characteristics made BTO a good candidate for capacitor applications. The wide variety of multifunctional properties shown by BTO is due to its perovskite structure, which can be chemically modified to enhance different properties and can be utilised in a wide range of applications in semiconductors, thermistors, and piezoelectric devices, and has become one of the most important ferroelectric ceramics.

BTO was one of the very first polycrystalline ceramic materials that exhibited ferroelectricity. During World War II, this material became of interest as a ceramic material that has a very high dielectric permittivity for capacitor applications. At that time, naturally occurring Rochelle salt and related hydrogen bonding crystals were the only materials believed to have ferroelectricity. In 1945 and 1946, the work of Hippel's group [2] at the Massachusetts Institute of Technology and Wul and Goldman [3] in the USSR established that the source of the unusually high dielectric constant in BTO was associated with its ferroelectric properties. After this discovery, the physical properties and phase transitions of BTO were extensively studied by various researchers around the world. The crystal structure description of BTO was proposed by Megaw [4], Kay and Voudsen [5] in the United Kingdom, and soon confirmed by Miyake and Ueda [6] in Japan. The discovery of the alignment of domains in BTO, with the application of an external electric field, gave the scientific world the idea of a polycrystalline material to act as a single crystal and introduced the piezoelectric properties in ferroelectric BTO [7]. After this, the ferroelectric switching of domains under mechanical stress has been investigated by

Forsbergh [8]. This makes a breakthrough in the industry in electromechanically active ceramics for commercial applications [9].

Currently, miniaturisations of electronic devices need giant dielectric constant ceramics with a large electromechanical coupling factor, a wide range of temperature stability, high energy storage density with efficiency, high mechanical strength, and multifunctional properties, which can be achieved by different modifications in $BaTiO_3$. Multifunctionality on $BaTiO_3$ is a constant requirement for technology developments that will lead to a significant number of industrial and commercial applications. Multiferroicity in BTO is in an infant stage of industrialisation. Extensive research in this area can lift the field to an extensive breakthrough in the commercialisation of these materials. Hence, this thesis is entirely devoted to enhancing the functional properties of lead-free $BaTiO_3$-based ferroelectric material, mainly focusing on the multiferroic, dielectric, and transport properties.

1.2 Perovskite Oxide (ABO_3)

The word perovskite came into existence after the discovery of the mineral $CaTiO_3$'s structure in 1993 by Gustav Rose from the Ural Mountains [10]. The structure of this mineral was named after Russian mineralogist Lev Perovski as perovskite. Perovskites are one of the versatile materials for use in various electronics applications that have gained more attention and grown rapidly due to their low cost, versatile structures, and various physical and chemical properties [11].

Perovskites are of the form ABX_3, with the A-site being 12-coordinated and occupied by rare earth or alkaline earth ions with large ionic radii. The B-site is octahedrally coordinated and typically occupied by a transition metal (TM) ion or a rare-earth ion with smaller ionic radii. X site occupied by usually Oxygen or Halide ions [12]. Perovskite oxides are in the family of oxides with formula ABO_3 and are the first discovered perovskite-type materials from the earth's surface. It contains corner-

sharing BO_6 octahedra, and the voids are filled by the larger radius A cations.

The various crystallographic arrangements of the cations, which result in stable structures, are the reason for the multiple functionalities of these materials. Hence, the alteration of crystal structure can exhibit a wide variety of physicochemical, optical, and electronic functional properties. The structure correlation of various properties shown by different materials is an active area of research. The ideal structure of perovskite oxides is shown in Figure 1.1, for two identical arrangements of atoms, which is the general structure of perovskites. Figure 1.1(a) B cation is placed in the center of the cube, and A cations at the corners of the cube, and an anion O occupies the face center of the cubic structure. An identical arrangement is also possible in which the center of the cube is occupied by A cation and a B cation is located at each corner, and 12 edge centres are occupied by O atoms, Figure 1.1(b).

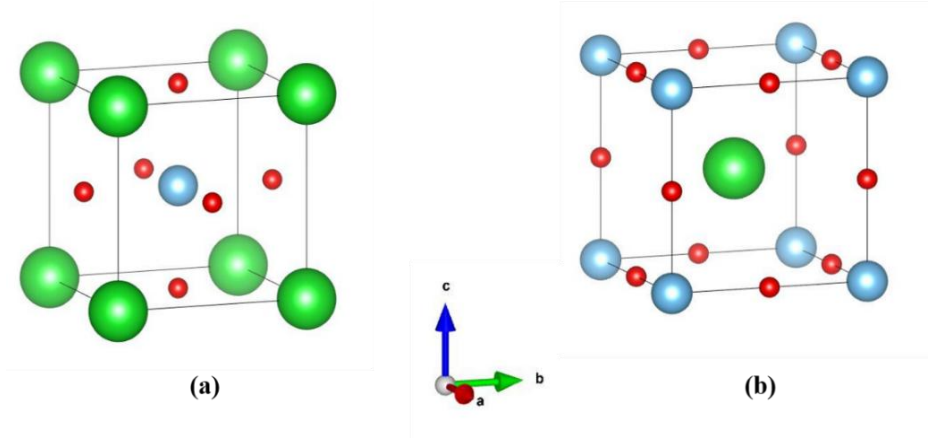

Figure 1.1: *Two types of arrangement of ABO_3 perovskite structure (a) B site ion at the center of the unit cell (b) A site ion at the center of the unit cell*

The selection of A and B cations is vital in exhibiting the different properties shown by the perovskite material. These oxides show different structures of cubic, tetragonal, orthorhombic, rhombohedral, and hexagonal structures depending on the temperature, pressure, cation radii, synthesis conditions, etc. In order to tune the desired properties, proper substitution

of cations can be done to modify the crystal structure and enable the material for various applications.

In addition to the above normal perovskite structure, there are Layered perovskites, having a layered structure that consists of infinite 2D slabs of the ABO_3 type structure, which are separated by some motif. The general formula is $A_{(n-1)}B_{(n)}O_{(3n+1)}$, where "n" indicates the size of the 2D slabs. n=1 means the slab is one BO_6 octahedron thick. n=2 means two BO_6 octahedra thick, etc. The differentiating characteristics for the layered perovskites are 1) the motif that separates the layers, and 2) the offsetting of the layers from each other. Sr_2RuO_4 (n=1) and $Sr_3Ru_2O_7$ (n=2) are examples for layered perovskites [13].

Double perovskites are another category of perovskite with an ordered arrangement of cations in the perovskite lattice. Fractional substitution to a different extent at A and B lattice sites with an ordered cationic structure provides a double perovskite structure. A site ordering leads to $AA'B_2O_6$ double perovskite, B site ordering can form $A_2BB'O_6$ double perovskite, and both A site and B site ordering can form $AA'B'B''O_6$ double perovskite structures [12]. The double perovskite structure is so named because the unit cell is twice that of perovskite. This ordering can generate various exceptional properties that can lead to multifunctionalities for various applications [14].

The crystal structure of perovskite shown in Figure 1 is an ideal arrangement, but in practice, there will be a lot of distortions related to the ionic radii of cations, octahedra distortions, variations with chemical doping, external factors such as temperature and pressure.

1.2.1 Distorted Perovskite oxide

The distortions in the ideal perovskite structure can be due to changes in the ideal chemical composition, external factors like temperature and pressure, tilting of octahedra, Jahn-Teller distortions, etc. The symmetry of

the crystal structure is thus reduced by these distortions and incorporates various physical properties. These distortions can also be carried out by modifying the structure with A and/or B substitutions. The variations in the chemical structure of the perovskites due to different factors are described below;

1.2.1.1 Tolerance factor

The stability of the ABO_3 perovskite can be described by the Tolerance factor, which is related to the cations' ionic radii. In 1926, Victor Goldschmidt introduced the concept of the tolerance factor [15]. He has derived a formula for describing the tolerance factor calculated from the radii of the cations and anions in the crystal lattice.

For a cubic unit cell, the axis 'a is geometrically related to the ionic radii of A-site atom (R_A), B-site atom (R_B), and O atom (R_O) as given by the following equation:

$$\sqrt{2} \times (R_A + R_O) = 2 \times (R_B + R_O)$$

The ratio of these two expressions of the cell length is known as Goldschmidt's tolerance factor (t). It gives an estimation of the degree of distortion. Substitution creates lattice strain in the perovskite structure; as a result, the unit cell structure departs from the ideal cubic symmetry. This is based on the ionic radii. The tolerance factor for the compound with ionic bonding is given by [16];

$$t = \frac{R_A + R_B}{\sqrt{2}(R_B + R_O)}$$

Where R_A, R_B, and R_O are the ionic radii of A-site, B-site, and O ions, respectively. For an ideal perovskite structure, the value of the tolerance factor is one.

1.2.1.2 Jahn-Teller distortion

In the electronically degenerate state, the orbitals are said to be asymmetrically occupied and hence get more energy. Therefore, the system tries to get rid of extra energy by lowering the overall symmetry of the molecule, i.e., undergoing distortion, which is otherwise known as Jahn-Teller distortion (effect) [17]. Transition metal TM ions at the B site occupying the BO_6 octahedra in ABO_3 perovskite have degenerate d orbitals [Figure 1.2]. The Jahn–Teller distortion (JTD) occurs because the unequal occupation of orbitals in these degenerate energy levels is unfavourable. To avoid these unfavourable electronic configurations, molecules distort (lowering their symmetry) to render these orbitals no longer degenerate. This distortion leads to the elongation and compression of the ideal octahedral bonds and results in the deformation of the oxygen octahedra surrounding the B cation due to the splitting of the degeneracy of the d orbitals to e_g and t_{2g} levels and resulting in the lowering of electronic energy. For example, in manganites, having Mn^{3+} cations ($3d^4$) in an octahedral environment exhibits JTD, whereas the Mn^{4+} cations ($3d^3$) would not show this effect because there is no unequal occupation of electrons in the degenerate energy levels and hence no net lowering of the electronic energy by a distortion. This effect is termed as first-order Jahn-Teller effect.

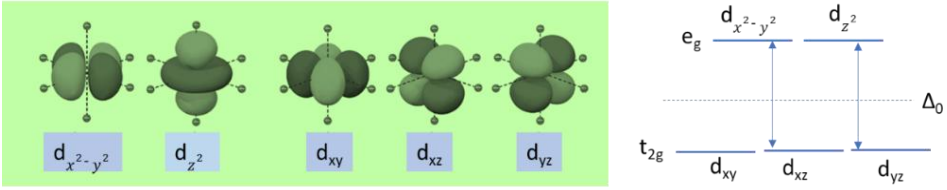

Figure 1.2: *degenerate d orbitals and the crystal field splitting of the orbitals into e_g and t_{2g} states.*

In an extension of the JTD, there is a possibility that spontaneous distortion can take place even if the ground state is non-degenerate. This distortion will happen due to the interaction with the surrounding ligand or

nearby atoms and goes to an excited state in which the degeneracy is slightly removed. This will lead to an excited state of the transition metal has unequal occupation of d-orbitals with identical energies. This is called the second-order Jahn-Teller distortion. Since it arises due to the vibronic coupling between two electronic states (ground and excited) due to pseudo-degeneracy, it is also named as Pseudo Jahn-Teller distortion (PJTD) [18].

In BTO, Ti^{4+} has d^0 electrons, and there is no possibility of the Jahn-Teller effect. However, the presence of Ti^{3+} or other TM ions in the octahedral environment of BTO can induce spontaneous polarisation due to local vibronic interactions, resulting in pseudo Jahn-Teller effects and can facilitate ferroelectricity [19].

1.2.1.3 Deviation from the ideal chemical composition

The variable valence state in the A or B site of the ABO_3 perovskite can lead to distortions in the crystal structure. The valence states variations in the cations can also result in variations in O content and lead to tilting of the octahedra, or changes in the bond lengths. This can lead to a transition to different space groups. For example, in $SrFeO_3$, Sr is in the +2-oxidation state, and Fe should be +4 ideally. Whereas, Fe ion's valence state can change between '+3 and +4' by heating, and reducing/oxidising environment. This will create oxygen vacancies (O_v), and FeO_5 square pyramids are formed, leading to $SrFeO_{3-\delta}$. This is an example of defect perovskite. [20].

Distortions in the perovskite structure can also be made by chemical modification of the BTO lattice by doping. For example, doping of Zr in the Ti site of BTO can induce an orthorhombic space group of BTO. By the modification of the tetragonal structure, La or Sr doping in the Ba site transforms the tetragonal BTO to a cubic space group [21]. TM doping at the Ti site in BTO can trigger hexagonal BTO due to the increase in O_v and further formation of dimers instead of single octahedra. [22].

1.2.1.4 Influence of external factors

External factors like temperature and pressure can induce structural modifications and octahedral tilting, and the displacement of atoms leads to structural transitions with temperature or pressure. Depending on the synthesis methods, different crystal structures, morphologies, and particle sizes of the BTO can be varied.

Temperature can influence the phase transition of BTO. Temperature-induced displacement of ions and variations in the ordering of the dipoles can induce various phase transitions at different temperatures. BTO shows four structural transitions with increasing temperature: Rhombohedral (*R3m*) → -90 ºC → Orthorhombic (*Amm2*) → 5 ºC →Tetragonal (*P4mm*) →120 ºC →Cubic ($Pm\bar{3}m$) [1]. In addition to this, there is polymorphic form of BTO formed due to the face sharing of two octahedra, the hexagonal ($P6_3/mmc$). The calcination and sintering temperatures determine this polymorphic form. For example, sintering at 1200 °C can lead to the tetragonal *P4mm* space group, whereas sintering above 1430 °C leads to stabilisation of hexagonal $P6_3/mmc$ space group of BTO [23].

The influence of pressure can change the electronic structure and bond type, often accompanied by changes in the coordination geometry of BTO. The ferroelectric and piezoelectric properties of BTO can be varied by the application of pressure. The high-pressure synthesis of BTO can provide different morphologies in BTO [24].

The synthesis conditions of BTO can have a great influence on the structural stabilisation. The precursors used for the synthesis, temperature, pressure, pH of the synthesis condition, physical or chemical route of synthesis, etc, will determine the exact crystal structure stabilised for BTO.

1.3 Crystal structure and Phase transitions of $BaTiO_3$

Perovskite BTO can exist in four different space groups, as shown in Table 1. The phase transition from one space group to another can be

described in terms of the displacive nature of the Ti ion that can induce spontaneous polarisation or the order-disorder nature of the Ti sites around the centrosymmetric position.

Over the past several years, the dynamics of phase transition in BTO have been classified in terms of being either displacive or order-disorder type. A displacive phase transition (microscopically nonpolar) accompanies a breaking of the point group symmetry of the unit cell, i.e., a structural phase transition of a crystal at a certain temperature. This transition typically occurs in materials where a soft transverse optic phonon mode becomes unstable. Some other experimental data, like inelastic neutron scattering, also support this mechanism [25]. Some of the studies indicate that the displacement of Ti from the centrosymmetric cubic phase leads to phonon instability, whose eigenvector in each phase has the symmetry of the ionic displacements that lead to the next lower ferroelectric phase [26]. On the other hand, diffuse X-ray scattering data suggest that the transition also occurs via an order-disorder transition (microscopically polar) mechanism. An order-disorder crystal is characterised by local atomic configurations that do not necessarily share symmetry elements with the macroscopic order parameter. In this scenario, the overall crystal structure remains the same, but the dipoles become thermally randomised. Neutron diffraction and NMR were performed on the crystals, doped with paramagnetic centres. These studies have revealed the existence of strong anharmonicity of the local potential of Ti ions [27]. Along with that, theoretical studies also provide substantial proof for the coexistence of both mechanisms in the case of BTO.

According to the displacive phase transition, the off-center displacement of the Ti ion in the TiO_6 Octahedra of the prototype cubic lattice from the centrosymmetric position leads to polar forms. Each of these polar forms can be considered as deformations of the cubic unit cell along an edge [00l] in tetragonal, along a face diagonal [011] in orthorhombic, or

along a body diagonal [111] in rhombohedral. Hence, the orientation of electric dipoles will be accordingly in these directions for different polar forms. The spontaneous polarisation in these polar forms may be parallel to any of the eight equivalent directions in the cubic phase. The long range of the electric dipoles results in macroscopic spontaneous polarisation (P_s), ferroelectricity, and spontaneous polarisation [28].

Table 1: Unit cell parameters of perovskite $BaTiO_3$ in different space groups

Crystal structure	Space group	Lattice Parameters	Volume	Spontaneous Polarisation Direction	T_c
Rhombohedral	*R3m*	a=b=c=4.00385 α=β=γ=89.843°	64.1722	[111]	-80°C to -90 °C
Orthorhombic	*Amm2*	a=3.99, b=5.669, c=5.682 α=β=γ=90°	128.522	[011]	-5 °C –15 °C
Tetragonal	*P4mm*	a=b=3.9905, c=4.0412 α=β=γ=90°	64.3524	[001]	120 °C –130 °C
Cubic	*Pm-3m*	a=b=c=4.00730 α=β=γ=90°	64.3510	0	

From calculations of the local adiabatic potential, Bersuker suggested that the titanium atom sits in one of eight potential minima, which are displaced from the cell center in the eight (1 1 1) directions [Figure 1.3].

At very low temperatures, titanium atoms in barium titanate (BTO) show a strong, long-range connection in all three spatial directions; they move together in a coordinated way from one unit cell to the next. In this state, known as the rhombohedral phase, all the titanium atoms shift in the same (111) direction. As the temperature increases and the material goes through different phase transitions, these connections gradually weaken, losing coordination in one direction at each step. This causes the titanium atoms to become more randomly arranged among the possible (111) directions.

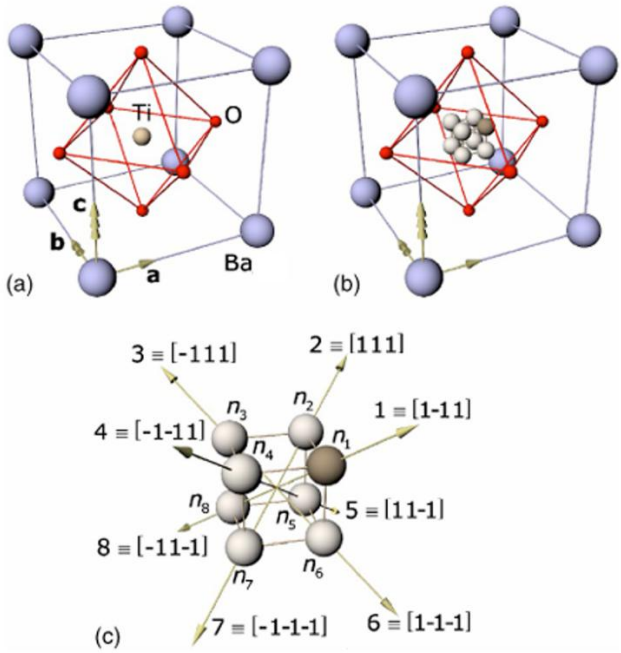

Figure 1.3: *Possible titanium ion positions, compatible with the Oh symmetry in the paraelectric phase: (a) static Ti at the ideal position in the center of the unit cell; (b) Ti disordered among eight off-center displacements along the eight <111> directions. Ti shifts are shown greatly exaggerated. (c) The assignment of off-center positions.* n_i *is the probability of and the Ti ion in the ith off-center site* [29].

In the orthorhombic phase, the atoms still favour one of two directions and remain coordinated in two of the three directions, but not the third. As the material transitions to the tetragonal phase, another direction loses its coherence, allowing the atoms to spread across four (111) directions. Finally, in the cubic phase, the highest temperature phase, the remaining order disappears, and the atoms are randomly spread across all eight (111) directions.

Interestingly, even though the average structure becomes more symmetrical with increasing temperature, the local movements of the titanium atoms always have a rhombohedral character. These local shifts are still there, just disorganised, so when averaged over large distances, they create the overall structure we observe. Because of this, the large-scale

polarisation (the main property we measure) might not match the symmetry of what's happening at the atomic level.

Today, researchers increasingly agree based on both theory and experiments that BTO's ferroelectric transition involves a mix of two behaviours: one where atoms shift positions gradually (displacive) and another where they jump between set positions (order-disorder).

1.3.1 Order of Phase Transition

A symmetry-based theoretical analysis to explain the equilibrium behaviour near a phase transition was first deduced by Landau [30]. Landau characterised the transition in terms of an order parameter, a physical entity that is finite in the low-symmetry (ordered) phase and tends to zero continuously once the symmetry is maximised (disordered). Devonshire introduced the Landau formalism to explain long-range interactions of the FE system by considering the spatially uniform P as the order parameter [31]. The free energy (F), in the vicinity of the transition, is then expanded as a power series of the order parameter P as (F(P)), retaining only symmetry-compatible terms:

$$F(P) = a_0(T - T_0)P^2 + bP^4 + cP^6 - EP$$

Where T_0 is the Curie temperature, a_0, b, and c are the material-dependent expansion coefficients. The equilibrium is achieved at the minima of F(P), at a finite polarisation $P = \pm P_s$, where P_s denotes the spontaneous polarisation in the FE phase. On increasing the temperature, the minima shift to the P=0, representing the non-polar PE phase. The coefficients a_0 and c are positive and have been verified experimentally. Whereas, the constant 'b' can be positive or negative depending on the evolution of the polarisation being continuous or discontinuous at $T < T_0$. This classifies the FE-PE transitions into two categories, i.e., First order (b<0) and second order (b>0) [32].

In the first-order phase transition [Figure 1.4(a)], the P_s jumps discontinuously to zero in a sharp transition. Thus, the T_0 and T_c are not the same. Here, the spontaneous polarisation and so the F(P) minima at $P \neq 0$, do not get into the global minima of P=0 at T_0. It decreases up to T_c, at which the shift to P=0 happens as a sudden occurrence, and explains the discontinuity in the P_s vs T plot. Note that, at T_0, this global minimum is still not at P=0. Hence, here $T_0 < T_c$.

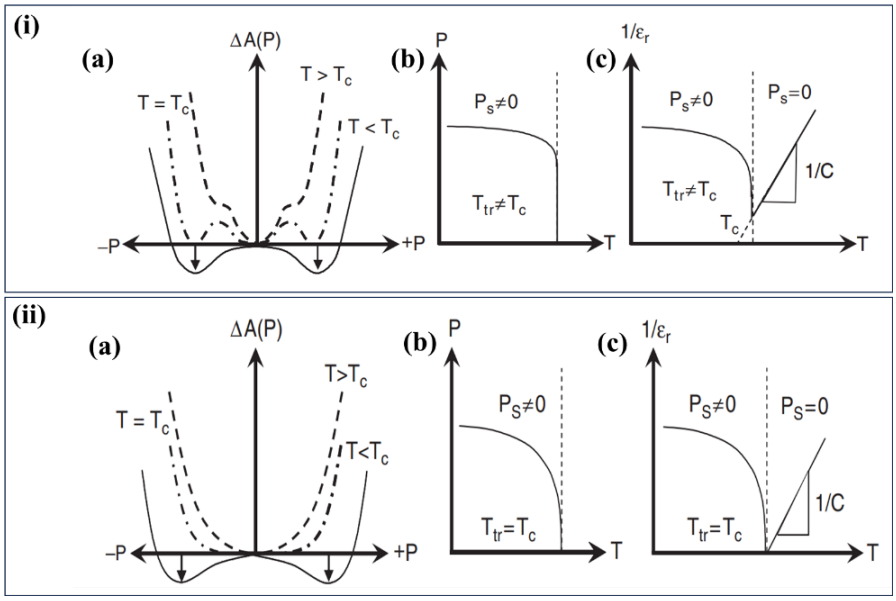

Figure 1.4: *(a) Variation of free energy density with temperature and polarisation. Arrows in wells indicate spontaneous polarisation states, (b) Variation of spontaneous polarisation with temperature, and (c) Variation of reciprocal dielectric constant with temperature for a* ***(i)*** *First order transition* ***(ii)*** *Second order transition* [32].

In the second-order phase transition [Figure 1.4(b)], the two minima corresponding to the non-zero spontaneous polarisation get continuously transformed to the P=0 phase at T_0. Thus, the P_s continuously decreases up to this temperature. Simultaneously, the polar FE phase also gets transformed to the non-polar PE phase at the same temperature. So, in this case, $T_c \sim T_0$.

1.3.2. Hexagonal Polymorph of perovskite $BaTiO_3$

Hexagonal $BaTiO_3$ crystallizes in the space group $P6_3/mmc$ with cell parameters a = 5.7238 Å, c= 13.9649 Å, and V = 396.22 $Å^3$ [33]. Hexagonal BTO can be stabilised in two ways, one by sintering at higher temperatures (>1430 °C) [23] and others by doping it with transition metals like Mn, Fe, Co [22].

There are two types of Ti and Ba in a hexagonal lattice. One type of Ti is in a centrosymmetric octahedra (represented as light blue colour in figure 5). The other type is inside a dimer, which forms by two face-sharing octahedra (represented by violet colour in figure 5). Similarly, Ba occupies two sites, one at the edges of the unit cell (orange colour), and the other inside the unit cell (yellow colour) [Figure 1.5].

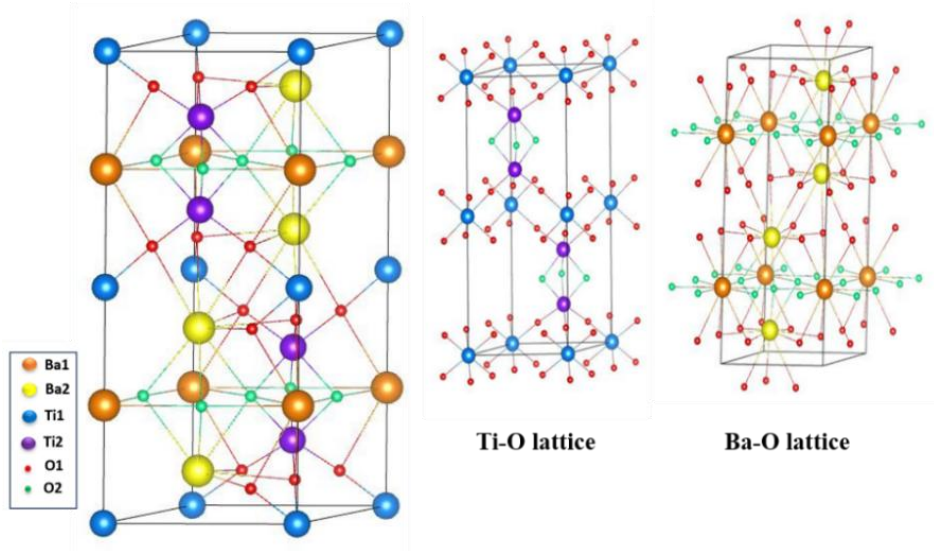

Figure 1.5: *Schematic of the Hexagonal unit cell with Ti-O lattice and Ba-O lattice*

The hexagonal polymorph of BTO arises due to the O_v in BTO. As the oxygen is not sufficient enough two octahedra come together and form a face-shared octahedral dimer, which stabilises the structure. This dimer formation leads to the hexagonal structure of BTO. Usually, higher sintering

of BTO will lead to O_vs and trigger the hexagonal polymorph. Another way of forming of hexagonal phase is by doping the TM ions in the Ti sites, which alters the stability of tetragonal BTO and triggers the dimer formation.

The hexagonal BTO phase is paraelectric. Hexagonal phase triggers due to doping with TMs in BTO lead to the presence of d electrons inside the dimers that can induce 90° ferromagnetic double exchange interaction. Long-range ordering of such exchange interaction can induce ferromagnetism in BTO. However, the emergence of paraelectric hexagonal phase decreases the ferroelectricity, though it favours ferromagnetism. Hence, the existence of both ferroelectric ordering and ferromagnetic ordering is troublesome in BTO.

1.4 Ferroelectricity

When a dielectric material is exposed to an external electric field (E_{ext}), it responds by creating its internal electric field (E_{int}). This happens because of the movement of free charges, alignment of electric dipoles, or the way atoms within the material become polarised. These internal effects generally work to reduce or "screen" the influence of the external field. In some cases, the dipoles inside the material naturally line up in the same direction, even without an external field. This is known as spontaneous polarisation, and the phenomenon is called ferroelectricity, first discovered in 1920 [34]. Ferroelectric (FE) materials have a specific temperature called the Curie temperature (T_c) that marks the change from a non-polar (paraelectric) to a polar (ferroelectric) phase. These materials are widely used in practical applications like sensors, adjustable capacitors, and especially in ferroelectric memory devices, where data is stored using the material's lasting (remanent) polarisation. [35].

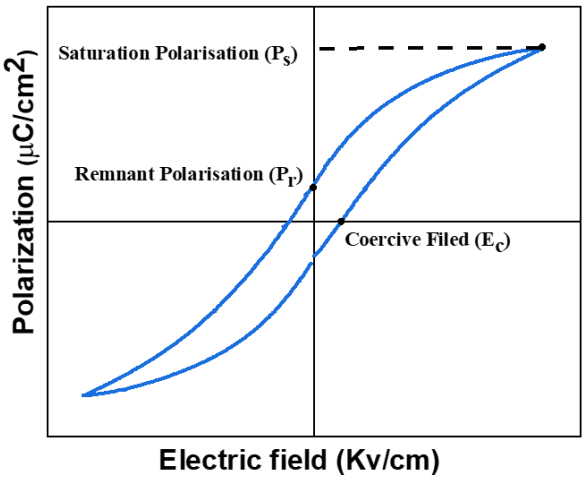

Figure 1.6: *P-E hysteresis loop of ferroelectric*

Ferroelectrics are polar materials that possess spontaneous polarisation in the absence of an electric field. The direction of the polarisation vector can be reoriented by the application of a sufficiently high external electric field. Ferroelectric materials are identified by the ferroelectric hysteresis loop in the polarisation (P) vs electric field (E) [Figure 1.6].

A typical ferroelectric hysteresis loop is shown in the Figure. Polarisation (P) increases with the electric field; hence, it is field-induced. Initially, for a small applied field, the force is not enough to orient all the ferroelectric domains. With increasing electric field, P increases nonlinearly with the ferroelectric domains orienting gradually along the direction of the applied electric field. Depending on the properties of the materials, at an appropriate applied electric field, 'P' saturates at a state of maximum polarisation in which maximum ferroelectric domains are aligned in the direction of the field, called saturated polarisation (Ps). When the external field is reversed, some ferroelectric domains switch back to their original direction due to local stress, but some feel energetically preferable to remain fully or partially in the direction of the previously applied field. This gives rise to a remnant polarisation (P_r) due to the non-reversibility of some ferroelectric domains to the original non-aligned state. These domains can

be reoriented after applying an electric field in the opposite direction. This critical electric field is termed a coercive field (E_c). On further reversal of the field direction, all the ferroelectric domains aligned will be in the negative direction, and the cycle can be completed by switching the field direction.

Ferroelectric materials exhibit regions known as domains, within which the electric polarisation is uniformly aligned. The interfaces separating these domains are referred to as domain walls, which typically form to minimise the system's total free energy. When adjacent domains possess polarisation vectors in opposite directions, the boundary is termed a 180° domain wall. In contrast, boundaries between domains with orthogonal polarisation directions are identified as 90° domain walls. [36]. The orientation and type of domain walls are largely dictated by the crystallographic symmetry of the material. For instance, in the tetragonal phase of barium titanate (BTO), both 180° and 90° domain walls are commonly observed. Materials with orthorhombic symmetry permit domain wall angles of 60°, 90°, 120°, and 180°, while rhombohedral phases can accommodate 71°, 109°, and 180° domain orientations [36]. Under the influence of an external electric field, the polarisation within the domains tends to reorient in the direction of the applied field. This process can lead to the transformation of a multi-domain structure into a single-domain configuration. Ferroelectricity is characteristically observed in polar, non-centrosymmetric crystal structures.

In most of the FE perovskites, the B-site atom has an empty d electron shell, allowing covalent bonding with the full p orbitals of the O atoms. In BTO, Ti is Ti^{4+} state with d^0 electron, favouring the ferroelectricity. Ferroelectricity can also occur due to the existence of lone pairs of electrons on the outer shell of the A-site atom, which are highly susceptible to polarisation [37].

1.5 Dielectric Properties

The dielectric constant signifies the efficiency of a dielectric material to store electrical energy, and the dielectric loss indicates the loss of electrical energy in the form of heat energy. In AC fields, permittivity becomes a complex quantity and has real and imaginary parts ($\varepsilon^* = \varepsilon' + i\varepsilon''$). The real part is an indication of the degree of polarisation, and the imaginary part is associated with the dielectric losses. Real part is expressed as relative permittivity, $\varepsilon_r = \varepsilon'/\varepsilon_0$, where ε_0 is the permittivity of the free space and has a constant value of 8.85×10^{-12} F/m. The greater the degree of polarisation greater the value of ε'.

The dielectric constant depends on the frequency of the applied electric field. As the frequency increases, the value of ε' decreases because the polarisation mechanisms within the material struggle to keep pace with the rapidly changing field. This phenomenon is related to the relaxation behaviour of the material, which arises from orientation polarisation that varies with frequency. At lower frequencies, permanent dipoles have sufficient time to align with the electric field, significantly contributing to the material's overall polarisation. However, at higher frequencies, the field changes too quickly for the dipoles to respond effectively, resulting in a diminished contribution to the total polarisation and a corresponding decrease in dielectric permittivity. Therefore, the dielectric constant (ε') tends to drop as frequency rises.

The real part of permittivity, ε', is typically measured by observing the change in capacitance when a dielectric material is placed between the electrodes of a capacitor. The imaginary part, ε", is related to dielectric losses and can be calculated from the loss tangent (tanδ), defined as $\tan\delta = \varepsilon''/\varepsilon'$. In high-frequency alternating fields, a phase difference exists between the polarisation and the applied field, which leads to energy dissipation within the dielectric. This energy loss, quantified by tanδ, corresponds to the energy absorbed per cycle. The frequency dependence of dielectric loss

is linked to relaxation polarisation, where dipoles lag behind the changing field due to frictional forces resisting their reorientation. Also, due to the change in polarisation of the dielectric, a polarising current flowing in the dielectric is induced by the relaxation rate. This current induces dielectric loss in the material.

1.5.1 Polarisation Mechanisms in dielectric material

Dielectric polarisation is described by various atomic mechanisms. Under the influence of the externally applied field, the material is polarised, and dipoles are created with a moment (p). This is directly proportional to the local electric field.

$$p=\alpha E_{loc}$$

The total polarizability (α) is the sum of four polarising mechanisms given below:

$$\text{Polarizability } (\alpha) = \text{Space charge } (\alpha_s) + \text{Orientational/Dipolar } (\alpha_i) + \text{Atomic } (\alpha_a) + \text{Electronic } (\alpha_e)$$

The contribution of each polarisation also depends on the types of material. These polarisation mechanisms are demonstrated in Figure 1.7.

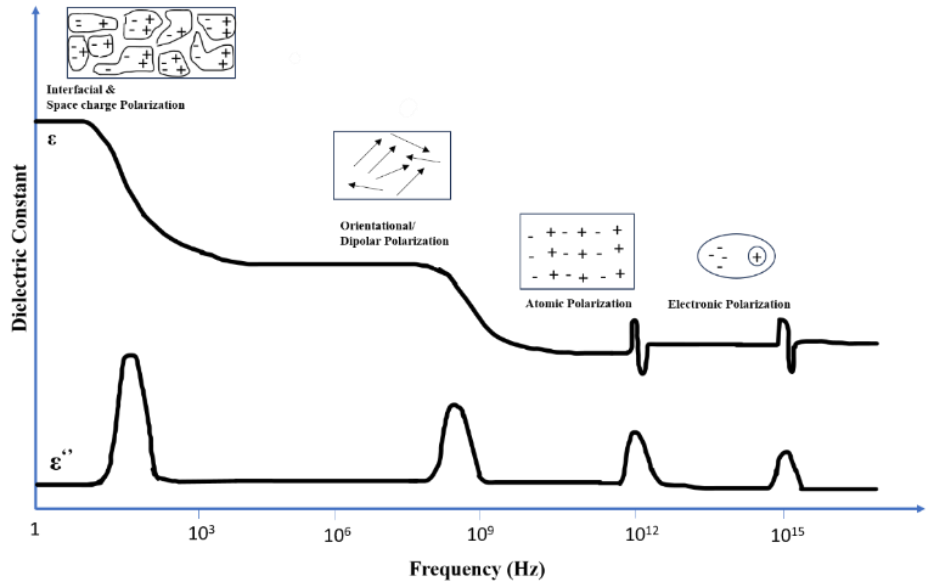

Figure 1.7: *Different polarisation mechanisms corresponding to the different frequency ranges.*

i) Interface or Space Charge Polarisation

This type of polarisation occurs when charge carriers have limited mobility and accumulate at interfaces such as grain boundaries or electrode-material junctions. As electrons move freely within grains, they encounter defects that act as potential barriers, causing charges to build up at these boundaries. This accumulation of space charge is particularly significant at low frequencies and elevated temperatures.

ii) Dipolar or Orientation Polarisation

This mechanism is associated with the alignment of molecular dipoles in response to an applied electric field. Under normal conditions, these dipoles are randomly oriented due to thermal motion, but the external field induces them to align along its direction, resulting in polarisation.

iii) Ionic Polarisation

In ionic solids, the crystal lattice typically exhibits symmetrical arrangements where individual ionic dipoles cancel each other out. However, when subjected to an external electric field, the ions are displaced slightly from their equilibrium positions, generating a net dipole moment and thus contributing to polarisation.

iv) Electronic or Atomic Polarisation

This form of polarisation arises from the relative displacement between the electron cloud and the nucleus within an atom when an electric field is applied. The shift of the negatively charged electron cloud relative to the positively charged nucleus induces polarisation. This process is reversible; once the external field is removed, the electrons and nucleus return to their original positions. Because all materials are composed of

atoms, electronic polarisation is a universal contribution to the overall dielectric response.

Materials exhibiting a single relaxation time constant are often modelled using the Debye relation. According to this model, the real part of the permittivity (ε′) remains relatively constant both above and below the relaxation frequency, with a smooth transition occurring near this frequency. Meanwhile, the imaginary part of the permittivity (ε″) typically displays a peak at the relaxation frequency, marking the region of maximum energy dissipation.

1.5.2 Temperature-dependent dielectric and phase transitions

Temperature-dependent variation of dielectric properties gives details about the nature of the phase transition, Curie temperature T_c, Disorder in the lattice, etc. For BTO, there is a sharp rise in permittivity at phase transitions.

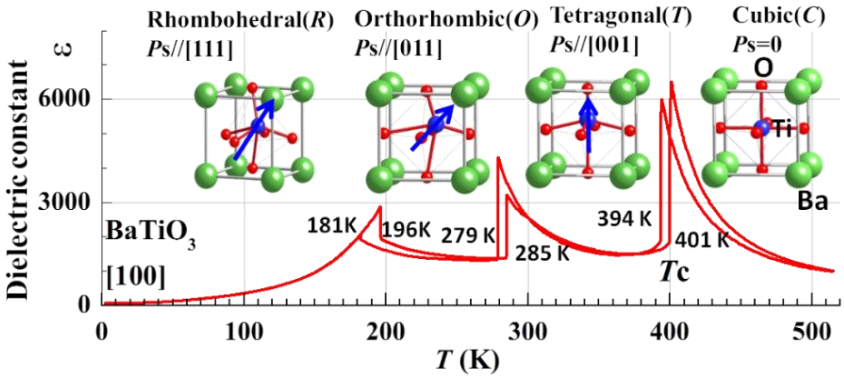

Figure 1.8: *Phase transition obtained in dielectric permittivity in $BaTiO_3$* [1]

The perovskite form of Barium titanate can exist in different crystallographic structures, such as cubic, tetragonal, orthorhombic, and rhombohedral, depending on different temperature ranges. The structural phase transition from the paraelectric phase to the lower symmetry ferroelectric phases occurs at different temperatures related to the softening of the zone-boundary phonon modes at the Curie temperature (T_c). On

cooling from the high temperature, since there are six equivalent directions in the cubic phase, the polar axis can be any one of these directions. These phase transitions occur with strong dielectric softening. At the Curie temperature, T_C 120 °C –130 °C, it turns from the high-temperature paraelectric cubic form (C, *Pm3m*) to the ferroelectric tetragonal structure (T, *P4mm*). On further cooling, two other ferroelectric phases are observed: orthorhombic (O, Amm2), below -5 °C –15 °C, and rhombohedral (*R3m*), below -80 °C to -90 °C [Figure 1.8].

Near the transition $T \rightarrow T_c$, in the FE phase, though P_s decreases, the dielectric constant (ε') increases. According to Landau's theory, it is inversely proportional to T. As the temperature increases towards T_c, the domain walls become more mobile, and the phonon-phonon interaction increases, causing deviations from a simple inverse-temperature dependence. P_s measures the spontaneous dipole alignment, whereas the ε' depends on the sum of all kinds of polarisation in the material in response to the external electric field. With an increase in temperature, the loss of dipole order in the FE phase reduces P_s. Whereas the softening of the structure supports critical fluctuations in the order parameters at the time of transition, making it easier to polarise it with a little external field, which in turn increases the ε' monotonously, before the transition.

1.5.3 Normal phase transition and Diffuse Phase transition

The phase transitions described above happen at a particular temperature (T_c) [Figure 1.9(a)]. However, the phase transition is extended over a wide temperature range around a maximum value of ε_r' (ε_m') at a temperature (T_m) that corresponds to the diffused phase transition (DPT), [Figure 1.9(b)]. This temperature interval is commonly referred to as the Curie range [38].

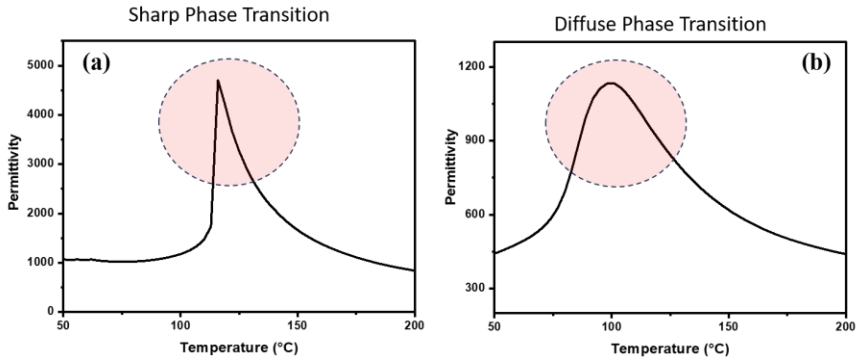

Figure 1.9: *Dielectric constant versus temperature showing (a) sharp phase transition, (b) diffused phase transition*

BTO exhibits a first-order phase transition with a sharp rise in permittivity. The electrical susceptibility (χ) follows the Curie-Weiss law above the sharp phase transition temperature T_c of the materials

$$\chi = \frac{C}{T - T_C} \quad T \geq T_c$$

where C and T are the Curie constant and absolute temperature, respectively

DPT is not necessarily a result of the size distribution of grains or domains. In the pristine polycrystalline BTO, although there are different domains within the system with different directional orientations and sizes, the activation energy required to transform the polar FE phase into the non-polar PE phase is the same for each of them. Thus, the transition obtained here is sharp, and it follows the Curie-Weiss law immediately after the transition. But in the compositionally disordered system, due to the presence of various modifications, polar regions of different dielectric nature start to appear with different transition temperatures. Different cations are distributed randomly among the equivalent lattice sites and in different amounts. This, in general, modifies both the strength of dipole-dipole interaction and the activation energy for structural transformation from one polar region to another. It leads to the transition of different polar regions to happen within a wide temperature range known as the Curie range. Within

the Curie range, the dielectric permittivity achieves its highest value (ε′) at T_m, and the ferroelectric material displays its most distinguishable features.

Diffused transition behaviour cannot be explained by the Curie-Weiss law. It follows the modified Curie-Weiss law.

$$\frac{1}{\varepsilon'} - \frac{1}{\varepsilon'_m} = \frac{(T - T_m)^\gamma}{C}$$

Where, γ ($1 \leq \gamma \leq 2$) is the degree of diffuseness, for an ideal sharp phase transition, γ = 1, while for a relaxor phase transition, γ = 2.

Relaxor Ferroelectrics are a special class in which the ferroelectric to paraelectric phase transition temperature is frequency dependent. It shows DPT nature with a large frequency dispersion in ε′. This can be explained by describing the formation of macro or nano-polar regions (PNRs) dispersed in a disordered matrix. Such PNRs are believed to be dynamic and become reduced in size as the temperature increases after phase transition, which results in the frequency dependence of the T_m [39]. Here in this thesis, we are dealing with the Normal first-order ferroelectric phase transition in BTO and the DPT nature of modified BTO.

1.5.4 AC conductivity studies

The ac conductivity, in most of the materials, due to localised states, is expressed by Jonscher's power law; $\sigma = \sigma_{dc} + A\omega^n$. For complex systems, to incorporate high mobility at higher frequencies, Jonscher's double power law: $\sigma_{ac} = \sigma_{dc} + A\omega^n + B\omega^m$, where A, B are constants, n and m are frequency exponents. Long-range translational motion of charge carriers contributes to the dc conductivity σ_{dc}. Short-range translational motion contributes to the low-frequency dispersion region $A\omega^n$ where $0<n< 1$. Re-orientational motion at high frequencies contributes to the third term, $B\omega^m$, where $0 < m<2$ [40], [41].

Variation of n with temperature can be used to explain distinct mechanisms for carrier conduction: Quantum Mechanical Tunnelling (QMT) through the barrier separating the localised sites and Correlated Barrier Hopping (CBH) over the same barrier, Non-overlapping Small Polaron Tunnelling (NSPH), Overlapping Large Polaron Tunnelling (OLPT) [42]. In these models, the exponent n is found to have two different trends with temperature and frequency. If the ac conductivity is assumed to originate from QMT, n is predicted to be temperature independent, but is expected to show a decreasing trend with ω, while for CBH, the value of n should show a decreasing trend with an increase in temperature. The exponent n increases with temperature in the NSPH model. The OLPT model shows an initial decrease in exponent n with temperature, attains a minimum, and thereafter increases with temperature [42].

Hence, the variation of n with temperature can give the nature of the ac conduction mechanism possible in these materials and further details about the charge carriers in the modified BTO samples.

1.5.5 Impedance and Modulus formalism

The dielectric properties of materials can be analysed using complex impedance (Z*) and complex modulus (M*). These two quantities are connected through the complex permittivity (ε*), which is given by the relation $\varepsilon^* = 1 / (i\omega C_0 Z^*)$, where C_0 is the capacitance of an empty measurement cell and ω is the angular frequency. The complex impedance Z* consists of a real part (Z′) and an imaginary part (Z″), which are calculated based on the material's resistance and capacitance. The impedance data primarily highlight the largest resistance contributions from the microscopic components within the material [43].

On the other hand, the electric modulus provides valuable insight into the relaxation of free charge phenomena that may not be visible in permittivity measurements. By studying the imaginary part of the modulus, we can better understand how these materials relax electrically. Modulus

spectroscopy thus offers a clearer picture of the dielectric relaxation process. The relationship can be written as $M^* = M' + iM'' = i\omega C_0 Z^*$ [43].

To fully understand relaxation behaviour in ceramics, it is useful to combine both electrical modulus and impedance analyses. The modulus spectrum tends to focus on the smallest capacitive elements at the microscopic level and reduces the effects caused by electrode interfaces [44]. Physically, the electrical modulus represents how the electric field inside the material relaxes when the electric displacement remains fixed.

The frequency dependence of the peaks observed in the imaginary part of the impedance and modulus spectra for different temperatures gives an idea about the short-range or long-range conduction mechanisms in ceramic material. Also, the variations in the activation energy, relaxation times can be analysed through this different analysis.

1.6 Literature Survey on the structural and functional properties of modified $BaTiO_3$

1.6.1 A site and B site doping in $BaTiO_3$

Undoped barium titanate ceramics and single crystals' dielectric, electromechanical, optical, and multiferroic properties show a significant temperature dependence. Hence, the range of temperature at which it can be used for the application is limited. On the other hand, the strong increase of the dielectric and piezoelectric properties approaching the phase transition temperatures would be of high interest for the fabrication of devices with better performances. The development of BTO-based materials and the modification of BTO and their use in commercial applications has been driven by the need to find a compromise between these two contrasting trends.

Doping in BTO can be used to modify the properties for various applications. Doping strategies are generally separated into iso- and aliovalent (donors and acceptors) and into A- and B-site species within the

perovskite structure. This structure can accept ions of different sizes, so that a large number of different dopants can be placed in the BTO lattice.

In A site doped BTO, Ba can be replaced by Isovalent dopants include Sr^{2+}, Ca^{2+}, Pb^{2+} and Cu^{2+} [45] , [46], and aliovalent acceptor ions like Ag^{+}, Na^{+}, K^{+}, [47], [48]and aliovalent doner ions La^{3+}, Nd^{3+}, Ce^{3+}, Ni^{3+} etc [49].

B-site modifications include isovalent ions Zr^{4+}, Hf^{4+}, Sn^{4+}, V^{4+}, Mn^{4+}, [50], [51] and aliovalent acceptor species such as Fe^{3+}, Mn^{3+}/Mn^{2+}, Ni^{2+}, Sc^{3+}, Lu^{3+}, Yb^{3+}, Li^{+} [52], [53]and aliovalent donor ions Nb^{5+}, Ta^{5+} and Sb^{5+} [49], [54].

Certain cations are known to exhibit amphoteric behaviour in terms of site occupancy, meaning they can occupy either the A or B sites depending on factors such as stoichiometry, phase composition, and the thermal conditions during processing. These ions typically have ionic radii similar to those of Ba^{2+} and Ti^{4+}. For instance, Y^{3+} and some rare earth elements have been shown to display this amphoteric nature, although they generally prefer the A site, exhibiting higher solid solubility there [55]. Magnesium (Mg^{2+}) presents a particularly interesting case; numerous studies investigating Mg doping in barium titanate (BTO) have reported its ability to occupy both A and B sites, depending on the starting stoichiometry [56]. As a result, it is commonly accepted that Mg^{2+} can incorporate into either site with relatively high solubility, acting as an isovalent dopant when substituting at the A site and as an aliovalent dopant when occupying the B site.

Simultaneous doping at both A and B sites of $BaTiO_3$ can also be possible, in which the emergence of undesired properties arises due to one doping site can be overcome by the doping in the other site. For example, doping TM ions at the B site induces a paraelectric hexagonal phase, which is not desirable. The simultaneous doping of Ca, Bi, and La can reduce the hexagonal phase and bring the tetragonal phase back [22]. A site Ca-doped and B-site Zr-doped BTO, commonly known as BCZT, enhances the energy

storage and electrocaloric performance [57]. A site Bi-doped and B-site Fe-doped BTO can not only induce multiferroicity in BTO it can also induce relaxor behaviour [58].

These A-site and B-site substitutions can also have a marked difference on the T_C of the overall ceramic, raising or lowering T_C, which contributes to the stability of the material over a given temperature range. In the bulk material, unlike single crystals, grain boundaries can negatively contribute to the overall permittivity, so it is important to balance these competing contributions when optimising grain size.

1.6.2 Multiferroicity in modified BTO

Two ferroic orders in a single material are termed as multiferroic [Figure 1.10]. It includes a ferroelectric order in which spontaneous polarisation and ferromagnetic order in which spontaneous magnetisation can be switched by an externally applied electric field and magnetic field, respectively. It can be a ferroelastic order where spontaneous and stable deformation can be switched by an applied stress.

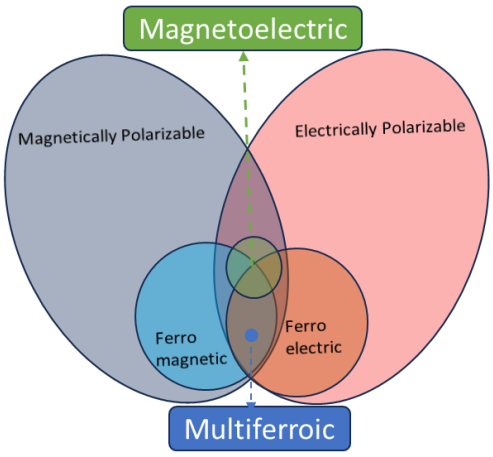

Figure 1.10: *Relationship between multiferroic and magnetoelectric materials. Illustrates the requirements to achieve both in a material*

Ferroelectric BTO has Ti^{4+} states with d^0 electrons, which do not show any magnetic properties. The presence of unpaired electrons is mainly exhibited by materials containing TMs, which is induced by their partially filled d orbitals. Hence, doping TM in BTO can generate unpaired electrons within the lattice. When the magnetic moments are oriented randomly, it will show paramagnetism, and the moments can be aligned by the applied external magnetic field. When there is exchange coupling between these unpaired electrons, it can induce ferromagnetic and antiferromagnetic properties in BTO, depending on the type of exchange mechanism between these electrons. There is another possibility of magnetism due to O_v in the BTO lattice, due to the reduction of Ti^{4+} to Ti^{3+}. These O_vs can trap the electrons and can lead to the F center exchange mechanism that induces magnetism in BTO. Another way is by the doping of TM ions in BTO that can trigger the hexagonal BTO phase, which induces double exchange FM interaction due to the presence of d electrons inside the dimers in the hexagonal phase. Such type of interactions create magnetic ordering in the BTO material.

Deka *et al.* [59] experimentally observed a ferromagnetic ordering in Fe-doped BTO, which is described as a result of Ov-mediated F-centre exchange phenomena in Bound Magnetic Polarons (BMP). Similarly, BMP models have been used to explain the ferromagnetism in Hf and Co-doped BTO [60], Mn-doped BTO [51], Fe-doped BTO [61], Pb and Fe dope BTO [62].

Apostolova *et al.* [63] Theoretical investigation of the ferromagnetic properties of TM-doped BTO at room temperature, which leads to multiferroic properties. This magnetic ordering has been explained due to the superexchange interactions between Fe^{3+} ions in different occupational sites associated with O_v and to the exchange coupling of Fe ions with mixed valence, Fe^{3+} and Fe^{4+}. Whereas the magnetisation and the magnetic phase transition temperature increase with increasing the Fe-ion concentration, the

polarisation and the ferroelectric critical temperature decrease [64]. Senthilkumar *et al.* [65] Explained a theoretical study on the O_v constituted bound magnetic polaron (BMP) model in Ce-doped BTO to explain the enhancement in ferromagnetism.

Apart from the BMP model, the double exchange interaction in the hexagonal phase of BTO, emerging due to the O_vs in BTO, can also be a reason for the magnetic ordering in doped BTO. Dang *et al.* [66] Studied the room temperature ferromagnetism introduced by Mn doping in BTO. They have reported the coexistence of two ferromagnetic phases with different coercivities, which are associated with tetragonal and hexagonal Mn-doped BTO structures.

Pal *et al*. [22] Studied the hexagonal phase emergence and the introduction of ferromagnetism with TM doping in BTO. To retain the ferroelectricity, simultaneous doping at the A site with cations La, Sr, Ca, Bi, etc. has been studied for the multiferroicity in the single-phase BTO. Among possible combinations of A site and B site doping, they have obtained Bi and Fe doped materials that have maximum multiferroicity shown in single-phase BTO. The optimisation of tetragonal and hexagonal phases by controlling Bi and Fe doping in BTO has been engineered for room temperature multiferroicity. [67].

1.6.3 Magnetoelectric Coupling in modified BTO

The interaction between the different ferroelectric and ferromagnetic orders in a multiferroic material can lead to magnetoelectric coupling (MEC). In such materials, the polarisation can be switched by a magnetic field, and magnetisation can be switched by an electric field. Such types of materials can be used for ME phase control in devices such as memories or switching devices with magnetic control of the electrical polarisation, and vice versa. The coupling between ferroelasticity and ferroelectricity leads to piezoelectricity, and the interlink between

ferromagnetism and ferroelasticity can lead to magnetostriction [Figure 1. 11].

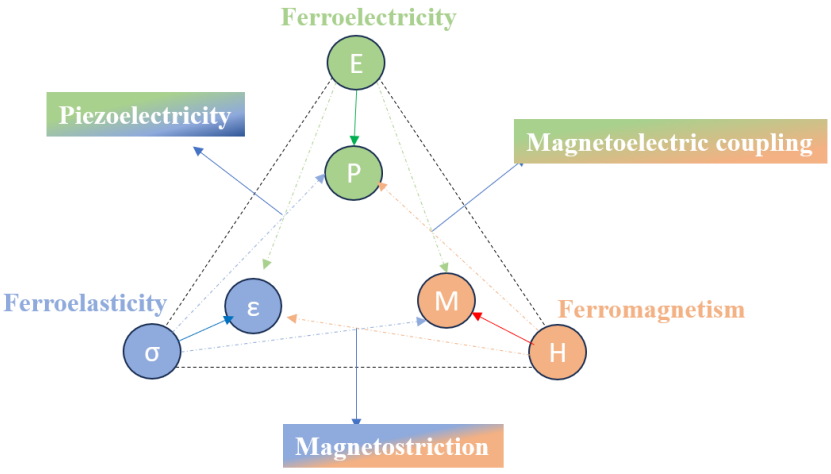

Figure 1.11: *Schematic illustrating different types of coupling present in materials interconnection between Piezoelectricity, magnetoelectric coupling, and magnetostriction*

Magnetoelectric coupling can be introduced in BTO by doping the Ti site with TM ions to induce magnetic ordering in the material. The multiple oxidation states of TM and the O_v can generate different types of exchange interactions and help in ferromagnetism in BTO. One of the main problems that needs to be faced by doping with TM ions is the emergence of a paraelectric hexagonal phase that will reduce the ferroelectricity and enhance the lossy nature in the material. That means the enhancement of ferromagnetism reduces the ferroelectricity, and the enhancement of ferroelectricity leads to a reduction of ferromagnetism. Hence, there will be an optimum level of dopants in which both FE and FM exist in the same material to be multiferroic.

There are various studies of ME coupling induced by doping in the B site with TM ions. [68], [69]. Shah *et al.* studied the ME coupling in Cr doped BTO [68]. In this study, the induced electric polarisation due to the application of an external magnetic field creates local interaction of d electron spins with disordered electric dipoles via O_vs created by the Cr doping in BTO. There are reports in which A site modification can also

generate magnetism in BTO due to O_v generated by the substitution of higher oxidation state of dopant ions, such as Ce^{3+}. [70] in place of the Ba^{2+} site.

Apart from this intrinsic coupling in single BTO material, there is a wide range of studies on the composite formation with ferromagnetic material that can generate large magnetoelectric coupling. A well-studied composite for this application is a composite of BTO with ferromagnetic $CoFe_2O_4$. $BaTiO_3$-$CoFe_2O_4$ multiferroic composite shows ME coupling due to the strain created between the two phases [71]. The strain-induced coupling in the ferroelectric order in $BaTiO_3$ and ferromagnetic order from $CuFe_2O_4$ generates a large ME coupling voltage. Similar studies on composite ME coupling have been done for $BaTiO_3$-$NiFe_2O_4$ [72], $BaTiO_3$-$BaFe_{12}O_{19}$ [73], $BaTiO_3$- Fe_3O_4 [74], and Ni particles in $BaTiO_3$ [75].

1.6.4 Dielectric Properties in modified BTO

The high dielectric constant, low dielectric loss, high insulation resistivity, and reliability make BTO an exceptional candidate for various dielectric applications. Chemical modifications of BTO can effectively enhance the grain growth and control the leakage current, resulting in enhanced dielectric performance.

Hisiang *et al.* [76] Studied the Ca-doped BTO (BCT) for enhancing the dielectric properties. BCT samples displayed relatively smaller grain sizes, resulting in a greater number of grain boundaries, which in turn increased the insulation resistivity. BCT had a lower O_v concentration, thus resulting in lower leakage currents at high temperatures than BTO. Substituting BCT for BTO resulted in higher activation energies for conductivity in the core, shell, and grain boundary. This investigation demonstrates that BCT can enhance the dielectric properties, insulation resistance, and reliability.

Dielectric permittivity increases with Nd^{3+} doping [77]. Ganguly et al. [78] Wang *et al.* [54] Shows that La^{3+} doping reduces the dielectric permittivity, shows that increasing the La^{3+} doping content in $BaTiO_3$ ceramics inhibits the grain growth, and that both the room and maximum dielectric constants diminish monotonously.

In acceptor-doped BTO, positively charged O_v s are induced for charge compensation. The existence of O_vs decreases the mobility of domain walls, contributing to the decrease in the permittivity. Moreover, O_vs contribute to the conductivity and increase the dielectric loss. B site doped Zn^{2+}, Fe^{3+}, Mn^{3+} shows a decrease in the dielectric permittivity [79].

1.6.5 Theoretical studies on band structure and electron localisation of modified BTO

Density of states (DOS) calculations help to identify the electronic band structure modifications, new defect states formed, the shift in valence band and conduction band, conductivity, and optical properties with doping in BTO. Density Functional Theory (DFT) calculates the DOS by analysing the electronic wavefunctions obtained from calculations. These results can provide theoretical support for the experimentally observed band gap modifications.

BTO has an optical band gap in the range 2.5 eV to 3.4 eV. The band structure of BTO is formed mainly due to Ti_{3d} (CB) and O_{2p} (VB) orbitals [80]. Changes in the overlapping pattern of the Ti and O orbitals can lead to modifications in the energy gap. It can exhibit both direct band gap and indirect band gap depending on the crystalline structure, synthesis conditions, temperature, dopants, etc.[81], [82]. Both theoretical and experimental studies have shown that the band gap can be modified by doping impurities in BTO. Modifications of electronic hybridisation ultimately redefine the energy gap. Doping with different ions in the BTO lattice can create defect states within the band gap that can effectively

reduce the band gap to the visible region, enabling BTO to effectively use the electromagnetic spectrum.

A theoretical study on Sr-doped BTO [83], the band gap is found to increase with increasing Sr due to the resonant interaction of O_2*p* orbitals mixed with Sr_4*d* states with the top of the valence band. Sr-doped BTO exhibits a direct band gap covering the wavelength range ~397–436 nm. With La doping in BTO, the band gap has been decreased, and the conduction band has been partially shifted towards the valence band with the appearance of new gamma points [84]. The band gap reduction is due to La-5d states, which make a greater contribution to the conduction band. Similarly, doping Fe in Ti sites. [85] Reported Fe creates some defect states in the energy band, which changes in the Ti-O hybridisation and reduces the band gap.

Electron Localisation Function (ELF) calculations help to understand the empirical concept of electron localisation. The ELF was introduced by Becke and Edgecombe [86] and thereafter applied to a great range of systems, to atoms, molecules, and solids. It is related to the covariance of the electron pair distribution. Just as with the electron localisation function, the local covariance does not seem to be, in and of itself, a useful quantity for elucidating shell structure. The ELF provides the variation of charge density around the atoms and gives an idea about the type of bonds, charge localisation, and variations in the local charge density near chemical modifications.

1.7 Applications of modified BTO

The unique combination of ferroelectric, piezoelectric, and dielectric properties of multiferroic BTO widens the application areas of BTO to energy storage, sensor technology, advanced electronic devices, memory devices, microwave devices, and materials with enhanced shielding capabilities, etc.

- ➔ Electronic Devices: In the field of the electronic industry, BTO is a preferred choice for high-performance ceramic capacitors and ferroelectric memories. The high dielectric performance helps BTO to play a pivotal role in energy storage, signal coupling, and signal filtering.
- ➔ Piezoelectric Devices: The piezoelectric properties exhibited by BTO are widely used for sensor and energy harvesting device applications. This can be meticulously engineered to measure and detect an array of physical quantities, encompassing pressure, strain, and acceleration. It is also used as an actuator, capable of propelling a wide range of mechanical and acoustic devices with unparalleled efficiency and accuracy.
- ➔ Ultrasonic Facilities: BTO ceramics play a pivotal role in the creation of ultrasonic equipment. In the field of ultrasonic cleaners to remove surface dirt and impurities, ultrasonic humidifiers are used to enhance the humidity of the air. High-temperature resistance of these ceramics ensures the reliability and longevity of such humidifiers.
- ➔ Acoustic Devices: BTO ceramics are instrumental in the development of acoustic filters to regulate and fine-tune the transmission and frequency of sound waves. It is also used for sonar sensors, heralding a new era of sound wave reception and emission technology. These sensors are designed to detect and transmit sound waves, a capability with far-reaching implications in fields such as marine navigation, underwater exploration, and defence.
- ➔ High-Temperature Applications: The remarkable thermal stability and outstanding high-temperature performance of BTO bulk ceramics have positioned them as indispensable assets in environments characterised by extreme heat, paving the way for a spectrum of high-temperature applications. BTO plays a pivotal role in the development of high-temperature sensors, engineered to

measure and monitor temperature and pressure in settings where conventional materials would falter.

- ➔ ME Coupling applications: Based on the direct ME coupling, multiferroic BTO can sense and harvest the ambient magnetic energy. When compared to the piezoelectric materials, ME materials can harvest/sense magnetic energy and are more suitable for the construction of technical devices for wireless communication. It can effectively utilise the waste magnetic energy from electromagnetic devices and can be used for low-voltage applications.
- ➔ High frequency applications: Electrically tunable high frequency devices via modulation of ferromagnetic resonance frequency (FMR) by switching ferroelectric polarisation of multiferroic [87]. Giant voltage-controlled FMR has been demonstrated in strain-mediated magnetic/piezoelectric heterostructures, providing routes for applications in voltage-tunable RF and microwave devices, phase shifters, and mini antennas.
- ➔ Photovoltaics: It also offers a promising application for photocurrent generation by virtue of its low band gap. The photocurrent generation in multiferroics is fundamentally similar to the photo-voltaic effect in ferroelectrics. [64]. The electron hole pair in the dipoles gets separated by absorption of a solar photon, and the depolarisation electric field in the ferroelectric crystal maintains the separation between the photogenerated charge carriers, resulting in open circuit voltage (Voc).

1.8 Objective of the Present Work

As discussed in the introduction part, the $BaTiO_3$ ceramic has been investigated by various researchers to investigate the physics of structural phase transition and to improve its dielectric and ferroelectric properties. During a detailed literature survey, it is noticed that there are not many studies on the intrinsic multiferroicity and magnetoelectric coupling of

Simultaneous substitution of A site and B site $BaTiO_3$ for optimising the ferroic orders at room temperature applications. Most of the studies focus on the composite materials of $BaTiO_3$ with ferromagnetic materials because of the large strain-induced magnetoelectric coupling. However, the MEC in single-phase material, though it is very less in magnitude, will be of much interest due to the fast-switching time for direct MEC applications. Moreover, a detailed structural correlation with multiple characterisation tools to explore the multifunctionalities for the A and B site modified $BaTiO_3$ has been studied in detail. Experimental results obtained are tried to explain in support of the theoretical calculations. In this work, a detailed experimental and theoretical investigation of the structure correlation between the dielectric, magnetic, and multiferroic properties has been conducted for different chemical modifications of $BaTiO_3$.

The Main key aspect of the thesis work is being pointed out in bullet form:

- Investigation of the multiferroicity and magnetodielectric, magnetoelectric effect in La/Fe co-doped $BaTiO_3$ and Ca/Mn La/Fe co-doped $BaTiO_3$.
- Defect/ Disorder correlated transport properties in modified $BaTiO_3$.
- Doping induces variations in the Density of states and Electron localisation variations in $BaTiO_3$.
- Experimental and theoretical investigation on the hexagonal polymorphism-induced dielectric properties in modified $BaTiO_3$.
- Room temperature intrinsic magnetoelectric coupling studies in modified $BaTiO_3$.

1.9 Thesis Outline

- **Chapter 1: Introduction**

This chapter includes the introduction to the thesis topic and familiarises the scientific terms used in the thesis. It details $BaTiO_3$ crystal structure, phase transitions, Multifunctional properties such as ferroelectricity, magnetism, multiferroicity, and magnetoelectric coupling. The literature survey on the multiferroicity in $BaTiO_3$ and various research works carried out in this field are explained in detail.

- **Chapter 2: Experimental Methods and Characterisation Techniques.**

In this chapter, details about the synthesis and characterisation techniques relevant to this work have been provided. The Sol-gel synthesis route for the preparation of doped BTO has been discussed in detail. The basic description of characterization techniques such as X Ray diffraction (XRD), UV-Vis Diffuse Reflectance Spectroscopy (DRS), Dielectric spectroscopy, Raman spectroscopy, X-Ray Absorption Near Edge Spectroscopy (XANES), Transmission Electron Microscopy (TEM), Scanning Electron Microscopy (SEM), Electron Paramagnetic Resonance Spectroscopy (EPR), and Photo-Emission Spectroscopy (PES) have been discussed. The experiments, such as Ferroelectric measurements, Magnetic measurements, Magneto-Dielectric measurements, Magnetoelectric measurements, have been done to explore the multifunctionalities. Details of the Density of State (DOS) and Electron Localisation Function (ELF) calculations are also detailed. To explain the basic working principle of the setups used, a schematic representation has been used.

- **Chapter 3: Room temperature multiferroicity and magnetoelectric coupling in Ca/Mn-modified $BaTiO_3$.**

Materials with magnetoelectric coupling (MEC) between ferroic orders at room temperature are an emerging field in modern technology and physics. $BaTiO_3$ is a robust ferroelectric in which several dopings have led to MEC. In Ca and Mn modified $BaTiO_3$ has been studied with a series of $Ba_{(1-x)}Ca_{(x)}Ti_{(1-y)}Mn_{(y)}O_3$ (x=y= 0, 0.03, 0.06, 0.09), in this MEC was only observed in x=0.03. A mixed phase of tetragonal *P4mm* and hexagonal *$P6_3/mmc$* space groups of $BaTiO_3$ is observed in the substituted samples, with a nominal contribution of the hexagonal phase for x=0.03. The structural modifications with changing substitution reveal a reduced Ti-O-Ti bond angle and a large number of defects in the tetragonal phase for this sample, and lead to weak ferromagnetism in the material. A valence state study using XPS and XANES reveals the presence of an enhanced proportion of Mn^{3+} ions in the sample, which supports a pseudo Jahn-Teller distortion, thereby supporting the ferroelectricity, also induces weak magnetic ordering due to short-range magnetic exchange interactions and due to bound magnetic polarons in the tetragonal phase of x=0.03. The simultaneous existence of ferroelectricity and ferromagnetism in the tetragonal phase induces magnetoelectric coupling in this material. Transmission Electron Microscopy (TEM) to explore the hexagonal and tetragonal coexistence with doping in these samples. The linear response of polarisation with the applied ac magnetic field indicates the direct ME coupling in this material. A magnetoelectric coupling coefficient, α_{ME} ~0.704 $mVcm^{-1}Oe^{-1}$, was obtained for a dc magnetic field of 800 Oe and an ac field of 40 Oe. Such MEC was not observed for higher substitution, which emphasises the sensitivity of the structural properties to substitution.

- **Chapter 4: Experimental and theoretical investigation on the hexagonal polymorphism induced dielectric properties in Ca/Mn-doped $BaTiO_3$.**

This study involves the structural investigation of the Ca and Mn modified $BaTiO_3$ with a series of $Ba_{(1-x)}Ca_{(x)}Ti_{(1-y)}Mn_{(y)}O_3$ (x=y= 0, 0.03, 0.06, 0.09). X-ray absorption spectra analysis is used to investigate the oxidation state and local structural changes due to doping at the Mn and Ti sites. Band gap modification and Urbach tail in UV-DRS and valence band modification in PES measurement for analysis of the valence band are modified with doping corresponding to localised defects in the material, and supported with theoretical Density of States calculation. The electron localisation function calculation is used to analyse the changes in the localised electron density near the dopant atoms. Variation of dielectric properties corresponds to the structural modifications and defect formation are also explored in this work.

- **Chapter 5: Effect of oxygen vacancies and cationic valence state on multiferroicity and magnetodielectric coupling in La and Fe-doped $BaTiO_3$.**

A solid solution of $Ba_{(1-x)}La_{(x)}Ti_{(1-y)}Fe_{(y)}O_3$ (x =0, 0.01, 0.03, 0.06) has been investigated for room temperature multiferroicity and magnetodielectric effect. The incorporation of La and Fe ions in ferroelectric $BaTiO_3$ leads to increased lattice disorder and the generation of O_vs that induce magnetism. A detailed correlated study using XRD, XPS, and Raman spectroscopy is being reported. EPR measurements show signals corresponding to defect complexes. A typical ferromagnetic and ferroelectric nature of each sample is confirmed by MH and P–E hysteresis loops, respectively, at room temperature. Temperature-dependent dielectric studies reveal the decrease of the transition temperature from undoped BTO

to room temperature with increasing substitution. The changes in the dielectric property with the applied magnetic field show the indications of the magnetodielectric effect. For x =0.015, the existence of both proper ferroelectric without lossy properties and ferromagnetic properties in a single tetragonal phase makes it a perfect room temperature multiferroic material. For this sample, the magnetodielectric coupling is the strongest with Magnetocapacitance of ~2.7% at 10 kHz and 1 T. The multiferroicity and the magnetodielectric effect exhibited by this material have been correlated to the structural properties, electric and magnetic properties, changes in valence states, and O_v.

- **Chapter 6: Defect/ Disorder correlated transport properties in La and Fe-doped $BaTiO_3$.**

Crystal structure, band gap, and the changes in the charge conduction mechanisms in ceramics are interrelated, and the underlying physics unifies all these different phenomena. The experimental and theoretical evaluation of the electronic properties of the solid solution of $Ba_{(1-x)}La_{(x)}Ti_{(1-y)}Fe_{(y)}O_3$ (x=0, 0.01, 0.03, 0.06) is attempted in this work. Band gap was observed to be tunable with La/Fe doping from 3.2 eV (x=0) to 2.6 eV (x=0.06), while the lattice disorder was found to increase. A theoretical assessment confirms a considerable shift of valence band maxima and conduction band minima with the introduction of additional defect states within the band gap. Electron localisation was also confirmed theoretically with doping. Such changes in the electronic properties were experimentally confirmed from dielectric/ac-conductivity/impedance spectroscopy studies. From different transportation models, correlated barrier hopping is a preferred mechanism in the less distorted $BaTiO_3$. However, a large polaron tunnelling process can be justified for the doped samples. The transportation is affected by the grain boundaries as much as the grains themselves. Competing contributions of these regions to the transportation mechanism are

correlated to the disorder/ distortions in the lattice in terms of the formation of O_vs.

- **Chapter 7: Conclusions and Future Scope**

This chapter summarises the results of the present thesis research work with concluding remarks. The possible future scope of the present study has also been discussed.

- **APPENDIX**

This section includes the additional research works carried out apart from the thesis works detailed in the previous chapters. An overview of the results and discussion is given in this chapter.

Appendix A: Magnetoelectric Ca/Mn modified $BaTiO_3$ for Dielectric Resonator Antenna Application

Appendix B: $BaTiO_3$ and $CaMnO_3$ epitaxial film through Pulsed Laser Deposition

CHAPTER 2

EXPERIMENTAL METHODS AND CHARACTERISATION TECHNIQUES

This chapter provides information about the synthesis route, and the different characterisation techniques used during the The present research work is elaborated and explained. The experimental measurements and the theoretical details are also provided.

2.1` Sample Synthesis

2.1.1 Sol-Gel synthesis of $BaTiO_3$

Sol-gel process is a wet chemical synthesis route in which the homogenous preparation of metal oxides and perovskite oxides can be achieved. It is a cost-effective method and requires a low reaction temperature compared to other synthesis routes. A good control over the chemical composition of the product can be achieved through this route. It is widely used for making ceramic materials at lower temperatures and as an intermediate stage between thin films of oxides in various applications. The basis of the sol-gel method is the production of a homogeneous sol from the precursors and its conversion into a gel. The solvent in the gel is then removed from the gel structure, and the remaining gel is dried.

A sol-gel method was adopted to synthesise chemically homogeneous polycrystalline powders of the desired compositions. The homogeneity was ensured by mixing the precursors of Ba, Ti in the right proportions and dissolving them in DI water. For these high-purity water-soluble precursors, Barium nitrate (99.9%), Dihydroxy bis (ammonium lactate) Titanium (IV) 50% w/w aqua solution (99.9%) are taken in stoichiometric amounts and dissolved in DI water. This solution is stirred continuously to properly dissolve the salts and for homogeneous mixing. The solutions were mixed well for two hours to ensure a homogenously distributed elemental configuration. The solution was maintained on stirring for further times to ensure that the homogeneity is maintained. In another beaker, citric acid and glycerol (1:2 ratio) were mixed in DI water to form monomers, which can form polymers upon heating. This monomeric solution was added to the stirring precursor solution to ensure the attachment of the individual elements to some monomeric form. Upon heating, the uniformly distributed combinations of element-attached monomers formed long polymeric chains, thereby arresting the homogeneity of the distributions of the different elements. The polymeric

solution of the elements and the polymers thus obtained was dehydrated gradually on the hot plate to form homogeneous gels. These gels were further dehydrated to obtain dark brown powders of the homogenously mixed elements. These brown powders were further decarbonised at 450 °C for 6 hours and 600 °C for 6 hours to eliminate all the carbonaceous and nitrogen compounds. The calcination has been done at 1200 °C for 3 hours. A schematic of the different stages in the sol-gel process is shown in Figure 2.1.

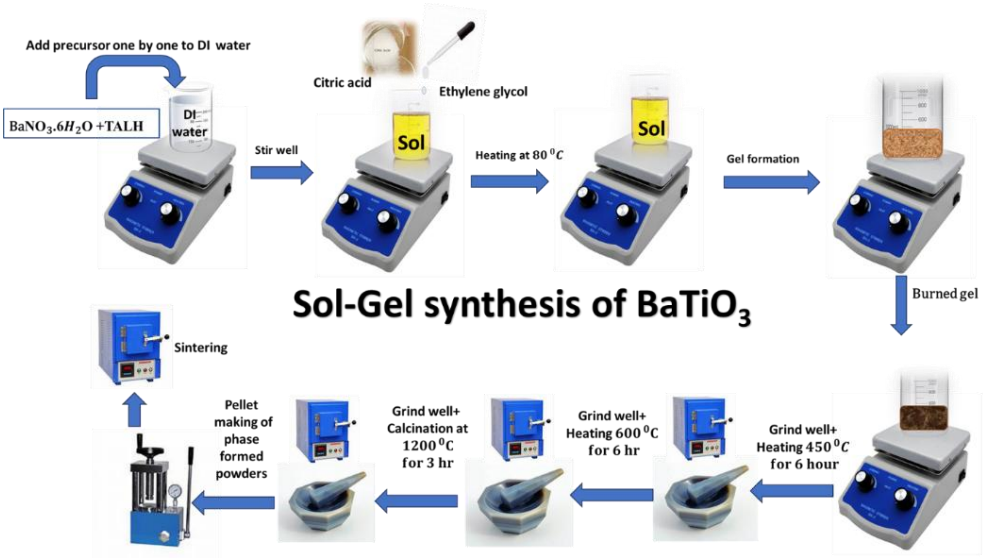

Figure 2.1: *Schematic of the Sol-Gel process*

2.1.2 Sintering of pellets

The phase-formed powder samples have been used to prepare dense pellets for further characterisations and experimental measurements. The phase formed powder sample is ground well, and using a 10mm circular die set and a high-pressure hydraulic press, the powder is pressed into circular pellets. A pressure of 2 tons is applied for 2 minutes. The prepared pellets are sintered at a high-temperature muffle furnace in normal air for densification.

In the case of dielectric and ferroelectric measurement for making more compact pellets, polyvinyl alcohol (PVA) is used as a binder. The

powder is mixed with a few drops of PVA and ground well for proper mixing of the binder with the powder sample. This mixed powder is pressed into pellets. The formed pellets are heated at 600 °C for 6 hours to remove the binder PVA before sintering at a higher temperature. Sintering helps to enhance the grain growth, crystalline quality, densification, etc. For pure BTO sintering temperature is 1350 °C, and it varies with doping with different ions.

For dielectric and ferroelectric measurements, silver paste is used as an electrode on both sides and dried. These pellets are heated at 550 °C for 30 minutes for curing. Curing is the process of making proper adhesion of the silver electrode to the pellets.

2.1.3 La and Fe-doped $BaTiO_3$ sample preparation

The precursors of Ba, Ti, and Fe are taken in the right proportions and dissolved in DI water. For these high-purity water-soluble precursors, Barium nitrate (99.9%), Dihydroxy bis (ammonium lactate) Titanium (IV) 50% w/w aqua solution (99.9 %), and Ferrous nitrate, FeNO3 · xH2O (99.9%) are taken in a stoichiometric amount and dissolved in DI water. Lanthanum oxide, La_2O_3, is used as a lanthanum precursor. Since it is not soluble in water, a few drops of nitric acid are added to dissolve La_2O_3 in DI water kept in a separate beaker. After complete dissolution of La_2O_3, the solution is transferred to the beaker in which other precursors are dissolved. This precursor solution is stirred well for 2 hours for homogeneous mixing. After this, citric acid and ethylene glycol are added and followed by the same procedure for the preparation of a pure BTO sample. After the calcination at 1200 °C, all the prepared pellets are sintered at 1350 °C for 4 hours.

2.1.3 Ca and Mn doped $BaTiO_3$ sample preparation

The precursors of Ba, Ti, Ca, and Mn are taken in the right proportions and dissolved in DI water. For these high-purity water-soluble

precursors, Barium nitrate, $BaNO_3$ (99.9%), Dihydroxy bis (ammonium lactate) Titanium (IV) 50% w/w aqua solution, TALH (99.9%), Calcium nitrate, $CaNO_3$ (99.9%) and Manganese nitrate, $MnNO_3.xH_2O$ (99.9%) are taken in a stoichiometric amount and dissolved in DI water. This precursor solution is stirred well for 2 hours for homogeneous mixing. After this, citric acid and ethylene glycol are added, and the same procedure is followed for the preparation of a pure BTO sample. After the calcination at 1200 °C, all the prepared pellets are sintered at 1330 °C for 3 hours.

2.2 Characterisation Techniques

2.2.1 X-Ray Diffraction (XRD)

X-ray powder diffraction is a powerful non-destructive characterisation technique for determining the crystal structure of materials. This can be applied in determining the type and quantity of the phases present in the sample, unit cell parameters, crystal structure, crystalline texture, crystalline size, macro stress, and micro strain, etc. [Figure 2.2].

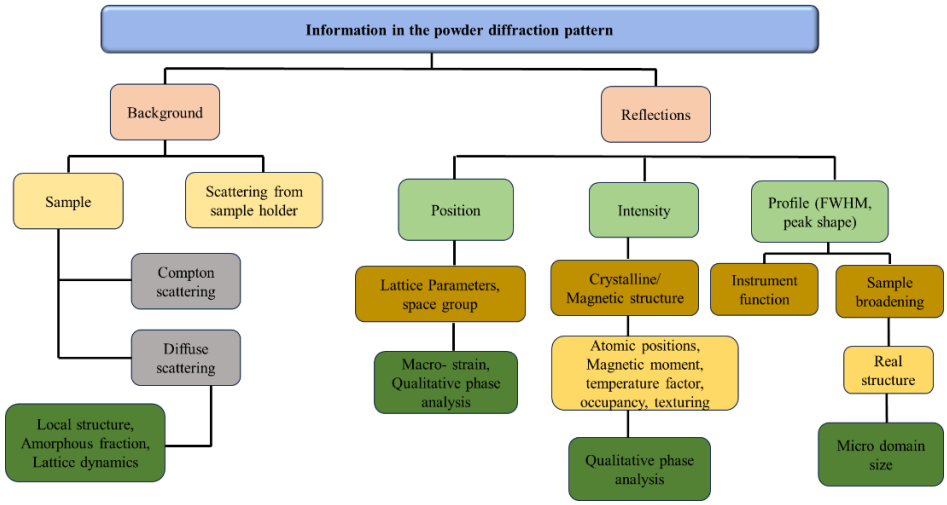

Figure 2.2: *Flow chart of the different information obtained from the powder diffraction.*

The interaction of X-rays and electrons of atoms results in the interference of diffracted rays. Depending on the atomic arrangement, when the path difference between two diffracted rays differs by an integral

number of wavelengths results in constructive interference results. This condition can be described by Bragg's law.

$$n\lambda = 2d\sin\theta$$

where n is the order of diffraction, d is the interplanar spacing, θ is the angle between the incident beam and the normal to the reflecting crystal planes, and λ is the wavelength of the x-rays [Figure 2.3].

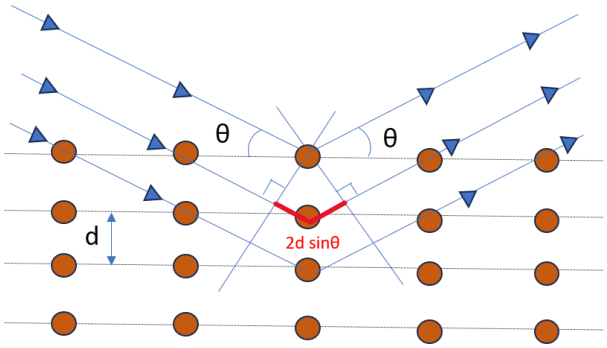

Figure 2.3: *Schematic of the Bragg equation*

The powder sample contains a finely ground large number of small crystals, called crystallites, which are randomly oriented. To obtain a precise measurement of the intensity of diffracted rays, the crystallite size must be small, i.e., typically 10 μm or less, and the number of crystallites should be large, depending on the characteristics of the specimen, like absorption, shape, etc., and the diffraction geometry. Due to the random orientation of powder material, the sample is scanned through a range of 2θ angles so that all possible diffraction directions of the lattice can be obtained. As every compound has a set of unique d-spacings, by converting the diffraction peaks to d-spacings, the resultant compound can be obtained.

The relative intensity of the diffraction lines on a powder pattern is related to six factors of the material: 1) structure factor (F_{hkl}), 2) polarisation factor (P), 3) multiplicity factor (j), 4. Lorentz factor (L), 5. absorption factor (A), 6. temperature factor (M). Hence, the intensity can be written as [88];

$$I_{hkl} = cjPLAMF_{hkl}^2$$

Here, c is a constant scale factor; it depends on the amount of X-ray exposure, the sensitivity of the detector, etc.

Here, the structure factor, F, corresponds to the atomic arrangement of the atom in the crystal. It is obtained by simply adding together all the waves scattered by the individual atoms. $F_{hkl} = fe^{2\pi i(hu+kv+lw)}$. The quantity f is the atomic scattering factor, used to describe the "efficiency" of scattering of a given atom in each direction. It will be different with the arrangement of atoms given by different values of u, v, and w, which affect the scattered beam. For any atom scattering in the forward direction, have f=Z, the atomic number. The waves scattered by individual electrons will be more out of phase with an increase in θ value, and hence the value of f decreases. As the wavelength of the incident beam is shorter, the path difference will be larger, leading to greater interference between the scattered beams for a fixed value of θ. This will lead to a smaller value of f. The net effect is the decrease of the f value as the quantity $\sin\theta/\lambda$ increases. f is also called as form factor because it depends on the distribution of electrons around the nucleus [88]. Hence, the detailed analysis of the intensity profile of the XRD pattern leads to the structural identification

X-ray diffractometers consist of three basic elements: an X-ray tube, a sample holder, and an X-ray detector. The mechanical assembly that makes up the sample holder, detector arm, and associated gearing is referred to as the goniometer.

X-Ray tube:

X-rays are generated in a cathode ray tube by heating a filament to produce electrons. The generated electrons are accelerated by applying a voltage and bombard the powder material under investigation. Characteristic X-ray spectra are produced when electrons have sufficient energy to dislodge the inner shell electrons of the target material. The wavelengths of the X-rays produced are specific to the target material, like Cu, Fe, Mo, and Cr. These X-ray spectra consist of several components, the

most common being K_α and K_β. K_α consists, in part, of $K_{\alpha1}$ and $K_{\alpha2}$. $K_{\alpha1}$ has a slightly shorter wavelength and twice the intensity of $K_{\alpha2}$ [Figure 2.4]. Monochromatic X-rays needed for diffraction are attained by filtering with foils or using crystal monochromators. $K_{\alpha1}$and $K_{\alpha2}$ are sufficiently close in wavelength such that a weighted average of the two is used. Copper is the most common target material for single-crystal diffraction, with Cu K_α radiation = 1.5418Å. The collimated X-ray produced is directed onto the powder sample.

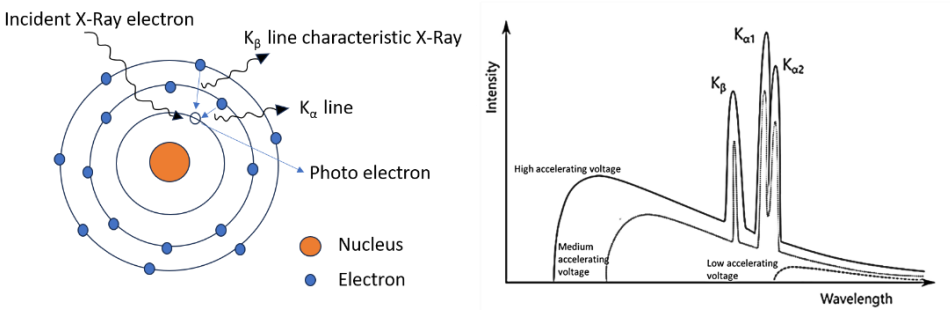

Figure 2.4: *Schematic of the X-Ray generation and the characteristic radiations generated.*

Sample holder:

The sample holder is an important stage in the XRD instrument. Different kinds of sample holders are available depending on the nature of samples, like powders, bulk, and thin films. Sample homogeneity is an important parameter for obtaining accurate XRD results. For achieving proper uniformity, grinding, mixing, and blending techniques should be employed. Surface effects, such as preferred orientation and surface roughness, can significantly impact XRD data. These effects can distort peak intensities and positions, leading to inaccuracies in phase identification and quantification. Hence, the sample is evenly distributed and packed to achieve good coverage of the holder surface without overloading, and needs to be tapped or gently compressed on the powder surface to achieve a flat and uniform surface. Filling the sample-on-sample holder too high or too low will lead to erroneous data and a shift of peak positions. If there is a

very small amount of sample, then proper silicon sample holders need to be used to avoid the background signal.

X-Ray detector:

In lab source XRD, the X-ray photons that should be detected typically have an energy range from 5 to 20 keV. The background bremsstrahlung photons, an unwanted by-product, have energies up to 55 keV. Detectors are classified as photon counting detectors or digital detectors and integrating detectors, or analog detectors. The conversion of a photon's energy into electric charge is integrated and measured in an analog detector. In this, the detector loses the information about the photons detected is lost and not recoverable. While in the case of photon counting detectors, each photon converts its energy into charge. Each charge package is registered by the system. These types of detectors have the advantage of zero detector noise, no read-out dead time moderate to good energy resolution for the photons of interest [89].

XRD can be done in two geometries, one is Debye Scherrer diffractometry and Bragg Brentano parafocusing geometry [Figure 2.5]. Debye Scherrer uses a capillary geometry with a long, thin sample in a closed chamber, usually used for thin film samples. Bragg Brentano places a sample in a goniometer with a symmetric reflection geometry common for a powder sample. In this research work, we have used Bragg-Brentano geometry.

Two types of scans are possible in this geometry

1) θ-2θ goniometer: In this scan, the X-ray tube is stationary. Simultaneous movement of the sample by the angle θ and the detector by the angle 2θ is happening during the measurement. The distance between the X-ray source and the detector from the sample is the same. As the movement of the sample holder and detector in

a 1:2 relation, the reflected beam always focuses on a circle of constant radius in which the detector moves.

2) θ-θ goniometer: In this scan, the sample is stationary in the horizontal position, and the X-ray tube and the detector both move simultaneously over the angular range θ.

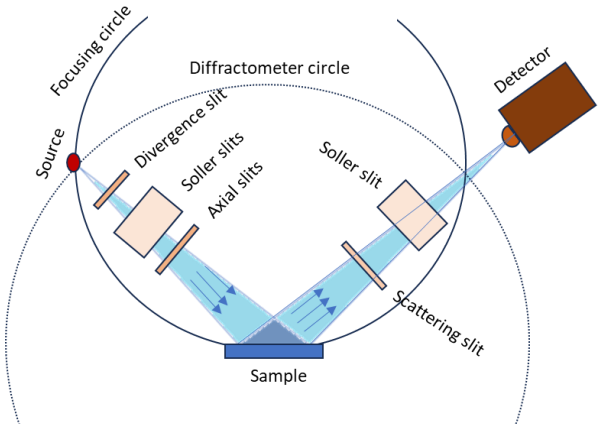

Figure 2.5: *Schematic diagram of the Bragg Brantano geometry*

2.2.1.1 Rietveld Refinement

Analysis of the XRD pattern is necessary to explore the structural factors of the material under investigation [Figure 2.6]. Rietveld refinement is a method described by Hugo Rietveld for characterizing crystalline material. A theoretical profile is matched with the measured profile through the Rietveld approach [90]. The difference between the calculated intensity (model) to the observed intensity (sample) is minimised by least squares refinement. It is a full pattern-fitting approach. This process is possible for already known material with a structure that already exists. It cannot be used for solving the crystal structure. The results of refinement contain the information about the cell parameters, anisotropy, atomic displacements, crystallite size, strain, etc. This also helps with the quantitative analysis of the weight percentage of different phases present in the sample.

There are different software available for refinement like MAUD, TOPAS, GSAS-II, FullProf, etc. The calculated pattern of the structure is usually a Crystallographic Information File (CIF). The Crystallography Open Database (COD) contains a large number of CIF files to be downloaded. Depending on the phases present in the sample, CIF information can be downloaded from COD. The experimental XRD pattern needs to be measured with a long scan rate with proper sample preparation. Both the experimental and calculated patterns, background, peak profile, etc, need to be given as input to the refinement software and start refining the parameters corresponding to the instrument, sample, structure, etc.

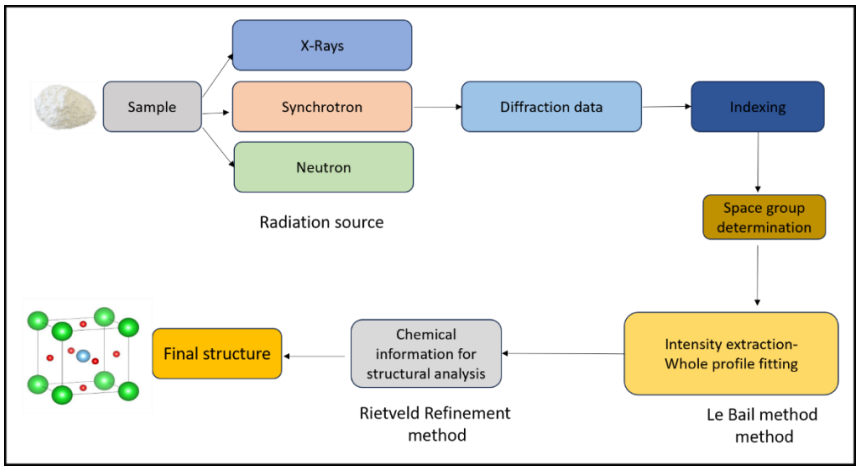

Figure 2.6: *Flow chart of steps in the process of structural analysis from Powder Diffraction Data*

The residual difference (R) between the theoretical and measured results determines the quality of the refinement. Small values of R correspond to the better fitting and more accurate crystal structure analysis. The commonly used R values are the Residual variance factor (R_p) and the weighted residual variance factor (R_{wp}), which are defined as follows [91];

$$R_p = \sum |Y_{oi} - Y_{ci}| / \sum Y_{oi}$$

$$R_{wp} = \left[\sum w_i (Y_{oi} - Y_{ci})^2 / \sum w_i {Y_{oi}}^2 \right]^{1/2}$$

The measured XRD intensity is Y_{oi}, the calculated intensity is Y_{ci} at point i, and w_i is the statistical weight factor. The change of R_{wp} towards a lower value indicates the refinement direction towards better fitting refinement results. The ratio of R_p to R_{wp} value is the goodness of fit χ^2. In general, χ^2 value close to 1 and an R_{wp} value close to 10% or less is a good fit, and refined parameters are considered reliable. However, refinement cannot be completely relied on the R_{wp} value; sometimes there will be pseudo-convergence phenomena. Hence, along with the χ^2 and R_{wp} value, the chemical parameters of the refinement structure model, such as atomic coordinates, atomic proportions, etc., should be physically possible. Apart from all these factors visual assessment of the fitting of the experimental and theoretical model is also important.

In this work, a Bruker D2 phaser XRD instrument [Figure 2.7] with Cu K_α (λ = 1.54 Å) radiation was employed and operated at an applied voltage of 30 kV and current of 10 mA using Bragg Brentano geometry with a θ-θ goniometer. A silicon XRD sample holder is used, and the 2θ range is from 20° to 80° with a step size of 0.02° and a scan time of 0.6 seconds. Full Prof software is used for the Rietveld refinement process, and the refined CIF file is analysed and plotted in Visualisation of Electronic and Structural analysis (VESTA) and Mercury software.

Figure 2.7: *Picture of D2 PHASER XRD*

System Specifications

Make: Bruker

Model: D2 Phaser

2 theta range: -3°-160°

X-Ray Source: Cu K_α radiation

Detector: LYNXEYE one-dimensional strip detector.

2.2.2 Raman Spectroscopy

When light incident on a material, there will be energy transfer between the incident radiation and the material, which leads to inelastic scattering. The scattered light can provide information about the vibrational state of matter. Raman spectroscopy is the study of inelastic scattering of light. Raman scattering is named after Indian physicist Chandrasekhara Venkata Raman, who discovered it in 1928. He used mercury lamps as a monochromatic source of photons and a photographic plate to record spectra; he won the Nobel prize in physics in 1930 for the discovery of the Raman effect.

A monochromatic light source is focused on a sample, and the radiation after scattered from the sample. The process of elastic scattering in which the majority of the light scattered has the same energy as that of the incident energy is called Raleigh scattering. A small fraction of light is scattered with different energy than that of the incident energy due to inelastic scattering, known as Raman scattering. The scattered light consists of the Raleigh line, which is a strong line having a frequency the same as that of the incident light. Weak lines of higher frequency, higher than the exciting line, are anti-Stokes lines, and weak lines of lower frequency than the exciting lines are called Stokes lines. The schematic representation of Raman scattering is shown in Figure 2.8.

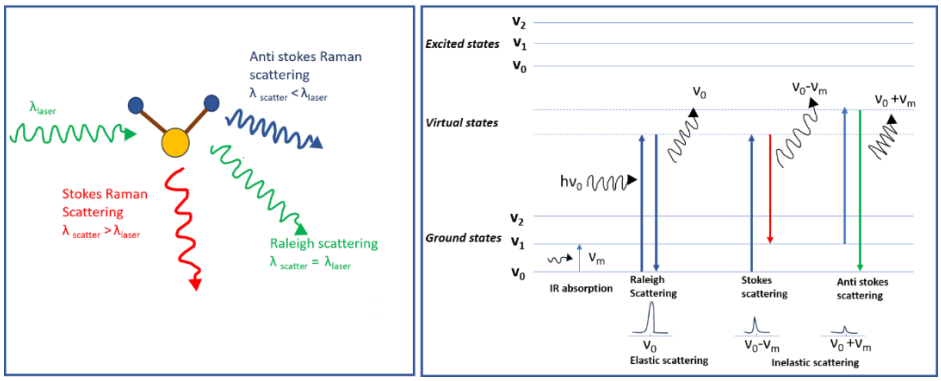

Figure 2.8: *(a) Schematic of the different lines in Raman scattering, (b) Energy excitation diagram of different Raman lines.*

The interaction between the electron cloud of the sample and monochromatic light induces the changes in the vibrational state and generates the Raman mode. Group theory provides selection rules on symmetry considerations to identify the Raman active modes. A Raman spectrometer consists of a Laser source, a sample illumination system, spectrometer. Details of all the components are shown in Figure 2.9.

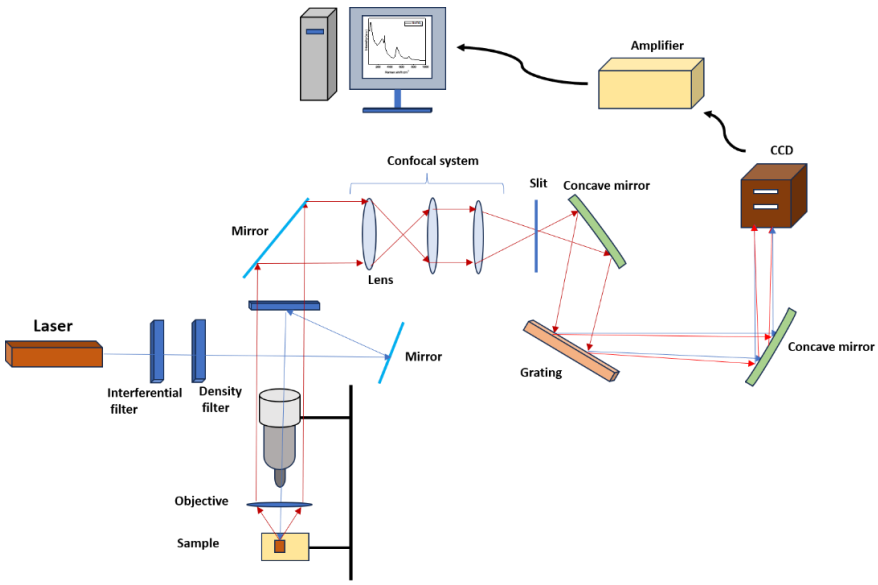

Figure 2.9: *Block diagram of the instrumentation of the Raman spectrometer*

Laser source

Mercury arc lamp of 435.8 nm line of a coiled low-pressure source was used as a light source in Raman spectrophotometers until the 1960s

[92]. Laser sources became available in the late 1960s and completely replaced the mercury lamp. These laser sources provide a stable and intense beam of radiation. The table provides a list of different sources of lasers used for different wavelength regions.

Table 2.1: Laser sources of Raman spectroscopy with wavelength

Laser	Wavelength (nm)
Argon ion	488 or 514.5
Krypton ion	530.9 or 647.1
Helium Neon	632.8
Near IR diode	785
Nd-Yag Laser	1064

Sample illumination system

In Raman spectroscopy, there is no need for a separate sample holder; the sample can be placed on a glass plate, and a very small sample can be investigated. The laser beam is focused on the sample by means of different lenses, and the calibration is done by using a Si film. The measurement is done on back-scattered geometry in which the sample is irradiated with a laser beam, and the scattered light is collected and focused back towards the detector, typically at a 180° angle.

Spectrometer

One of the great challenges in the Raman spectrometer is to remove the Rayleigh signal. Thus, the most critical component in a Raman spectrometer is the filter that damps the Rayleigh scattered light. For this, either a notch, edge pass, or bandpass filters are used, depending upon the laser wavelength. The Rayleigh line is filtered out by using a suitable filter, while the rest of the scattered light is dispersed onto a detector. A charge-coupled device (CCD) is used as the detector in the Raman spectrometer. A CCD is a silicon-based multichannel array detector of the UV, Visible, and near-infrared region. The high sensitivity of the CCD makes it suitable to

detect weak Raman signals, and the entire Raman spectrum can be detected in a single acquisition through multi-channel operation.

CCD detector contains 1D or 2D arrays of millions of individual detector elements (Pixels). Each of these elements interacts with light and builds up charge. The scattered light is dispersed with a diffraction grating, and the dispersed light will fall on the long axis of the CCD array. Each element in the detector will detect the light from the different spectral regions. The charge registered will be more as the interaction is longer and the light. After the measurement, each charge reading is measured. CCDs require cooling for their proper spectroscopy operations. Typically, this is done using Peltier cooling or liquid nitrogen cooling [93].

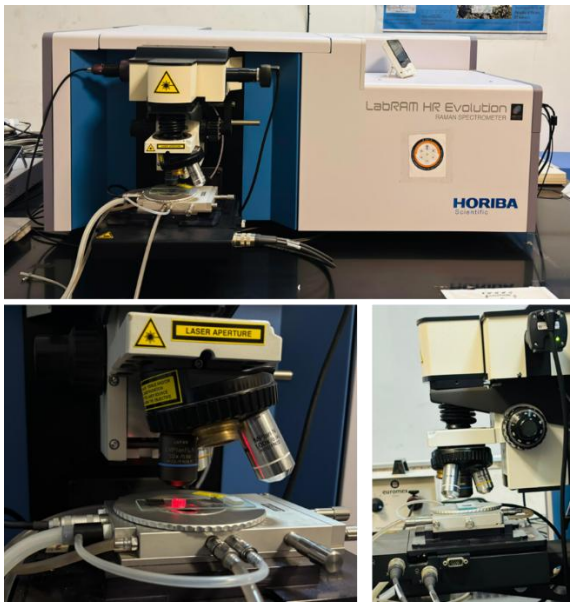

Figure 2.10: *Raman spectrometer*

System specifications:

Make: Jobin Yvon Horibra [Figure 2.10]

Model: LABRAM-HR visible (400−1100 nm)

Spectral Range: 5−4000 cm^{-1}

Excitation Laser Sources: He-Ne (632.8 nm) and Argon (488 nm)

Detector: CCD detector Spectral resolution: ~1 cm^{-1}

Optics: High stability confocal Microscope

2.2.3 UV-Visible Diffuse Reflectance Spectroscopy (UV-Vis DRS)

Specular reflection is the reflection of incident light symmetrically concerning the normal line, which satisfies the laws of reflection. However, Diffuse reflection is the reflection of incident light in all directions and does not follow the laws of reflection. When light incident on the surface of crystalline powder material, a part of the light undergoes specular reflection on each grain surface. The remaining part of the light will be refracted into the interior of the grains and undergo multiple times of absorption, reflection, and refraction. Finally, radiation will come out from the surface of the powder in all directions is called diffuse reflection [Figure 2.11].

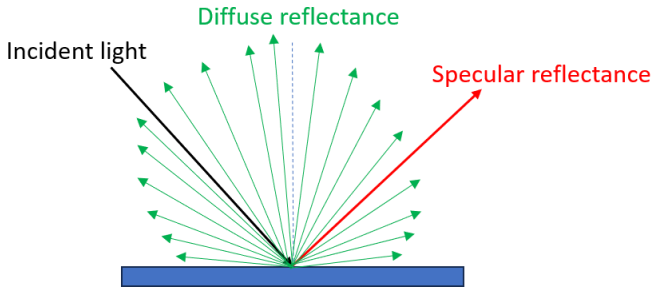

Figure 2.11: *Schematic of the specular reflection and Diffuse reflectance*

This diffuse reflectance is used to probe the important parameters of semiconducting material, such as bandgap (E_g), electronic disorder, i.e., Urbach energy (E_U), and defect states using the UV-visible optical absorption.

The most accepted model of the theory of diffuse reflectance is the Kubelka-Munk model. The model proposes that the behaviour of light inside a light scattering grain of infinitely thick, opaque material can be written as

$$F(R_\infty) = \frac{(1-R_\infty)^2}{2R_\infty} = \frac{K}{S}$$

$F(R_\infty)$ is the Kubelka Munk function, K is the molar absorption coefficient, s is the scattering coefficient, and R_∞ is the relative diffuse reflectance of the sample over a standard sample.

$$R_\infty = \frac{R_{Sample}}{R_{standard}}.$$

$F(R_\infty)$ is proportional to the absorption coefficient of the material, α, and can be written as

$$F(R_\infty) = \alpha = C\,\frac{(h\nu - E_g)^{1/n}}{h\nu}$$

Where C is the proportionality constant, hν is the photon energy, and E_g is the band gap. It can be written in the form of a linear equation $(\alpha\, h\nu)^n = h\nu\text{-}E_g$ [94]. The Tauc plot shows the quantity hν on the abscissa and the quantity $(\alpha h\nu)^n$ on the ordinate. Hence, a plot of $(\alpha h\nu)^n$ v/s hν produces a straight line, and the intercept on the energy axis gives the value of the band gap of the sample

Urbach energy, E_U, is characterised by the exponential tail observed near the band gap as a tail in the disordered crystalline material [95]. These tails are arising due to the localised states in these materials due to defects and disorder, which extend into the band gap. In the spectral region corresponding to transitions involving the tails of the electronic density of states, the spectral dependence of the absorption coefficient α is described by the Urbach equation, $\alpha = \alpha_0 exp\left(\frac{h\nu - E_g}{E_U}\right)$, where α_0 is a constant, E_U reflects structural disorder and defects of a semiconductor [95].

Instrumentation:

The instrumentation for UV-Vis-DRS typically consists of a light source, a sample holder with an integrating sphere, and a detector [Figure 2.12]. The light source is usually a xenon lamp or a light-emitting diode

(LED), which provides a broad spectrum of light in the UV and visible regions. The sample holder is designed to hold the sample in a specific position and to minimise the effects of stray light. Integrating spheres are spherical with an inner surface and inner wall made of light-scattering material, such as barium sulphate, having high reflectance [Figure 2.12].

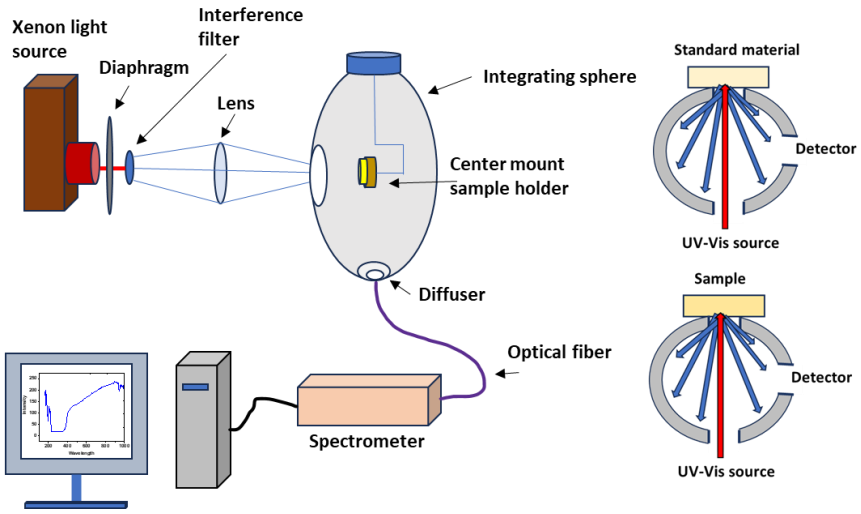

Figure 2.12: *Schematic of the instrumentation of the UV-DRS*

The detector is usually a photomultiplier tube or a charge-coupled device (CCD), which measures the intensity of the reflected light as a function of wavelength.

For the measurement, initially, the baseline correction is done by placing the standard sample white board filled with barium sulphate at the reflection position, and then the diffuse reflected light is measured by converging the scattered light in all directions through an integrating sphere.

System specifications:

Make: Shimadzu [Figure 2.13]

Model: UV 2600i

Spectral Range: 220 nm to 1400 nm,

Excitation Laser Sources:

Detector: Photo multiplier Tube

Figure 2.13: *Shimadzu UV-Vis DRS spectrophotometer*

2.2.4 X-Ray Photoelectron Spectroscopy (XPS) for core level studies

The XPS spectra consist of the electron counts or the number of electrons (intensity) ejected from the sample surface with a kinetic energy after overcoming its binding energy (B.E.) to the atom. For a particular atom, the binding energy is the signature of the electronic orbitals. Irradiation of the sample with monoenergetic soft X-rays (energy less than ~ 6 keV), leads to emission of electrons due to the photoelectric effect. Usually, Mg K_a (1253.6 eV, line width ~ 0.70 eV) and Al K_a (1486.6 eV, line width ~ 0.85 eV) sources generate X-rays for XPS measurement [96], [97]. The rays can penetrate up to a few nanometres into the depth of the sample surface. The energy spectrum is collected using an electron spectrometer. The energy of the irradiated photons is the total energy *hv*, which is supplied

by the X-rays. This energy is distributed in overcoming the B.E. of the atomic orbital from which the emission of electrons takes place, and the work function, φ_{Sp}, of the surface of the material, while the remaining part provides the kinetic energy (K.E) of the ejected electrons [97], [98]. The relation can be expressed as:

$$K.E.+B.E.+\varphi_{Sp} = h\nu$$

Hence, the K.E. can be expressed as:

$$K.E. = h\nu - B.E. - \varphi_{Sp}$$

The spectra collect the information of the K.E. of the emitted electrons, and information on the B.E. is collected using the relation:

$$B.E = h\nu - K.E - \varphi_{Sp}$$

Figure 2.14 diagrammatically demonstrates the binding energy equation in terms of incident X-ray energy, K.E. of the ejected electrons, and φ_{Sp} of the material.

The process of photoelectron emission comprises three steps:

1. The interaction of the orbital electrons and X-rays leads to the photoelectrons/Auger electrons.
2. Scattering process due to the movement of some of these electrons from the bulk to the surface.
3. After overcoming the sample's threshold work function, emission of electrons are emitted from the vacuum surface.

The core electron has a B.E. concerning the Fermi energy (E_f) of the system, and not the vacuum-level energy. Hence, the difference between the final states and the initial states' energy when photo photo-excited electron has already left the atom is denoted as the B.E.

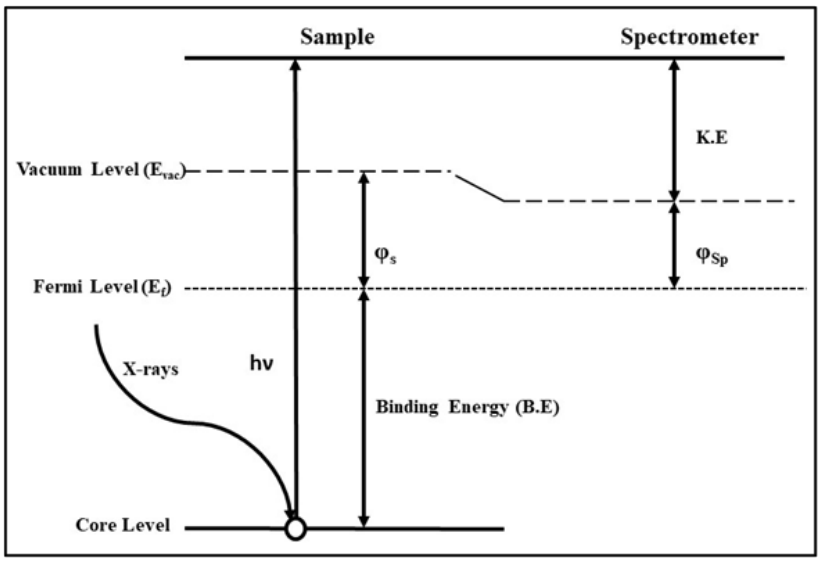

Figure 2.14: *Schematic diagram illustrating the XPS equation that includes X-ray energy (hv), binding energy (B.E.), and the kinetic energy measured (K.E.). The sample's work function is represented by φ_S and spectrometer work function (φ_{Sp}).*

The electrons have certain K.E. when moving through the material, penetrating some distance before losing their energy due to inelastic collisions. The range of energy used in XPS is generally from 50-1200 eV [99]. So, the mean free path of the electron is up to a few layers [100]. Hence, the photoelectrons originating from the atomic orbits are extremely surface-specific. In a typical XPS spectrum, several spectral lines are observed along with the background. The elastically scattered electrons, without any energy loss, emitted from the sample surface, contribute to the sample's composition.

Instrumentation:

XPS instruments have the following components [Figure 2.15] [101]:

- The system works under an ultrahigh vacuum, meaning it's kept at an extremely low pressure (less than 10^{-9} Torr). This is important because the photoelectrons produced don't travel far before they can get absorbed by gas molecules, since they have low energy.

- To excite the sample, X-rays like Al Kα or Mg Kα are used. A monochromator helps make sure only X-rays of a specific energy hit the sample, so the results are clear and consistent.
- The photoelectrons that come off the sample are then sorted by an electron energy analyser, which tells us their energy levels. A common type used is called the Concentric Hemispherical Analyser.
- An argon ion gun is used to clean the sample surface by gently sputtering away contaminants like leftover carbon from the air. It can also be used to look at different layers beneath the surface by sputtering deeper.
- Since some materials can build up a positive charge when electrons leave their surface, an electron flood gun sprays electrons back onto the sample to keep things balanced. This prevents shifts in the data caused by charging, and any small shifts can also be corrected by referencing a standard carbon peak in the spectrum.
- Finally, the data collected is processed by software and compared to known reference data to help identify what's on the sample surface.

X-ray photoelectron spectroscopy (XPS) was performed using a - to evaluate the chemical composition, bonding environment, and oxidation states of the elements present in the samples. was used to investigate the materials. A flood gun was used to irradiate the samples and neutralise the charging effects.

System specifications:

Make: Thermo-Scientific Escalab

Model: 250-Xi XPS spectrometer

Excitation Sources: Monochromatic Al-*Kα* X-rays source

Spectral Resolution: 0.3eV

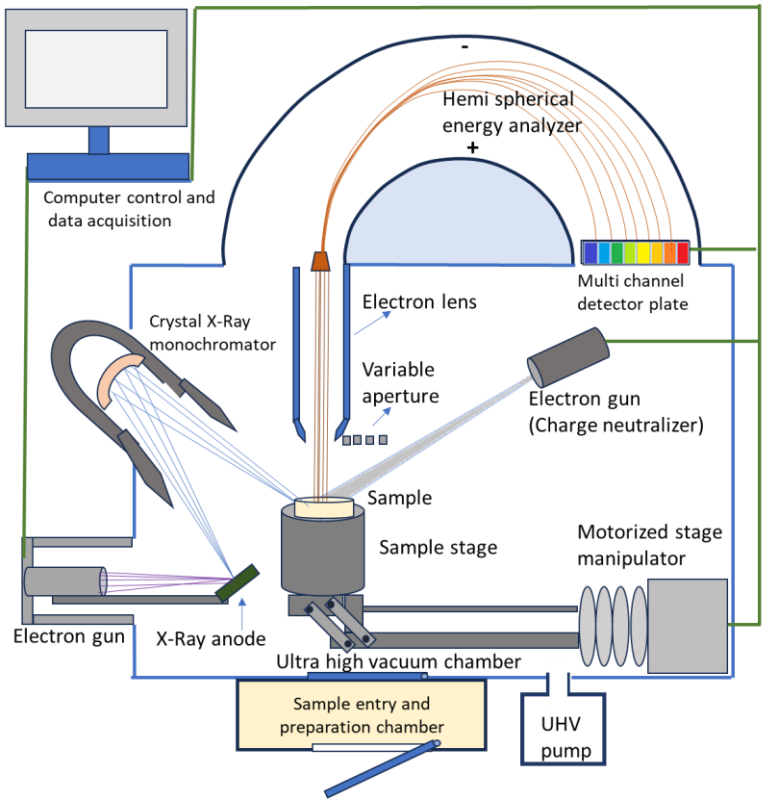

Figure 2.15: *Schematic of the XPS instrumentation*

2.2.5 Photo Electron Spectroscopy (PES) for valence band studies

PES is used to study the occupied electron density of states and the mapping of the valence band structure of solid-state materials. The principle of PES is the same as that of XPS, which utilises photo-ionisation and analysis of the kinetic energy distribution of the emitted photoelectrons. However, in this measurement, the energy of the source of radiation is very less and it is capable of ionising electrons from the outermost levels of atoms, the valence level. The valence band structure can be scanned by this spectroscopy. The valence band has different features corresponding to the different elements in the material. The features corresponding to the valence band contributions from different elements can be probed by resonant photoelectron spectroscopy.

Off-resonance: When the photon energy does not match any core level transition energy of any atom in the sample, then the VB spectra obtained are in off-resonance.

On resonance: When the photon energy matches a core-level transition, the signal from the valence band electrons associated with that atom is enhanced and modifies the feature corresponding to the particular atom in the VB.

A study of the off-resonance and on-resonance can be used to distinguish the different features in the valence band.

The instrumentation of PES is the same as described in the XPS section. The synchrotron beam is monochromatized using a variable line spacing plane grating (VLS-PG) based monochromator. The XPS measurement was used in Grating III and Grating IV, and the valence band measurement was used to do with Grating II with low energy. The experimental setup has separate preparation and analysis chambers. The preparation chamber has having sample cleaning facility, and it is equipped with LEED. The analysis chamber has the facility of a closed-cycle Cycle Refrigerator, a 5-axis manipulator, a hemispherical electron energy analyser, and a flood gun. All these chambers are under vacuum, and the sample can be transferred between the chambers without breaking the vacuum. BL 10 PES measurement facility is shown in Figure 2.16.

System specifications:

Make: Angle Resolved Photo Electron Spectroscopy (ARPES) Beamline (BL-10) of INDUS-2 Synchrotron Source, Raja Ramanna Centre for Advanced Technology (RRCAT), Indore.

Spectral Range: 30 eV to 1000 eV

Resolution: 35 meV at 90 eV photon energy

Flux: 5×1011 photons/sec/200 mA

Beam size: 300 µm (H) × 100 µm (V) approximately

Monochromator: Four VLS –Plane Gratings

Analysis chamber base pressure: $7x10^{-11}$ mbar

Figure 2.16: *Instrumentation of the PES in Beamline 10, Indus II synchrotron facility* [102].

2.2.6 X-Ray Absorption Spectroscopy (XAS)

When X-rays interact with matter, three main processes can occur: absorption, elastic scattering, and inelastic scattering.

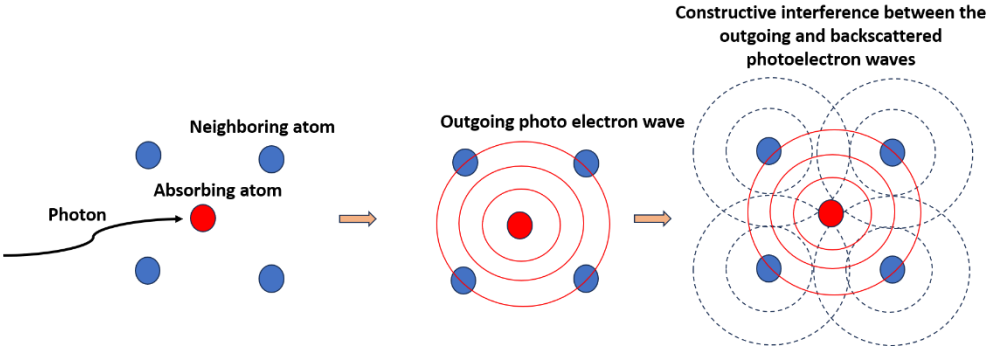

Figure 2.17: *Schematic of the X-Ray absorption and the scattering of the outgoing photoelectron wave.*

When an X-ray of energy E is absorbed by the atom, emission of a core electron of binding energy E_0 will take place with K.E ($E-E_0$). The core level from which emission takes place will eventually be filled by an electron and leading to the fluorescent X-Ray or Auger electron. The absorption coefficient $\mu(E)$ has a sharp step at the core level binding energy corresponding to the highest absorption of X-ray at that energy. After the absorption, if the atom is isolated, there is no chance of scattering with neighbouring electrons, and it shows a smooth function. However, the ejected photoelectron can scatter from neighbouring atoms. And shows an oscillatory function after the absorption edge [Figure 2.17].

XAS studies the X-ray absorption coefficient near and above an X-ray absorption edge. XAS can be broken into two regimes [Figure 2.18];

1) Extended X-Ray Absorption Fine Structure (EXAFS)
2) X-Ray Absorption Near Edge Structure (XANES)

XANES is the absorption fine structure close to the absorption edge. The approximate range of XANES includes 10 eV below the absorption edge and 20 eV above the edge. In this region, there will be a large variation of the absorption coefficient, and dominated by pre-edge and absorption edge features. This measurement can provide information about the unoccupied energy level. The soft X-Ray absorption spectra correspond to Near Edge X-Ray Absorption Fine Structure (NEXAFS) related to surface sciences and organic materials. The term XANES is used for hard X-ray spectra related to coordination geometry and for metal and inorganic materials [103].

XANES region contains pre-edge feature (Small features between the Fermi energy and the threshold), edge (the main rising part of XAS spectrum), and post-edge feature (Characteristic feature above absorption edge) [Figure 2.18]. The analysis of the shape, position, and pre-edge features of XANES reveals the oxidation state of the atom, coordination geometry, d-band occupancy, charge transfer, and orbital occupancy.

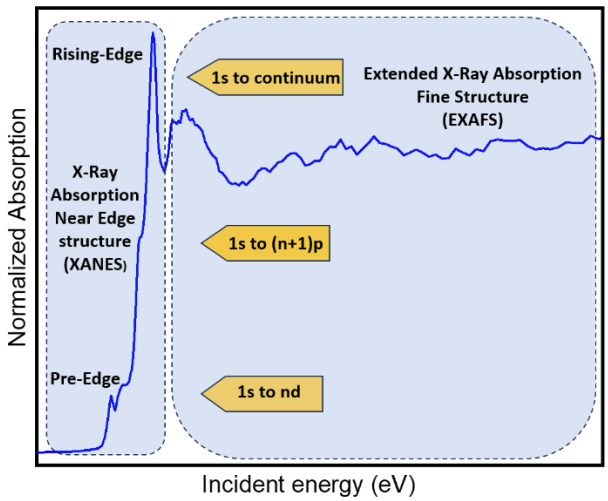

Figure 2.18: *Different regions of XAS spectra*

EXAFS data is the oscillatory data starting after the rising edge around ~50eV to extending up to ~1000 eV above the edge. After absorbing the X-ray, the ejected photo-electron can scatter from neighbouring atoms. The scattering of the photo-electron wave function interferes with itself. The absorption coefficient μ(E) depends on the density of states with energy (E-E_0) at the absorbing atom. The interference at the absorbing atom varies with energy, leading to an oscillatory feature for the absorption coefficient called the EXAFS regime. Taking the Fourier transform of this absorption data and fitting the oscillatory function through different scattering paths of electrons can yield the coordination number, the nature of neighbouring atom (approximate atomic number), distance between the central and neighbouring atom, bond distances, and quantify the degree of disorder and structural variations in the immediate environment of the absorbing atom.

EXAFS region can be defined as a function χ as a function of energy in terms of the absorption coefficient.

$$\chi(E) = \frac{\mu(E) - \mu_0(E)}{\Delta\mu_0}$$

Here, the numerator corresponds to the removal of the background and division by $\Delta\mu_0$ corresponds to the normalisation of the function, in which the normalisation function is considered as the sudden increase in the absorption coefficient edge. For the interpretation of EXAFS, it is general practice to use the photoelectron wave vector, k, which is an independent variable that is proportional to momentum rather than energy.

Instrumentation:

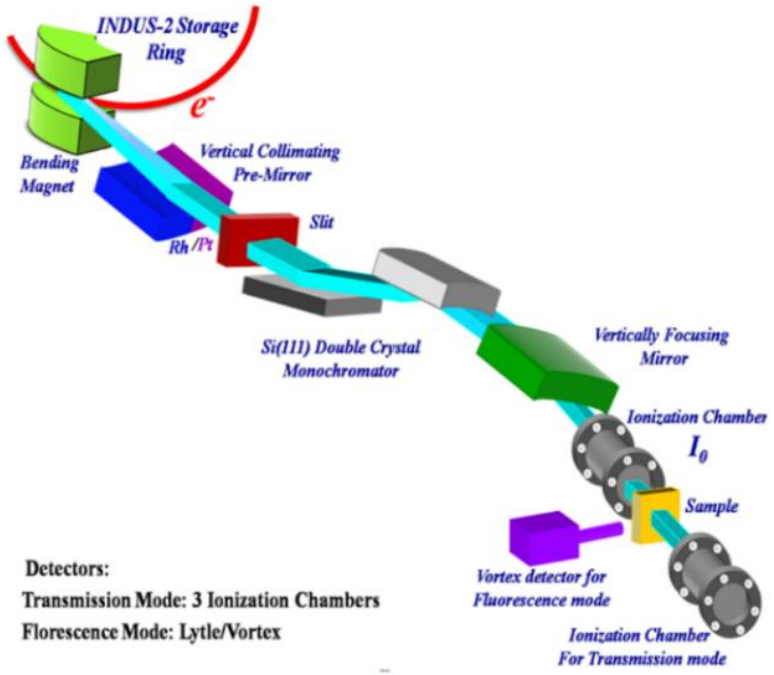

Figure 2.19: Block diagram of the EXAFS *measurement setup in Indus BL 9 synchrotron radiation facility* [102].

The K-edges of Ti (4966 eV) and Mn (6539 eV), X-ray absorption spectra were recorded. XANES measurements were carried out at room temperature, and the Ti K-edge was in transmission mode, and the Mn K-edge was in fluorescence mode. Ion chambers are filled with He, N_2, and Ar for the measurement of Ti and Mn K edges. The Ti and Mn foils are taken as a reference. The higher harmonic components are suppressed by the detuning of the monochromator by ~60% during the data collection.

Both transmission and florescent modes can be used to record EXAFS spectra. The sample is placed between two ionisation chamber detectors in the case of transmission mode. For measurements in the transmission mode, the sample is placed between two ionisation chamber detectors. The incident flux measured by the first ionisation chamber and the second ionisation chamber measures the transmitted intensity. Energy calibration measurement of the reference metal foils is done by a third ionisation chamber. Fluorescence mode is used for dilute samples or thin film samples. The EXAFS data is recorded using silicon drift detectors [Figure 2.19].

Samples are made in the form of pellets by mixing the sample with an inert binding agent, cellulose. The amount of sample required is calculated for each element based on the absorption coefficient of that element. The remaining amount is taken by the cellulose and pressed into pellets. In the case of fluorescence mode, the pellets are made by only the sample; no cellulose has been used. These pellets are covered with kepton tape and stuck on the sample holder and placed vertically to the synchrotron beam. The alignment of the sample holder is done according to the mode of measurement, for the transmission mode detector is placed along the direction of the sample, and for the fluorescence mode detector is placed in front of the sample at a 45º angle. ATHENA software version 0.9.26 is used for further analysis of the obtained EXAFS data, such as background subtraction and normalisation [104] .

System specifications:

Make: EXAFS Beamline (BL-09) of INDUS-2 Synchrotron Source, Raja Ramanna Centre for Advanced Technology (RRCAT), Indore [Figure 2.20].

Flux: 10^9 ph/sec at 10 keV

Beam size: 1 mm x 0.2 mm

Energy Range: 4 to 25 keV

Optics: Si (111) based double crystal monochromator for energy selection and meridional cylindrical mirror (Rh/Pt coated) for collimation.

Resolving power: 10^4

Excitation Sources: Synchrotron radiation 2.5 GeV ring operated at 120 mA injection current.

Detector: Lytle/ vortex (fluorescence mode), ionisation chamber (Transmission mode)

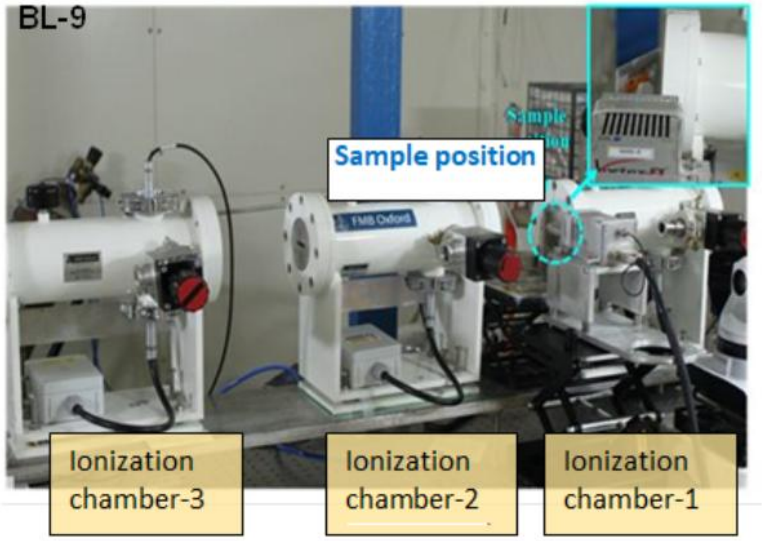

Figure 2 .20: *EXAFS measurement instrumentation in Beamline 9, Indus II synchrotron radiation facility* [102].

2.2.7 Field Emission Scanning Electron Microscope (FE-SEM)

A microstructure image of the materials is captured by FE-SEM. The morphology, surface structure, thickness, and particle size can be analysed from FE-SEM. An electron beam is used for imaging the material. When high-energy electrons impinge on the sample, different kinds of electrons, secondary, Auger, primary, and backscattered electrons, and X-rays are

generated depending on the depth of electron matter interaction [Figure 2.21].

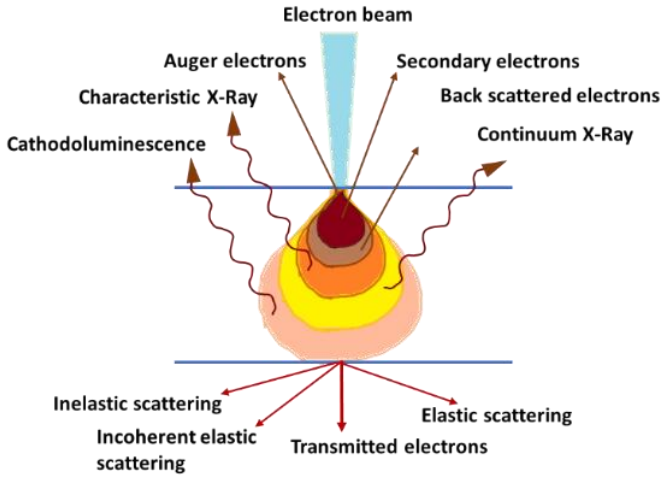

Figure 2.21: *Schematic of the different kinds of radiation emitted when high-energy electrons impinge on the sample*

- Secondary electrons (SE)

When the impinging electrons interact with a few nanometres of the sample, secondary electrons are generated. SE electrons undergo inelastic interaction between the beam and the sample. It is sensitive to surface structure and provides topographic information.

- Backscattered electrons (BSE)

Backscattered electrons are primary electrons that are back-reflected by the atoms in the sample. Back-scattered electrons are generated from a wide region within the interaction volume. These are high-energy electrons, scattered from deep inside the sample rather than the region of origin of SE (a few microns below the surface). This will provide compositional information about the sample. Backscattered electrons are reflected after elastic interactions between the beam and the sample. BSE shows high sensitivity to atomic number. As the atomic number of the element in a material increases brighter the BSE image of that particular element

compared to a lesser atomic number element in the same material. Hence, this technique can be utilised for chemical phase distribution.

- X-rays

When electrons incident on the sample, characteristic X-rays are produced below the depth of the origin of BSE. These X-rays give information about the elemental composition.

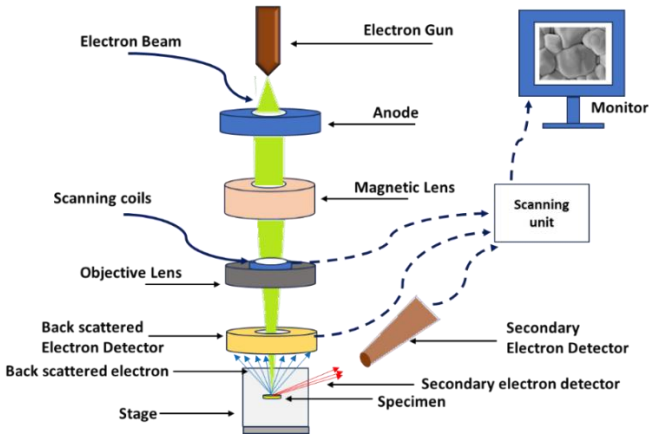

Figure 2.22: *Block diagram of the FE-SEM*

FE-SEM needs a vacuum environment to avoid the disturbance of the electron beam, SE, and BSE by the gas molecules. The electron gun of SEM consists of a field emission cathode that can provide spatial resolution and less sample charging effect. FESEM yields a less electrostatically distorted, clearer image with high magnification. Figure 2.22 shows the block diagram of the different parts of the FE SEM instrument.

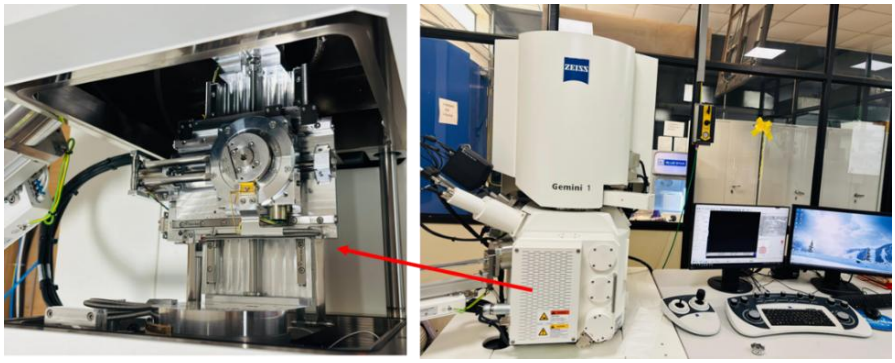

Figure 2 .23: *FE-SEM Instrument*

System specifications:

Make: Zeiss

Model: Gemini SEM 360 [Figure 2.23]

Magnification: 8 – 2,000,000

Probe current: 3 pA - 20 nA

Resolution: 0.7 nm @ 15 kV

Maximum field of view: 5 mm at 5 kV and WD = 8.5 mm.

2.2.8 High Resolution Transmission Electron Microscope (HR-TEM)

Transmission electron microscopy (TEM) is an analytical technique used to visualise the nanometer dimensions in matter. The electrons that are transmitted through the sample are detected to form an image. High resolution, shorter wavelength of electrons, increases the microscope resolution when accelerated through a strong magnetic field.

Since electrons can have a significantly shorter wavelength (about 100,000 times smaller) than that of visible light when accelerated through a strong electromagnetic field, this increases the microscope resolution by several orders of magnitude. Ultimately, by using a TEM, we can see the columns of atoms present in crystalline samples and the molecular machinery inside cells. It allows visualisation and analysis of specimens in the realms of microspace (1 micrometre = 1μm = 10^{-6} m) to nanospace (1 nanometre = 1 nm = 10^{-9} m).

TEM creates a bright field image of a sample by a beam of highly energetic electrons. While transmitting through the sample, electrons will be scattered or diffracted at the potentials of the atom, thereby changing the phase of the electron wave. The transmitted electrons are collected onto a phosphorescent screen or through a camera. The regions where electrons do

not pass through show a darker image, and the unscattered electron region shows a brighter image. There is a range of grey in between these two regions, depending on the interaction of electrons and scattering within the sample. This image can provide direct and highly resolved information about the sample under investigation. TEM provides information on the size, shape, and structure of nanomaterials. It can examine defects, grain structures, and layer thicknesses in microelectronic devices, aiding in quality control and new material development.

Instrumentation

The main components of the Source of electrons, electron gun, Electron beam, Electromagnetic lenses, Vacuum chamber, two condenser lenses, Objective and Intermediate lens, Sample holder and stage, (Imaging Device) Phosphor or fluorescent screen, Computer [Figure 2.24].

There are two common ways to produce electrons: thermionic emission and cold field emission. With thermionic emission, a tiny tip, often made from tungsten, a LaB_6 crystal, or a special ZrO/W Schottky emitter, is heated up by running an electric current through it. The heat gives the electrons enough energy to escape from the surface. At the same time, a high voltage between this electron source (the cathode) and a nearby plate (the anode) creates an electric field that helps steer and speed up the electrons. On the other hand, cold field emission doesn't need any heating. Instead, it uses an extremely sharp tungsten tip at room temperature. When a strong electric field is applied, electrons can actually "tunnel" out of the metal, escaping without any extra heat. These sources have a very high yield of electrons and a very low chromatic aberration of the electrons, allowing imaging at atomic resolutions [105].

Electromagnetic lenses consist of a huge bundle of windings of insulated copper wire, a soft iron cast, and a pole piece. A magnetic field is induced by the current in the winding and reaches its main strength at the pole piece of the lens. The accelerated electrons entering the magnetic field are deflected by Lorentz forces.

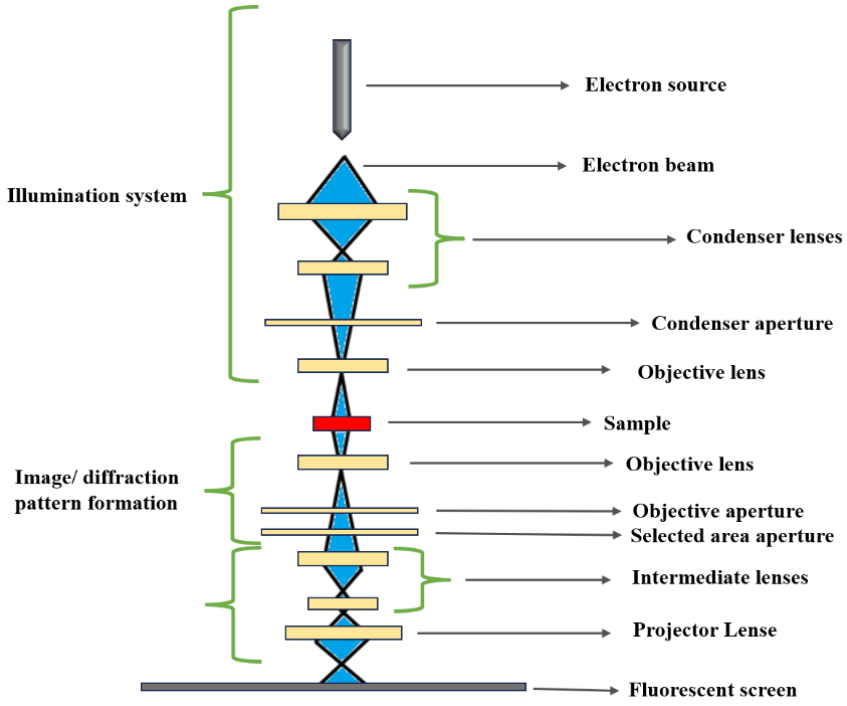

Figure 2.24: *Block diagram of the TEM instrument.*

The condenser lens system controls the beam diameter. The first condenser lens, which is strong, shrinks the image of the electron source down to about one hundredth of its original size. This creates a tiny, focused spot called the "crossover," which is much clearer and more precise than the larger tip of the filament. Then, the second condenser lens, which is a bit weaker, takes that small image and projects it onto the sample, making it roughly twice as big. Overall, this means the source is reduced in size by about fifty times. This lens also helps control how much the light spreads out on the screen. There is also a condenser aperture located just below or between these lenses, and its job is to narrow and shape the electron beam, as well

as adjust how bright it is. Objective lenses focus the electron beam through the specimen, and the intermediate lens helps to magnify the image or diffraction pattern.

The electron column does not offer a lot of space for the sample. The sample should be thin so that the electrons can penetrate the specimen to produce the image. Thin sections of the sample are mounted on copper grids, which are available in a wide variety of materials and mesh sizes. The grids with the sections on top are attached in a holder and introduced into the goniometer of the TEM through a vacuum lock. The goniometer is the mechanical setup that enables highly precise and stable control of the specimen holder during imaging.

When using a Transmission Electron Microscope (TEM) to look at a sample, there are two main ways to do it: Image mode and Diffraction mode. In Image mode, the microscope uses lenses and apertures to control the electron beam that hits the sample. The electrons that pass through are then focused and magnified to create an image on the screen, showing details like the size of grains or any defects in the material's structure. Diffraction mode works a bit differently; it produces a pattern on a fluorescent screen based on how the electrons scatter after hitting the sample. This pattern is like X-ray diffraction and is called a Selected Area Electron Diffraction (SAED) pattern. If the sample is a single crystal, there will be sharp spots in the pattern, but if it is polycrystalline, the pattern looks more like rings. The crystalline structure can be analysed by this SAED pattern [105].

In electron microscopy, there are two main ways to create images by using the objective aperture as a kind of filter: bright field and dark field microscopy. In bright field mode, the image is formed by electrons that travel straight through the sample without bouncing off, while the diffracted electrons are blocked by a diaphragm. On the other hand, dark field imaging works by using those diffracted electrons to create the picture instead

Figure 2.25: *JEOL JEM F200 TEM Instrument* [106]

System specifications:

Make: Jeol [Figure 2.25]

Model: JEM F200

Operating voltage: 200kV

Resolution: ≤0.11 nm (with Cold FEG)

2.2.9 Electron Paramagnetic Resonance spectroscopy

Electron Paramagnetic Resonance (EPR) refers to the phenomenon where paramagnetic substances absorb microwave radiation resonantly when subjected to an external magnetic field. This magnetic field causes a quantised orientation of electron spins, which corresponds to a splitting of their energy levels. Specifically, in the presence of a sufficiently strong magnetic field, the energy states associated with the electron spin

projections m_s=+1/2 and m_s=-1/2 become distinct, enabling resonance absorption of microwave photons as in Figure 2.26 [107].

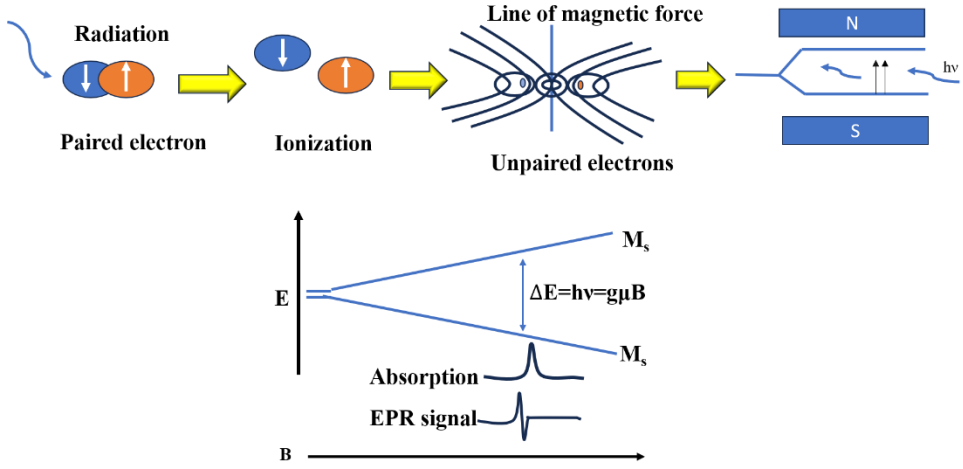

Figure 2.26: *Principle of EPR spectroscopy for the detection of unpaired electrons and energy levels in a magnetic field*

Resonance occurs when the energy of the applied microwave radiation precisely matches the energy gap between these split levels [Figure 2.26]. The intensity of this absorption is directly proportional to the concentration of unpaired electrons, or free radicals, within the sample. The energy separation of the relation can express ΔE:

$$\Delta E = h\nu = g_e \mu_B B_0$$

where h is Planck's constant, ν is the microwave frequency, g_e is the electron g-factor (a dimensionless parameter reflecting the ratio between the magnetic dipole moment and angular momentum of the electron), μ_B is the Bohr magneton, and B_0 represents the strength of the applied magnetic field.

The g-factor value is derived by comparing the microwave frequency to the magnetic field at which resonance occurs, typically calculated as $g = h\nu/\mu_B B_0$. In EPR spectroscopy, the recorded spectra are conventionally presented as the first derivative of the microwave absorption signal concerning the magnetic field [108].

The interaction between the unpaired electron's magnetic moment and the magnetic moments of nearby nuclei leads to the splitting of the EPR spectra called hyperfine splitting. Figure 2.27 shows the block diagram of the EPR spectrometer.

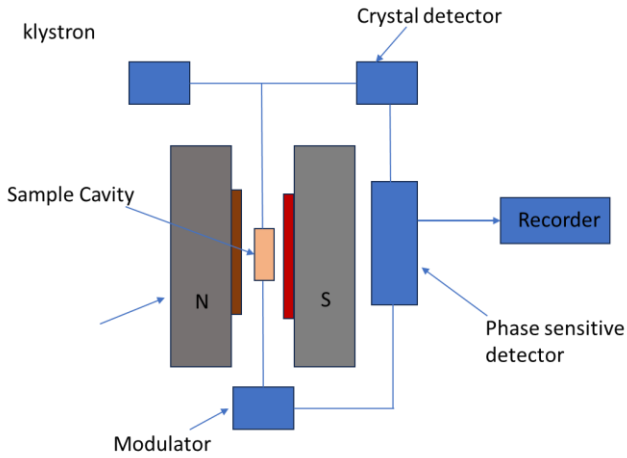

Figure 2.27: *Block diagram of EPR spectrometer*

This interaction causes a splitting of the EPR signal into multiple lines, providing valuable information about the molecule's structure and the environment of the unpaired electron. By analysing the resonance lines and hyperfine splitting in EPR, the possible oxidation states, O_v, and the electron interactions can be interpreted [109].

Figure 2.28: *EPR spectrometer*

System specifications:

Make: BRUKER BIOSPIN, Germany [Figure 2.28]

Model: EMXmicro A200-9.5/12/S/W

Source: Microwave X Band

Temperature Range: Room Temperature and down to 100 K

2.3 Experimental techniques

2.3.1 Ferroelectric measurements

A P-E loop for a device is a plot of the polarisation (P) developed against the field applied to that device (E) at a given frequency. The most often quoted method of hysteresis loop measurement is based on Sawyer and Tower.

Polarisation may be defined as P=Q/A, where Q is the charge developed on the plates and A is the area of the plates (m^2).

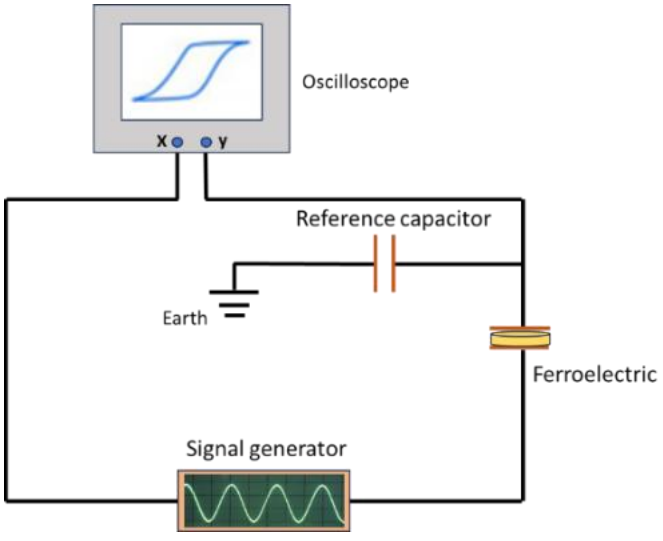

Figure 2.29: *Block diagram of Sawyer tower circuit for ferroelectric hysteresis measurement.*

The voltage is cycled with a signal generator. The voltage across the reference capacitor is measured. The charge on the capacitor must be the same as the charge on the ferroelectric capacitor, as they are in series. This means the charge on the ferroelectric can be found by:

$$Q = C \times V$$

Think of C as the capacitance of a reference capacitor, and V as the voltage across it. To understand how a material polarises in an oscillating electric field, we can plot the voltage applied to the material on the oscilloscope's x-axis and the surface charge on the y-axis [Figure 2.29]. This works because the reference capacitor has a much higher capacitance than the ferroelectric material, so most of the voltage drops across the ferroelectric. To measure the polarisation, we cycle the voltage across the ferroelectric, which in turn cycles its polarisation. We can't measure the exact polarisation instantly, but by looking at how it changes as we cycle the voltage, we can figure out its absolute values. [110].

Figure 2 .30: *Experimental setup for P-E loop measurement*

System specifications:

Make: Radiant Technologies

Model: Precision Material Analyser Workstation based on Virtual Ground System [Figure 2.30].

Sample holder: Home-made sample holder with Cu needle, immersed in silicon oil.

2.3.1.1 Positive Up Negative Down measurement (PUND)

The "Positive Up, Negative Down" (PUND) measurement method is a technique used in ferroelectric materials to measure polarisation switching current. It involves applying a series of electrical pulses to the sample, specifically a positive pulse followed by a negative pulse, to induce polarisation switching and measure the resulting current. This method helps in separating the switching current from other contributions like leakage current, allowing for a more accurate measurement of polarisation. The PUND measurement setup will be the same as described for the P-E loop measurement.

The PUND test is used to check ferroelectric materials by sending five pulses one after the other with the same voltage strength, just with different directions. Each pulse lasts the same amount of time, and there is a fixed pause between them. The first pulse goes in the negative direction; it is not measured but used to set the starting polarisation of the sample. Then, two pulses come in the positive direction: the first one flips the polarisation, and the second one does not, so we can see the difference between switched and unchanged polarisation. During each pulse, measurements are taken twice, once while the voltage is applied and once after the voltage goes back to zero, after waiting for the same amount of time as the pulse length. Finally, two more pulses go in the negative direction: one switches the sample back, and the last one keeps it in that switched state. During the first voltage pulse (P), all active mechanisms will bring their contribution to the measured current, including leakage currents, dielectric displacement current, and ferroelectric displacement current. During the second voltage pulse of the same polarity (U), since all dipoles have been switched, leakage currents, dielectric displacement current will

contribute to this pulse. Hence, the subtraction of polarisation in U from polarisation in P gives the value of actual polarisation.

Figure 2.31: *PUND measurement setup*

System specifications:

Make: Radiant technology

Model: Precision Premier II, FE loop tracer [Figure 2.31]

2.3.2 Magnetic measurements

A vibrating sample magnetometer, sometimes called a Foner magnetometer, is a tool scientists use to measure how magnetic a material is. It works based on Faraday's Law, which basically says that when a magnetic field changes near a wire, it creates an electric voltage in that wire.

The sample to be tested will be placed inside a steady magnetic field. If the sample is magnetic, this field will cause its tiny magnetic regions, called domains, to line up, making the sample magnetised. The stronger the magnetic field, the more these domains align. As the sample vibrates, the magnetic field around it changes, and this change is picked up by coils nearby. These coils detect the changing magnetic field and turn it into an electrical signal. That signal gets boosted by amplifiers and sent to a computer, where special software figures out how magnetic the sample is and how much the steady magnetic field influenced it.

Instrumentation

This technique works by gently shaking the sample near a special coil that picks up tiny signals. When the sample moves, it creates a very small voltage in the coil, which the system detects, timed exactly with the vibration. These vibrations are about 1 to 3 millimetres at roughly 40 times per second, the setup is sensitive enough to notice incredibly small changes in magnetisation, smaller than a millionth of a magnetic unit. The VSM (Vibrating Sample Magnetometer) option that comes with the PPMS system includes a motor to make the sample vibrate, a coil to detect the signals, electronics to control everything and read the data, and software called MultiVu for easy automation and control.

The sample sits on the end of a rod that moves back and forth in a smooth, wave-like motion. This oscillation is carefully centered right in the middle of a coil called a gradiometer pickup coil. The position and how far the rod moves are controlled by the VSM motor module, which uses an optical sensor to keep everything precise. As the sample vibrates, the coil picks up a voltage signal, which is then amplified and processed in the VSM detection module. This module uses the position information from the motor to sync up perfectly with the signal it is detecting. The motor module sends signals from the optical sensor, which the detection module uses to separate the signals into two parts for better accuracy. These signals are averaged and sent to the computer software for analysis.

To create the magnetic field needed to magnetise the sample, there is an actively cooled electromagnet that keeps the field steady. The sensor coils, sometimes called pickup coils, detect the tiny electric current generated by the vibrating sample. This current is then boosted by an amplifier. The vibration exciter is attached to the rod holding the sample, making it vibrate at about 85 times per second. The rod itself can also rotate the sample to position it just right. A control unit keeps the vibration steady at 85 Hz. Finally, the magnetic field strength is measured using a

magnetometer, and the data is recorded and managed through software on a computer interface.

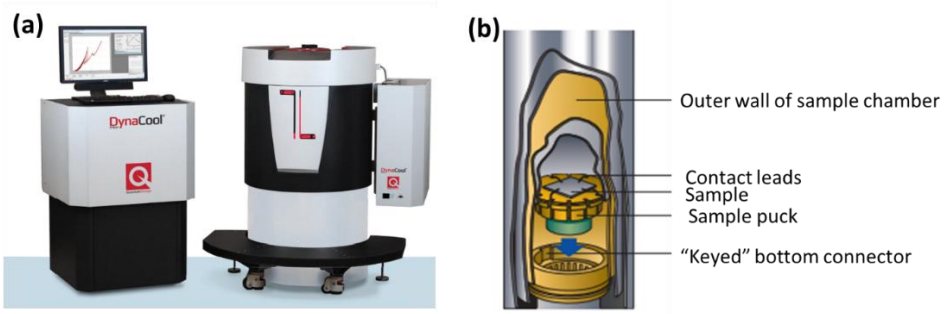

Figure 2.32: *(a) Dynacool 9T PPMS setup (b) sample holder* [111]

System specifications

Make: Quantum Design, Physical Property Measurement System (PPMS) using a vibrating sample magnetometer (VSM), installed at the State University of New York, Buffalo State University, USA.

Model: Dyna cool 9T [Figure 2.32]

Operating temperature:1.8K to 400K

Stability: +/-0.1% for T < 20 K (typical) +/-0.02% for T > 20 K (typical)

Power requirements: System Cabinet: 200-230 V, 50/60 Hz, 30 A, single phase

2.3.3 Dielectric measurements

Dielectric materials are generally insulators or poor conductors with low dielectric loss. There is a wide variety of these materials. Under the effect of an external electric field, the dielectric materials are polarised. In other words, with the application of the electric field, the positive and negative centers are separated, and electric dipoles are formed. The dipole moment per unit volume is known as polarisation. This property originates from the structural non-centrosymmetry. Dielectric permittivity is the

ability of a material to store electrical potential energy under the influence of an electric field. It is dependent on the applied frequency and temperature.

In the present study, dielectric properties were measured on circular disk-like pellets. Silver paste electrodes were prepared on both sides of well-sintered pellets. The electrodes were cured at ~ 550 ºC for 10 minutes. This enables better adhesion of the electrodes to the pellets and ensures proper contact.

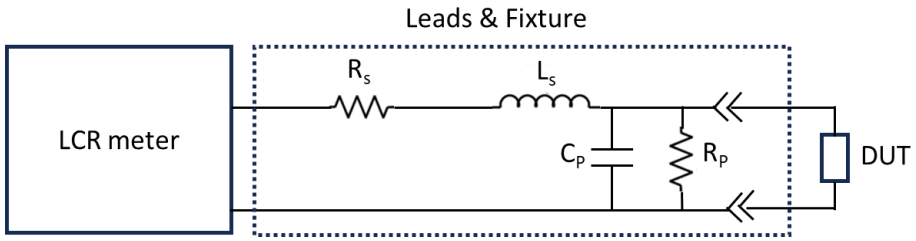

Figure 2.33: *Block diagram of LCR meter setup*

Newton's 4th Ltd. PSM 1735 phase-sensitive LCR-meter was used to measure the dielectric response with signal strength ~ 1 Vrms. The basic accuracy of this device is 0.1 % and the temperature variation in the furnace used for high-temperature dielectric measurement is ± 3 ºC.

The LCR meter is modelled as a two-lead measuring device [Figure 2.30]. The leads are modelled as having a resistance R_s and an inductance L_s. As the leads are likely wires insulated with dielectric insulating material, these leads also form a lossy capacitor that is modelled by the capacitance C_p and resistance R_p. The Kelvin fixture is used to model the dotted section in Figure 2.30. A Sample of silver pasted on both sides will be connected through silver wire in the Device Under Test (DUT) portion. The LCR meter will measure the reading for a frequency sweep.

Dielectric measurement was carried out in parallel plate capacitance mode. Dielectric constant or relative permittivity, ε_r, is a complex quantity, containing real (ε') and imaginary (ε'') parts: $\varepsilon_r = \varepsilon' + \varepsilon''$. Dielectric constant,

the real part of ε_r (ε'), quantifies the stored energy, and the imaginary part (ε'') gives the dielectric loss factor, which is the electric energy loss due to the movement of atoms/molecules in a continuously changing applied field. The dielectric loss tangent is represented by the formula. This component also gives rise to a phase difference between the field function and the resulting polarisation. Both components are frequency-dependent. The capacitance of pellets was estimated as: where 'C' is capacitance, 'A' cross-sectional area of the pellet, 'd' the separation between the pellets, and '$\varepsilon_o \sim 8.854 * 10^{-12}$ F/m is the permittivity of the free space.

For measuring the temperature-dependent dielectric properties, the DUT portion in the figure contains a temperature bath in which the sample is placed with a proper sample holder. The sample holder region is covered with glassy cotton, which increases the temperature in steps. The dielectric parameters are measured at regular intervals of temperature. The temperature bath can have a range of temperatures from 50 °C to 450 °C.

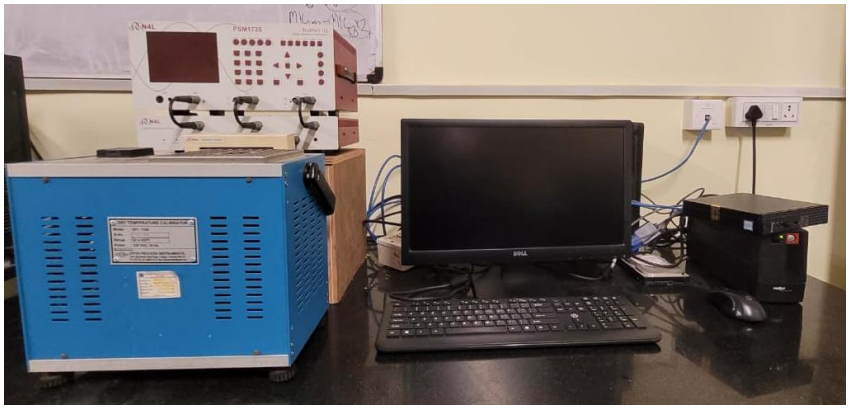

Figure 2 .34: *Dielectric measurement setup*

System specifications:

Make: N4L Impedance Analyser Interface [Figure 2.34]

Model: PSMCOM1735

Frequency Range: 1Hz to 1MHz

2.3.4 Magnetodielectric Measurements

Magneto dielectric measurements have been done by measuring the dielectric permittivity by the application of a dc magnetic field. The magnetic field is applied using a Helmholtz coil. The sample is placed in between the Helmoltz coil perpendicular to the magnetic field direction [Figure 2.35]. The electrodes on both sides of the pellet are connected to Newton's 4th Ltd. PSM 1735 phase-sensitive LCR meter through silver wires. One magnetic field is applied in a Helmoltz coil and stabilised by keeping it for some time, then the permittivity measurement is done at that field. After the measurement, the magnetic field increased, and the corresponding permittivity was measured. The measurement has been done in the range from 0.01 T - 0.1T.

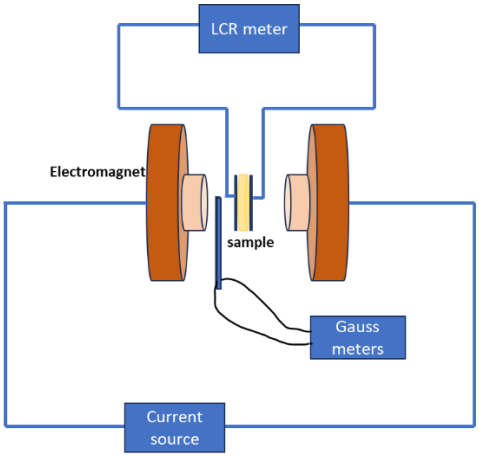

Figure 2.35: *Block diagram of magnetodielectric setup*

Dielectric permittivity at zero magnetic field has been measured initially, then the magnetic field is increased slowly by increasing the current in the electromagnet. After the specific magnetic field attained a time of 2 minutes kept before taking the measurement to make the field stable. The variation of capacitance with magnetic field, Magnetocapacitance (MC), is calculated with the formula;

$$\mathbf{MC} = \frac{\epsilon'(\mathbf{B}) - \epsilon'(\mathbf{0})}{\epsilon'(\mathbf{0})}$$

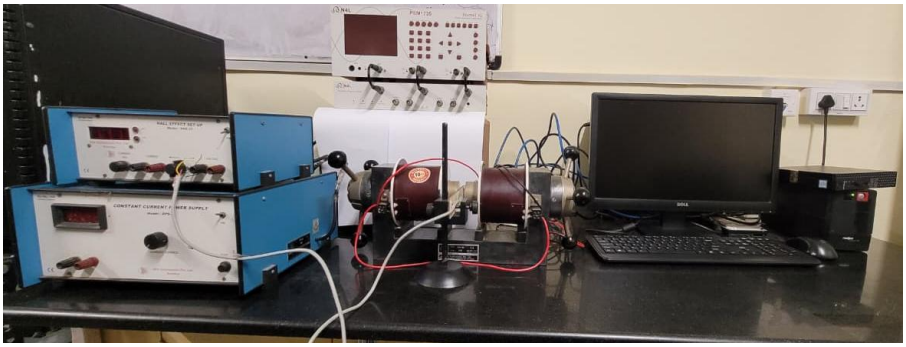

Figure 2.36: *Magneto dielectric measurement setup*

System specifications:

Same LCR meter specification as given in the dielectric measurement section.

Make: SES instruments [Figure 2.36]

Magnetic field range: 0 to 1T

2.3.5 Magnetoelectric Measurements

Theoretically, magnetoelectric coupling interaction is obtained by Landau's theory, where the free energy of a homogeneous magnetoelectric system at constant temperature is approximated by ME order parameters, Magnetisation (M) and Polarisation (P) [9].

The expansion of free energy is given by:

$$F(E,H) = F_0 - P_i^s E_i - M_i^s H_i - \tfrac{1}{2}\varepsilon_0\varepsilon_{ij}E_iE_j - \tfrac{1}{2}\mu_0\mu_{ij}H_iH_j - \alpha_{ij}H_jE_i - 1/2\beta_{ijk}E_iH_jH_k - \tfrac{1}{2}\gamma_{ijk}H_iE_jH_k$$

where F_0 is the ground state free energy, subscripts (i, j, k) refer to the three components of a variable in spatial coordinates, components of spontaneous polarisation and magnetisation are represented as P_i^s and $M_i^{s,}$ respectively. E_i and H_j are the components of the electric field E and magnetic field H, while ε_0 and μ_0 are the dielectric and magnetic susceptibilities of vacuum, ε_{ij} and μ_{ij} are the second-order tensor of dielectric and magnetic

susceptibilities, respectively. β_{ijk} and γ_{ijk} are third-order tensor coefficients. α_{ij} is the component of the tensor, which is designated as the linear ME coefficient. The components of total electric polarisation can be obtained by differentiation of the free energy equation w.r.t. electric field in the form

$$P_i\,(E, H) = -\frac{\partial F}{\partial E} = P_i^s + \varepsilon_0\varepsilon_{ij}E_j + \alpha_{ij}H_j + 1/2\beta_{ijk}H_jH_k + 1/2\gamma_{ijk}H_jE_k$$

$$M_i\,(E, H) = -\frac{\partial F}{\partial H} = M_i^s + \mu_0\mu_{ij}H_j + \alpha_{ij}E_j + 1/2\beta_{ijk}E_jE_k + 1/2\gamma_{ijk}E_jH_k$$

Magnetic field-induced total polarisation in the absence of applied electric field (E = 0) is given by:

$$P_i\,(H) = \alpha_{ij}H_j + 1/2\beta_{ijk}H_jH_k$$

This equation gives the induced polarisation due to the direct ME effect. Hence, experimentally, the change of polarisation with applied magnetic field can be measured to obtain the ME coupling coefficients and can quantitatively analyse the strength of ME coupling in the material. Hence, the polarisation with the applied magnetic field can provide the magnetoelectric coupling coefficient.

Instrumentation

The instrumentation part of the multiferroic tester includes the Helmholtz coil for providing the ac magnetic field, an electromagnet for the dc magnetic field, the current amplifier, the Gaussmeter with a Hall Effect sensor, a current sensor in-line with the Helmholtz coil, a shield box to avoid external noise, precision tester [Figure 2.37].

The shield box is aluminium and non-magnetic. The coax cables go into the box to connect to a small PC board holding the sample. The BNC (Bayonet Neill–Concelman) connectors have their shields connected to the box metal, so connecting coax cables to the connectors will automatically connect the outside box to the ground shields of the tester connectors. A non-magnetic battery holder conveniently holds the sample. The shield box

is attached to a wooden base to place the sample at the correct height to be at the central axis of the Helmholtz coil [112].

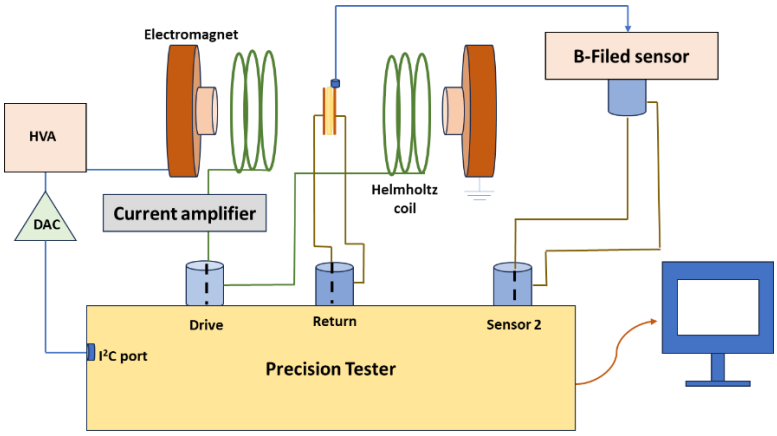

Figure 2.37: *Block diagram of Magnetoelectric measurement setup*

Since one side of the sample is grounded during the MR Task execution, two BNCs are not needed on the shield box. The second BNC allows us to execute Polarisation Hysteresis vs. Magnetic Field and Small Signal Capacitance vs. Voltage tests on the sample, since both tests require the DRIVE and RETURN to be connected to the sample.

First dry run of the MR Task with no sample inserted into the sample holder needs to be done. The sample holder will be shortened. This test will evaluate the amount of current generated in the RETURN cable that enters the active area of the Helmholtz coil. If the current is significant, this data will be used to correct the actual measurement for this parasitic contribution. The second will be the MR Task measurement of the sample itself. The measurements can be done with a fixed AC magnetic field for various DC biases. A zero-field measurement of the MR Task to determine the noise coupling into the sample from external sources. Finally, capacitance measurement v/s magnetic field [112].

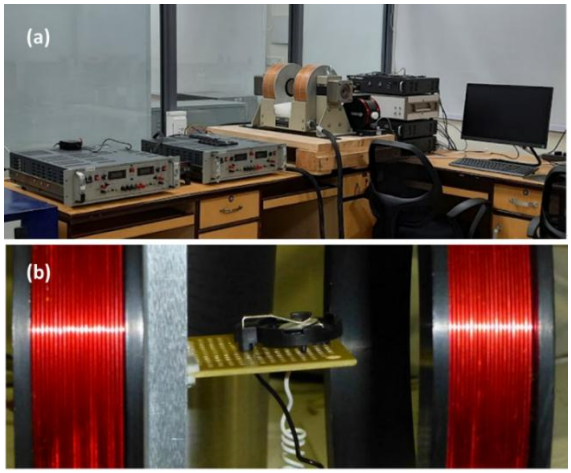

Figure 2.38: *(a) Magnetoelectric measurement setup, (b) Sample holder*

System specifications:

Make: Radiant Technologies

Model: Precision multiferroic II ferroelectric tester [Figure 2.38]

Magnetic field range: 0 to 1500 Oe

AC magnetic field frequency range: 1Hz to 10Hz

2.4 Theoretical Density of States and Electron Localisation Function Calculations

Theoretical Density of States (DOS) analysis involves calculating the number of electron states available at each energy level within a material. This is done by considering the spatial dimensions and the dispersion relation of the material, which describes how electron energy changes with momentum. Through DOS calculations, the carrier concentration, Transport properties, and electronic properties, etc.

Electron Localization Function (ELF) calculations help to understand the empirical concept of electron localization. The ELF was introduced by Becke and Edgecombe [86] and thereafter applied to a great

range of systems from atoms, molecules, and solids. It is related to the covariance of the electron pair distribution. Just as with the electron localization function, the local covariance does not seem to be, in and of itself, a useful quantity for elucidating shell structure. The ELF provides the variation of charge density around the atoms and gives an idea about the type of bonds, charge localization, and variations in the local charge density near chemical modifications.

The total energy and electronic DOS calculations are based on density functional theory as implemented in the Vienna Ab-initio Software Package (VASP) [113], [114]. Projected augmented wave (PAW) pseudopotentials in generalized gradient approximation (GGA) have been used to perform the calculations, which are applied to the Perdew-Burke-Ernerhof (PBE) exchange-correlation function [115]. The calculations were performed on a unit cell (5 atoms) of tetragonal BTO, and a plane-wave energy cutoff of 800 eV was used. The energy convergence criterion was set to 10^{-6} eV, and an 8x8x8 K-point mesh was used. We have also calculated the electronic DOS and total energy for La and Fe-doped BTO using a (2x2x4) supercell (80 atoms). To simulate the Fe-doped system, we have replaced one Ti by Fe out of 16 available Ti sites ($BaTi_{0.9375}Fe_{0.0625}O_3$) and additionally replaced Ba by La to simulate $Ba_{0.9375}La_{0.0625}Ti_{0.9375}Fe_{0.0625}O_3$. The total energy and electronic DOS in all the systems were calculated in fully relaxed structures. We have used denser 8×8×4 k-grid points in the Brillouin zone for the electron localization function and electronic DOS.

First-principles calculations were performed using the Vienna Ab initio Simulation Package (VASP) within the framework of density functional theory (DFT) [116], [117]. The projector augmented-wave (PAW) method was employed with the Perdew–Burke–Ernzerhof (PBE) exchange-correlation functional [118]. The pseudopotentials used include for Ca ($3s^2\ 3p^6\ 4s^2$), Ba ($5s^2\ 5p^6\ 5d^{0.01}6s^{1.99}$), Mn ($3d^6\ 4s^1$), Ti ($3d^3\ 4s^1$), and O($2s^2\ 2p^4$), ensuring accurate treatment of core and valence electrons. A high plane-wave energy cutoff of 700 eV was used to ensure convergence

of total energy and electronic properties. The electronic self-consistency loop was converged with a stringent criterion $1.0E^{-7}$ eV, while ionic relaxation was controlled using $1.0E^{-3}$ eV/Å, indicating force-based convergence. Structural optimization was carried out using the conjugate gradient algorithm with full relaxation of atomic positions and cell parameters. Spin-polarized calculations were performed for all the cases. Brillouin zone sampling was done using a Monkhorst-Pack grid of 4×4×4 [119]. Post-relaxation, the band structure was calculated along high-symmetry paths to analyze electronic dispersion. The density of states (DOS) was computed using a dense k-grid of 10x10x10 to examine the distribution of electronic states across energy levels, and the electronic localization function (ELF) was evaluated to visualize bonding characteristics

CHAPTER 3

Room temperature multiferroicity and magnetoelectric coupling in

Ca/Mn-modified $BaTiO_3$

$Ba_{(1-x)}Ca_{(x)}Ti_{(1-y)}Mn_{(y)}O_3$ (x=y=0, 0.03, 0.06, 0.09)

This chapter details the structural modification of Ca/Mn-modified $BaTiO_3$ with XRD, Raman, and TEM analysis. Oxidation states have been studied with XPS. Ferroelectric studies and magnetic studies indicate multiferroicity. Magnetoelectric coupling studies explore a room-temperature magnetoelectric coupling coefficient for the optimised doping percentage, $Ba_{(0.97)}Ca_{(0.03)}Ti_{(0.97)}Mn_{(0.03)}O_3$.

3.1 Introduction

Magnetoelectric (ME) and multiferroic materials are required for developing next-generation novel multifunctional devices. Hence, these are high-priority ferroic research materials. Experimentally discovered about sixty years ago, the ME effect has thus far been important in the fields of microelectronics and sensors [120]. To date, intensive research has been conducted in the field of magnetic and electric ordering and their coupling. Various materials and coupling mechanisms have been explored for magnetoelectric coupling (MEC) [121], [122], [123]. $BaTiO_3$ (BTO) is a well-known ferroelectric (FE) material. BTO can be chemically modified to impart ferromagnetism (FM) to the crystal structure and develop ME properties in the material [124]. Transition metal (TM) doping at the Ti site is an effective method to achieve BTO-based magnetoelectric materials [125], [126] $BaTiO_3$-$BiFeO_3$ [127], $BaTiO_3$–$LaFeO_3$ [128], $BaTiO_3$–$La_{0.7}Ba_{0.3}MnO_3$ [129], Mn- and Co modified $BaTiO_3$–$BiFeO_3$ [130], [131], etc., are some examples of the solid solutions of BTO with magnetic (ABO_3) perovskite materials that demonstrate MEC. Apart from doping magnetic ions and solid solutions, composites with ferromagnetic materials, core-shell structures with magnetic materials [132], and heterojunction thin films of BTO with ferromagnetic films [133], [134] facilitate MEC. Excellent MEC was revealed in most of these materials, leading to the exploration of physical properties and utilisation for industrial applications.

Compared with a composite or heterostructure material, a single-phase compound can show intrinsic ME behaviour. Unfortunately, no single-phase ME material that meets room temperature (RT) applications has been discovered yet [122]. The most severe weaknesses of single-phase ME materials are linked not only to their operational temperatures (mostly well below RT) but also to the magnitudes of the order parameters. The introduction of a new ferroic order in a single-phase ferroic material leads to the decrease of the existing ferroic order in the material. Their extremely

low switchable polarisation (usually in the order of magnitude of nC/cm^2) can be useful for fast switching applications. The development of single-phase multiferroic materials is constrained by factors such as different symmetry breaking and different physical requirements of magnetism and FE owing to ferroic ordering at extremely low temperatures. However, composite materials show enhanced coupling through the contribution of different strong ferroic orders from different phases in the material. In ME composites, MEC takes place as FE and FM domains are coupled through their secondary (ferro/magneto) elastic domains because of electrostriction and magnetostriction. Significantly advanced MEC that induces coupling through interface-induced strain has been observed for thin film heterostructures [135].

BTO can be made multiferroic by doping with a TM ion at the Ti-site to induce magnetism in BTO and simultaneously substitution Ba with elements such as Ca, Bi, Sr, and La at the A-site to retain the FE of the structure [125], [136]. This will show magnetic orderings while retaining the FE of BTO, leading to multiferroicity and MEC. Khedri *et al.* [137] investigated Ca-doped BTO and revealed the retention of the tetragonal *P4mm* structure even up to 20% Ca doping. Hasan *et al.* [138] supported the experimental work with a theoretical study on the structural and physical properties of Ca-doped BTO. On the other hand, Tong *et al.* [139] experimentally revealed a FM exchange mechanism in Mn-doped BTO that involved a spin-polarised hole trapped at Ti vacancies, leading to effective exchange interactions between hole carriers and magnetic Mn ions. A second-order Jahn-Teller effect through Mn^{3+} ions at Ti sites, favouring FE, supports FM due to its magnetic exchange interaction. Hence, FM can be induced by retaining FE by both A-site Ca-doping and B-site Mn^{3+}-doping in BTO. Multiferroicity can occur due to the FM exchange interactions of the d electrons in TM ions. Hence, this work attempted to incorporate Ca and Mn at the A and B-sites, respectively, to investigate a structure correlated multiferroicity and probable MEC in modified BTO.

Nayak *et al.* [140] studied the emergence of hexagonal *P6₃/mmc* with Cr doping at the Ti site of BTO. Dang *et al.* [141] investigated structural polymorphism from *P4mm* to *P6₃/mmc* with Mn doping in the Ti site of BTO. Pal *et al.* [142] reported the role of the hexagonal *P6₃/mmc* space group in inducing FM in Fe-doped and Mn-doped tetragonal BTO. They also studied tuning this hexagonal phase to zero in Fe- and Mn-doped BTO by simultaneous doping at the A-site with various elements. Hence, doping at the A-site and B-site with suitable elements in BTO can effectively tune the simultaneous presence of tetragonal *P4mm* and hexagonal *P6₃/mmc* structures. This dual-phase presence can not only tune the multiferroicity but also couple these phases to impart MEC.

This work aims to induce Multiferroicity by incorporating ferromagnetic ordering in ferroelectric $BaTiO_3$.The previous reports and our experience indicate that the incorporation of transition metal (TM) at the Ti site completely removes the ferroelectricity of BTO and cannot be a good multiferroic choice. The triggering of the paraelectric hexagonal phase of BTO is the main reason for the reduction in ferroelectricity. However, suitable substitution of the Ba site of BTO can be helpful to stabilise the tetragonal structure responsible for the ferroelectricity, even for very high doping percentages. Hence, the loss of tetragonality by B-site TM doping can be reduced by suitable A-site modification, and possibly retain the ferroelectricity. Simultaneous substitution of the A-site by Bi/La/Sr/Ca, and B-site by Fe/Mn/Ni/Cr can generate magnetism, retaining the ferroelectricity, and thereby lead to multiferroicity [143]. Out of these combinations, Bi+ Fe [144], Bi+ Mn [143], and La+ Fe [128] have already been explored.

The choice of Ca+ Mn in this study is because Ca and Ba have the same oxidation state, thereby reducing the possibility of conductive losses due to multiple valence states at the A-site, and Mn has the possibility of being in the Mn^{4+} state as compared to the other possibilities like Fe/Ni/Cr. However, Mn generally tends to be in a mixed valence state of Mn^{3+}/Mn^{4+},

thereby introducing the possibility of a double exchange ferromagnetic interaction. Mn also introduces a pseudo-Jahn-Teller distortion (PJTD) due to the Mn^{3+} ion, which can favour ferroelectricity through distortion of the BO_6 octahedra, along with inducing ferromagnetic ordering in the modified lattice. Moreover, Ca substitution at the A-site has also been reported to stabilise the tetragonal structure even up to 20% substitution [138]. Hence, the combination of Ca+ Mn is expected to retain ferroelectricity and simultaneously generate magnetism, thereby resulting in multiferroicity and a possible magnetoelectric coupling in the modified material.

Structure correlation of the FE and FM properties is investigated in detail, and coupling of the electric and magnetic orders is measured and quantified as the ME voltage generated in the material. A complete structural correlation linked with the physical properties of Ca and Mn-modified BTO has been reported in this work. $Ba_{(1-x)}Ca_{(x)}Ti_{(1-y)}Mn_{(y)}O_3$ (x=y=0, 0.03, 0.06, 0.09) samples named as BTO (x=0), BCTMO1(x=0.03), BCTMO2(x=0.06), BCTMO3(x=0.09) have been studied.

3.2 Results and analysis

3.2.1 X-Ray diffraction analysis

XRD data of the BTO sample confirms a tetragonal *P4mm* structure. All BCTMO samples have a mixed phase tetragonal *P4mm* and hexagonal *$P6_3/mmc$* structure of $BaTiO_3$ [Figure 3.1a]. There is a minor peak observed at ~29° in all samples. This may be an indication of the presence of secondary barium orthotitanate (Ba_2TiO_4) in the samples [145]. These peaks arise from the nonstoichiometry of Ba: Ti due to the lower amount of titanium present in the precursor solution. A very minute peak of $BaCO_3$ at ~24.6° is observed [146] in the BTO sample, almost at the level of the background, which is not visible for the doped samples.

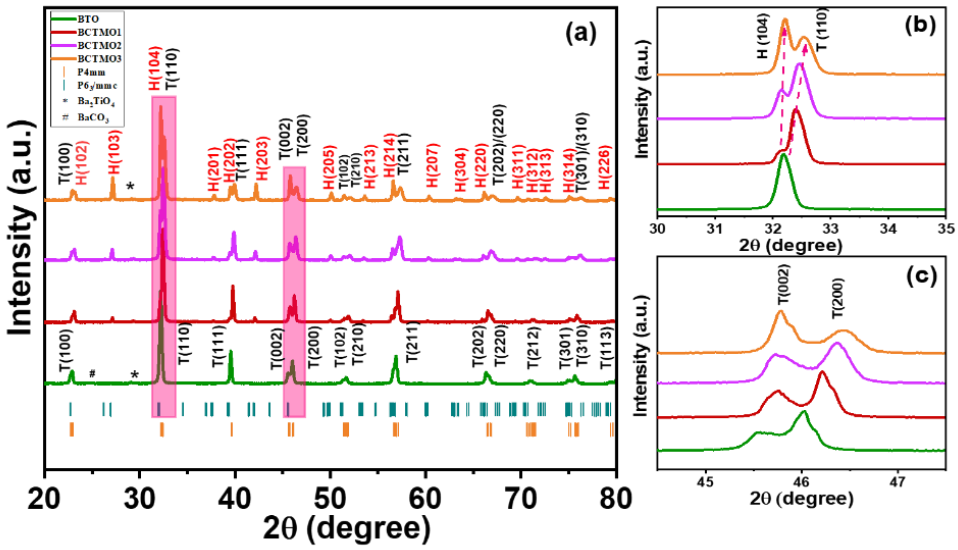

Figure 3.1 *(a) XRD data of all samples with the CIF file of the P4mm and P63/mmc space groups. (b) Zoomed-in image of the variation in the intensity of the hexagonal peak H(104) and tetragonal peak T(110) with composition. (c) Zoomed-in image of the splitting of tetragonal T(002) and T(200) peaks.*

Figure 3.1(b) shows a zoomed image of the highest intensity tetragonal peak, T(110). The existence of an additional peak corresponding to the highest intensity hexagonal peak H(104) as a shoulder peak to the T(110) peak starts to appear from BCTMO1 onwards, and its intensity gradually increases as the doping increases [Figure 3.1(b)]. This indicates the increase in the hexagonal phase percentage in the samples. The tetragonality of the samples is indicated by the splitting of T(002) and T(200) peaks as shown in Figure 3.1(c). The splitting of these peaks for all samples indicates that the tetragonal phase still coexists with the hexagonal phase of $BaTiO_3$.

The structure was analysed by Rietveld refinement using Fullprof software for all samples [Figure 3.1_1]. The XRD data have been refined with the tetragonal *P4mm* standard CIF file-COD151325229 and hexagonal *$P6_3/mmc$* standard CIF file-MP4830 obtained from the Crystallography Open Database [Figure 3.2(c)].

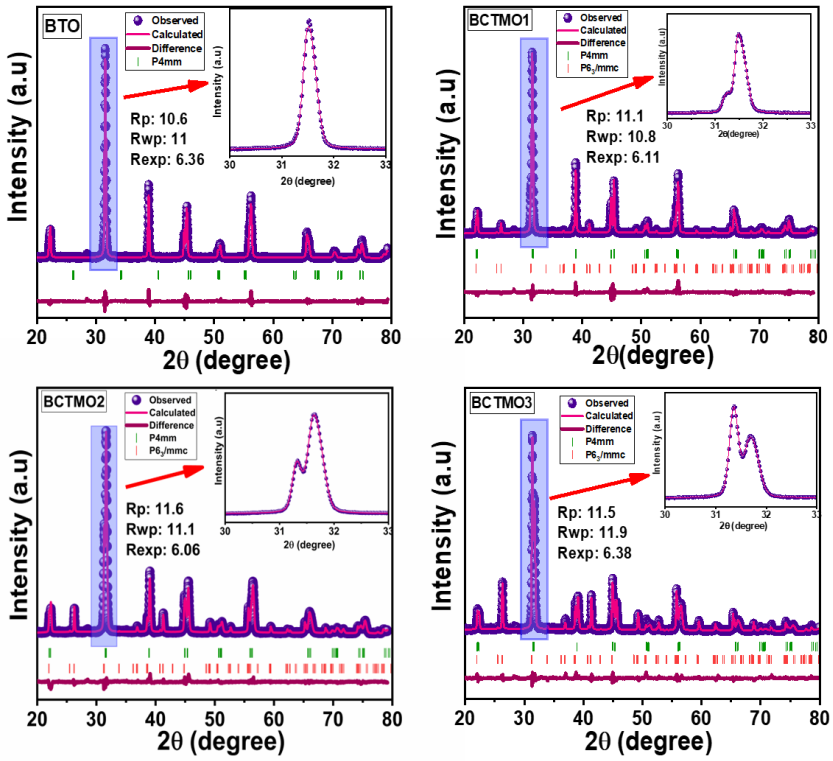

Figure 3.1_1: *Refinement plots of all the samples, the inset shows the zoomed image of the fitting of H(104) and T(110) peaks*

A six-coefficient polynomial is used for the background subtraction. All the XRD peaks are fitted with pseudo-Voigt-type peak profiles. Initially, a tetragonal CIF file was used to refine the XRD data. After attaining the least residue, the hexagonal phase was added as the secondary phase, and the refinement was simultaneously done with both phases. Sample parameters, instrumental parameters, lattice parameters, atomic positions, and U, V, W peak profile parameters were refined until the fit converged to acceptable fitting parameters of R_p and R_{wp} values of <12 and $\chi^2 < 3.5$ for all the samples. At this point, the theoretical fit matched well with the experimental data.

The phase percentage, lattice parameters, bond lengths, and bond angles are extracted from the refined CIF files of the samples. VESTA crystallographic software was used for analysing the crystal structure. The tetragonal phase reduces from 100% (BTO) to 88% (BCTMO1), 71%

(BCTMO2), and 45% (BCTMO3). Hence, the hexagonal phase increases from 0% (BTO) to 12% (BCTMO1), 29% (BCTMO2), and 55% (BCTMO3) [Figure 3.2(b)]. Therefore, a major tetragonal *P4mm* phase was observed in BTO, BCTMO1, and BCTMO2, while a major hexagonal *P63/mmc* phase was observed in BCTMO3. The presence of d electrons in transition metals (TM) is reported to trigger the hexagonal phase ($P6_3/mmc$) when doped at the B-site of BTO [143].

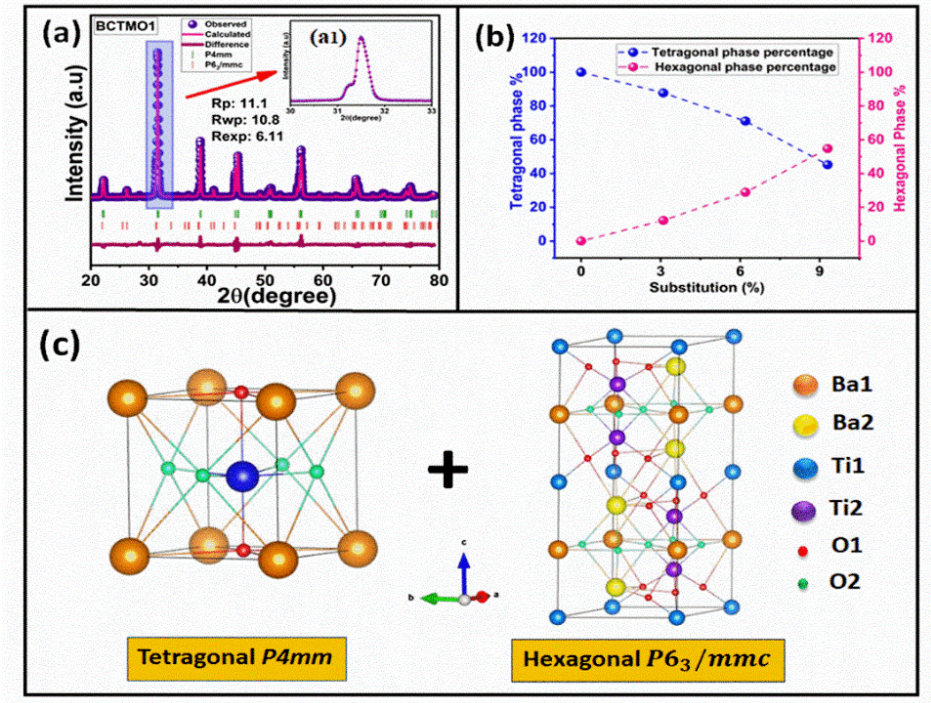

Figure 3.2 *(a) Rietveld refinement of the BCTMO1 sample with the P4mm and P63/mmc space groups. Inset: (a1) Zoomed-in image of the T(110) and H(104) peaks of the refinement using both phases. (b) Variation in the phase percentage of the tetragonal and hexagonal phases with composition. (c) Schematic of the crystal structure of tetragonal P4mm and hexagonal $P6_3/mmc$ using VESTA software.*

Note that the hexagonal phase induced in the doped samples represents the hexagonal phase of $BaTiO_3$ itself and not that of $BaMnO_3$ [147] and $CaMnO_3$ [148]. This can be confirmed from the 2θ values and the intensity profile of the two structures. Hence, the incorporation of Mn in $BaTiO_3$ is solely responsible for the drastic conversion of the structure from a *P4mm* to $P6_3/mmc$ space group and the incorporation of Ca in $BaTiO_3$.

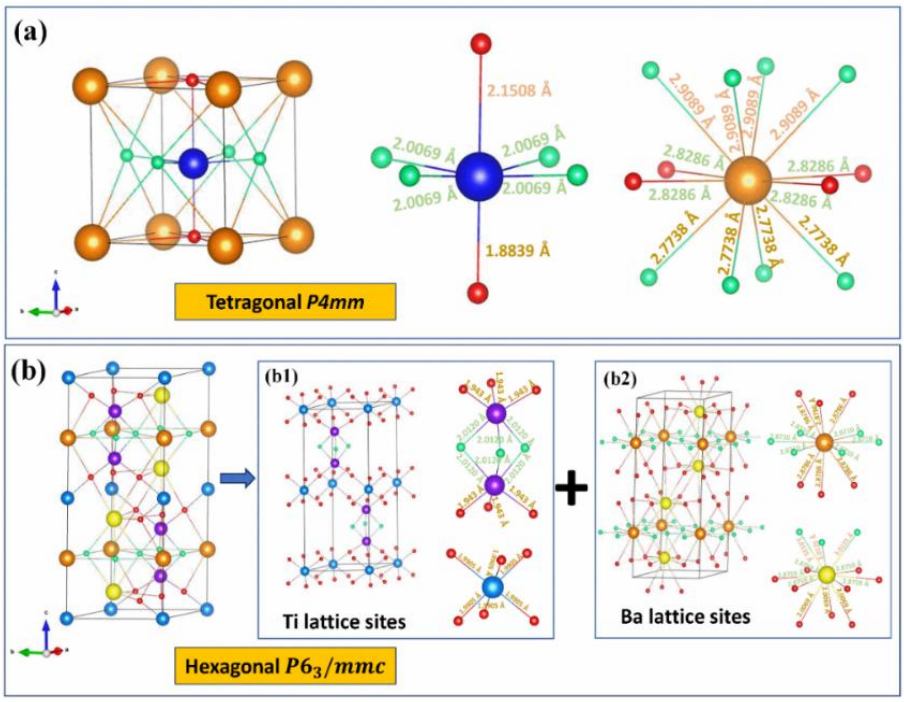

Figure 3.3 *(a) Schematic of the P4mm structure and different types of Ti–O and Ba–O bonds. (b)Schematic of the P63/mmc structure. (b1) Schematic of the Ti and O lattice in the P63/mmc structure with two types of Ti–O bonds. (b2) Schematic of the Ba and O lattice in the P63/mmc structure with two types of Ba–O bonds.*

In an ideal $BaTiO_3$, Ti will be in the Ti^{4+} oxidation state. However, it is challenging to achieve an exclusive Ti^{4+} valence state in an experimental sample. Hence, a mixture of Ti^{3+} and Ti^{4+} is obtained in most reported samples, thereby inducing defects like O_vs. Similarly, Mn doping can lead to the possibility of Mn^{3+} and Mn^{4+} states with d^4 and d^3 electrons and can trigger structural distortion leading to transformation to a *$P6_3/mmc$* phase, inciting an instability of the tetragonal polar phase. This can be due to the changes in the TM 3d–O2p hybridisation or pseudo Jahn-Teller distortion induced by Mn^{3+}, which is absent in Ti^{4+} ions.

The non-centrosymmetry of the Ti atom (blue atom in Figure 3.3a) in the TiO_6 octahedra of the P4mm structure is responsible for the FE in BTO. However, the unit cell in the *$P6_3/mmc$* structure consists of eight corner shared Ti atoms and four edge shared Ti atoms of the first kind, Ti1 (blue atoms in Figure 3.3b), and four internal Ti atoms of the second type, Ti2 (violet-coloured atoms in Figure 3.3b). Both Ti1 and Ti2atoms form two

types of TiO_6 octahedra in terms of symmetry. Ti1 forms TiO_6 octahedra, which are symmetric with six equal Ti–O bond lengths of ~1.9905 Å. On the other hand, two neighbouring octahedra of Ti2 atoms share a face of three O atoms, represented as O2 (pale green atoms in Figure 3.3b). Such a conjunct pair of face-shared octahedra is generally called a dimer. These internal Ti2 atoms in the dimer form TiO_6 octahedra that are distorted. The arrangement of these distorted TiO_6 octahedra is a result of the trans formation from the *P4mm* to the *$P6_3/mmc$* structure.

The distance between the Ti2 ions inside the dimer is close to ~2.8 Å for the hexagonal $BaTiO_3$ [30]. The repulsion between the two Ti2 atoms results in a longer Ti–O bond near the O3 face of the dimer, resulting in six Ti–O bonds (~1.992 Å) and three shorter Ti–O bonds (~1.958 Å) that are part of each Ti2 atom away from the O3 face. Hence, the two TiO_6 octahedra in the dimer are distorted, with three shorter and three longer Ti–O bonds [Figure 3.3b1]. The relative displacement of Ti2 ions concerning the O-cage of the distorted TiO_6 octahedra in the hexagonal $BaTiO_3$ is on opposite sides, thereby negating the possibility of FE due to Ti ions [Figure 3.4a]. With the initial Mn incorporation, the average Ti–Ti separation changes to 2.78 Å in BCTMO1, 2.67 Å in BCTMO2, and 2.423 Å in BCTMO3 [Figure 3.3_1].

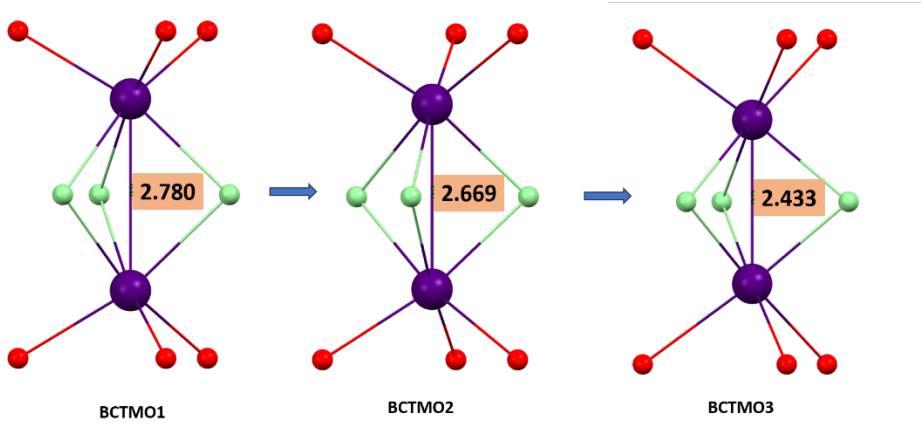

Figure 3.3_1*: Variation of Ti-Ti separation in octahedral dimer in hexagonal $BaTiO_3$ with Mn doping*

Hence, it appears that the Ti atoms are moving closer to each other. Note that a trend of reducing TiO_6 octahedral volume was observed with increasing doping concentration, although it is difficult to comment on the O position from the XRD results. Hence, there is a serious indication of a strong Ti–Ti interaction. The reason behind such an increase in the strength of this interaction needs to be explored and may be related to the modifications, like the Ti-site, namely, the nature of the valence state of the Ti atom or Mn atom.

Apart from the TiO_6 octahedra, the *$P6_3/mmc$* structure consists of a repeating pattern of three Ba–O planes [(Ba2–O1), (Ba1–O2), and (Ba2–O1)] as shown in Figure 3.3b2. Within this structure, consecutive Ba2 atoms are displaced from the O1 plane in the opposite direction along the c axis [Figure 3.4b]. Similarly, there is minimal separation of Ba1 from the O2 plane in the opposite direction along the b axis when considering the two consecutive Ba1–O2 planes of one repeating pattern with the Ba1–O2 plane of the consecutive repeating pattern [Figure 3.4b].

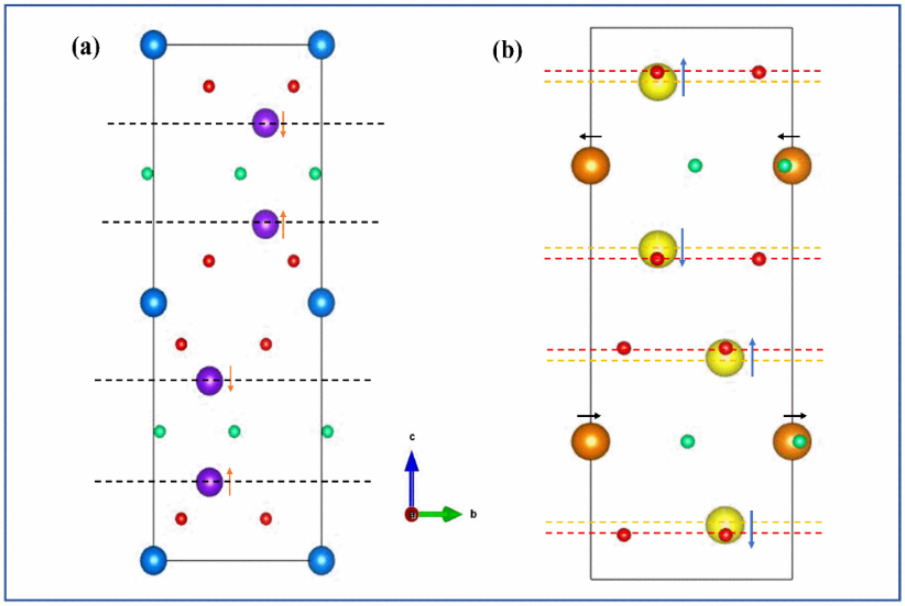

Figure 3.4*: (a) Displacement of Ti2 atoms in the opposite direction from the centrosymmetric position of the Ti_2O_9 dimers. (b) Displacement of consecutive Ba atoms in the opposite direction from the Ba–O plane along the c direction (represented by blue arrows) and the b direction (represented by black arrows).*

The displacement of Ba2 from the Ba2–O1 plane along the c direction is larger than that of the displacement of Ba1 from Ba1–O2 along the b direction. The displacement of two consecutive Ba1 and Ba2 atoms is displaced from the corresponding Ba–O plane in opposite directions and negates the possibility of FE. The separation of the Ba2 atom from Ba2–O1 decreases with substitution from 0.25 Å (BCTMO1) to 0.21 Å (BCTMO2) and 0.16 Å (BCTMO3). On the other hand, the separation of the Ba1 atom from the Ba1–O2 plane negligibly decreases with substitution from 0.18368 Å (BCTMO1) to 0.18323 Å (BCTMO2) and 0.18304 Å (BCTMO3), which is technically unreliable. However, there is a trend of reduction in the separation. Hence, one can visualise the effect as a probability without commenting strongly on such calculations.

Hence, it is observed that the introduction of Mn enables the TM ions in the dimer to come closer to each other, whereas the introduction of Ca enables the reduction of the separations of the Ba(Ca) and O planes. Mn doping promotes the phase transition from *P4mm* to *$P6_3/mmc$,* and with higher doping to $R\bar{3}c$ while up to 20% Ca doping retains the *P4mm* phase [137]. Hence, a possible phase transition towards *$P6_3/mmc$* with doping of Mn can be counteracted through a simultaneous doping of Ca that tends to retain the *P4mm* structure. This struggle between the two mechanisms may have generated a mixed phase of the doped samples.

The a and c lattice parameters of both phases reduce with substitution [Figure 3.5a]. Hence, the volume of the unit cell seems to be decreasing with an increase in doping concentration. This happens for both the *P63/mmc* and *P4mm* space group. As a result of this volume contraction, the c/a ratio of the *P4mm* phase also reduces continuously [Figure 3.5b]. The tetragonal lattice parameters a and c negligibly change from BTO to BCTMO1, then gradually decrease to BCTMO3. Similarly, the a and c lattice parameters of the hexagonal phase show a gradual decrease from BCTMO1 to BCTMO3. Changes in the lattice parameters can be explained

through the ionic radii of the dopants in the A-site and B-site. Ba^{2+} [1.75 Å (XII)] is replaced by smaller ionic radii Ca^{2+} [1.48 Å (XII)] at the A-site of BTO. However, Mn can have Mn^{3+} [0.785 Å (VI) high spin, 0.72 Å (VI) low spin] and Mn^{4+} [0.67 Å (VI) oxidation state] in the Ti^{4+} [0.745 Å (VI)] and Ti^{3+} [0.81 Å (VI)] sites [149]. The doping of lower ionic radii Mn^{4+} in the Ti^{4+} site reduces the lattice parameters. Meanwhile, Mn^{3+} doping will enhance the lattice parameters. Although there is a reduction in lattice parameters due to A-site modifications arising from the competition of Mn^{3+} and Mn^{4+} oxidation states in the Ti site, the lattice parameters are not changed drastically. There are only minor changes in the c/a ratio, indicating the retention of tetragonality even for the highest doped samples.

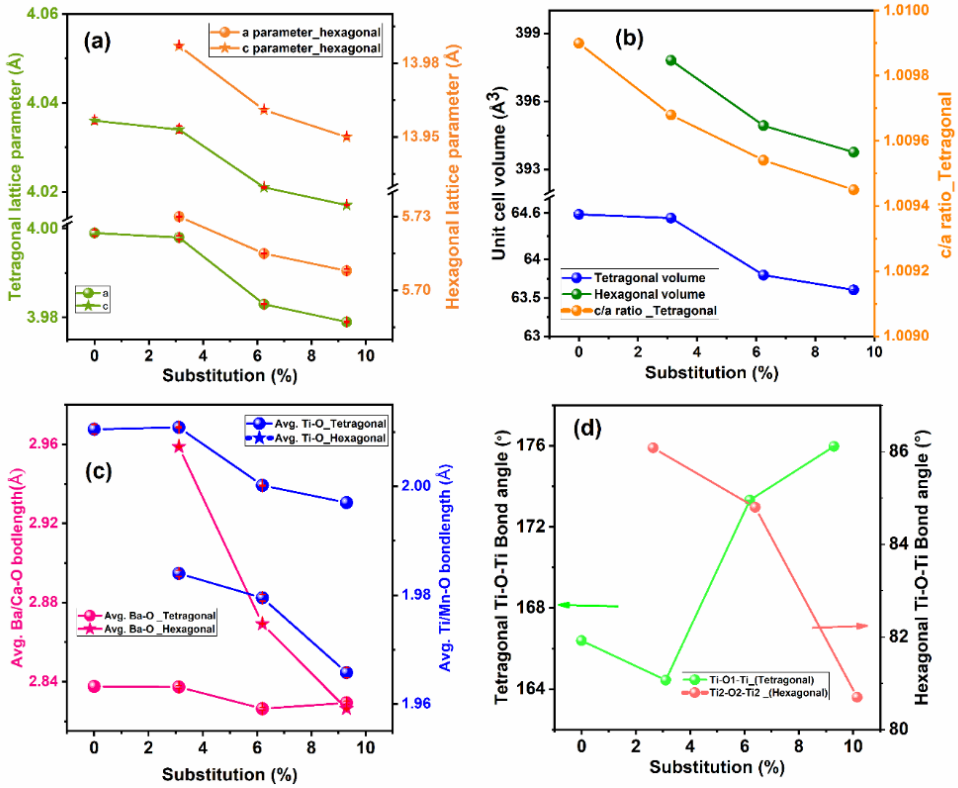

Figure 3.5*: (a) Variation in tetragonal and hexagonal lattice parameters with composition. (b) Variation in the average Ba/Ca–O and Ti/Mn–O bond lengths with composition. (c) Variation in the tetragonal and hexagonal volumes and the tetragonal c/a ratio with composition. (d) Variation in the tetragonal and hexagonal Ti–O–Ti bond angles with composition.*

The dopant ionic radii also influence the average Ti/Mn–O and Ba/Ca–O bond lengths. There is a gradual reduction in these average bond lengths [Figure 3.5c]. Variations in the 180° Ti O–Ti bond angle in the tetragonal lattice were analysed and plotted [Figure 3.5d]. There is a slight decrease in the bond angle from BTO to BCTMO1, and then it gradually increases for BCTMO2 and BCTMO3. The hexagonal phase variation in the 90° Ti2–O1–Ti2 bond angle shows a decreasing trend. The changes in the bond angle in both phases indicated variations in the overlapping atomic orbitals and led to changes in the magnetic exchange interactions and variation in the magnetic properties. The probable changes in the magnetic exchange with the structure will be discussed later.

3.2.2 Raman spectroscopy analysis

The Raman spectrum of all the samples reveal an E(TO) phonon mode at 40 cm^{-1}, A_1(TO) mode at 280 cm^{-1}, B_1/E(LO + TO) mode at 305 cm^{-1}, A_1(TO)/E(TO) mode at 520 cm^{-1}, and A_1(LO)/E(LO) mode at 720 cm^{-1} corresponding to a tetragonal *P4mm* structure [Figure 3.6(a)] [150]. As the doping percentage increases, all the modes corresponding to the tetragonal structure were broader. This is an indication of the presence of different types of vibration due to the dopant-induced variations of bonds. Some phonon modes corresponding to the hexagonal phase are present in the doped samples at ~100 cm^{-1} [A_{1g}], ~420 cm^{-1} [E_{2g}], and 635 cm^{-1} [A_{1g}] [151]. The coexistence of the characteristic peaks of both tetragonal and hexagonal phases in the doped samples confirms the dual-phase nature of the samples. Figure 3.6 b and c show the variation in intensity and broadening of the tetragonal B_1/E(LO + TO) mode at ~305 cm^{-1} and hexagonal A_{1g} mode at ~635cm^{-1}, respectively. The intensity of the ~305 cm^{-1} mode was extracted by subtracting the background. The relative intensity of this peak for each sample concerning the BTO sample (I_{sample}/I_{BTO}) was calculated and found to decrease with increasing doping

concentration, revealing the reduction of the tetragonal phase. On the other hand, the relative intensity of the hexagonal $A_{1}g$ mode at ~635 cm^{-1} (I_{sample}/I_{BCTMO3}) was calculated and found to increase with higher doping concentrations, revealing the enhancement of the hexagonal phase. This is by the correlated XRD studies [Figure 3.6(d)]. Due to the presence of a heavier Mn ion with respect to the Ti ion, a probable redshift is observed for the characteristic peaks of both the phases [Figure 3.6(e)].

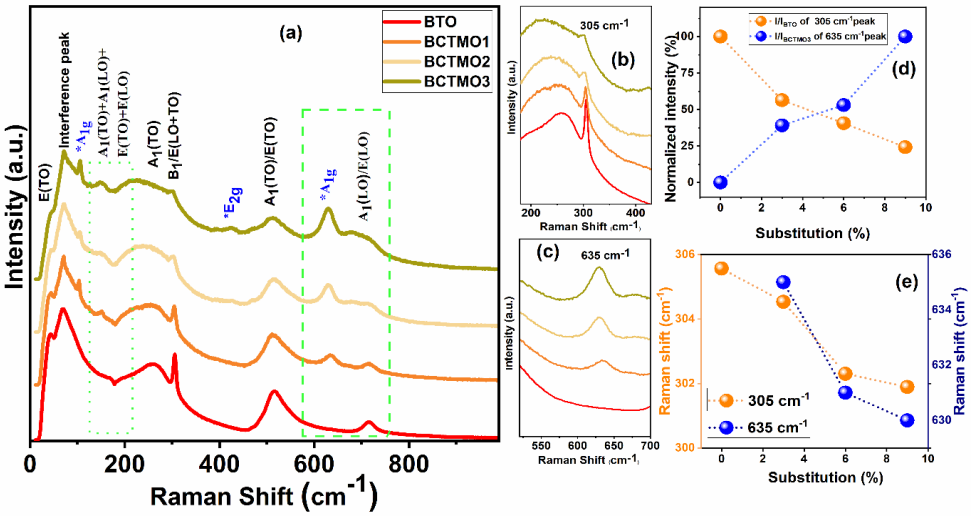

Figure 3.6*: (a) Raman spectra of all samples. (b) Zoomed image of the variation in the 305 cm^{-1} tetragonal mode. (c) Zoomed image of the variation in the 635 cm^{-1} hexagonal mode and 720 cm^{-1} tetragonal mode. (d) Variation in the intensity of the 305 cm^{-1} and 635 cm^{-1} modes with composition. (e) Variation in the Raman shift of the 305 cm^{-1} and 635 cm^{-1} modes with composition.*

3.2.3 XPS analysis

XPS analysis of each element was performed to understand the oxidation states of various elements present in the material. The oxidation state is important to understand, as the bonding of electrons with the neighbouring ions correlates to the structure and hence the physical properties. Due to spin-orbit interactions, Ba 3d, Ca 2p, Ti 2p, and Mn 2p peaks display doublet features with two separated peaks. The area fraction of each ion can be calculated with the general formula $[A^{n+}]/([A^{n+}]+[A^{m+}])$, where A is an ion with multiple oxidation states (n+ and m+), with $[A^{n+}]$

and [A^{m+}] being the area under the corresponding peaks in the XPS spectrum. This area fraction can be treated as the contribution of A^{n+} content over A^{m+}. The area fractions of Ti^{3+} over Ti^{4+} (f_{Ti3+}) and Mn^{3+} over Mn^{4+} (f_{Mn3+}) are calculated from the deconvoluted XPS spectra. The fractions f_{Ti3+} and f_{Mn3+} contain information about the loss of positive charge. It should be noted that Ba and Ca are predominantly in the +2-charge state without the possibility of any other state. Hence, the effective cationic valence state will be dictated by these fractions. To maintain the charge neutrality of the crystal structure, an easy solution is to have an oxygen deficiency. Therefore, f_{Ti3+} and f_{Mn3+} were analysed with increasing amounts of doping since the variation of the amount of these 3+ cations can indirectly provide the variation of O_V in the material.

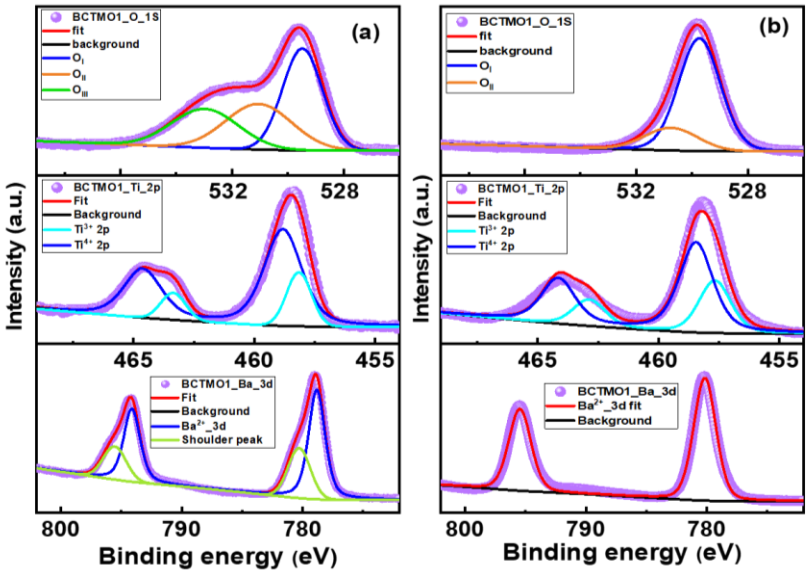

***Figure 3.7**: Deconvoluted XPS spectra of the BCTMO1 sample. (a) Ba 3d, Ti 2p, and O 1s data before etching. (b) Ba 3d, Ti 2p, and O 1s data after etching.*

To investigate the differences between the surface construction and the bulk structure, the samples were investigated before and after etching with Ar gas. The comparison of the data before and after etching revealed interesting removal of XPS peaks corresponding to the adsorbed species on the surface for the O 1s and Ba 3d XPS spectra. The deconvoluted XPS spectra before and after etching for BCTMO1 are shown in Figures 3.7 and

3.8. Figure 3.10_1 to 3.10_5 shows the deconvoluted spectra of all samples for Ba 3d, Ca 2p, Ti 2p, Mn 2p, and O 1s.

The Ba XPS spectra [Figure 3.10_1(a)] reveal a doublet corresponding to the Ba^{2+} state Ba $3d_{5/2}$ at 779.6 eV and Ba $3d_{3/2}$ at 794.9 eV in BTO with spin-orbit splitting energy of 15.3 eV. These peaks resemble the reported features of the Ba^{2+} state in the perovskite $BaTiO_3$ [152]. Shoulder peaks appear for both features corresponding to the different chemical state of the Ba atom on the surface. There is a decrease of binding energy (B.E.) ~1eV for Ba $3d_{5/2}$ for all doped samples concerning BTO, indicating the modification of the Ba environment with doping. The etched data shows a shift towards a higher B.E. of ~1eV for the doublet in comparison with that before the etching process. The shoulder peaks of Ba disappeared in the etched data [Figure 3.7b]. This corresponds to the surface adsorbed phase, which is removed after the etching process. Some reports claim that this is the adsorbed $BaCO_3$ on the surface of the sample [153], while another claim is surface phase related to a relaxation of the residual strain [154]. Wegmann *et al.* [155] stated that the observation of carbonate in the XPS spectra is difficult because it forms discrete particles rather than a continuous surface layer. Hence, the residual strain near the surface plays a major role in the origin of this shoulder peak, while $BaCO_3$ contamination does not.

The Ca 2p XPS spectra of the BCTMO sample [Figure 3.10_2(a)] shows a doublet corresponding to the Ca^{2+} state at 347.63 eV ($2p_{3/2}$) and 351.23 eV ($2p_{1/2}$) with a spin-orbit splitting energy of 3.6 eV. These peaks resemble the reported features of the Ca^{2+} state in the perovskite $CaTiO_3$ [156]. Note that no prominent shoulder peaks are revealed for both features, hinting at no probable different chemical state of the Ca atom on the surface. This indicates that Ca may not be prominently diffused to the surface of the particles or may not have participated in the process of adsorption. The positions of the Ca $3d_{5/2}$ and Ca $3d_{3/2}$ doublets have no major changes in the

binding energies of the Ca ions in the doped samples, maintaining the spin-orbit splitting energy of 3.6 eV, indicating a similarity in the Ca environment or bonding. There were no significant changes observed in the Ca 2p XPS spectra after the etching process [Figure 3.10_2(b)].

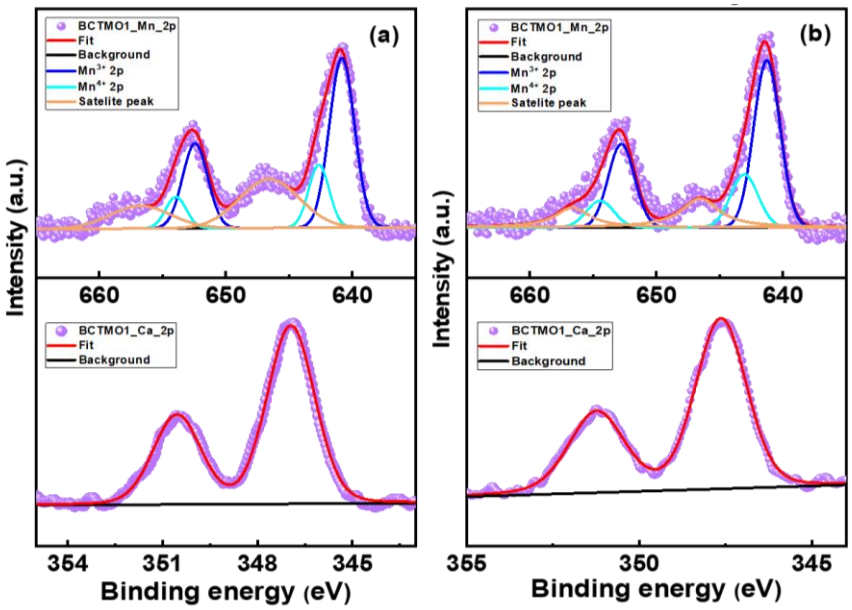

***Figure 3.8**: Deconvoluted XPS spectra of all the samples. (a) Ca 2p and Mn 2p data before etching. (b) Ca 2p and Mn 2p data after etching.*

The O 1s XPS spectra of BTO can be deconvoluted to three peaks [Figure 3.10_5(a)] corresponding to the binding energy (B.E.) of lattice oxygen (O_I) at ~529–530 eV, a second peak feature (O_{II}) at ~531–532 eV, and a third feature corresponding to adsorbed oxygen (O_{III}) at ~532.5–533.5 eV. These values are in accordance with the literature [157]. The contribution of O_I is from the O atoms bonded to Ba, Ca, Ti, and Mn ions in the samples. On the other hand, the origin of O_{II} is controversial and has been explained as a contribution from both chemisorbed oxygen species (e.g., hydroxyl groups) [158], [159] and oxygen vacancies O_V [160], [161], [162]. A third feature of O_{III} is a contribution from the surface adsorbed carbonates (CO_3^{2-}) and water molecules (H_2O) [158]. In natural conditions, there is an adsorption of water molecules that contributes to the O_{III} feature due to atmospheric exposure.

There are numerous reports relating the O_{II} feature (B.E. between 531–532 eV) to the presence of O_V. For example, Wang *et al.* reported that the generation of O_V with an increase in the O_{II} peak intensity in Fe_2O_3 with an increasing annealing time in an N_2 atmosphere; namely, a reduced atmosphere reveals the connection between O_{II} and O_V [162]. However, this was an ex-situ study, which could have involved contributions from external contaminants. A recent in situ XPS study revealed an unchanged spectrum before and after reduction [163], [164], providing strong support for the non-O_V origin of O_{II}. Also, the absence of an O 1s electron in the case of an O_V has been projected as a non-O_V origin of O_{II} [159], [165]. Hence, it is difficult to judge the actual origin of O_{II} from the literature.

However, it is hard to believe that a crystal is so perfect that no O_V will be present, and the presence of O_V will leave no mark on the XPS spectra. A loss of one O-atom should lead to a change in the electronic charge distribution of the neighbouring cations, which can be evident from a dislocation of the position of these cations [162]. Moreover, the coordination and valence state of the cations will likely differ due to the O_V [160]. This dislocation and modification will affect the local bonding of the nearest O atoms and lead to changes in the binding energy. Hence, one should see an O_V feature in the XPS spectra. However, it is questionable whether the O_{II} contribution is from O_V or chemisorbed species. The O 1s XPS data of the etched samples [Figure 3.10_5(b)] revealed a complete removal of the O_{III} feature with a reduction of the OII feature. Note that etching is a process where inert atoms are bombarded on the sample surface to tear off the surface atoms from the surface layers and expose the inner bulk layers, where chemisorption is not possible. A complete removal of the O_{III} feature is strong evidence of this occurrence. The reduction of the O_{II} feature also supports the view that O_{II} does have a component of chemisorption. However, the retention of the feature in a reduced form may be the contribution of other sources, such as O_V. Analysis of the etched O 1s XPS data reveals a continuous rise of O_{II} with doping [Figure 3.9b].

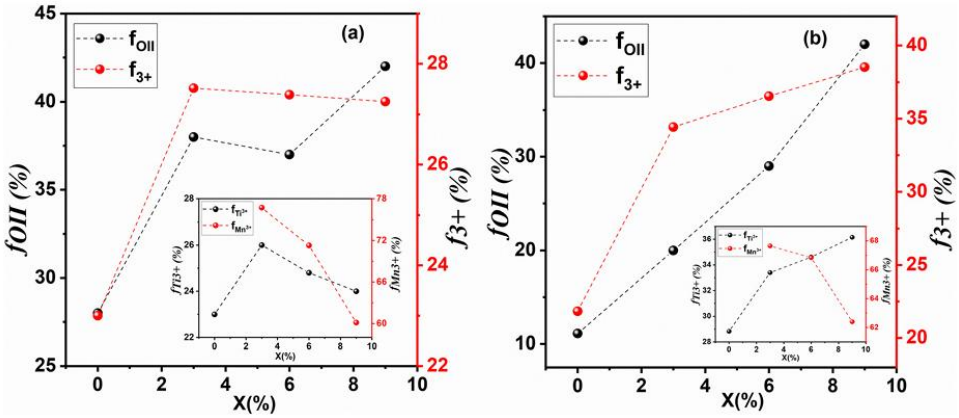

Figure 3.9: *Fractional variation in f_{OII}, f_{3+} (a) before etching and (b) after etching [inset shows the individual variation of the fractional area of f_{Ti3+}, f_{Mn3+}*

The Ti 2p XPS spectra in $BaTiO_3$ are a strong feature and reveal a doublet Ti 2p3/2 and Ti $2p_{1/2}$. In the BTO sample, this doublet is observed at ~459.16 eV (Ti $2p_{3/2}$) and ~464.86 eV (Ti $2p_{1/2}$) with a spin-orbit splitting energy of 1.7 eV [Figure 3.10_3(a)]. These peaks are consistent with the Ti^{4+} oxidation state [150]. Peaks corresponding to Ti^{3+} are obtained at ~458.61 eV (Ti $2p_{3/2}$) and ~463.91 eV (Ti $2p_{1/2}$) [166]. There is an increase of B.E. by ~0.5 eV for Ti $2p_{1/2}$ for all doped samples concerning BTO, indicating the modification of the Ti environment with doping. There was a slight increase in the area fraction of f_{Ti3+} from ~23% to 26% from BTO to BCTMO1. Thereafter, there was a reduction to 24.8% in BTCMO2 and 24% in BCTMO3 [Figure 3.9(a) inset]. There are minor differences in the area fractions of f_{Ti3+} between the BCTMO samples. Ti 2p etched XPS data shows a shift of ~1 eV lower B.E. after the etching process [Figure 3.10_3(b)]. There is a shift towards higher B.E. for Ba after etching. This corresponds to the structural influence of the etching process on the material [167]. After etching, f_{Ti3+} shows a gradual increase from ~29% to 36% from BTO to BCTMO3 [Figure 3.9(b) inset].

The Mn2p XPS spectra of the doped BCTMO samples [Figure 3.10_4(a)] revealed two doublets corresponding to Mn^{3+} at binding energies of 641.05 eV and 652.45 eV with spin–orbit splitting of 11.4 eV and

doublets for Mn^{4+} at 642.59 eV and 653.89 eV for BCTMO1 [168]. The area fraction of f_{Mn3+} and f_{Mn4+} reveals the presence of both Mn^{4+} and Mn^{3+} ions, with a dominance of Mn^{3+} over Mn^{4+}. The value of f_{Mn3+} decreased from BCTMO1 to BCTMO3 for both before and after the etching process [inset of Figure 1 .9(a) and (b)]. The simultaneous variation of Ti^{3+} and Mn^{3+} will contribute to the effective charge of 3+ cations. Hence, the fraction of 3+ valence state ions can be calculated from the equation $f_{3+} = (1-x)f_{Ti3+} +(x)f_{Mn3+}$, where x is the doping fraction. There was an increase of f_{3+} from 23% in BTO to 27.5% in BCTMO1; thereafter, it remained unaffected in BCTMO2 and BCTMO3 [Figure 3.9(a)] before the etching process. Meanwhile, there is a gradual increase of f_{3+} from 22% to 38% with doping after the etching process [Figure 3.9(b)]. Although the origin of the O_{II} peak in the O 1s spectra cannot be claimed as proof for the O_V, the increase in f_{3+} correspondingly increases the O_V in these samples.

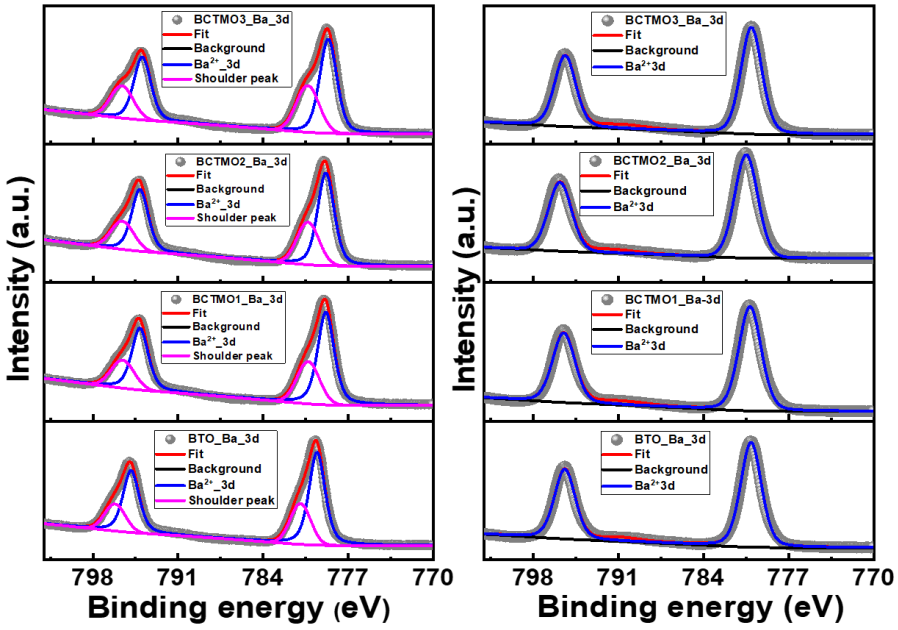

***Figure 3.10_1**: Deconvoluted XPS spectra of all the samples. (a) Ba 3d before etching. (b) Ba 3d after etching*

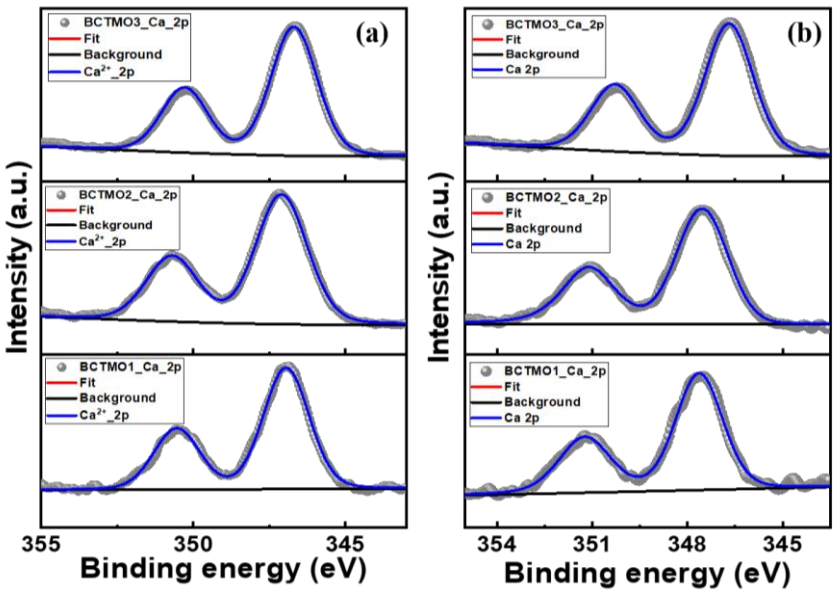

***Figure 3.10_2**: Deconvoluted XPS spectra of all the samples. (a) Ca 2p before etching. (b) Ca 2p after etching.*

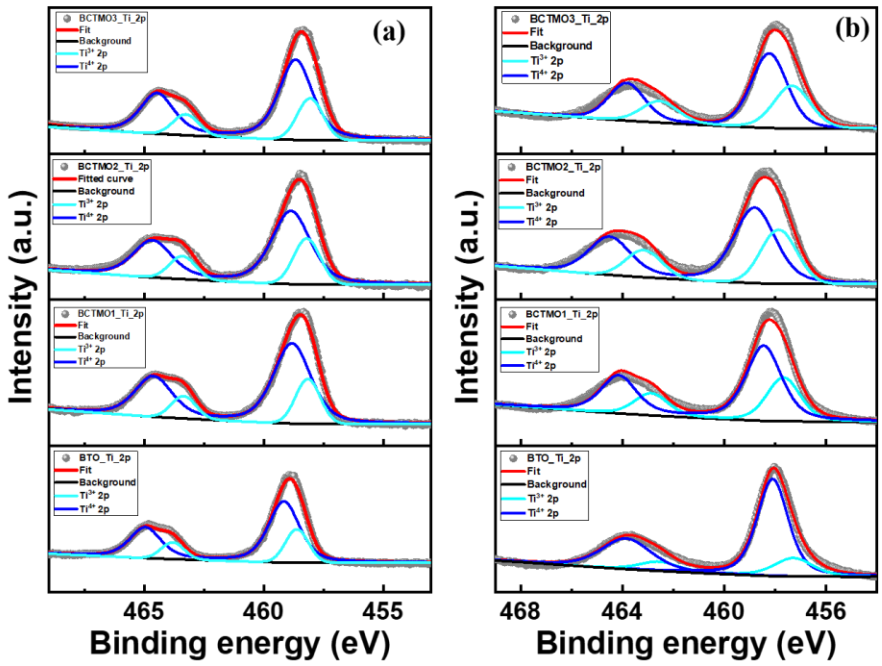

***Figure 3.10_3**: Deconvoluted XPS spectra of all the samples. (a) Ti 2p before etching. (b) Ti 2p after etching.*

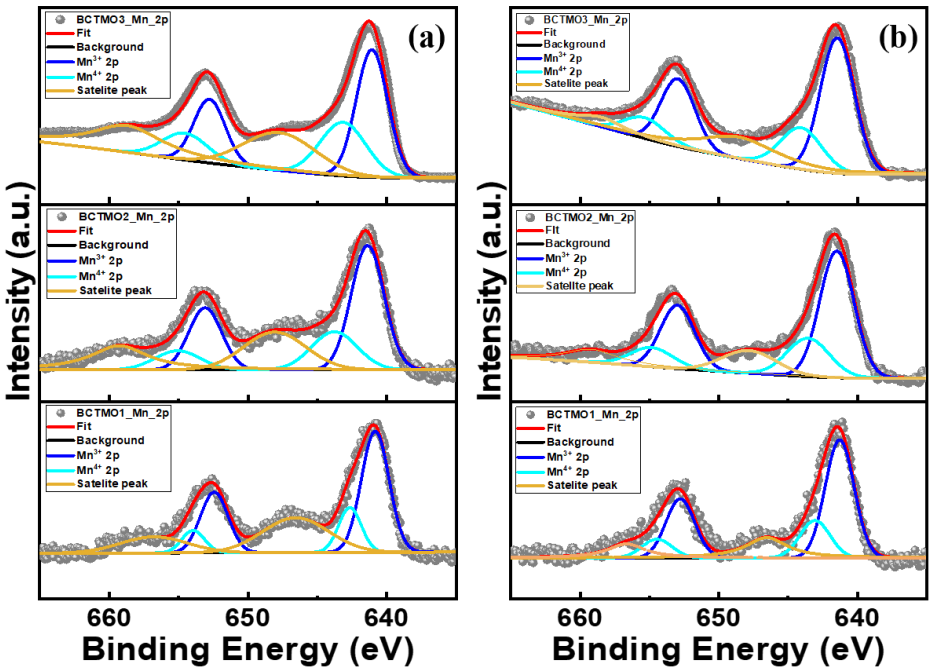

***Figure 3.10_4**: Deconvoluted XPS spectra of all the samples. (a) Mn 2p before etching. (b) Mn 2p after etching.*

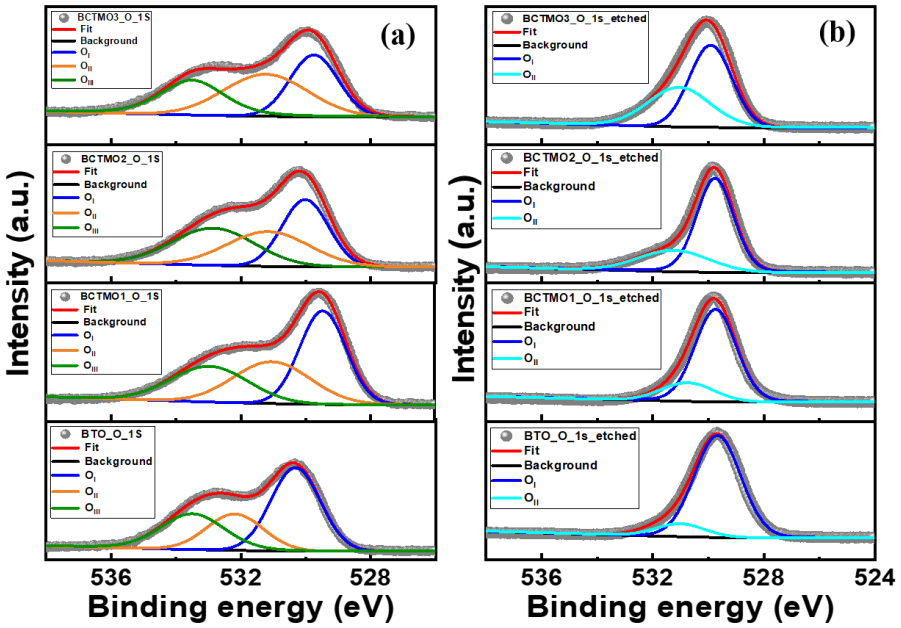

***Figure 3.10_5**: Deconvoluted XPS spectra of all the samples. (a) O 1s before etching. (b) O 1s after etching.*

3.2.4 Magnetic properties

Incorporating Mn ions introduces magnetic properties in the materials, which can be realised from RT M–H plots of the materials [Figure 3.11]. Magnetisation in emu per gram (emu per g) is plotted with applied magnetic field in Oersted (Oe). Pure BTO is diamagnetic, exhibiting a negative magnetic moment with an applied magnetic field. This diamagnetic nature also confirms that the Ti ions are in the Ti^{4+} state, having d^0 electrons with no possibility of a magnetic moment. The 's' type nature of the diamagnetic loop [Figure 3.11(a)] indicates the feeble FM ordering. Figure 3.11a1 shows the M–H loop after diamagnetic subtraction. The zoomed image of this FM hysteresis [Figure 3.11(a2)] shows remnant magnetization, M_r of ~0.35 $\times 10^{-3}$ emu per g, saturation magnetization, M_s ~4 $\times 10^{-3}$ emu per g and a coercive field, H_c of ~85 Oe. An 's' type M–H loop is observed with an unsaturated magnetic moment with the incorporation of Ca and Mn in the BCTMO1 sample [Figure 3.11(b)] due to the presence of a weak FM in the paramagnetic background. After careful subtraction of this paramagnetic background, a saturated ferromagnetic loop is obtained [Figure 3.11(b1)]. The magnetisation values obtained for the BCTMO1 sample are an M_r of 1.800 $\times 10^{-3}$ emu per g, M_s of ~17 $\times 10^{-3}$ emu per g, and H_c of ~138 Oe [Figure 3.11(b2)].

Note that the M_r and M_s of BCTMO1 are three times higher than the BTO sample (Table 3.1). However, an entirely paramagnetic behaviour is observed in BCTMO2 and BCTMO3 samples with no opening of a possible loop [Figure 3.11c and d]. The comparison of the variation of the diamagnetic subtracted M–H loop of BTO, paramagnetic subtracted M–H loop of BCTMO1, together with BCTMO2 and BCTMO3, is plotted in Figure 1.12, and the inset shows the zoomed image of the M–H loop indicating the variation of M_r.

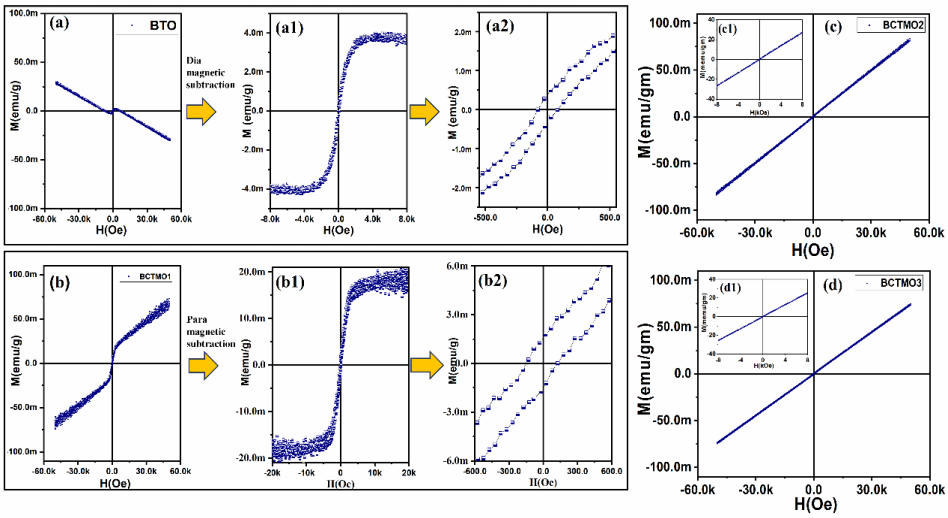

Figure 3.11: *M–Hloop of (a) BTO. (a1) Diamagnetic subtracted M–H loop of BTO. (a2) Zoomed-in plot of the diamagnetic subtracted M–H loop of BTO. (b) M–HloopofBCTMO1.(a1) Paramagnetic subtracted M–H loop of BCTMO1. (a2) Zoomed-in plot of the paramagnetic subtracted M–H loop of BCTMO1. (c) M–H loop of BCTMO2. (d) M–H loop of BCTMO3.*

There is a gradual increase in the hexagonal phase from 12% to 55% from BCTMO1 to BCTMO3. However, FM is only observed for the BCTMO1 sample. Hence, the contribution of FM has a different origin. A literature survey reveals that FM can occur from a double exchange mechanism in the dimer section (between Ti2 sites) of the structure in the hexagonal phase. In the case of Mn doped BTO, Mn^{3+}–O–Mn^{4+} (90°), Mn^{3+}–O–Ti^{4+} (90°), Mn^{4+}–O–Ti^{3+} (90°) or a Ti^{3+}–O–Ti^{4+} (90°) double exchange mechanism can induce FM and Ti^{3+}–O–Ti^{3+}, Mn^{3+}–O–Mn^{3+} (90°), Mn^{4+}–O–Mn^{4+} (90°), and Mn^{3+}–O–Ti^{3+} (90°) can induce AFM. Statistically, the chances of Mn^{3+} being in the vicinity of another Mn^{3+} for lower percentages of doping are low. Similarly, the same can be said about the proximity of Mn^{3+} with Ti^{3+} or Ti^{3+} with another Ti^{3+} inside the dimer due to the low percentage of doping in these samples. Hence, double exchange FM mechanisms are the most likely to occur with Ti^{3+}–O–Ti^{4+} (901) and Mn^{3+}–O–Ti^{4+} (901). On the other hand, the exchange interaction between the Ti1 sites and the Ti1 and Ti2 sites in Mn-doped $BaTiO_3$ is reported to be very weak and considered as paramagnetic behaviour [169].

Considering the percentage of the hexagonal phase and the magnetisation results, it is logical to believe that the hexagonal phase leads to paramagnetic behaviour in these materials and does not contribute to magnetic ordering.

The most described mechanism of magnetic ordering in tetragonal BTO for such lower magnetisation values (~meV) is correlated with the bound magnetic polarons (BMPs) formed due to the trapped electrons in the O_V [170], [171]. Many TM-doped tetragonal BTO samples exhibit a magnetic nature due to BMPs. O_Vs in BTO can trap the electrons locally and create F centers. The magnetism due to the F-center exchange mechanism arises in the O_V–Ti^{3+}/Mn^{3+}/Mn^{4+} networks. The spin polarisation of the 3d electron occurs when an electron at the O_v site binds with the localised 3d electron.

The electrons in the (O_v) and 3d electrons of TM ions exhibit FM exchange interaction, resulting in the formation of BMPs. The short-range ordering of these BMPs includes exchange interactions, and several such BMPs can lead to magnetic ordering in the material. The origin of weak ferromagnetism shown by BTO is due to these BMPs.

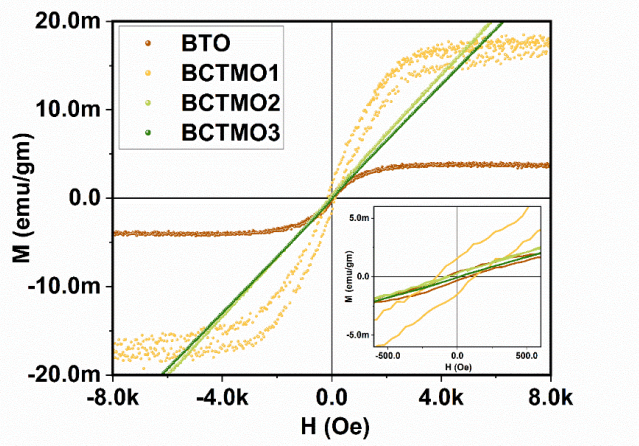

Figure 3.12: *M–Hloop of BTO (after diamagnetic subtraction), BCTMO1 (after paramagnetic subtraction), BCTMO2, and BCTMO3. The inset shows the zoomed image of the M–H loop.*

Table 3.1: Magnetic measurement results			
Sample	**M_s (emu per g) ($\times 10^{-3}$)**	**M_r (emu per g) ($\times 10^{-3}$)**	**H_c (Oe)**
BTO	4	0.35	85
BCTMO1	17	1.8	138
BCTMO2	-	-	-
BCTMO3	-	-	-

In the BCTMO1 sample, the tetragonal phase is the dominant phase, and the enhanced number of O_Vs leads to an increase in BMPs. The presence of Ti^{3+} and Mn^{3+} contributions leads to a short-range FM exchange interaction of Mn^{3+}/Ti^{3+}–O Ti^{4+} in the tetragonal lattice. This exchange interaction and the BMPs contribution result in a weak FM along with a paramagnetic background of the hexagonal phase in BCTMO1. Another supportive structural indication for FM of BCTMO1 is from the XRD analysis. The ~180° Ti/Mn–O Ti/Mn bond angle was found to be the minimum for the BCTMO1 sample. This angle was ~167° for BTO, 164° for BCTMO1, 174° forBCTMO2 and 172° for BCTMO3. A stronger hybridisation of the orbitals is possible for a lower bond angle, which favours a stronger superexchange interaction. The minimum Ti–O–Ti bond angle in BCTMO1 is supportive of the strongest Mn^{3+}/Ti^{3+}–O–Ti^{4+} FM exchange interaction. These interactions are short-range, leading to weak magnetic ordering.

In BCTMO2 and BCTMO3 samples, the incorporation of more dopants accelerates the tetragonal to hexagonal phase transition due to the increase of O_V. It is logical to expect the hexagonal phase to absorb the O_V and the 3+ cations that were formed, thereby reducing the number of defects (3+ ions and O_V) in the tetragonal lattice. This reduces the chances of BMPs and Mn^{3+}/Ti^{3+}–O–Ti^{4+} FM exchange interactions in the tetragonal phase. As the hexagonal phase increases, the samples become completely paramagnetic. This is the reason why magnetic ordering is absent in

BCTMO2 and BCTMO3, and they completely behave as paramagnetic materials.

3.2.5 Ferroelectric properties

The P–E hysteresis loop is a characteristic of FE in materials. Before the application of any electric field, E = 0, any FE material should display zero net polarisation due to the randomly oriented FE domains. P–E measurements are performed by the application of an AC electric field with a magnitude of 20 $kVcm^{-1}$and frequency of 20 Hz [Figure 3.13]. In the case of lossy FE, this method yields a faulty assessment of the saturation polarisation due to the response of the dipoles to the electric field in the presence of active transport possibilities of charge carriers. Hence, a P–E loop is not conclusive to determine whether the material has an FE component for electrically conductive FE materials. To overcome this problem, the PUND measurement is a standard FE test to determine the switched and unswitched polarisation, with the difference providing the actual FE polarisation [172].

A proper saturated P–E loop is observed for BTO with a saturation polarisation P_s of ~11.5 $\mu C/cm^2$ and remnant polarisation, P_r of ~4.5 $\mu C/cm^2$. This is due to the formation and alignment of the domains and domain wall movements with the application of the field. The grain size, domain wall density, O_Vs, and multiple valence states of the dopant ions can significantly influence the FE properties of these materials [173].

Cigar-shaped [174] lossy unsaturated pinched P–E loops are observed for the BCTMO samples. A closer look at the polarisation hysteresis loops [Figure 3.13(a)] reveals the unsaturated P–E loops for BCTMO1, BCTMO2, and BCTMO3. The unsaturated nature is a signature of the conductive properties of these samples, while the loop itself is the proof of a weak FE in these materials. The unsaturated nature is a result of leakage currents and dielectric (non-FE) polarisation due to defect dipoles, mostly in the hexagonal phase. Meanwhile, it is difficult to deconvolute the

contributions from the FE and non-FE components of the polarisation except for attaining a combined result in the form of unsaturated P–E loops. Variation of P–E loops between the samples is shown in [Figure 3.13(b)] and the inset shows the zoomed image of the P–E loop indicating the variations of remnant polarisation between the samples.

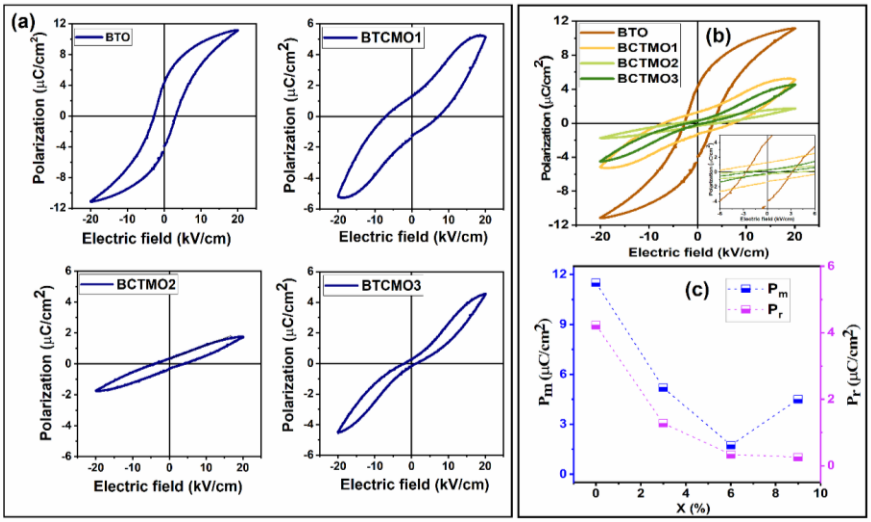

Figure 3.13: *(a) Room temperature P–E loop of all the samples. (b) Comparison of the room temperature P–E loop of all the samples. [Inset: zoomed-in image showing the variation in the Pr value of all the samples. (c) Variation in Pm and Pr obtained from the unsaturated P–E loop.*

Since there is no saturation polarisation, the highest polarisation obtained can be named as maximum polarisation, P_m. It can be an accumulation of both the FE and non-FE components of the polarisations. This is better understood in these materials as the P_r continuously decreases with the reduction of the tetragonal phase content, while the P_m reduces until BCTMO2 but increases for BCTMO3, where the contributions of the defect dipoles increase with the drastic increase of the hexagonal phase component [Figure 3.13(c)].

Pinching of the P–E loops arises from the pinning of the charged defect dipoles on domain wall motion in perovskite ceramics [175]. Three main microscopic mechanisms have been proposed for the origin of the pinching effect for the P–E loop: (a) volume effect, (b) domain wall effect,

and (c) grain boundary effect [176]. According to the volume effect model, unintentional and intentional defects that can be present in the system are stabilised in preferred lattice sites, creating an internal bias that constrains the switching of the polarisation along specific directions. The presence of O_V in the bulk $BaTiO_3$ can create defect dipoles with trivalent cations like Ti^{3+}–O_V and dopant cations like Mn^{3+}–O_V, which can stabilise the domain structures [177], [178]. Upon the application of a field, the bulk dipoles align with the field. However, these defect dipoles cannot orient along the field due to their structural limitations. Following removal of the field, a restoring force is created due to the rigidity of these defect dipoles that accelerates the domain back-switching to its original state towards zero net polarisation. Therefore, the remnant polarisation will decrease at a particular reducing field than what it would have been in the absence of the defect dipoles due to the intrinsic FE, since the polarisation will be lower. This gives the P–E loop a pinched nature [178]. The domain wall effect is based on the concept that mobile defects can diffuse towards domain walls to minimise the local depolarising fields and may act as pinning agents on domain walls. The O_Vs migrate to the domain walls and fix the motion [179]. These defects in the domain walls have a fixed dipole moment that restricts the movement of the domain dipoles, thereby having a pinching effect. In the grain boundary effect, the interface regions between dissimilar phases, such as undesired secondary phases, pores, and electrodes, are often the location of space charge accumulation. Such space charge defects are yet another source of internal bias field responsible for the deformations and asymmetries in the hysteresis loops [176].

From the XPS, it is already observed that there are multiple oxidation states of Mn and Ti in BCTMO samples. The ideal oxidation state of the B site is Ti^{4+}, which should be ideally replaced by Mn^{4+}. However, the incorporation of Mn in the lattice results in a net increase in concentrations of +3 valence cations (Ti^{3+} and Mn^{3+}) from BTO to BCTMO1, and it remains steady thereafter. There has been a continuous

increase in the quantity of O_V. Hence, the pinching should increase proportionately from BCTMO1 to BCTMO3. However, an insignificant pinching is visible for the BCTMO2 sample. This anomalous behaviour of BCTMO2 concerning BCTMO1 and BCTMO3 can be explained by different pinching mechanisms between these samples.

In the BCTMO1 sample, the major phase is tetragonal. Hence, there is a dominant presence of Mn^{3+} and O_V in the tetragonal lattice, thereby increasing the chances of a bulk effect of pinching. In BCTMO2, the proportion of the hexagonal phase increased. The hexagonal phase arises due to the presence of O_vs and increased trivalent B-site cations. Hence, the hexagonal phase is most probably an absorber of trivalent cations and a larger proportion of the O_vs in this sample, thereby reducing the bulk defect dipoles and pinching due to the bulk or domain wall contribution. However, the grain boundary contribution should contribute to the pinching, which is much less in BCTMO2 than in BCTMO3, which has a major hexagonal phase. Hence, one can observe a variation of the mechanism of pinching from a bulk to a more grain boundary effect in these samples.

One must also note that ageing of the samples is sometimes responsible for such pinched loops [180]. In these samples, the ageing effect can be negated as the data have been taken from freshly prepared samples.

3.2.5.1 PUND measurement

The P–E loop of the doped samples is not saturated and shows a leaky behaviour. To distinguish FE switching from artefacts for non-saturated P–E loop PUND (positive-up and negative down), pulse measurements were done. In this method, a series of voltage pulses was applied, and polarisation was measured by switching and non-switching voltages. This allows for the separation of the different components of the electrical response of an FE material.

The PUND measurement is a standard ferroelectric test consisting of five pulses applied in sequence. The pulses are of the same (programmable) pulse width, with a fixed delay time between the pulses, and are of the same magnitude ($|V_{Max}|$). The first pulse is in the negative V_{Max} direction. It is not measured, but is used to preset the sample into the particular polarisation ($\mu C/cm^2$) state. The next two pulses are in the positive V_{Max} direction. The first switches the polarisation, and the second does not, so that both switched and unswitched polarisations are measured. At each pulse, measurements are made with the pulse voltage applied after the pulse width and again after the voltage returns to zero, and a delay of the pulse width (ms). The last two pulses are in the negative V_{Max} direction, with the first pulse switching the sample and the last pulse maintaining the switched state. During the first voltage pulse (P), all active mechanisms will bring their contribution to the measured current, including leakage currents, dielectric displacement current, and ferroelectric displacement current. During the second voltage pulse of the same polarity (U), since all dipoles have been switched, leakage currents, dielectric displacement current will contribute to this pulse. Hence, the subtraction of polarisation in U from polarisation in P gives the value of actual polarisation.

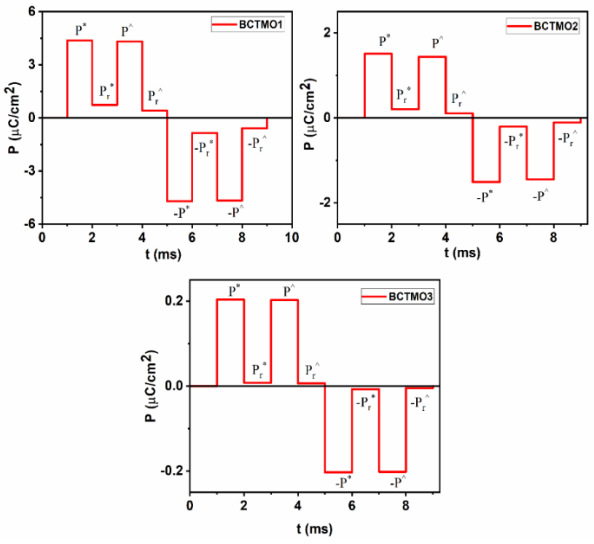

***Figure 3.14**: PUND measurement of all doped samples at 1.5 kV.*

The PUND measurement was done at a voltage of 1.5kV with a pulse width of 1 ms and a delay time of 1 ms. Switched and unswitched polarisation is measured in both the positive and negative directions at the pulse voltage and zero volts. Switched measurements are designated ‘‘P*’’ (P-Star) and unswitched measurements are called ‘‘P^’’ (P-Hat). Measurements at zero volts are distinguished by an appended ‘‘r’’. Therefore, the eight measurements are ±Pand±P^ and ±P^r. The net switching polarisation (dP) was evaluated using the following relation: 2(dP) = [(+P*) - (+P^)] + [(-P*)-(-P^)] and the true remnant polarisation $2dP_r$= [(+P^*_r)-(+P^)]+[(-P^*_r)-(-P^). The results obtained from PUND for all doped samples are plotted in Figure 3.14, and the obtained values are added in Table 3.2. The switching polarisation and true remnant polarisation from FE are obtained as 0.0495 μC/cm^2 and 0.2929 μC/cm^2 for BCTMO1, 0.0259 μC/cm^2 and 0.0957 μC/cm^2 for BCTMO2, and 0.0012 μC/cm^2 and 0.0020 μC/cm^2 for BCTMO3. These values of a finite switching polarisation and remnant polarisation confirm the presence of FE in these materials. However, the transport properties of these materials are enhanced due to the presence of O_Vs and Ti^{3+}, thereby transforming these materials into leaky FE. Although the P–E loops of the doped samples are unsaturated and indicate leaky behaviour, the PUND measurement proved that the samples are not completely leaky, with BCTMO1 exhibiting the maximum FE among the doped samples and contributing to the actual FE polarisation.

Thus, a balance of FM and FE only coexists in the BCTMO1 sample, thereby introducing a multiferroic nature. Higher doping in BCTMO2 and BCTMO3 enhances the hexagonal phase and reduces the possibilities of FM exchange interaction and F center exchange in BMPs, and introduces a lossy nature in the lattice, thereby destroying the chances of multiferroicity.

Table 3.2: PUND measurement results of the BCTMO samples with unsaturated P-E loops					
Pulse	Applied voltage (kV) (V_{max})	Measured values	BCTMO1 ($\mu C/cm^2$)	BCTMO2 ($\mu C/cm^2$)	BCTMO3 ($\mu C/cm^2$)
1	-1.5	None	-	-	-
2	1.5	P^*	4.36908	1.51114	0.20365
	0	P_r^*	0.73448	0.20373	0.00794
3	1.5	P^	4.32061	1.4952	0.20256
	0	$P_r^\wedge$	0.41005	0.10576	0.00619
4	-1.5	P^*	-4.71032	-1.50941	-0.203
	0	P_r^*	-0.8522	-0.20289	-0.00729
5	1.5	P^	-4.65976	-1.47351	-0.20169
	0	$P_r^\wedge$	-0.59091	-0.10943	-0.00501
Net Switching Polarisation, dP			0.04951	0.02592	0.0012
True remnant polarisation dP_r			0.2929	0.0957	0.0020

3.2.6 Transmission Electron Microscopy

High Resolution TEM image of all samples is shown in Figure 3.15. The BTO sample shows a long-range tetragonal lattice in (111) directions with a d spacing of 2.31 Å. The selected area electron diffraction pattern with bright spots in a ring pattern indicates the reflections from different zone axes of the tetragonal lattice structure. In the x=0.03 sample, there are two kinds of lattice structure corresponding to the tetragonal and hexagonal lattices. The (103) planes of a hexagonal lattice with d spacing 3.4 Å are parallel with the (102) planes of a tetragonal lattice with d spacing 1.8 Å.

The boundary between the two lattices indicates a deviation from the lattice planes of the tetragonal and hexagonal lattices. x=0.06 sample shows the coexistence of parallel tetragonal (002) (d spacing 2.01 Å) planes and hexagonal (006) (d spacing 2.01 Å) planes. X=0.09 shows the tetragonal (101) and hexagonal (104) planes.

SAED pattern of the x=0.09 hexagonal region shows blurred spots with ring patterns for different lattice planes of the hexagonal lattice. The existence of both lattice structures in doped samples indicates that Ca and Mn doping stabilise the hexagonal structure in tetragonal BTO. The TEM

image shows how the hexagonal and tetragonal lattices are interlinked with each other, which leads to the influence of one lattice modification over the other and related MEC.

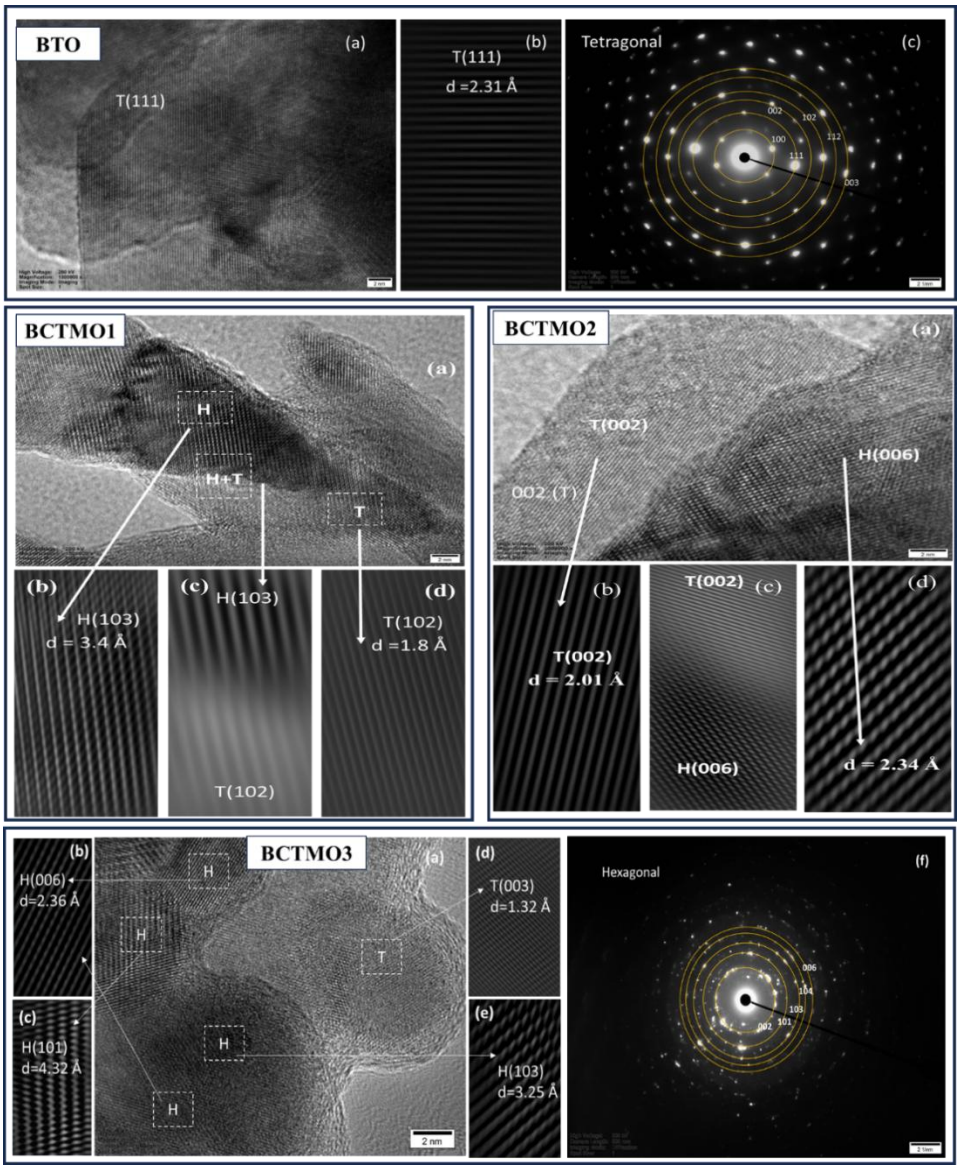

Figure 3.15: *x=0 → (a) TEM image of tetragonal lattice, (b) background subtracted lattice plane image of (a), SAED pattern of (a), x=0.03 → (a) TEM image of hexagonal and tetragonal lattice, (b),(c),(d) background subtracted lattice plane image of selected region. x=0.06 → (a) TEM image of hexagonal and tetragonal lattice, (b),(c),(d) background-subtracted lattice plane image of selected region. x=0.09 → (a) TEM image of hexagonal and tetragonal lattice, (b),(c),(d),(e) background-subtracted lattice plane image of selected region, (f) SAED pattern corresponding to the hexagonal region.*

3.2.7 Magnetoelectric coupling in BCTMO1

BCTMO1 shows both Fe and FM ordering, indicating multiferroicity in the material [Figure 3.16(a) and (b)]. However, the existence of two ferroic orders does not ensure coupling between the two. In this case, coupling between FM and FE (i.e., a ME coupling) is more desirable for practical applications than just the mere presence of the two.

According to Landau's theory, ME coupling interactions are obtained by the free energy of a system in terms of magneto-electric order parameters, with magnetisation (M) and polarisation (P) at constant temperature, approximated by Taylor's expansion of the free energy [123]:

$$F(E, H) = F_0 - P_i^s E_i - M_i^s H_i - \tfrac{1}{2}\varepsilon_0\varepsilon_{ij}E_iE_j - \tfrac{1}{2}\mu_0\mu_{ij}H_iH_j - \alpha_{ij}H_jE_i - 1/2\beta_{ijk}E_iH_jH_k - \tfrac{1}{2}\gamma_{ijk}H_iE_jH_k$$

Where F_0 is the ground state free energy, subscripts (i, j, k) refer to the three components of a variables in spatial coordinates, spontaneous polarization and magnetization is represented by P_i^s and M_i^s, E_i and H_j are the components of the electric field E and magnetic field H. Dielectric and magnetic susceptibilities of a vacuum are given as ε_0 and μ_0 and ε_{ij} and μ_{ij} are the second order tensor of dielectric and magnetic susceptibilities. α_{ij} is the component of the tensor α, which is designated as the linear ME coefficient, and β_{ijk} and γ_{ijk} are third-order tensor coefficients.

The components of total electric polarisation, P, and magnetisation, M, can be obtained by the above equation concerning the electric field in the following equations:

$$P_i(E, H) = -\frac{\partial F}{\partial E} = P_i^s + \varepsilon_0\varepsilon_{ij}E_j + \alpha_{ij}H_j + 1/2\beta_{ijk}H_jH_k + 1/2\gamma_{ijk}H_jE_k$$

$$M_i(E, H) = -\frac{\partial F}{\partial H} = M_i^s + \mu_0\mu_{ij}H_j + \alpha_{ij}E_j + 1/2\beta_{ijk}E_jE_k + 1/2\gamma_{ijk}E_jH_k$$

Magnetic field-induced total polarisation in the absence of applied electric field (E=0) is given by the following equation:

$$P_i\ (H) = \alpha_{ij}H_j + 1/2\beta_{ijk}H_jH_k$$

These equations are used for experimental calculations of the ME coupling coefficient [18]. The magnitude of the linear ME effect in the material is determined by the tensor α_{ij}, and nonlinear ME effects are determined by the tensors β_{ijk}:

$$\delta P_i/\delta H_j = \alpha_{ij} + 1/2\beta_{ijk}H_k$$

Hence, P_i varies linearly with H_j for the linear ME coupling effect. The numerical value for ME coupling is denoted by α_{ME}, which is the voltage generated in the ME material by the application of a magnetic field. The coefficient α_{ME} is related to α_{ij} as $\alpha_{ME} = \alpha_{ij}/\varepsilon_0\varepsilon_r$ [183].

The ME measurement can be determined using three methods: static, quasi-static, and dynamic [129]. Induced electric charge is measured as a function of increased DC magnetic field in static ME measurements. The ME signal is measured as a function of time-varying applied magnetic field in the quasistatic method. Static and quasi-static methods have the drawback of charge accumulation at the sample surface. Dynamic ME coupling measurements avoid the errors due to charge accumulation. In this method, a DC magnetic field is provided by an electromagnet, and a small AC field is provided by a Helmholtz coil. Electrode charging and charge accumulation are avoided by superimposing an AC field of small magnitude on a DC magnetic field as bias. The usual practice of measuring magnetically induced α_{ME} is by measuring the open circuit induced voltage generated by the application of an AC +DC magnetic field [184]. Another possible approach to measure the α_{ME} is the net electric polarisation induced in the sample by the application of an AC+DC magnetic field. This method involves the measurement of the short circuit-induced current: electric polarisation. In this case, the experimental setup is like that used to measure electric polarisation hysteresis loops, except that the multiferroic sample is excited by external AC and DC magnetic fields instead of applied voltages. Since the sample was short-circuited when stimulated by the magnetic field,

the polarisation in the sample is measured, yielding α_{ij}. This value needs to be divided by the small signal capacitance of the sample at that magnetic field strength to convert it to α_{ME}.

In this work, a dynamic ME measurement was performed on the samples by applying a combination of steady (DC) and alternating (AC) magnetic fields. The DC field was varied from 0 to 1500 Oe in steps of 100 Oe, while an AC field of amplitude 40 Oe with a frequency of 1 Hz was applied. The generated polarisation, P, due to an applied magnetic field, H, is measured. The magneto-electric coefficient, $\alpha_{ij} = dP_i/dH_j$, is measured by fitting the P vs. H plot.

The structural ferroelectric and magnetic studies reveal that the existence of both ferroelectric and ferromagnetic ordering is obtained for BCTMO1 and is multiferroic in nature, and there is a possibility of coupling of this ferroic order that can lead to magnetoelectric coupling. Whereas BCTMO2 and BCTMO3 are not showing ferromagnetic ordering and show completely lossy ferroelectric behaviour, indicating no multiferroicity and hence no magnetoelectric coupling. While BTO shows very weak ferromagnetism along with ferroelectricity, and has a possibility of very weak ME coupling. Hence, ME coupling is possible for BTO and BCTMO1. For the ME voltage measurement, we have studied all the compositions. Since BCTMO2 and BCTMO3 are not multiferroic, there were no P-H loops obtained for these compositions; however, for BTO, the P-H loop obtained was almost at the level of noise, and analysis was not reliable for the ME coupling voltage generated and making it impossible to get a proper reading for the analysis. Hence, we report only BCTMO1, which is multiferroic and has a possibility of magnetoelectric coupling and provides a reliable P-H measurement for the analysis.

The response of the P vs. H plot [Figure 3.16(c)] for a Hac of 40 Oe and 700 Oe DC field shows linear behaviour, indicating the direct coupling of ferroic orders. The obtained α_{ME} is plotted in Figure 3.16(d) by fitting the

P vs. H plot for different DC fields. The α_{ME} value increases with an applied DC field until 600 Oe, with nominal changes with an increase in the DC field thereafter. The highest value of coefficient α_{ME} obtained for this sample is weak, of the order of ~0.704 meV in an 800 Oe DC field and 40 Oe AC field. The fitted value of α_{ij} is 0.0382, and β_{ijk} is 3×10^{-6} and a small signal capacitance of 0.6169 nF at this magnetic field. In BTO, the ME coupling measurement provided noisy P–H measurement data, and analysis was not possible. For BCTMO2 and BCTMO3, paramagnetic behaviour and a high-loss FE nature neglect the possibility of ME coupling and do not yield proper P–H measurement results. Hence, the measurement of the ME coupling coefficient was not possible.

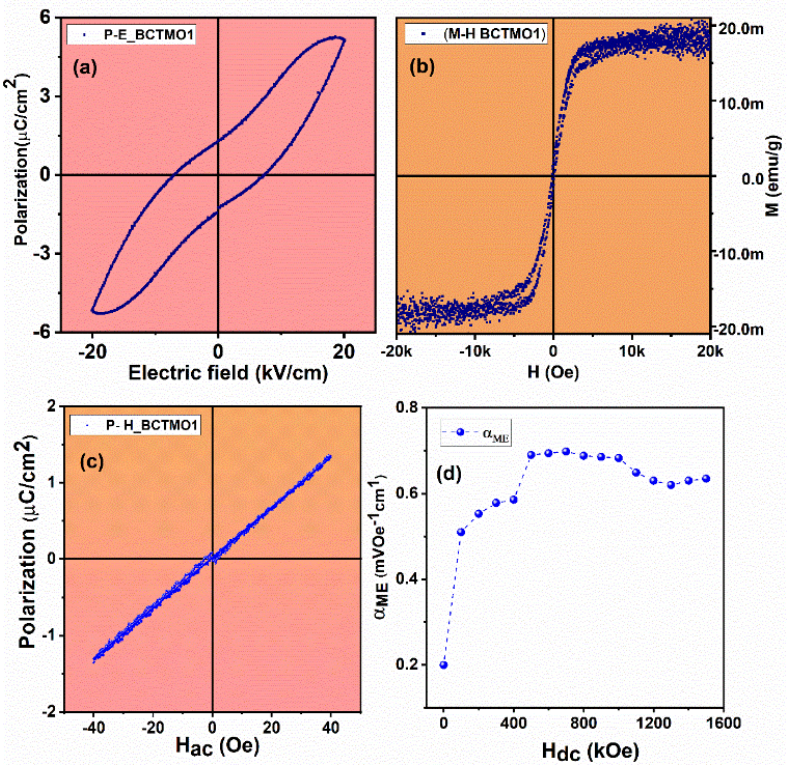

Figure 3.16: *(a) P–E hysteresis of BCTMO1. (b) M–H hysteresis of BCTMO1. (c) Polarisation with an AC magnetic field with a bias DC magnetic field of 600 Oe. (d) Variation in a_{ME} with a DC magnetic field at a constant AC magnetic field of 5 Oe.*

In the BCTMO1 sample, the short-range exchange interactions and BMPs in the tetragonal phase induce magnetic ordering with the application of a magnetic field, and this ordering is directly coupled with the tetragonal

FE domains and induced polarisation in the material. In the ME material, the nature of coupling [i.e., the coupling between the polarization (P) and magnetization (M)] might be bilinear (P–M), linear quadratic ($P–M^2$), quadratic–linear ($P^2–M$), biquadratic ($P^2–M^2$), linear–cubic ($P–M^3$), cubic–linear ($P^3–M$), or involve higher order terms [68]. Among the possible natures of ME coupling, only P–M is direct coupling, while the other coupling takes place through elastic interactions.

As we have obtained a linear response of induced polarisation with applied AC magnetic field, this indicates that ME coupling in this material is a bilinear P–M interaction through direct coupling of ferroic orders present in the same tetragonal phase. Also, the values of the linear coupling coefficient α_{ij} of the order of $\sim 10^{-2}$ and the nonlinear coupling coefficient β_{ijk} of the order of $\sim 10^{-6}$ indicate that the coupling is linear. Here, both magnetic and electric ordering are contributed by the tetragonal phase. The role of the hexagonal phase is to maintain an optimum number of defects in the tetragonal phase for the simultaneous existence of FM and FE and the ME coupling in BCTMO1.

Table 3.3: Maximum polarisation, Saturation magnetisation, and magnetoelectric coupling values reported for single chemical phase bulk material at room temperature

No	Sample	Maximum polarization P_m ($\mu C/cm^2$)	Saturation magnetization M_s emu/gm	α_{ME} mV/cm. Oe	Ref
1	$BaTiO_3$-$LaFeO_3$ solid solution	-	1.034	1.56	[185]
2	$BaTiO_3$-$BiFeO_3$ solid solution	17	-	0.89	[186]
3	Fe-doped $BaTiO_3$	-	0.082	16	[187]
4	Cr doped $BaTiO_3$	3.7	0.008	13	[188]
5	Sm doped 0.67-$BiFeO_3$0.33$BaTiO_3$	35	-	0.55	[189]
6	Er, Nb-doped $BiFeO_3$	0.46	0.093	0.22	[190]
7	$Na_{0.5}Bi_{0.5}TiO_3$	31	5	4.18	[191]
8	Sm and Fe doped $Bi_4Ti_3FeO_{12+\delta}$	12	22	0.84	[192]
9	Yb and Mo doped $BiFeO_3$	0.3	0.4	0.264	[193]
10	Ca and Mn-doped $BaTiO_3$	4.23	0.017	0.704	This work

Hence, the incorporation of Ca and Mn in BaTiO3 is responsible for the structural transformation from a solely *P4mm* phase to a mixture of *P4mm* and *P6₃/mmc* phases, with a major *P4mm* phase for x=0.03, 0.06, and a major *P6₃/mmc* phase for x=0.09. For x=0.03, the magnetism induced in the sample is FM in nature, while the FM nature weakens with higher doping percentages. The FE in the materials is modified within the corporation of Ca and Mn. The loss of FE, along with the incorporation of magnetic properties (especially in the case of x=0.03), seems to be influencing each other through direct magneto-electric coupling. The linear response of inducing polarisation with an AC magnetic field indicates direct ME coupling of the ferroic orders in x=0.03 and a lack of such coupling for higher doping. Table 3.3 shows a comparison of the different reported values of α_{ME} for bulk materials of a single chemical phase at room temperature. Although composite and heterostructures reveal a much higher value for α_{ME}, the direct coupling of ferroic orders, weakening of one ferroic order by the introduction of another ferroic order within the single phase, results in very weak coupling values in these materials.

3.3 Conclusion

$Ba_{(1-x)}Ca_{(x)}Ti_{(1-y)}Mn_{(y)}O3$ (x=y=0,0.03,0.06,0.09), has been prepared through sol–gel synthesis. XRD and Raman spectroscopy reveal characteristic peaks corresponding to a dual phase of ferroelectric tetragonal *P4mm* and ferromagnetic hexagonal *P6₃/mmc* space groups of $BaTiO_3$. The ferroelectric hysteresis shows a saturated P–E loop for x = 0 and a lossy unsaturated pinched P–E loops for doped samples. M–H loops indicate diamagnetism for x=0, ferromagnetic hysteresis for x=0.03, and paramagnetic behaviour for the other samples. The multiple oxidation states of Mn^{3+}, Mn^{4+}, Ti^{3+}, $Ti^{4+,}$ and the number of O_vs are the reasons for the ferromagnetism. A reduced O–Ti–O angle may be a consequence of an increased hybridisation of the 2p–3d orbitals in the x = 0.03 sample compared with the other samples, which may correlate with the enhanced

ferromagnetic double exchange interaction. The existence of both ferroelectric and ferromagnetism in x=0.03 leads to multiferroicity and magnetoelectric coupling. The structural studies confirm the presence of a major tetragonal phase for x = 0, 0.03, and 0.06. However, a hexagonal phase appears for the doped samples, and for x=0.09, the sample was mostly hexagonal. The hexagonal phase was minimal for x=0.03, hence the possibility of a ME coupling seems to be maximum. The magnetic studies, on the other hand, reveal that ferromagnetism was also maximum for the x=0.03 sample. This combination of maximised ferroelectricity and ferromagnetism ensures the possibility of ME coupling in the material. Note that the x=0.06 and x=0.09 do not reveal ferromagnetic ordering and are lossy ferroelectrics. Hence, the possibility of ME coupling is nullified. Induced polarisation with an applied magnetic field shows a linear response, indicating direct ME coupling in this material. A weak magnetoelectric coupling coefficient of α_{ME} ~0.704 $mVcm^{-1}Oe^{-1}$ was obtained for a DC magnetic field of 800 Oe and an AC magnetic field of 40 Oe. Hence, $Ba_{(0.97)}Ca_{(0.03)}Ti_{(0.97)}Mn_{(0.03)}O_3$ is a magnetoelectrically coupled material. This ME coupling is absent for higher percentages of doping, revealing the adverse effect of higher percentages of Mn.

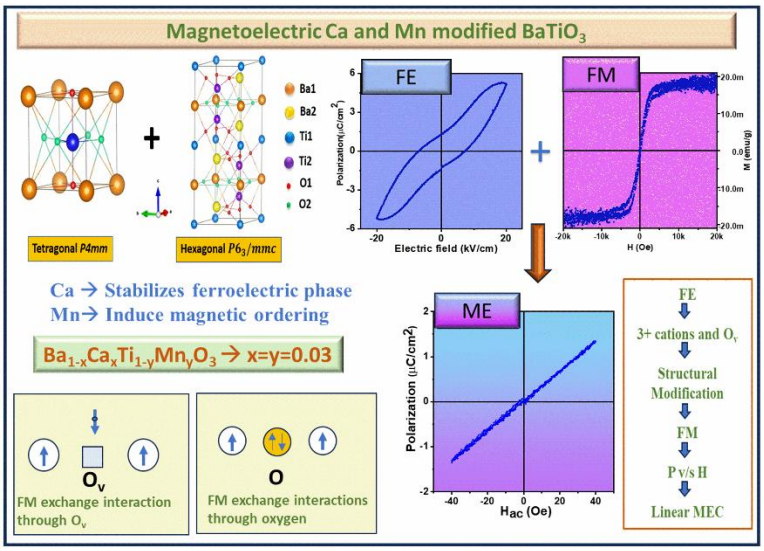

CHAPTER 4

Hexagonal polymorphism induced structural disorder and dielectric anomalies of

Ca/Mn modified $BaTiO_3$

$Ba_{(1-x)}Ca_{(x)}Ti_{(1-y)}Mn_{(y)}O_3$ (x=y=0, 0.03, 0.06, 0.09)

This chapter details the optical band gap modification of the Ca/Mn-modified $BaTiO_3$. XAS analysis shows the valence state changes and local structural distortions. Experimental UV-DRS, PES studies, and Theoretical DOS and ELF calculations indicate the defect state formation within the band gap and the shift of band edges, and lattice distortion. Dielectric anomalies and diffuse phase transition have been studied in correlation with the structural changes.

4.1 Introduction

Crystal structure is an inevitable part of determining multiple properties exhibited by different crystalline materials. $BaTiO_3$ (BTO), one among the good ferroelectric materials, has been intensively studied for its multiferroic properties by doping it with Transition metal (TM) elements. With the modification, there may or may not be multiferroicity; however, these dopings can play an important role in the manipulation of the disorder-induced electronic, dielectric, and ac conductivity of these materials. Depending on how the disorder influences these physical properties can be effectively used for various multifunctional applications like sensors, actuators, antennas, optoelectronic devices, etc.

The modification of $BaTiO_3$ through A-site and B-site doping is a widely explored method to tune its band gap for various applications, including optoelectronics and photovoltaics [194], [195], [196]. Its wide band gap (>3 eV) can hinder its application in fields like ferroelectric photovoltaics, as it limits the absorption of a significant portion of the solar spectrum. Substituting Sr^{2+} for Ba^{2+} in BTO ($Ba_{1-x}Sr_xTiO_3$) can lead to a reduction in the band gap [197]. Experimental and theoretical studies on these ceramics have shown variation in the energy band gap from 3.615 eV to 3.212 eV with Sr substitution, correlating with crystal symmetry transition. Doping Sn at the [198] A-site of BTO can generate impurity bands that alter the direct bandgap to an indirect one and decrease its value, reducing the electron excitation energy. $(Ba_{0.875}Sn_{0.125})TiO_3$ exhibits p-type semiconductor characteristics, which improve the conductivity of BTO. The co-substitution of La^{3+} and Na^{+} in BTO ceramics, forming $Ba_{(1-x)}(La,Na)_xTiO_3$ (BLNT), introduces structural disorder and A-site vacancies, which leads to the creation of shallow defects and a narrowing of the band gap energy [199]. The replacement of transition metal ions at B-sites in BTO-based solid solutions can lead to a significant decrease in band gaps. Doping BTO with Fe ($BaTi_{0.88}Fe_{0.12}O_{3-\delta}$) results in a smaller band gap

compared to pure BTO. Fe doping also creates donor impurity levels in the forbidden band due to the presence of Fe^{3+} and Fe^{4+} forms and positively-charged O_vs. With Mn and Nb doping, the band gap of BTO can decrease from 3.2 eV to approximately 2.7 eV for a 7.5% doped sample [200]. Experimental studies have observed a redshift in UV-absorption spectra, indicating a decrease in the optical band gap from 3.13 eV to 2.71 eV as Mn^{2+} doping increases [201]. Apart from the band structure modification, doping can change the T_c and the permittivity and make a diffuse kind of phase transition from ferroelectric to paraelectric. La doping in BTO shifts the Curie point to lower temperatures and controls grain growth efficiently. The dielectric constant of La-doped $BaTiO_3$ ceramics increased with increasing La content [202]. Uniform distribution of Ca^{2+} ions in the BTO matrix makes the transition from the ferroelectric to the paraelectric phase more diffuse and free from relaxational effects up to 10 KHz [203].

Structural studies of Ca and Mn-modified $BaTiO_3$, described in the previous chapter, indicate a pure Tetragonal *P4mm* structure for the x=0 sample and multiple phases of major tetragonal *P4mm* and minor Hexagonal $P6_3/mmc$ for x=0.03, 0.06, and majority Hexagonal $P6_3/mmc$ with minor tetragonal *P4mm* for x=0.09. The multiferroic and magnetoelectric studies revealed that x=0.03 exhibits magnetoelectric coupling at room temperature. The variation of the multiple oxidation states of Ti^{3+}, Ti^{4+}, $Mn^{3+,}$ and Mn^{4+} and the structural changes lead to the magnetoelectric behaviour exhibited by this material.

This study involves the structural investigation of the samples using X-ray absorption spectra analysis to investigate the oxidation state and local structural changes due to doping at the Mn and Ti sites. Band gap modification and Urbach tail in UV-DRS and changes in the valence band observed in PES measurement due to localised defects in the material, and supported with theoretical Density of States calculation. The electron localisation function calculation is used to analyse the changes in the

localised electron density near the dopant atoms. Variation of dielectric properties corresponds to the structural modifications and defect formation are also explored in this work.

4.2 Results and Discussion

4.2.1 X-Ray Absorption Spectroscopy Analysis

To further confirm the oxidation states, site occupancy, and the local geometry of Ti and Mn ions, X-ray absorption spectroscopy was performed. The special pre-edge features and the absorption edge position in XAS, including the XANES spectra, provide details of the symmetry of the orbitals, hybridisation, and the oxidation states of the absorbing atom. The changes in the absorbing energy indicated by the shifts in the XANES spectra are indications of probable changes in the oxidation states of the atom. Oscillations after the absorption edge, including EXAFS spectra, provide the scattering paths that include local structural changes surrounding the atom. The standard normalisation and background subtraction procedures were executed using ATHENA software version 0.9.26 to obtain normalised XANES spectra [204].

The Ti-K edges of the samples [Figure 4.1] reveal sharp absorption features with a main peak at ~4987 eV (feature E) corresponding to the Ti 1s- 4p transition and indicating the density of states of unoccupied Ti 4p [205]. This feature carries the information of the oxidation state of Ti in the crystal structure. The positions of this feature for the present samples are nominally shifted from ~4987 eV to lower energies with doping. This indicates a major Ti^{4+} state in these samples. The main absorption peak intensity increases with doping. This is an indication of a reduction in the non-centrosymmetric location of the Ti ion [206]. The non-centrosymmetricity introduces broadening of the 4p electronic states due to different hybridisations with the neighbouring oxygen [205]. Hence, an increase in the centrosymmetric nature is observed with doping. The nominal shift of the Ti-K absorption edge to a lower energy value is

observed mainly for BCTMO3 [inset of Figure 4.1(b1)]. This indicates a decrease in the oxidation state from Ti^{4+} to Ti^{3+}.

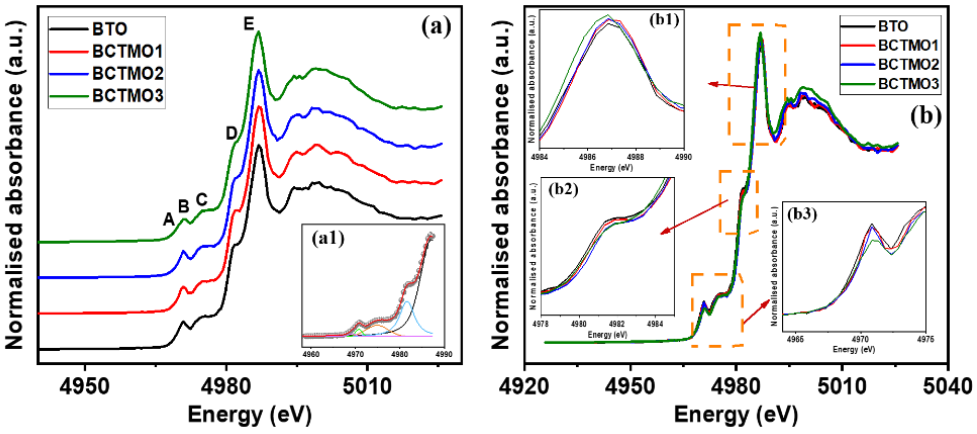

Figure 4.1: *(a) XANES data of the Ti K-edge with the absorption peak E and all the pre-edge features marked as A, B, C, and D. (b) Variation in the features with samples. Inset (b1) is the zoomed-in image of absorption peak E. Inset (b2) is the zoomed-in image of the pre-edge feature C. Inset (b3) is the zoomed-in image of the pre-edge feature B.*

Small features at a lower energy (4965–4985 eV) represent the Ti 3d pre-edge features. There are four features marked as A (~4968 eV), B (~4971 eV), C (~4975 eV), and D (~4982 eV) [Figure 4.1(a)] [207], [208]. The pre-edge region of the XANES spectra can be deconvoluted into four peaks in the Athena software, as in Figure 4.2.

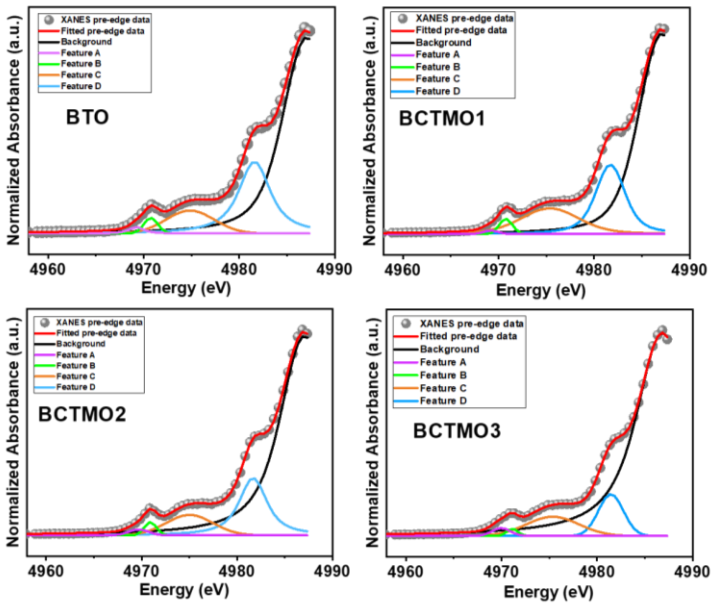

Figure 4.2: *Deconvoluted XANES spectra of the Ti edge of all samples.*

In the case of an octahedral symmetry, the five-fold degenerate 3d orbitals split into three-fold (t_{2g}) and two-fold (e_g) degenerate states. These degenerate states manifest as two pre-edge features: a minor hump-like feature A for a Ti 1s- Ti 3d(t_{2g}) quadrupolar transition and a sharp peak, B, for 1s- Ti 3d(e_g) O 2p hybridised states, which is mostly a dipolar contribution. Feature A is forbidden in a dipole approximation and is allowed in a quadrupole approximation, making it a very weak [205]. This feature is so weak that the analysis of this peak is irrelevant. As the hybridisation between the Ti 3d e_g orbitals and O 2p orbitals becomes more pronounced, the local distortion in the TiO_6 octahedron increases, resulting in a relatively large dipole component; hence, the intensity of the e_g peak (B) increases. The intensity of B and the mean-square displacement of the Ti ion from the center of the symmetric position of the TiO_6 octahedron are proportional; thereby, the B feature representing asymmetry of the TiO_6 octahedra is absent if the TiO_6 octahedra are centrosymmetric [209], [210]. Note that this B feature is present in all samples, indicating a non-centrosymmetric TiO_6 octahedra in all the samples [inset of Figure 4.1b3]. This is a clear indication of the retention of the tetragonal phase with doping in all the samples. The intensity of feature B gradually decreases with doping, hinting at a gradual transformation towards a more centrosymmetric TiO_6 octahedra [Figure 4.2(a)]; namely, a reduction of the tetragonality. This information matches the XRD results [Figure 4.2(b)]. It is interesting to note that the hexagonal phase is composed of both centrosymmetric and non-centrosymmetric octahedra in this mixed phase material. The non-centrosymmetric TiO_6 octahedra form dimers. From the XRD studies, these octahedra continuously evolve with doping with respect to the position of the Ti atoms. The Ti atoms move closer to each other. However, this distortion was much less compared with the octahedral distortion in the tetragonal phase.

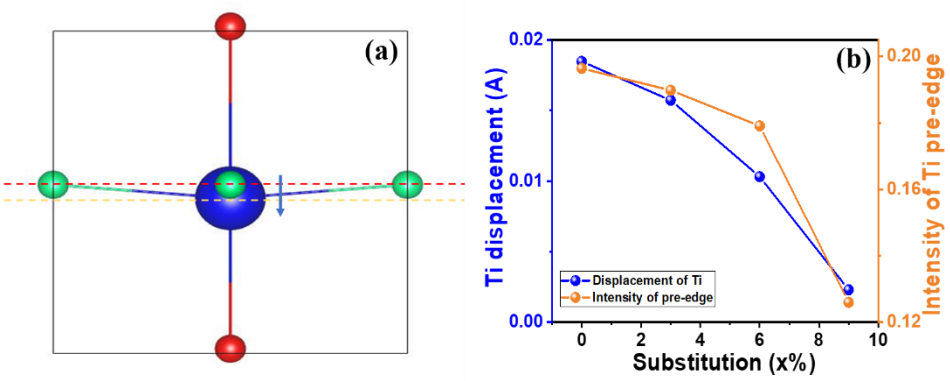

Figure 4.3: *(a) Schematic of the displacement of Ti from the centrosymmetric position in the P4mm tetragonal structure of BTO. (b) Variation in Ti displacement from the centrosymmetric position of BTO (P4mm) and variation in the intensity of the Ti pre-edge feature B with composition.*

Feature C (~4975 eV) appears due to the interaction with the neighbouring Ti atoms and has a dipolar character [208]. There is no trend in the intensity profile of this feature, indicating a dynamic change of Ti–O–Ti bond angles and Ti–O bond lengths. The shoulder structure D (~4982 eV) is a characteristic of tetragonal $BaTiO_3$ [inset of Figure 4.1(b2)] [205]. The identification of the electronic states responsible for this shoulder feature was not made, but there are some conclusions that have been reported with the shoulder structure, indicating the contribution of the A-site and B-site ions in the FE perovskite. This reflects the electronic hybridisation between Ti and Ba in the perovskite. A theoretical background for this claim, based on the Born effective charges of each constituent atom, is reported by Ghosez *et al.* [211] Modification of the Ba site and Ti site of $BaTiO_3$ induces changes in the intensity of the shoulder peak, indicating that it correlates with the electronic hybridisation between the A-site and B-site through O atoms. The gradual reduction in the intensity of peak D indicates a gradual decrease in the A–B bond with Ca and Mn doping in the Ba and Ti sites, respectively.

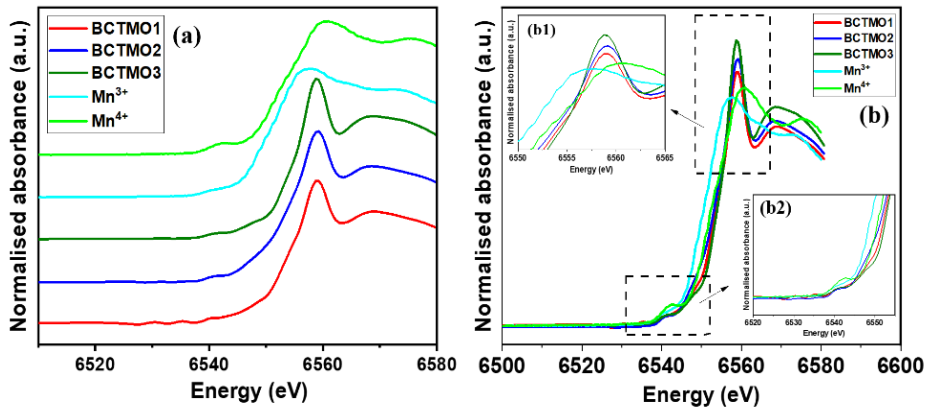

Figure 4.4: *(a) XANES data of the Mn K edge. (b) Variation in the features with samples. Inset (b1) shows the zoomed-in images of the absorption peak. Inset (b2) shows the zoomed-in image of the pre-edge feature.*

The Mn-K edge XANES absorption peak of Mn^{3+} is observed at ~6555 eV, while Mn^{4+} appears at ~6562 eV [212]. The normalised Mn-K edge in fluorescence mode for all samples [Figure 4.4] is observed at ~6558 eV, which is in between the absorption peaks of Mn^{3+} and Mn^{4+} [inset of Figure 4.4(b1)]. Pre-edge features corresponding to Mn 1s- 3d (t_{2g}) and 3d (e_g) states appear as a broad feature in the region ~6542 eV. These pre-edge features are not resolved experimentally due to core-hole lifetime broadening [209]. The intensity of the pre-edge feature for Mn^{4+} is generally more than that for Mn^{3+} [213]. The gradual evolution of the pre-edge intensity with doping indicates the relative increase of Mn^{4+} over Mn^{3+} with doping, as obtained in the XPS. Comparing the pre-edge intensities of Mn and Ti, a very feeble pre-edge intensity contribution is observed for Mn compared with Ti for all samples [Figure 4.4(b2)]. Therefore, the MnO_6 octahedra are expected to be relatively less distorted than the TiO_6 octahedra. The obtained XANES feature can also indicate the occupancy of Mn at the A site or B site. Mn will predominantly occupy the B site in all equilibrium growth conditions rather than going to the A site, according to first-principles calculations based on energetics [214]. Note that the sharp absorption peak of the main Mn-K edge without any pre-edge feature peak indicates a simultaneous replacement of Ba and Ti by Mn [215]. However,

the similar XANES features of the Ti K-edge and Mn K-edge with pre-edge features confirm the B-site occupancy of Mn in BTO.

The EXAFS data reveal the local environmental changes at the Ti and Mn sites. The k^2 -weighted Ti K-edge and Mn K-edge EXAFS spectra [216] were Fourier transformed (FT) in the range 0–5 Å [Figure 4.5].

Ti K-edge EXAFS for the samples is shown in Figure 4.5(a). The radial distance of the shell configuration, which is assignable to scattering paths of Ti-O, Ti−Ba, and Ti−O−Ti [217]. All three peaks shift towards a lower position with doping, corresponding to the decrease in the Ti-O, Ti-Ba, and Ti-Ti distances. An increase in the intensity of the EXAFS oscillation corresponding to the Ti-O bond with doping indicates the oxygen environment surrounding the Ti is less distorted. This indicates the centrosymmetric nature of Ti in the doped samples. Intensity of the Ti-Ba path shows a random behaviour with doping, while the Ti-O-Ti scattering path shows an increase in intensity of the peak up to 0.06 and then a decrease for x=0.09. For all doped samples, the intensity of the Ti-O-Ti path is more than the x=0 sample, indicating a less distorted Ti-O-Ti path with doping.

Mn EXAFS spectra [Figure 4.5(b) show the main feature at 1.35 Å, related to the first oxygen coordination shell (Mn–O) for all samples. The position of this peak slightly shifts to higher values with increasing Mn content. Note that in higher Mn-containing samples, Mn^{4+} is a dominant state, which has a smaller ionic radius than Mn^{3+}. Therefore, the enlargement of the Mn–O bond length with increasing Mn content is indicative of increasing Mn^{3+} proportions. The multipeak at ∼3.2 Å corresponds to the second (Ba) and third near neighbours (Ti, Mn, and Nb), including multiple scattering contributions from Mn−Ti−O paths [218]. This peak corresponds to a weighted sum of contributions from Mn−Ti, Mn−Mn, and Mn−Ba. This peak appears shifted towards lower values, corresponding to the decrease in the Mn-Ba/Ti/Mn bond with doping. The Mn−O peak amplitude tends to increase with doping, indicating that the

oxygen environment around the manganese is becoming less distorted, indicative of the transformation to more centrosymmetric, less tetragonal behaviour with doping [218]. However, the multipeak the intensity decreases gradually with doping, indicating the higher disorder of the second shell with doping. The contraction of the first shell and the expansion of the second shell, opposite changes in the variations in the intensity of the scattering paths of the first and second shell, reveal the modifications in the coordination sphere of Mn and thus the crystal structure changes with doping [219]. The third peak observed ~3.7 Å for the x=0.03 sample appears much smoother in other samples, which suggests the distribution of Interatomic distances for that shell is possibly more disordered with doping and not significantly observed in the higher-doped sample.

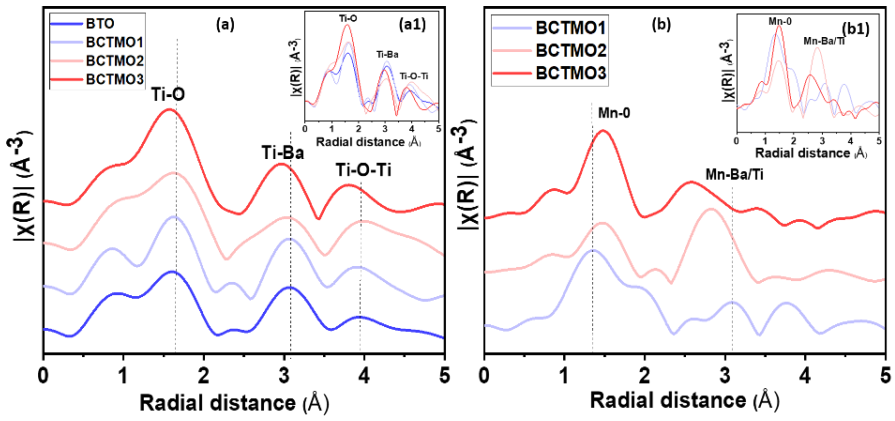

Figure 4.5: *Fourier transformed EXAFS spectra of (a)Ti edge, (b) Mn edge. Inset(a1)and (b1) show the EXAFS spectra without stacking.*

4.2.2 UV-Visible DRS analysis

The emergence of the hexagonal phase can induce band gap variations due to the defects and disorder created in the material. The defect states created can effectively modify the band gap energy (E_g). The band tails, which can be a material property of an imperfect semiconductor or can

be introduced into the material by doping. The exponential Urbach tail at the absorption edge results from transitions between these band tails below the band edges and changes an abrupt absorption to a bent absorption at the band gap energy. Hence, the analysis of the Urbach energy (E_U) indicates the disorder in the material.

E_g was measured using the UV-visible absorption spectrum and is estimated by fitting the absorption coefficient in Tauc's relation given by $(\alpha h\nu)^n = C(h\nu - E_g)$ [26], where C is the proportionality constant, h is the Planck constant, E_g is the optical bandgap, and n is 2 for the direct bandgap [27]. Tauc's plot of all the samples is given in Figure 4.6. The extrapolation of the straight portion of the curve to the energy axis will give the bandgap. The structural disorder and the defects in the lattice are associated with the E_U [28]. The spectral dependence of the absorption coefficient α in the spectral region corresponding to transitions involving the tails of the electronic density of states is described by the Urbach equation,

$$\alpha = \alpha_0 exp\left(\frac{h\upsilon - E_g}{E_U}\right),$$

where α_0 is a constant, E_U is the energy that reflects structural disorder and defects of a semiconductor.

The E_g and E_U are calculated from the $(\alpha h\nu)^n$ v/s hν plots. In polycrystalline metal oxides, which have disorder due to doping, the Urbach tail influence on the band gap is very high it can shift the band gap by a few hundred meV. Hence, $(\alpha h\nu)^n$ plots can be used to determine the bandgap of this material only when the influence of disorder on the absorption edge is not too strong. For this purpose, Viezbicke *et al.* [220] have developed the NEAR factor (Near-Edge Absorptivity Ratio) to describe the influence of band tails on the absorption edge. The NEAR factor for a direct allowed transition is determined using the following formula.

$$\text{NEAR} = \left\{\frac{(\alpha h)^2 \,|_{h\nu = E_g}}{(\alpha h)^2 \,|_{h\nu = 1.02E_g}}\right\} = \frac{\alpha(E_g)}{\alpha(1.02E_g)}$$

NEAR factor is intended to determine how steep the absorption edge is near the bandgap. To do so, the absorption at the energy of the bandgap is compared with the absorption at a photon energy enhanced by 2%, i.e., 1.02 E_g. When the Urbach tail is significant, NEAR approaches 1, while when the absorption edge is little affected by the Urbach tail, NEAR is small, ideally approaching 0. The $(ahv)^n$ plot should only be used if a NEAR factor < 0.5 can be achieved.

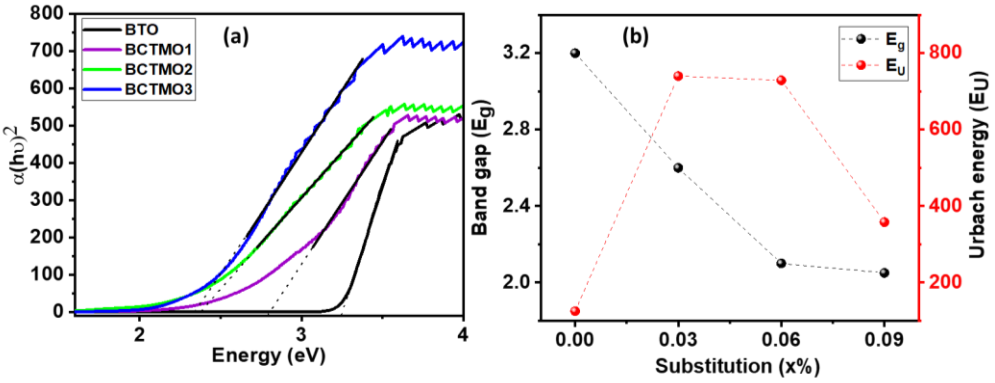

Figure 4.6: *(a) UV-DRS tauc plot of all samples, (b) Variation of E_g and E_U with substitution.*

In all the samples, the NEAR factor is calculated to be <0.5, and hence the influence of Urbach tail on the Band gap is negligible. The Tauc plot of all samples for direct band gap (n=2) is shown in Figure 4.6(a). The calculated E_g and E_U are plotted in Figure 4.6(b). E_g is showing a gradual decrement from 3.2 eV to 2.05 eV as the doping increases from x=0 to x=0.09. E_U shows an increment from 125 eV to 740 eV from x=0 to x=0.03, then decreases to 358 for x=0.09.

Table 2.1: Obtained values of E_g and E_U from UV-DRS

Sample	Band gap (eV)	Urbach energy (meV)
BTO	3.2	125
BCTMO1	2.6	740
BCTMO2	2.1	729
BCTMO3	2.0	358

A sudden decrease in the E_U from x=0.06 to x=0.09 is due to the drastic structural change from a minor hexagonal *P6₃/mmc* phase with major tetragonal *P4mm* in x=0.06 to a minor hexagonal *P6₃/mmc* phase percentage with major tetragonal *P4mm* phase percentage in x=0.09. E_U increases as the disorder in the tetragonal phase increases, and then for x=0.09, there is a complete structural change taking place in which the hexagonal *P6₃/mmc* phase is the major phase and the tetragonal phase is the minor phase. The disorder in the tetragonal phase attains its maximum at x=0.03, and then the crystal structure tries to minimise the strain due to doping and defect formation by triggering the hexagonal phase, which results in a decrease in E_U value. The drastic change observed in the E_g value corresponds to the defect states formed in the band gap due to doping.

4.2.3 X-Ray Photo Emission Spectroscopy

The electronic property was investigated using photoemission spectroscopy (PES). The valence band (VB) spectra for all compositions are shown in Figure 4.7. Analysing valence electron distribution provides essential information regarding the physical and chemical properties of the solid. The hybridisation of 2p electrons of oxygen with 3d electrons of Ti contributes to the primary share of the density of state (DOS) of the valence band (VB). The measured VB spectra are an integrated DOS throughout the entire Brillouin zone. For the interpretation of the partial DOS, it should be taken into account that the Ti state in XPS VB spectra demonstrates an overestimated contribution of the occupied 3d state due to a higher cross-section of Ti than for oxygen [221]. The valence band is deconvoluted into 3 Gaussian peaks of three electronic states: one pure O-2p orbital and two O-2p and Ti-3d hybridised states are called as regions A, B and C, respectively, for BTO and for doped samples, two additional ingap states (IGS) named as D and E are also observed [Figure 8(b)] [222].

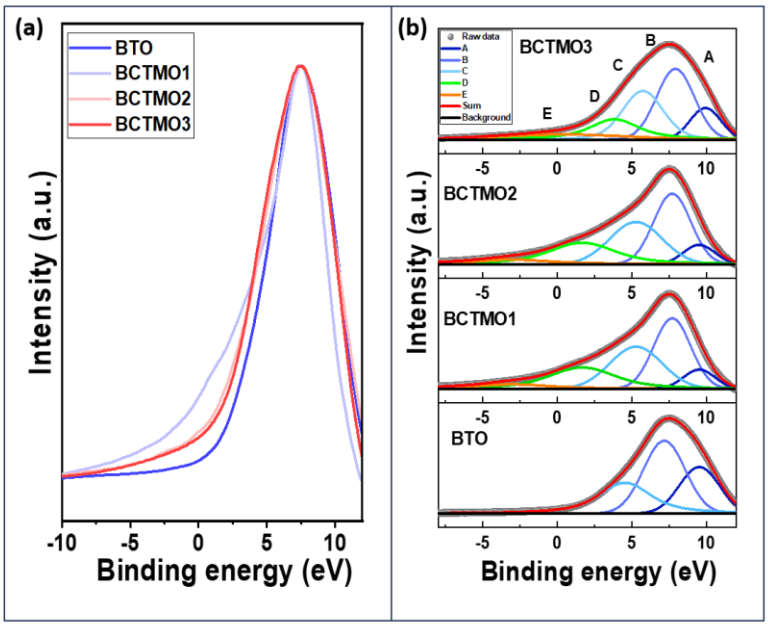

Figure 4.7: *(a)VB spectra of different samples, (b) Deconvoluted VB spectra*

The VB spectra reveal a growing intensity in valence states from 2 eV extending to about 11 eV in binding energy (BE). The onset of the valence band maximum (VBM), defined from the Fermi level (E_F) at 0 eV, also sees a clear shift towards lower BE as a function of doping. We interpret this shift in the valence band edge due to admixed dopant *d* states that hybridise with O 2*p,* which push the VBM towards the conduction band and reduce the bandgap [223].

For the doped samples, VB tail rising earlier than x=0 indicates the enhanced IGS in the sample. The IGS may arise due to the vacancies that form the trap centers. Such states are most commonly found to originate from oxygen defects [224], [225] and Ti^{3+} ions located in the vicinity of oxygen defects [226]. IGS are represented by the peaks D and E in the doped samples. Peak E corresponds to the collective effect of the Ti^{3+} defect state and deep trap due to oxygen defects, while peak D corresponds to the shallow trap due to oxygen defects [227]. From Figure 4.8, it is evident that the overall area of the peak profile of the IGS peak D is maximum for the BCTMO1 sample, then decreases with doping, whereas peak E increases

from BCTMO1 to BCTMO3. Variations of the normalised area of the IGS D and E are plotted in Figure 9.

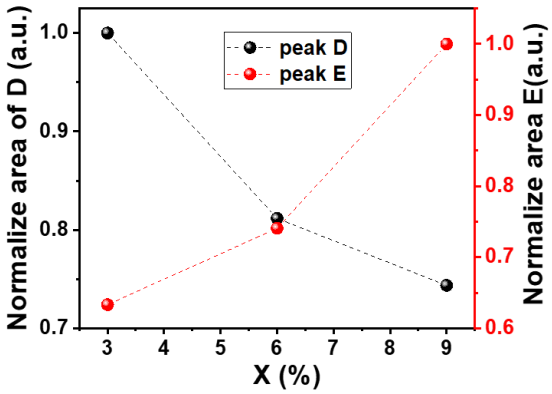

Figure 4.8: *Variation of the normalised area of IGS of peaks D and E with substitution.*

Hence, the concentration of O_v is maximum in the BCTMO1 sample and thereafter decreases as the structure goes towards a more hexagonal nature. And the defect states Ti^{3+} slowly increases from BCTMO1 to BCTMO3 [Figure 4.8]. The valence band tail crosses E_F due to doping-induced localized states. The origin of O_v and Ti^{3+} in BTO triggers the hexagonal phase of $BaTiO_3$, as the hexagonal phase percentages increase to minimize these defect states. Similar results were obtained in the E_U calculation from the UV-DRS spectrum. Urbach energy increases from BTO to BCTMO1, then decreases afterwards. PES and UV-DRS measurement both indicates the defect states within the bandgap that lead to Urbach tails in the valence band in PES and absorption spectrum in DRS.

4.2.4 Theoretical Studies

4.2.4.1 Density of States Calculation

To compare the experimentally obtained band gap modification, theoretical DOS calculations have been performed for x=0 and x=0.125 for tetragonal and hexagonal $BaTiO_3$, and are shown in Figure 4.9. The valence band of the BTO is mainly formed by the Ti 3d orbitals, and the conduction band is formed by the O 2p orbitals. Bandgap of the tetragonal x=0 sample

is obtained as 1.4 eV, Figure 4.9(a). DOS calculations of doping of Ca and Mn for x=0.125 in the tetragonal phase are shown in Figure 4.9(b). The band gap has reduced to 1.123 eV with doping in the tetragonal phase without any defect states within the band gap. Hexagonal BTO, x=0 sample shows band gap value of 1.053 eV [Figure 4.9(c)] and doping of Ca and Mn for x=0.125 hexagonal BTO becomes a nearly metallic state (band gap ~0eV) with a lot of defect states of Mn and O.

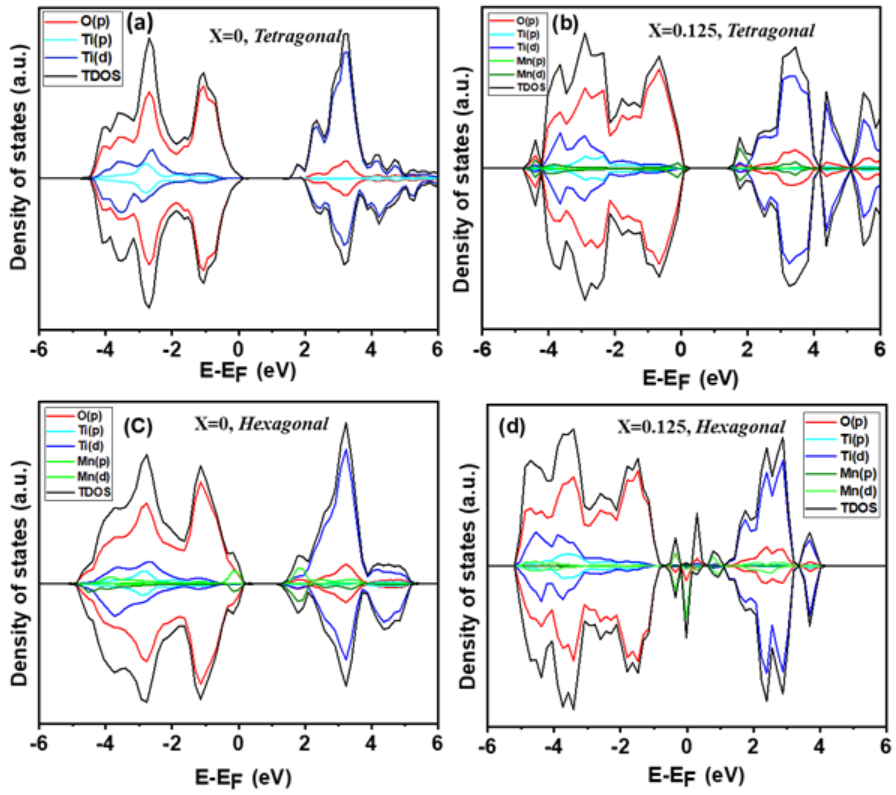

Figure 4.9: *(a) DOS plot of x=0 tetragonal, (b) DOS plot of x=0.125 Ca and Mn doped tetragonal, (c) DOS plot of x=0 hexagonal BTO, (a) DOS plot of x=0.125 Ca and Mn doped hexagonal BTO*

In the experimental study, the sample contains a mixture of these hexagonal and tetragonal BTO, with doping possible in both of these phases. Hence, doping in the tetragonal phase leads to the shifting of VB and CB and results in the reduction of the effective bandgap. However, doping in the hexagonal phase can generate Mn and O defect states such as Mn^{3+}, Mn^{4+}, $O_{v,}$ etc, and effectively reduces the band gap of the material. Both these effects are simultaneously occurring in all BCTMO1, BCTMO2, and

BCTMO3 samples, and the cumulative effect of shifting of VB and CB together with the defect states collectively reduces the effective band gap. As observed in PES, Urbach tails due to IGS are forming due to the doping of Mn and Ca in hexagonal BTO, as observed in Figure 4.9(d). The defect states are formed due to Mn(d) and O(p) states near the VBM. These defect formations are in correlation with the PES and UV-DRS measurements.

4.2.4.2 Electron Localisation Function Calculation

The local electronic cloud modification created in the tetragonal lattice due to doping and hexagonal structure polymorphism has been studied with Electron Localisation Function (ELF) calculation. Figure 4.10(a1) shows the ELF plots of the (001) plane of the Ca-doped Ba-O lattice, and Figure 4.10(a2) shows the Mn-doped Ti-O lattice in tetragonal BTO for x=0.125. It has been observed that there is a lattice contraction surrounding the dopant Ca atom. Lattice expansion is observed surrounding to dopant Mn atom. The lattice expansion created due to Mn substitution is not isotropic. Replacement of dimer Ti atoms by Mn atoms in the (-101) plane hexagonal lattice is shown in Figure 4.10(b1), and that of the (001) plane is shown in Figure 4.10(b2) for x=0.125. The replacement of centrosymmetric octahedral Ti atoms in the hexagonal lattice by Mn atoms is shown in the (-101) plane in [Figure 11 (c1)] and (001) plane [Figure 4.10(c2)].

It has been observed that Mn substitution shows lattice expansion for tetragonal octahedral substitution and hexagonal dimer (Ti2) substitution with Mn ions. This observation is in correlation with the EXAFS analysis of the Mn K edge with a shift of the Mn-O scattering path towards higher radial distance. However, Hexagonal centrosymmetric octahedral (Ti1) substitution with Mn ions indicates a lattice contraction surrounding the lattice. The confirmation of EXAFS and ELF indicates that Higher ionic radii Mn^{3+} ions are mainly substituting at the Tetragonal Ti site, and Hexagonal dimer Ti2 sites cause expansion of the lattice, and lesser

ionic radii Mn^{4+} ions are substituting the Hexagonal Ti1 sites causing the lattice contraction. Ca substitution of Ba in both lattices shows lattice contraction surrounding the dopant atoms in both tetragonal and hexagonal structure. These lattice modifications are localised changes that occur surrounding the dopant atoms.

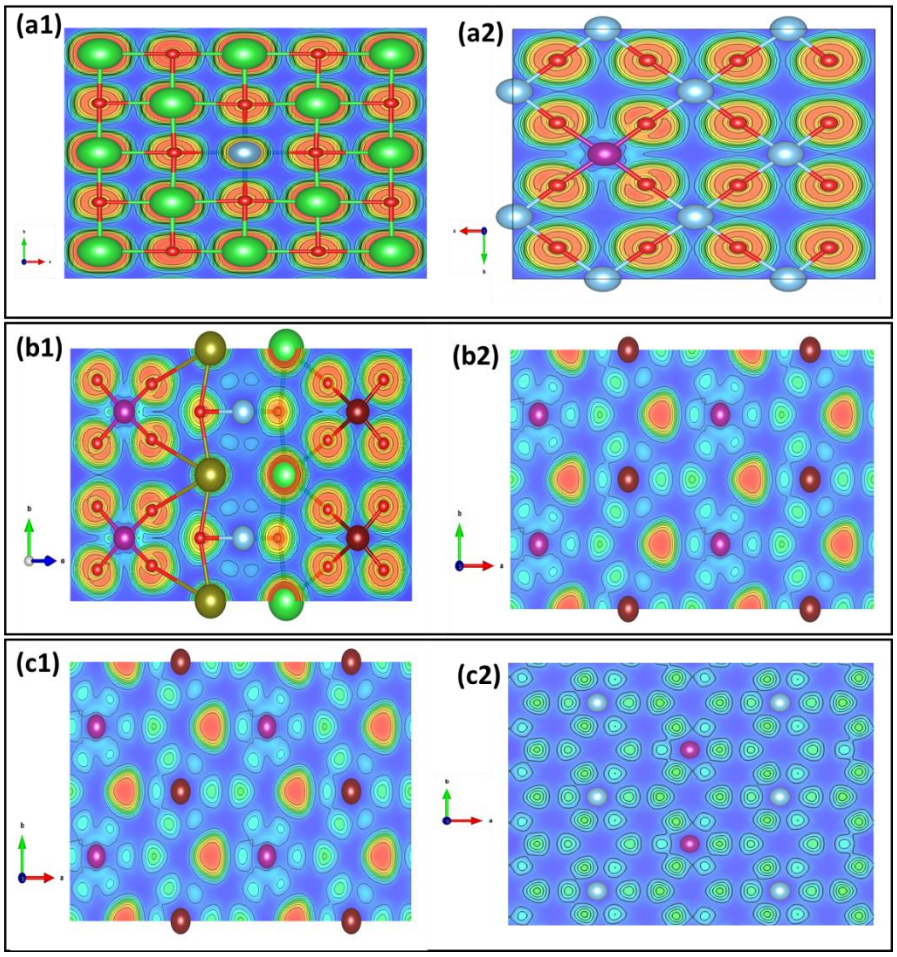

Figure 4.10: *(001) plane of tetragonal $BaTiO_3$ for x=0.125 (a1) Ca doped Ba-O lattice and (a2) Mn doped Ti-O lattice, Replacement of dimer Ti atoms by Mn atoms in (b1) (-101) plane hexagonal lattice and (b2) in (001) plane is shown in for x=0.125, The replacement of centrosymmetric octahedral Ti atoms in the hexagonal lattice by Mn atom (c1) in the (-101) plane and (c2)(001) plane for x=0.125.*

The structural modifications observed in EXAFS data and the defect states with doping observed in DRS, PES, DOS, and ELF results indicate that the defects induced a hexagonal lattice in tetragonal BTO. These

modifications can influence the dielectric properties exhibited by these materials.

4.2.5 FE-SEM Analysis

FESEM images of optimally sintered pellets show [Figure 4.11] a dense micrograin for all samples. The sintering of all the samples at 1330 °C for 4 h forms a crystalline nature with dense matter formation. All the sintered pellets have having relative density of more than 90%. Since the sintering temperature decreases with doping, the doped sample sintered more compared to the pure sample. During the sintering process, crystalline dense grains are formed by the site-to-site diffusion of ions.

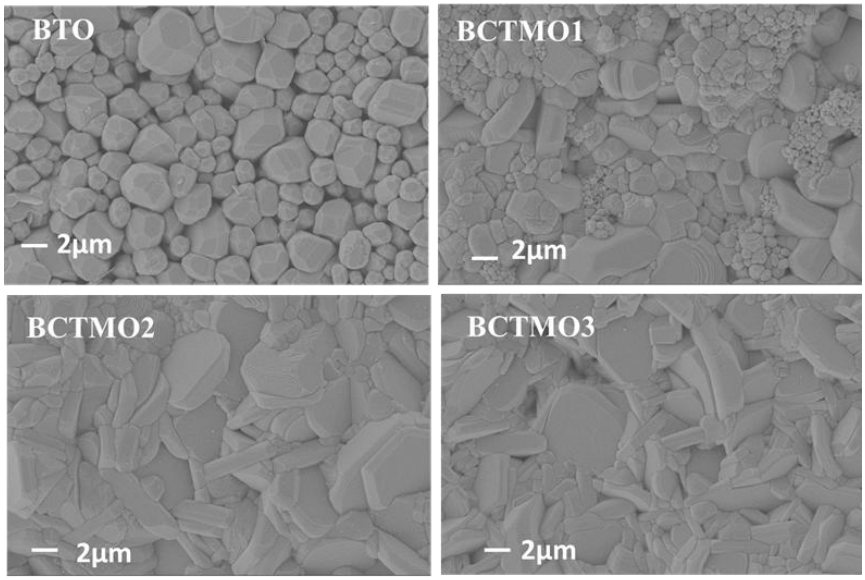

Figure 4.11: *FESEM micrographs of all samples.*

Vacancies in the lattice play a major role in materialising such an ion diffusion process. The O_V available in the lattice are important factor in the grain-growth mechanism. Pure BTO shows a cuboid morphology of grains, while BCTMO samples show two morphologies of cuboid one and needle type morphology. This lossy needle-like morphology corresponds to the 110-axial growth of the hexagonal structure along with the tetragonal

BTO cuboid grains. The fraction of non-cuboid grains increases with doping, indicating the phase transition of BTO from tetragonal to hexagonal structure.

4.2.6 Dielectric Properties

Room temperature frequency-dependent dielectric constant (ε_r) [Figure 4.12(a)] and loss factor (tanδ) [Figure 4.12(b)] was studied in detail. There is a decrease in the permittivity value with frequency has been observed, which can be related to the space charge polarisation. The dispersion of permittivity at lower frequencies is greater for BCTMO3, indicating an increase in interfacial polarisation that arises from the separation of charge carriers accumulated at the grain boundary and electrode sample interface. From the structural studies, it has been observed that with substitution, the non-centrosymmetric nature of Ti is reduced, and also the paraelectric hexagonal phase percentage increases. The cumulative effect of these factors reduces the effective polarisation within the samples that resulting in the reduction of the permittivity with doping.

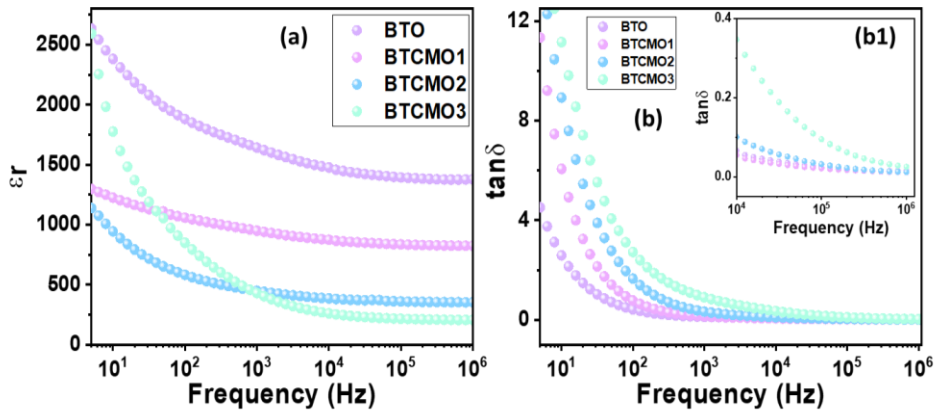

Figure 4.12: *(a)RT permittivity variation with frequency, (b) RT tanδ variation with frequency.*

Conduction losses in the materials are analysed by the measurement of tanδ, which shows the increment with doping. At lower frequencies, the value of tanδ will be high, and with frequencies, it decreases due to the space charge and interfacial contributions. Inset of Figure 4.12(b) [Figure 4.12(b1)] indicates the variation of tanδ at higher frequencies, which is

almost the same for all samples except BCTMO3, which shows the higher dielectric loss even at higher frequency. From the FESEM morphology, the lossy rod-like features increase with an increase in doping percentage, which is also obtained from the dielectric loss measurement. In addition to this, the increase in the presence of multivalent cations, as in Mn^{3+}/Mn^{4+} and Ti^{3+}/Ti^{4+}, enables more charge carriers to be freely available and leads to an increase in conductivity.

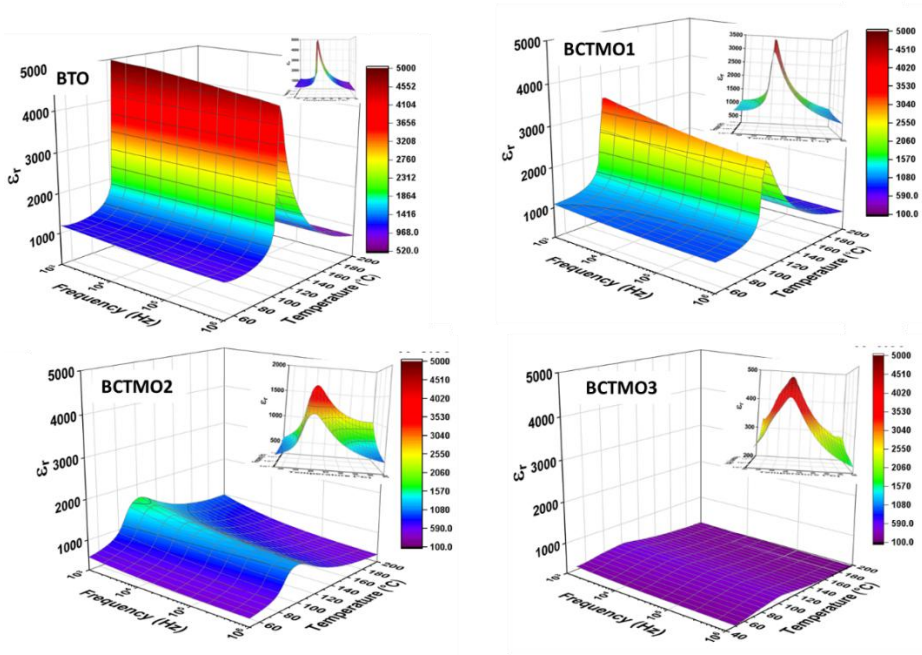

Figure 4.13: *Temperature-dependent permittivity variation showing ferroelectric to paraelectric phase transition.*

Variation of permittivity within the temperature range 50 °C to 200 °C for a frequency sweep of 10Hz to 1MHz is shown in Figure 4.13. All samples show a ferroelectric to paraelectric phase transition indicative of the presence of a non-centrosymmetric ferroelectric *P4mm* phase in these materials. The curie temperature is ~116 °C for BTO while ~104 °C for BCTMO1, ~99 °C for BCTMO2 and ~101 °C for BCTMO3. A decrease in Curie temperature is indicative of the decrease in the non-centrosymmetric behaviour as doping increases. The transition temperature value has no

variation as a function of frequency, which confirms that these compositions are not relaxor-type and exhibit classical ferroelectric type.

A sharp phase transition for BTO is modified into a broader diffuse type phase transition in doped samples. The diffuseness in the Curie temperature is due to the formation of nanopolar regions due to the Ca and Mn doping in BTO. The homogeneous nature of BTO leads to a single T_c for the ferroelectric to paraelectric phase transition. However, doping of Ca and Mn leads to variations in the polarisation in and around the doping sites, which creates polar regions with different polarisations and requires a temperature of phase transition with a distribution of $T_c \pm \delta$, which leads to the diffuse phase transition in the doped samples [Figure 4.14]. Moreover, the decrease in the non-centrosymmetry with doping leads to a decrease in the polarisation and hence requires a much lower temperature for the phase transition to occur. This implies the reduction of the T_c value with doping.

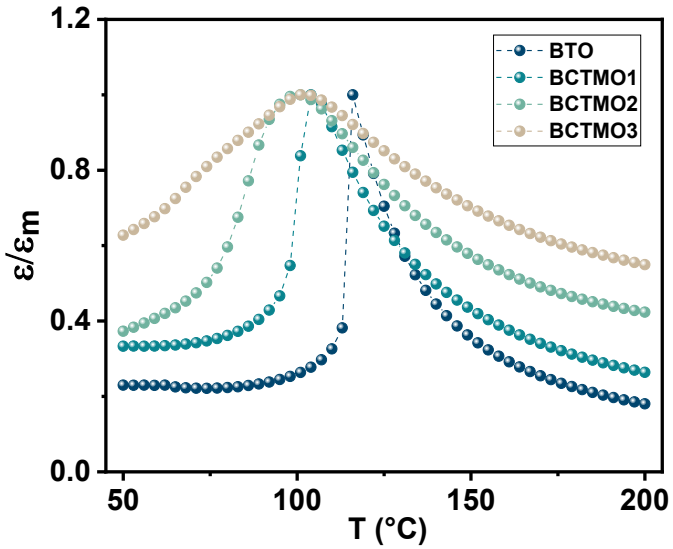

Figure 4.14: *Comparison of the phase transition from a sharp nature to a diffuse nature with doping.*

The dielectric permittivity, ϵ' of a normal ferroelectric above the Curie temperature follows the Curie–Weiss law described by [228]:

$$\epsilon' = \frac{C}{(T - T_m)} \quad for\ T > T_C$$

where T_m is the temperature at which ε has maximum value, ε_m, C is the Curie–Weiss constant, and T_C is the Curie temperature of the ferroelectric to paraelectric phase transition. For ferroelectrics, this expression is no more than a mean-field approximation applied to the fluctuating local electric fields in the crystal structure. Figure 4.15 shows the plot of inverse dielectric constant vs temperature for all samples. All the plots clearly show a deviation from the Curie-Weiss law near the phase transition temperature. For pure $BaTiO_3$, this deviation is taking place abruptly at the T_c, while for the doped samples, deviation from the Curie-Weiss law starts a few temperatures above T_c and shows a gradual diffusive nature near the T_c.

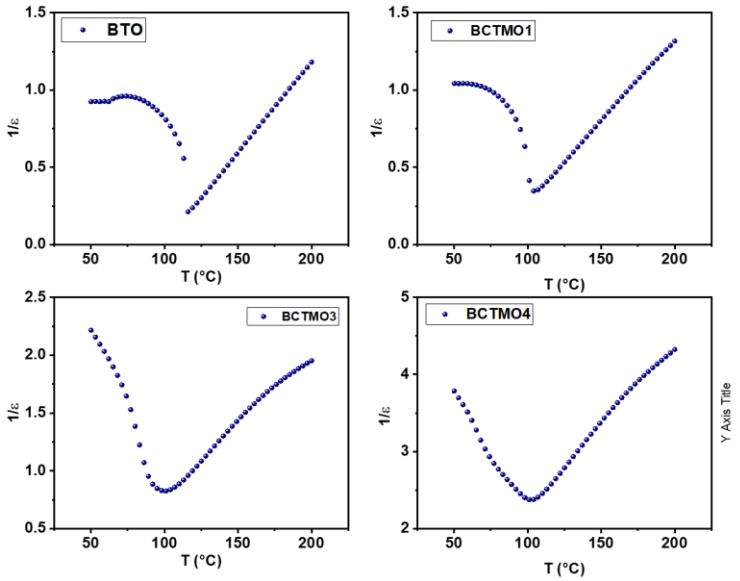

Figure 4.15: *1/ε v/s T plot of all samples.*

To better describe the dispersion degree of diffuse ferroelectric phase transition, the Curie–Weiss law has been revised and can be described by a modified Curie-Weiss law [228]:

$$\frac{1}{\varepsilon} - \frac{1}{\varepsilon_m} = \frac{(T - T_m)^\gamma}{C}$$

where ε_m is the dielectric constant (maxima) at T_m, γ ($1 \leq \gamma \leq 2$) is the degree of diffuseness, and C is the Curie-Weiss constant. For a purely ferroelectric material, $\gamma = 1$, $1 < \gamma < 2$ is a diffuse transition, and for a relaxor ferroelectric, $\gamma = 2$. Figure 4.16 shows a linear fit of ln $(1/\varepsilon - 1/\varepsilon_m)$ vs ln(T-Tm) plots for different frequencies. The slope of the plots gives the value of γ.

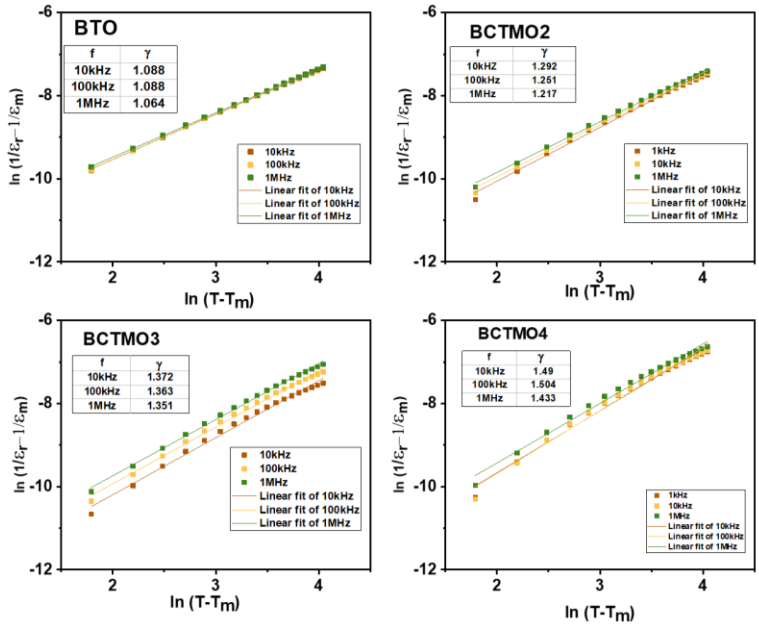

Figure 4.16: *ln $(1/\varepsilon - 1/\varepsilon_m)$ vs ln(T-Tm) plots for all samples*

All samples have a γ value in between 1 and 2 ($1 < \gamma < 2$), and there is no deviation of ε_m with frequencies, eliminating the possibility of a relaxor nature in these samples. The diffusive behaviour shown by these samples occurs because of the chemical disorder created due to the doping of Ca and Mn in BTO. Due to the random distribution of atoms, localised structural phase transition gives rise to the variation in phase transitions over a broad

range of temperatures. The value of γ increases with doping, which shows that the material is becoming disordered with doping. The broadness or diffusiveness occurs mainly due to compositional fluctuation and structural disordering in the arrangement of cations in one or more crystallographic sites of the structure. This suggests a microscopic heterogeneity in the compound with different local Curie points. The value of γ decreases with an increase in frequency. Figure 4.16 shows the Curie Weiss fitting of all the samples and calculated γ values for the frequencies 10kHz, 100kHz, and 1MHz.

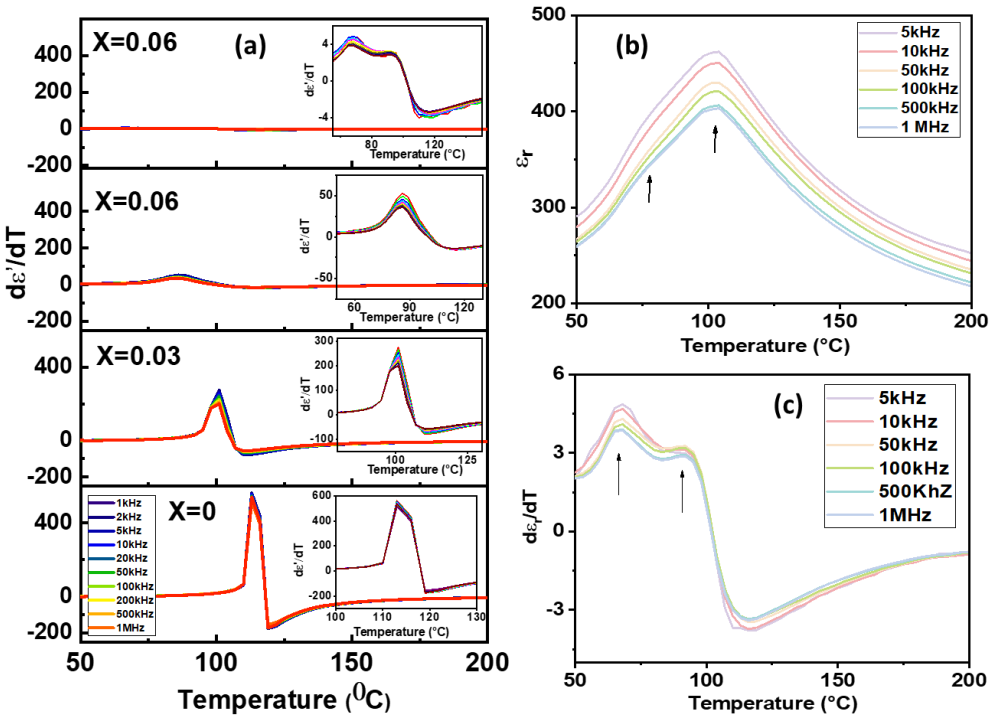

Figure 4.17: *(a) dεr/dT v/s T plots of all samples and (b)zoomed εr (c)zoomed dεr /dT plot of BCTMO3 sample*

In order to quantify the rate of change of permittivity with temperature, the derivative of ε has been taken with respect to T and plotted dε/dT with Temperature [Figure 4.17]. The derivative of ε with temperature indicates that the rate of change of ε at phase transition in the BCTMO1 sample reduced to 1/2, and for the BCTMO2 sample it reduces to 1/8, and for the BCTMO3 sample it reduces to 1/10 of the rate of change of ε for

BTO. This reduction of permittivity change at T_m is due to the decrease in the tetragonal percentage, which has a major contribution towards permittivity.

Another interesting fact is that the maximum permittivity at the phase transition, ε_m is constant for all frequencies in the BTO sample. However, ε_m value decreases with an increase in frequencies in doped samples [Figure 4.17]. The change in ε_m value with frequency is minimal in the case of BTO, whereas this change increases with doping, and the maximum deviation ε_m with frequency is shown by the BCTMO3 sample. This is due to the increase in space charge polarisation and defect dipoles contributions that reduce with frequency, and hence show a reduction in ε_m as frequency increases. This is also clearer in the derivative plot of dε'/dT, where the variation of ε shows significant dispersion in the doped samples [Inset Figure 4.17] and is maximum for the BCTMO3 sample. There is an abnormal hump like feature is observed for BCTMO3 before phase transition, as shown in Figure 4.17. For BCTMO1 and BCTMO2 samples, the hexagonal *$P6_3/mmc$* phase is a minor phase with the major tetragonal *P4mm* phase. However, for BCTMO3, hexagonal *$P6_3/mmc$* is the major phase, and there is a minor contribution of the tetragonal ferroelectric phase leads to the high diffuseness shown in modified Curie Weiss plots with frequency (Figure 4.16), a very less ε_m value (1/5 of the ε_m of the BTO sample) as shown in Figure 4.13, a Low value of $d\varepsilon_m/dT$ (~1/10 of the BTO sample) as in Figure 4.17, and high dependence of ε_m with frequency.

When analysing the phase transition temperature of BCTMO3, one can observe a shoulder-like feature just before T_c corresponding to another transition-like feature. This same observation is more visible in the $d\varepsilon_r/dT$ graph [Figure 4.17]. Here, another transition is occurring just before the T_c around ~65-70 °C. The diffused phase transition peaks that occur in these doped BTO are due to the disorder created due to doping, but the secondary peak observed in the BCTMO3 sample before the phase transition is

abnormal, and its origin has multiple reasons. Chemical inhomogeneity and strain effects linked to fine-grain size in chemically modified $BaTiO_3$ give rise to diffuse Curie peaks. One of the reasons may be the core-shell structure formed by a strong ferroelectric core surrounded by a weak ferroelectric shell, formed due to the doping. These two structures have different T→C phase transition temperatures. The weak ferroelectric shell T→C transition occurs at a lower temperature than the strong core ferroelectric transition. This kind of shoulder feature also can be corresponds to the presence of polar nanoregions (PNRs) in the paraelectric phase. This leads to polarisation fluctuations or partial ordering near the transition temperature. It can also be linked to the evolution of ferroelectric domain wall dynamics or intermediate phases, or relaxor-type behaviour induced by dopants. Polar nanoregions (PNRs) or local polarisation clusters exist as precursors to the full ferroelectric-paraelectric transition is reflecting complex local structural and dynamic phenomena preceding the tetragonal to cubic transition.

4.3 Conclusion

$Ba_{(1-x)}Ca_{(x)}Ti_{(1-y)}Mn_{(y)}O_3$ (x=y=0, 0.03, 0.06, 0.09) samples have been investigated for structural polymorphism, band gap tuning, and dielectric anomalies. TEM image of the doped samples indicates the existence of a hexagonal and tetragonal lattice, which are interlinked with each other. XANES analysis confirms the presence of Ti^{3+}, Ti^{4+}, $Mn^{3+,}$ and Mn^{4+} oxidation states and the structural transformation to a centrosymmetric structure. EXAFS analysis indicates the local structural modification near the Mn and Ti sites with doping. UV-DRS shows a reduction in optical band gap from 3.2 to 2.05 eV and a highest Urbach energy for the x=0.03 sample. The Valence band edge in PES is observed to be shifted towards E_F due to the presence of in-gap states. Density of states calculations reveal a shift of VB and CB with doping in the tetragonal lattice and the formation of defect states with doping in the hexagonal lattice. Electron localisation function

calculations indicate the lattice contraction with Ca doping in both tetragonal and hexagonal lattices; however, a lattice expansion is observed with Mn doping in both lattices. Dielectric studies show a decrease in the permittivity and an increase in tanδ corresponding to the decrease in tetragonality and increase of the hexagonal phase. A sharp tetragonal to cubic phase transition in BTO transforms to diffuse behaviour with Ca and Mn doping. For x=0.09, the major hexagonal phase sample shows an abnormal shoulder feature before phase transition that may correspond to the ordering of the defect dipoles in the hexagonal phase.

CHAPTER 5

Effect of oxygen vacancies and cationic valence state on multiferroicity and magnetodielectric coupling in La and Fe modified $BaTiO_3$

$Ba_{(1-x)}La_{(x)}Ti_{(1-y)}Fe_{(y)}O_3$ (x=y=0, 0.01, 0.03, 0.06)

This chapter details the structural modification of La/Fe modified $BaTiO_3$ with XRD and Raman analysis. XPS explores the oxidation state variation with doping. EPR measurement shows the unpaired electrons which can form charge defect complexes. Ferroelectric and magnetic studies detail the multiferroicity. Magnetocapacitance measurement provides indirect evidence for the Magnetoelectric coupling.

5.1 Introduction

Magnetoelectric (ME) ordering in multiferroics is technologically applicable in a variety of fields like ultra-low power and highly dense logic-memory, micro(nano) electronic, sensors, energy harvesting, actuators, spintronics, miniature antennas, terahertz emitters, electric-field controlled FM resonance, four-state memories, microwave filters, feRaM, MRAM, and Spintronics [229], [230], [231], [232]. Hence, it is one of the intriguing current research domains. However, generally ME effects are mild and materials have low Neel temperature. Most of the multiferroic materials exhibit ferroelectric (FE) and/or magnetic phase transitions at cryogenic temperatures [233], [234], [235]. Hence, practical devices are difficult to fabricate. There are a few single-phase multiferroic oxides, e.g., $LuMnO_3$ [236]. The large difference between the FE and magnetic ordering temperatures often suggests small Magnetoelectric coupling (MEC) [237], [238]. Realising strong ME coupling above RT in single-phase materials and understanding its origin is vitally important for practical applications. The magnetism can be introduced in an FE material due to the incorporation of magnetic ions, surface defects, cation vacancies, O_vs, lattice strain, and magnetic clusters [239], [240], [241]. The magneto dielectric effect is the variation of dielectric parameters, such as capacitance, with the application of a magnetic field. This phenomenon is an indirect method to investigate MEC.

ME coupling has been achieved in the well-known FE $BaTiO_3$ (BTO) by inducing magnetism in various ways [242]. Many strategies have been proposed to improve the electrical and magnetic properties of BTO, including the substitution of A, B, and combined A and B sites in BTO for metal ions [243] and formation of solid solutions with other stable ABO_3-type materials [244], [245]. There are reports in which the multiferroicity in BTO is due to the ferromagnetism (FM) induced by the surface states due to O_v, and the FE has a core contribution[246], [247], [248], [249]. Apart from O_v, Ti or Ba cationic vacancies also lead to FM in BTO [250].

There were efforts towards the realisation of multiferroicity in BTO by doping transition-metal ions (Mn, Fe, or Co) at Ti sites [242], [251]. Among these, the simultaneous coexistence of room-temperature (RT) FM and FE in Fe-doped BTO attracted a lot of attention. However, Fe doping leads to the transformation of the FE tetragonal BTO (t-BTO) into its hexagonal polymorph (h-BTO), which is paraelectric and ferromagnetic at RT [170]. FM was due to the 90^0 super-exchange interaction between two Fe ions [252]. The FM got enhanced with increasing O_v content [253], [254]. However, O_V also reduced the insulating FE properties of BTO [255].

Thus, it is important to find other possible ways to enhance the ferromagnetic properties without compromising the ferroelectric properties. Hence, a phase transformation from the FE tetragonal phase to the paraelectric hexagonal Fe-doped BTO is not desired. The understanding of the origin of FE and magnetic state is critical for tuning of RT multiferroic properties. Pal *et al.* [142] tried to retrieve the tetragonality of Fe-doped hexagonal $BaTiO_3$ by doping elements such as Bi, Sr, and Ca in the A site. They have successfully retrieved the tetragonal FE phase from the hexagonal paraelectric phase, completely with Bi doping [144]. Hence, doping transition elements at the B site to induce magnetism and with other elements in the A site to preserve the tetragonal FE is another method to introduce multiferroicity and ME coupling in BTO.

There are reports on the possibility of RT multiferrocity in $LaFeO_3$ (LFO) [256]. It has a high Neel temperature ~467 °C and a colossal dielectric constant [257]. $BaTiO_3$- $BiFeO_3$ solid solution has been studied for the ME application, and it shows high ferroelectricity and piezoelectricity, but the antiferromagnetic nature leads to weak FM. The magnetodielectric (MD) effect was studied in $BaTiO_3$-$LaMnO_3$. However, an increase in MD was observed, but that may be due to the increase in the magnetoresistance of the $(LaBa)MnO_3$ phase, rather than ME coupling [258].

LFO has an orthorhombic distorted perovskite structure, with antiferromagnetic characteristics. In the case of La and Fe doping in the Ba and Ti sites of BTO, the comparable ionic radii of La^{3+} and Ba^{2+} ions and those of Ti^{4+}/Ti^{3+} and Fe^{3+}/Fe^{2+} make the easy diffusion of La and Fe into the BTO lattice. The Fe introduction to the lattice can lead to several situations, including the creation of O_V, diverse valence states of cations, and even Ba-loss. Such effects can have an effect on magnetism as well as FE properties and thereby on ME coupling. A ferroelectric and magnetic study on the BTO-LFO solid solution was reported by Sahoo *et al.* [128], but a detailed correlation is missing. Another relevant study was performed by Qi *et al.* [244]on LFO-doped $BaTiO_3$ –$BiFeO_3$ solid solutions. They were able to achieve improved FM and ME properties. The novelty of this work lies in finding structural correlation with lattice disorder, O_V, and diverse valence states of the participating cations for the multiferroicity and magnetodielectric coupling in modified $BaTiO_3$, with La at the A-site and Fe at the B-site substitution. The series $Ba_{(1-x)}La_{(x)}Ti_{(1-y)}Fe_{(y)}O_3$ (x=y=0, 0.01, 0.03, 0.06) are named as BTO, BLFT1, BLFT2, and BLFT3.

5.2 Results and discussions

5.2.1 X Ray Diffraction Analysis

The XRD data of the BTO, BLFT1 samples revealed the presence of a pure tetragonal *P4mm* space group [Figure 5.1(a)]. However, for BLFT2 and BLFT3, a coexistence of tetragonal *P4mm* and cubic *Pm-3m* space groups has been obtained. The (110)/(101) Bragg reflection of BLFT samples shifted to higher angles when compared to pure BTO samples [Figure 5.1(b)], indicating a decrease in the d-spacing with the incorporation of La and Fe in the BTO lattice.

The radius of Ba^{2+}(XII) ion is ~ 1.75 Å, while that of La^{3+} is 1.5 Å. On the other hand, the radius of the Ti^{4+} (VI) is ~0.745 Å, whereas the Fe^{3+}(VI) is ~ 0.69 Å (low spin) and 0.785 Å (high spin). The possibilities

of having other valence states are also there. The radius of Ti^{3+} (VI) is ~0.81 Å, while Fe^{2+}(VI) can exist in ~ 0.75 Å (low spin) and 0.92 Å (high spin). The size of La^{3+} ions is much smaller than that of Ba^{2+} ions, and Ti^{4+} ions are of comparable size to Fe^{3+} ions. Hence, the incorporation of La and Fe ion in place of Ba and Ti sites lead to the compression of the BTO lattice for the doped compositions. The decrease in d spacing might be a consequence of such a change in the radii of these elements.

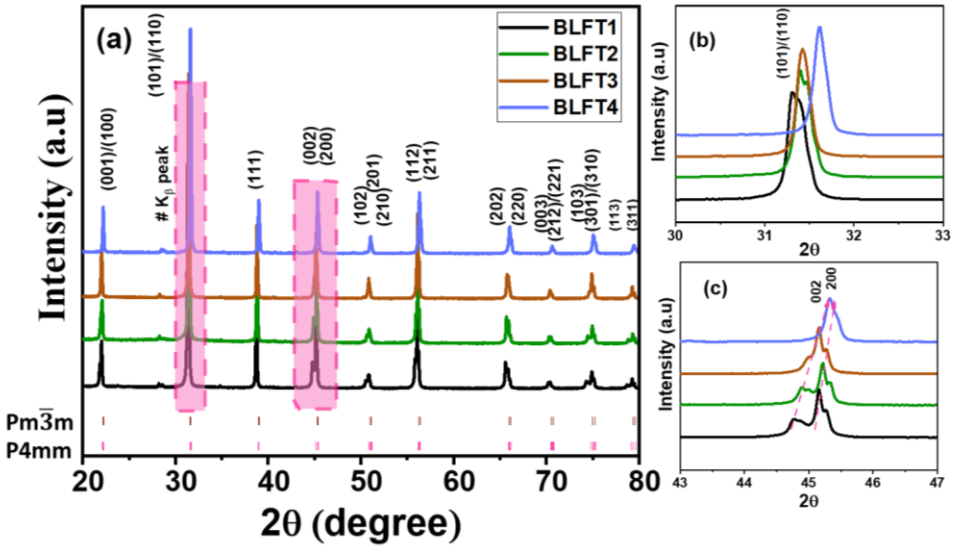

Figure 5.1: *(a) XRD pattern of all the prepared samples, (b) Shift of 101/110 peak, (c) Splitting of 002/200 peak.*

Rietveld refinement was carried out for all the compositions using the Full-Prof suite software [259] [Figure 5.2]. A Pseudo-Voigt peak profile was assumed to best fit the peak profiles. All the compositions show a good fit. The phase identification of these samples was obtained using such techniques. In pure BTO, the (002) and (200) reflections are split at 45°, confirming a tetragonal phase ($a = b \neq c$) [Figure 5.1(c)]. For a cubic structure ($a = b = c$), which removes this splitting. The c/a ratio is a measure of the tetragonality. The c/a ratio decreases almost linearly with the incorporation of La and Fe. The cubic phase appears for BLFT2 and BLFT3 when a merging of these two peaks was observed. However, just by looking at the peaks, the absence of a tetragonal phase cannot be confirmed. Hence, a structural refinement was extremely important for this study.

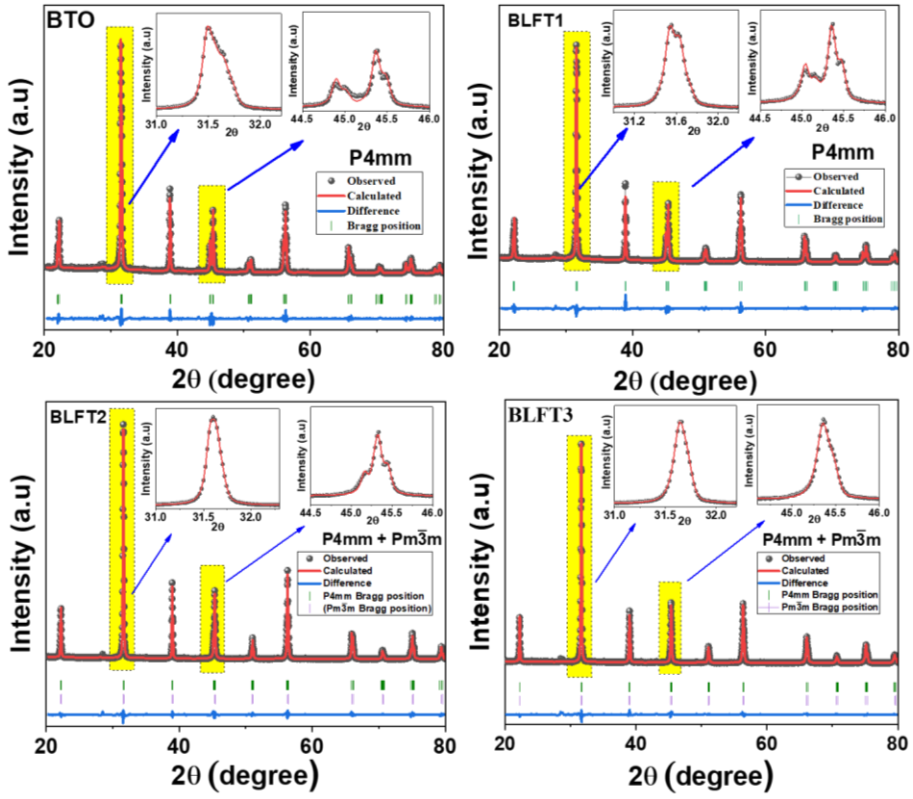

Figure 5.2: *Rietveld refinement plot of samples. The inset shows the zoomed image of the 101/110 peak and 002/200 mode.*

The Rietveld refinement ensured the presence of a mixed phase of tetragonal and cubic nature in the BLFT2 and BLFT3 samples. Approximately 89.39% of the tetragonal phase was observed in BLFT2, while approximately 72.80% was observed in BLFT3. It is interesting to notice that the c/a ratio reduced from 1.0099 in BTO to 1.0023 in BLFT3. However, the changes in the c-axis are extremely significant from 4.0357 Å in BTO to 4.0059 Å in BLFT3. On the other hand, the lattice parameter of the cubic phase changes from 3.996 Å in BLFT2 to 3.9968 Å in BLFT3. Note that the a and b axes are invariant with substitution in the tetragonal phase and are comparable to the lattice parameters of the cubic phase. Like the c/a ratio, the cell volume of the tetragonal phase reduces with substitution from BTO (64.446 Å3) to BLFT3 (63.958 Å3) [Figure 5.4(a) [inset]]. The above changes hint at very regular substitution of Ba and Ti by La and Fe, ensuring a homogeneous distribution of Ba, La, Ti, and Fe atoms

in the solid solution. The substitution of lesser radii La^{3+} (1.5 A) and Fe^{3+} (0.69 A) in place of Ba^{2+} (1.75 A) and Ti^{4+}(0.745 Å) leads to a decrease in the unit cell volume.

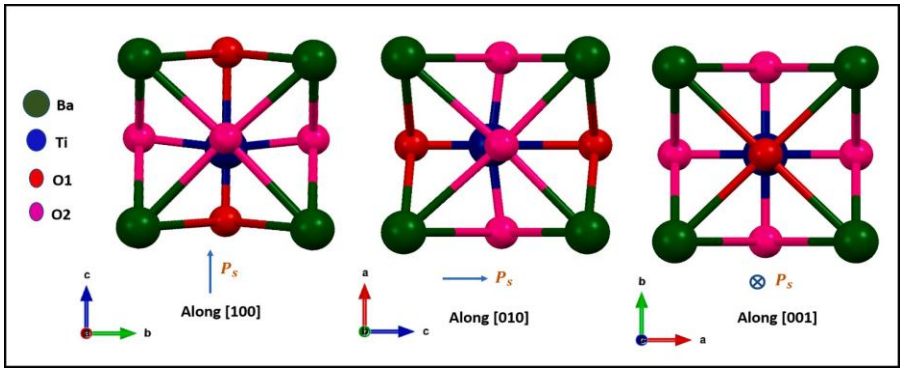

***Figure 5.3**: The schematic of the off-centering of Ti cation and O anion.*

The bond lengths and bond angles were calculated by using Mercury software from the CIF file obtained after the Rietveld refinement. In the BTO structure, the central TiO_6 octahedra have the Ti ion off-center. This off-centering is the source of the formation of dipoles due to the relative displacement along the (001) direction of the cations and anions in the structure. This provides a macroscopic polarisation P_s along the (001) direction, resulting in FE [Figure 5.3].

In the cubic phase of an ABO_3 perovskite, one expects no polarisation due to the centrosymmetric nature of the structure, which ensures that all the O-atoms are face-centered and the B-ion is body-centered. The BO_6 octahedra become the primary object of investigation when it comes to discussing FE or polarisation. It has been discussed that the prime reason for the deviation from the centro-symmetric nature is obtained from a strong A-O bond strength, which thereby shifts the O- ions from their face-centered positions, thereby creating different A-O bond lengths. As a result of this, the most affected is the BO_6 octahedra, which in turn gets distorted and thereby generates a spontaneous polarisation due to the non-centrosymmetric structural properties. In the cubic phase, all A-O and B-O bonds are equal.

To discuss the changes in the asymmetry of the structure, the unit

cell atoms have been named as O_p for the planar oxygens, O_a for the apical oxygens, A1, A2, A3, and A4 for the set of A atoms at the upper surface of the unit cell, while A1′, A2′, A3′, A4′ for the lower set [Figure 5.5(3a)]. An unaltered O_a-B-O_a bond angle of 180° is proof of non-deviation of the O_a and B ions from the central axis of the unit cell. Similarly, the O_a and O_a' atoms also remain at the center of the a-b plane. The position of O_a is at the center of the face, which is confirmed by a right-angled A1-O_a-A2 bond angle in the a-b plane. Also, there is only one type of A1-O_a-A2 bond angle. However, O_p is not located at the center of the a-c and b-c faces of the BTO unit cell. This off-centering is the origin of distortion and is due to the strength of the A-O bonds.

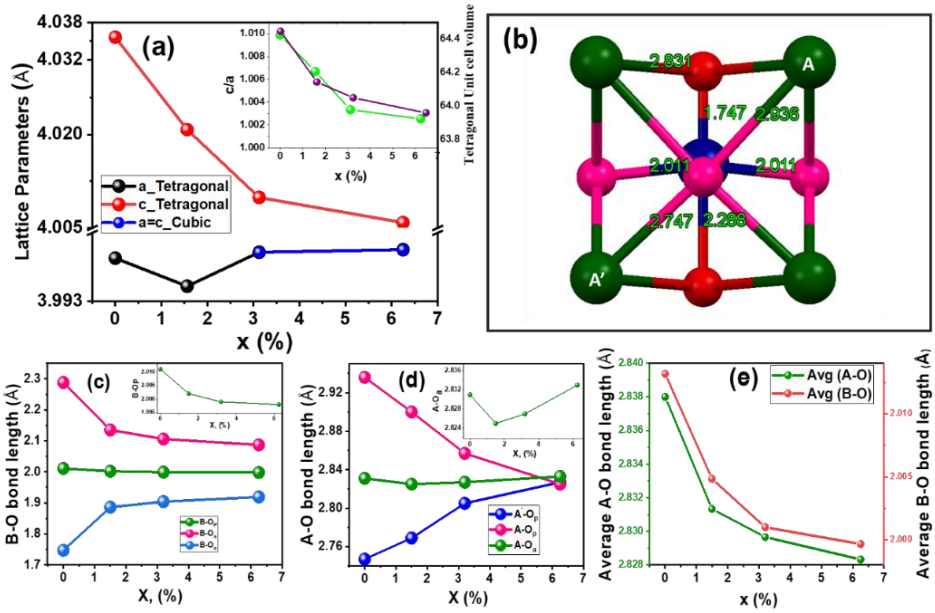

Figure 5.4: *(a) Variation of a,b, and c lattice parameters for tetragonal and cubic phase (inset) variation of c/a and unit cell volume with composition (b) Schematic of the tetragonal P4mm structure. (c) Variation of avg. A-O and B-O bond length (d). Variation of three B-O bond lengths (e) Variation of three A-O bond lengths.*

The stronger the bond, the more the off-centering. Hence, all the bond angles change. The bond angles, which can be instrumental to assess the distortion, are A1-O_a-A3, A1-O_p-B, A1-Oa-B, O_p-B-O_p, A1-O_p-A2, A1′-O_p-A2′, and A1-O_p-A2′ [Figure 5.5(3b-3c)].

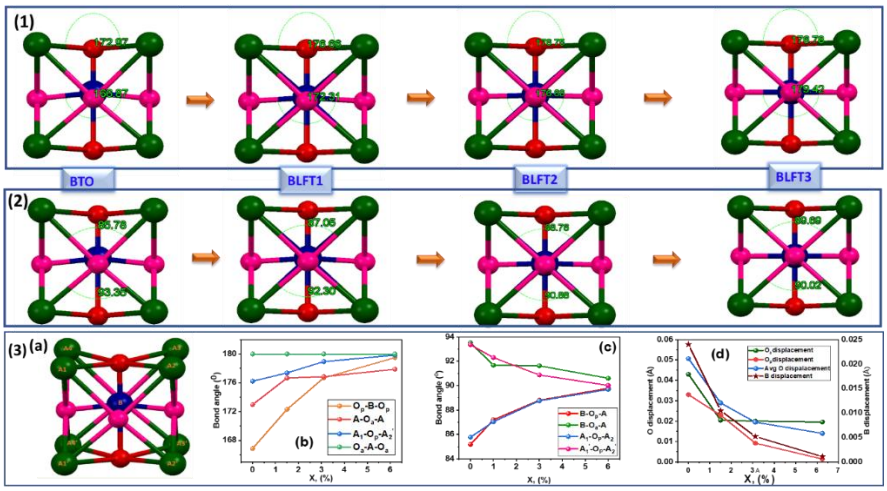

Figure 5.5: *(1) Schematic of the variation of 180^0 O_p-B-O_p and A_1-O_a-A_3 bond angles. (2) Schematic of the variation of two types of 90^0 bond angle A_1-O_p-A_2 and A1'-Op-A2' for all samples. (3a) Schematic of the BTO to represent the bond angles. (3b) O_p-B-O_p and A_1-O_a-A_3, A1-Op-A2', Oa-B-Oa bond angle with composition. (3c) Plot of A_1-O_p-A_2, A_1'-O_p-A_2', B-Oa-A, B-Op-A bond angles with composition. (3d) Plot of displacement of B ion and avg. A ion with composition.*

The B and the O_a atoms shift along the c axis, towards a centrosymmetric position, which involves changes in the B-O bond lengths along the c axis. This shift is confirmed by the increase of A1-O_a-A3 from ~173° in BTO to 176.8° in BLFT3. This implies that O_a ion is yet to reach the centrosymmetric point and is above the A-A plane. Similarly, the O_p-B-O_p bond angle changes from ~166.9° in BTO to 179.4° in BLFT3 [Figure 5.5(1)], meaning that the B-ion is somewhat away from the centrosymmetric point. On the other hand, the A1-O_p-A2′ bond angle increases from 176.2° in BTO to 179.84° in BLFT3, which is very close to the centrosymmetric point. This implies that the off-centrosymmetric was more pronounced for the O_a ion than the B ion and further than the O_p ion, even in BLFT3, which provides the remnant polarisation in the highly doped samples too. The symptoms of an asymmetric nature to a symmetric nature were also evident for other angles too, e.g., A1-O_p-A2 bond angles increase from 85.78° for BTO to 89.69° for BLFT3, whereas decrease in

the case of A1′-O_p-A2′ bond angle from 93.35° in BTO to 90.02° in BLFT3 in ac/bc plane [Figure 5.5 (3b)]. The difference between these two angles decreases and gradually shifts towards 90°, which is a centrosymmetric position.

The changes in the octahedral distortion angles are analysed by changes in A1-O_p-B, A1-O_a-B angles towards 90°. A1- O_p-B angle increases from 85.19° to 89.8°, and A1-O_a-B angle decreases from 93.51° to 91.6°. The variation of each bond angle is plotted along with the composition, and the schematic representation of the bond angles is also shown in Figure 5.5.

The changes in the structure modify the BO_6 octahedra. The octahedra consists of six B-O bonds. There are four B-O_p bonds along with one B-O_a (smaller) and one B-O_a′ (larger) bond. The above changes in structure reduce the four B-O_p bonds nominally from 2.012 Å in BTO to 1.998 Å in BLFT3. This change is nominal as compared to the changes of B-O_a and B-O_a′, whereas stronger B-O_a increases from 1.747 Å in BTO to 1.919 Å in BLFT3, the weaker B-O_a′ decreases from 2.288 Å in BTO to 2.087 Å in BLFT3 [Figure 5.4(c)]. Hence, the B-O_p bond seems to be less affected by substitution, while both B-O_a bonds are highly affected. On the other hand, at the A-site, twelve A-O bonds are available, out of which there are four A-O_p, four A′-O_p bonds, and four A-O_a bonds. The structural changes increase the stronger A′-O_p bonds from 2.747 Å in BTO to 2.827 Å in BLFT3 and decrease the weaker A′-O_p bonds from 2.936 Å in BTO to 2.825 Å in BLFT3. These changes are considerable to the changes in A-O_a bonds, which can be observed to be nominal as 2.8312 Å in BTO to 2.825 Å in BLFT1 and thereafter to 2.833 Å in BLFT3 [Figure 5.4(d)].

Table 5.1: Variation of unit cell parameters, phase fraction and unit cell volume with doping.								
Composition	**Lattice Parameters**							
	Tetragonal					**Cubic**		
	Phase fraction	a=b	c	c/a	volume	Phase fraction	a=b=c	volume
BTO	100	3.99615(4)	4.03564(7)	1.0099	64.446	0		
BLFT1	100	3.99410(4)	4.02079(6)	1.0067	64.143	0		
BLFT2	89.39	3.99658(4)	4.00990(8)	1.0033	64.0487	10.61	3.99658(4)	63.836
BLFT3	72.80	3.99578(3)	4.00587(16)	1.0023	63.9588	27.20	3.99578(3)	63.7977

Hence, the off-centrosymmetric location of different cations and anions in the structure is dependent on the different bond strengths between the different A-O and B-O bonds and ultimately offers a competing structural change, which technically reduces the structural distortion but lets the distortion be present even for the BLFT3 sample.

The displacement of B and O_a, O_p, and O_{avg} from the centrosymmetric position is plotted in Figure 5.5(3d). With substitution, this displacement decreases gradually and comes towards a centrosymmetric cubic structure. This shift of B, O_p, O_a towards the centrosymmetric cubic arrangement with La and Fe substitution has resulted in the reduction in tetragonality and the incorporation of the cubic phase for x = 0.03 and x = 0.06. The variation of lattice parameters, unit cell volume, and c/a ratio, and the tetragonal and cubic phase fraction are mentioned in Table 5.1. In BTO, BLFT1, the Ti ion is in an off-center position. This preserves the tetragonality. However, the reduction of distortion in the BO_6 octahedra reduces the tetragonality. For BLFT2 and BLFT3, Ti off-centering reduces and moves towards the centrosymmetric position, thereby creating a mixture of a cubic phase and an existing tetragonal phase. Note that the lattice parameters a and b in the tetragonal phase increase suddenly for BLFT2 and BLFT3 due to the presence of this mixed phase.

5.2.2 Raman spectroscopy analysis

In the tetragonal phase of the BTO, the factor group theoretical calculations result in Γ = 3A1 + 4E+B1 zone-center Γ-point optical phonon modes, which further show a splitting of polar modes in LO and TO branches in the ferroelectric tetragonal phase [260]. To get more insight into the local symmetry, Raman spectroscopy, which is sensitive to the same, has been carried out. The obtained spectra are consistent with the earlier reports [261].

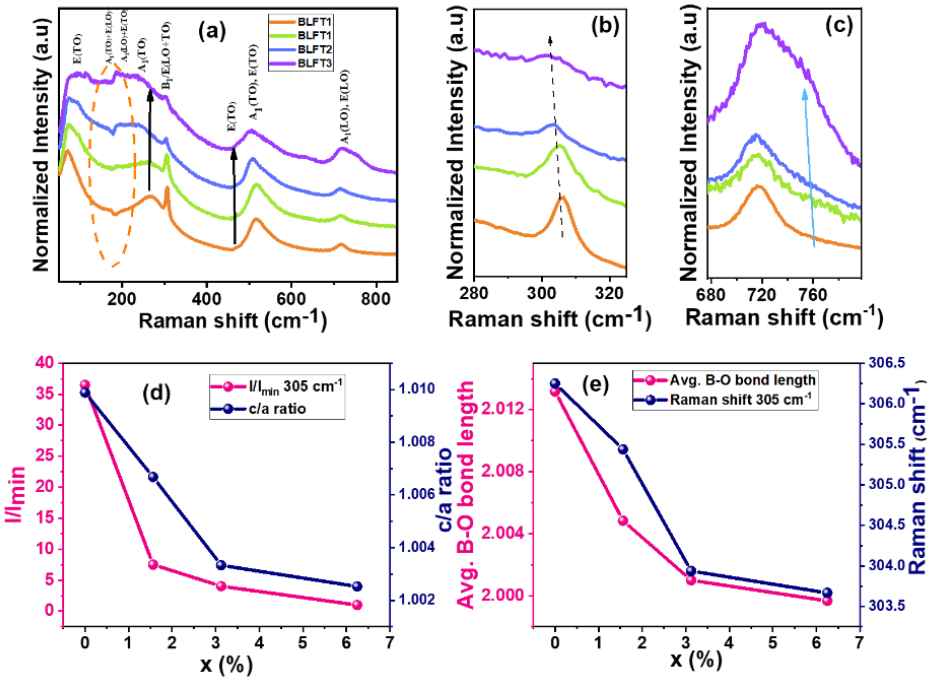

Figure 5.6: *(a) Raman spectrum of all samples, (b) Zoomed image of the characteristic tetragonal phonon mode at 305 cm^{-1}, (c) Zoomed image of the disorder phonon mode at 770 cm^{-1}, (d) Correlation of c/a ratio with intensity variation of 305 cm^{-1} with composition, (e) Correlation of the variation of B-O bond length and Raman shift of 305 cm^{-1} with composition.*

The Raman spectra of the ferroelectric tetragonal phase of $BaTiO_3$ can be observed to comprise the following modes:

(a) E(TO) mode ~40cm^{-1}

(b) A1(TO), E(LO), E(TO), and A1(LO) around ~180 cm^{-1}

(c) Broad A1(TO) mode at ~280 cm^{-1}

(d) Sharp B1, E(TO+ LO) mode at ~305 cm^{-1}

(e) Asymmetric A1, E(TO) broad bands at ~520 cm^{-1} and

(f) Highest frequency A1(LO), E(LO) mode at ~720 cm^{-1}

The Raman spectra of all the samples reveal [Figure 5.7 (a)] four distinct vibrational modes of BTO around ~180 cm^{-1}. These are the A1(TO), E(LO), E(TO), and A1(LO) modes [262]. These modes are generally due to A-O vibrations and are difficult to identify separately. Especially in the case of powder samples, the modes appear to be clubbed into a pair of two modes: [A1(TO), E(LO)] and [E(TO), A1(LO)]. These modes can only be resolved in the case of a single crystal by using polarised Raman spectroscopy [263]. These modes are extremely weak in these materials, and the spectra reveal a change in intensity of the peaks with composition. However, these changes are nominal enough to make a strong comment on these modes. Room temperature tetragonal phase is characterised by sharp bands corresponding to different phonons, E(TO +LO)+B1 at 305 cm^{-1} and an asymmetric broader A1(TO) mode at 280 cm^{-1} and 520 cm^{-1}, and an A1(LO) mode at 720 cm^{-1} [264]. These three modes at 280 cm^{-1}, 520 cm-1, 720 cm^{-1} can also be traced in the cubic paraelectric phase. However, the modes are much broader and more symmetrical than the ferroelectric phase. They are often attributed to second-order effects. However, it is better to correlate to the Ti displacements in the BO_6 octahedra [265], [266]. The A1(TO) phonons at 520 cm^{-1} correspond to the O–B–O symmetric stretching vibration of the BO_6 octahedral cluster, whereas the A1(LO) mode at 720 cm^{-1} is associated with the distortion of BO_6 octahedra [260]. Both of these peaks show red shifting with the La and Fe substitution.

A strong E(TO +LO)+B1 mode ~305 cm^{-1} is observed for all the BLFT samples. This originates from the asymmetry of the TiO_6 octahedra and is a signature of the tetragonal phase [260]. Hence, this mode strongly depends on the B-O bond vibrations. As this mode prevails even in the highest-doped BLFT3 sample, one may claim a tetragonal phase even when

the c/a ratio is 1.002. Hence, tetragonality at room temperature is confirmed in all the samples. However, with increasing La and Fe content, it weakens, redshifts, and broadens. The reduction in the peak intensity is due to the reduction in tetragonality of the BLFT samples as La and Fe substitution increases. This agrees with the decreasing c/a ratio [Figure 5.7(d)]. A redshift [Figure 5.7(e)] of this mode can be explained based on the larger atomic mass of Fe (55.845 a.m.u.) as compared to that of Ti (47.867 a.m.u.), as f $2\pi\sqrt{(k/m)}$, where `k′ is related to bond strength and m is reduced mass. The Fe is mostly in a Fe^{3+} or a Fe^{2+} state and is replacing a Ti^{4+}ion. Note that the electrostatic attraction between lesser charges will be less, thereby reducing the bond strength. Thereby, the bond strength of a Fe^{2+}/Fe^{3+}-O^{2-} bond is likely to be weaker than a Ti^{4+}-O^{2-} bond. From both aspects, there is a possibility of a red shift. Hence, the redshift is yet another proof of a replacement of the Ti atoms by Fe atoms.

The gradual decrease of intensity and wavenumber of tetragonal characteristic features at 280 cm^{-1}, 305 cm^{-1}, 520 cm^{-1}, and 720 $cm^{-1,}$ and the variation of structural parameters towards centrosymmetric position is an excellent proof of a partial but incomplete tetragonal to cubic transformation from a structure-correlated phonon study.

Near substitutional defects with a chemical substitution with heavier atoms, some localised vibrational modes (LVM) may be observed near 770 cm^{-1} in $BaTiO_3$ [267]. These are modes that can appear due to relaxation of Raman selection rules from defect-induced disorder. In these samples, lattice distortions happen due to the La and Fe ions' substitution for the BTO lattice. These distortions will disturb the phonon vibrations and lead to some disorder phonon modes [Figure 5.7 (b)]. The intensity of these phonon modes is observed weakly in BLTF1 and becomes most prominent in the BLTF3 sample. However, in the BLTF1 and BLTF2, the effect is mostly not visible. However, when the data was fitted with Pseudo-Voigt peaks, the hidden mode in these samples was exposed. The intensity variation of these disorder phonon modes can be correlated with the changes in the

structural parameters with doping [268].

5.2.3 FE-SEM Analysis

FESEM images of optimally sintered BLFT pellets show [Figure 5.8] dense micrograins for all samples. The average grain size is calculated using by Image **J** software. The sintering of all the samples at 1350^0 °C for 4 h forms a crystalline nature with dense matter formation. The relative density of all the samples is calculated using the formula;

$$\text{Relative density} = \frac{\text{Calculated density fo the pellets}}{\text{Theoretical density}}$$

where the calculated density of the pellets with radius r and thickness t is measured by the formula: mass of the pellet / $\pi r^2 t$. The theoretical density is obtained from the CIF files.

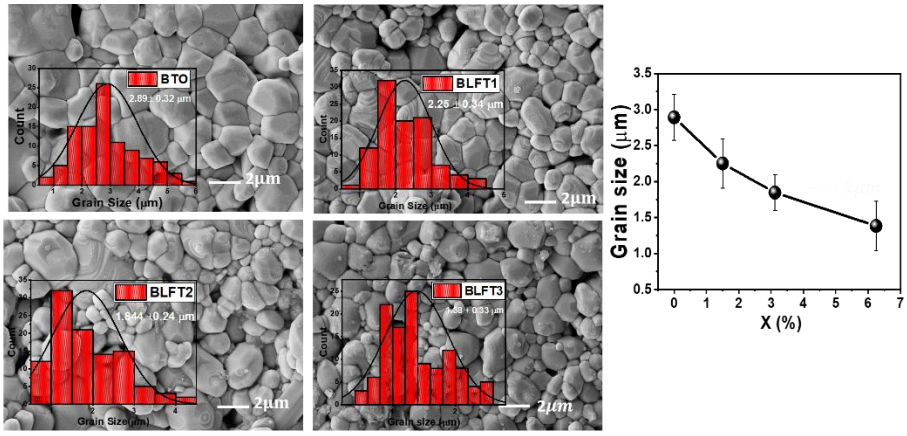

Figure 5.7: *Surface morphology of sintered pellets for (a)BTO, (b)BLFT1, (c)BLFT2, (d)BLFT3, (e) BLFT4 compositions, and the inset shows the grain size distribution curves for the respective compositions. (f) Variation of grain size with composition.*

All the sintered pellets have having relative density of more than 90%. During the sintering process, crystalline dense grains are formed by the site-to-site diffusion of ions. Vacancies in the lattice play a major role in materialising such an ion diffusion process. The O_V available in the lattice is an important factor in the grain-growth mechanism. The average

grain size of the pellets is found to decrease with an increase in x. The increase in the O_V can lead to the inhibition of ion diffusion and result in the reduction in the grain growth and decrease in the grain size.

5.2.4 XPS Analysis

Dopant La 3d core level spectrum

The La XPS spectra were extremely weak for the BLFT1 samples due to the extremely low percentage of La present in the sample. However, for BLTF3 and BLTF4, formidable signals were observed. La^{3+} XPS core level peaks are observed at ~836 eV and 853 eV with an energy separation of ~17 eV [269]. The La spectra of BLFT samples revealed $3d_{5/2}$ and $3d_{3/2}$ features with an energy separation of ~17 eV, confirming La^{3+} ions. Both the features were deconvoluted into two main peaks [Figure 5.9] due to the core contribution and due to the 'shakeup satellites' [270]. The formidable signals in the BLFT4 sample exhibit peaks of La-$3d_{5/2}$ at ~ 834.39 eV (core level), 838.28 eV (shakeup satellites), while the La-$3d_{3/2}$ was fitted with peaks at ~851.27 eV (core level), 855.07 eV (shakeup satellites).

When passing through the valence band, the photoelectron and valence band electrons will interact and transfer a particular amount of energy from the kinetic energy of the photoelectron to the valence band electron. The transition of valence state electrons from the valence band to the 4f state will happen by using this absorbed energy [271]. The energy difference due to this interaction is observed as satellite peaks in XPS. The binding energy peaks of La-$3d_{5/2}$ and La-$3d_{3/2}$ indicate a core hole with the vacant 4f orbital. Another broad feature is observed between the La-$3d_{5/2}$ and La-$3d_{3/2}$ features. A plasmon loss peak has been reported at ~841.57 eV [272]. Plasmon peaks are formed due to the collective oscillation of electrons by absorbing a specific amount of energy through the interaction with the photoelectron [273].

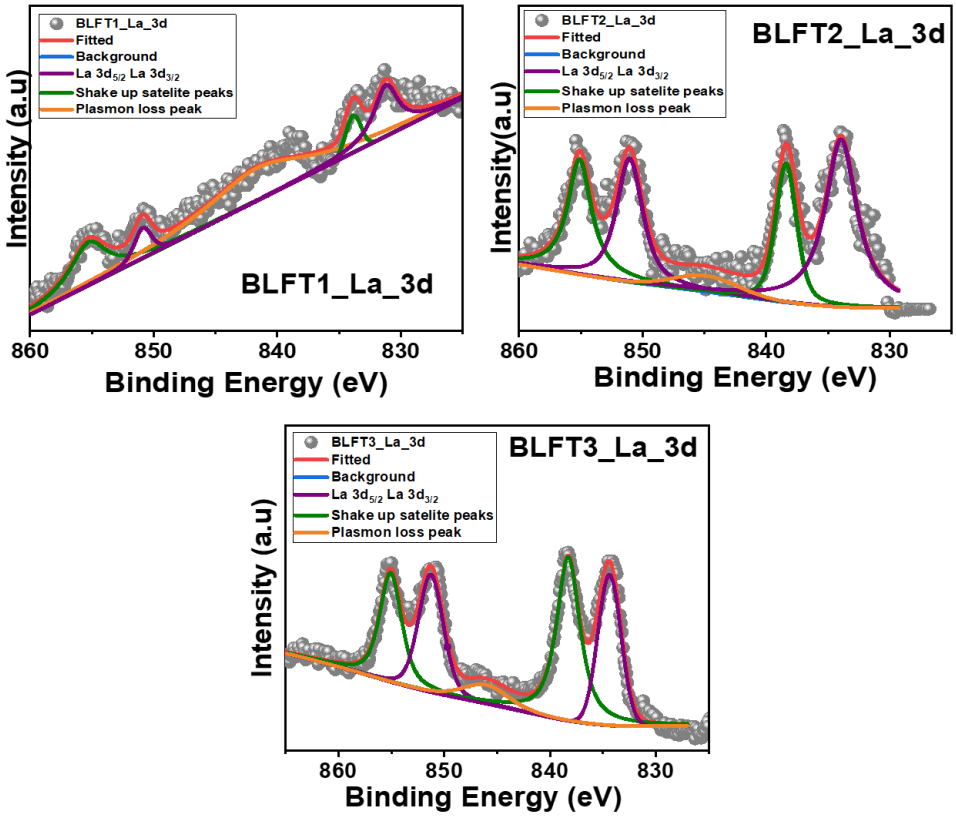

Figure 5.8: *La 3d core level XPS spectra of all samples.*

Dopant Fe 2p spectra

The Fe XPS spectra were formidable for all the samples, but were noisy. The Fe spectra revealed $2p_{3/2}$ and $2p_{1/2}$ broad features. Each feature comprises contributions from Fe^{3+} and Fe^{2+} ions with a spin-orbit coupling energy of ~13 eV [269] [Figure 5.10]. Hence, each feature was deconvoluted into three peaks, one belonging to the Fe^{3+} main peak, while another belonged to the Fe^{2+} main peak. The third peak corresponds to the satellite peak [274]. In $LaFeO_3$, the Fe^{2+} $2p_{3/2}$ XPS peaks are centered at 708.133 eV and 721.28 eV, and, Fe^{3+} -$2p_{3/2}$ and $2p_{1/2}$ peaks are centered at 710.216 eV and 723.243 eV, respectively [275]. The area fraction of Fe^{2+} to Fe^{3+} does not have a significant change. The fraction of Fe^{2+} content can be calculated from the ratio $f_{Fe2+}= [Fe^{2+}]/([Fe^{3+}]+[Fe^{2+}])$, where $[Fe^{2+}]$ and $[Fe^{3+}]$ are the concentrations of Fe^{2+} and Fe^{3+}. These values are estimated

relatively from the area under the curve of the corresponding peak. The f_{Fe2+} was found to increase with increasing substitution, from 0.495 (BLFT1), to 0.501 (BLFT2), 0.523 (BLFT3), and 0.555 (BLFT4). The satellite peak contribution in each sample decreases from BLFT1 to BLFT3.

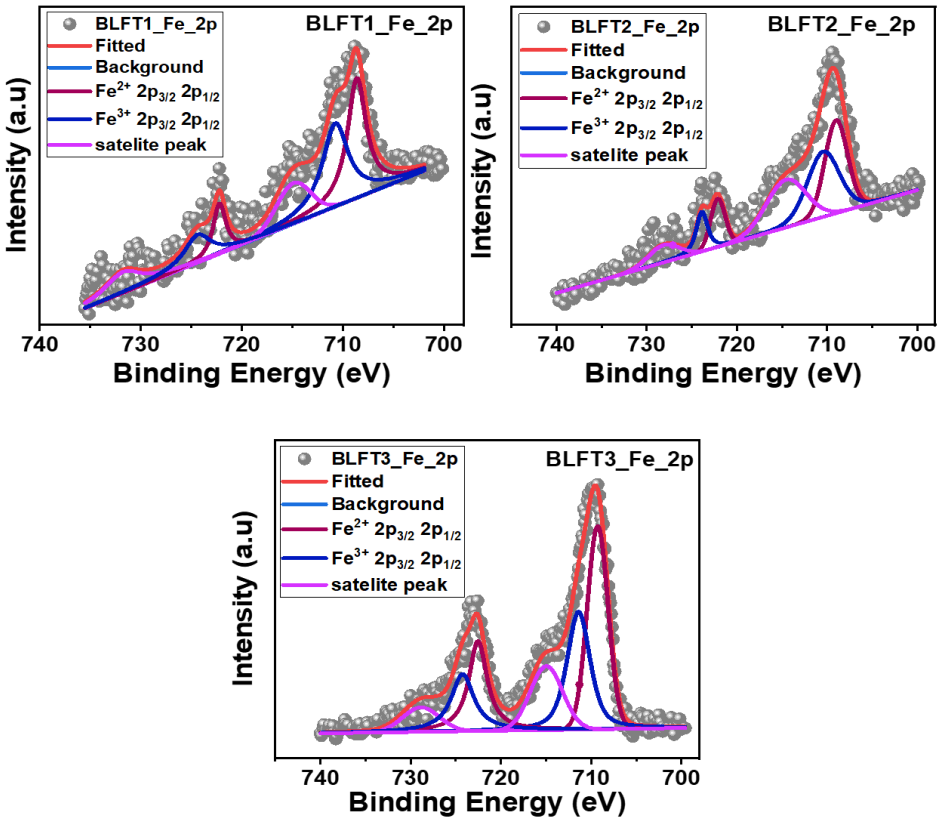

Figure 5.9: *Fe 2p core level XPS spectra of all samples*

Host Ti 2p core level spectra

For pure $BaTiO_3$, the Ti XPS spectra [Figure 5.11]is a strong feature and reveals a doublet $Ti2p_{3/2}$ (binding energy 458.06 eV) and $Ti\text{-}2p_{1/2}$ (binding energy 463.83 eV) arising from spin splitting energy separation of 5.7 eV [276]. These peaks are consistent with the Ti^{4+} oxidation state [276]. There is a shoulder peak at binding energy 459.67 eV belonging to the $Ti\text{-}2p_{1/2}$ feature that corresponds to the Ti^{3+} oxidation state [277]. The area ratio of this shoulder peak can be calculated from $f_{Ti\text{-}shoulder}$= [Ti-

shoulder]/([Ti-shoulder] +[Ti^{4+}]), where [Ti-shoulder] and [Ti^{4+}] are the areas of the corresponding features estimated relatively from the area under the curve of the corresponding peak. The $f_{Ti\text{-}shoulder}$ was found to increase with increasing substitution, from 0.065 (BTO), 0.128 (BLFT1) and 0.169 (BLFT2), and 0.219 (BLFT3). Since this feature is correlated with the Ti^{3+} oxidation state, the valence state of the average B site reduces from a 4+ state to a lesser state with substitution.

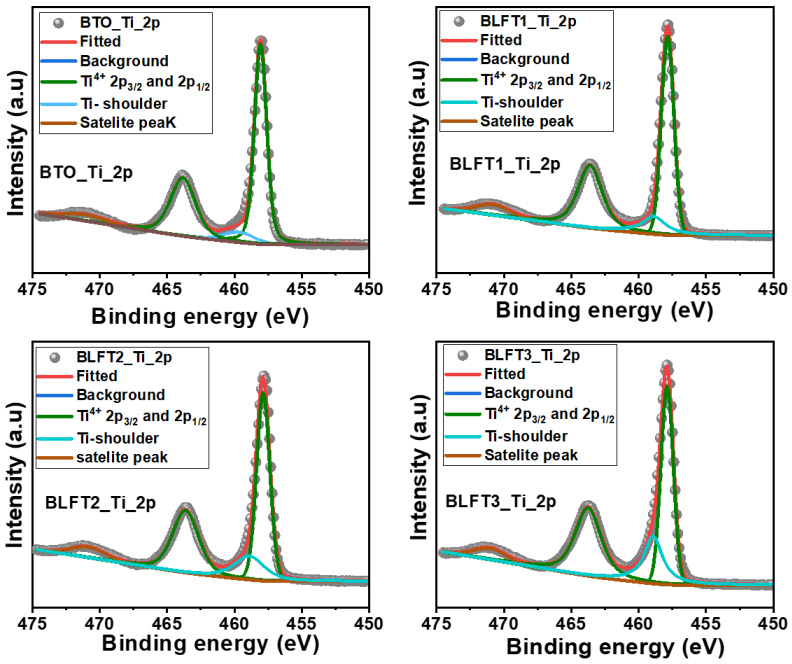

Figure 5.10: *Ti 2p core level XPS spectra of all samples.*

A comparison of the B.E. of the Ti^{4+}-2p position shows a decrease in B.E. with substitution. The reduction is more pronounced from BTO to BLFT1, but thereafter decreases gradually in BLFT2 and further in BLFT3. This indicates changes in the Ti-O bond strength with increasing Fe substitution. Note that with the advent of Fe into the lattice, the Ti B.E. weakens considerably. This has serious implications, hinting at the chemical environment of the ion. A reduction in the B.E. can imply a weakened bond between Ti and neighboring atoms, i.e., O anions. Hence, this implies a weakened Ti-O bond. The interaction between the Ti and Fe atoms and an

overlapping of their 3d orbitals is indicated by the shift in the peak.

Host Ba 3d core level spectra

For pure $BaTiO_3$, the Ba XPS spectra are a strong feature and reveal a doublet Ba-$3d_{5/2}$ (binding energy 778.36 eV) and Ba-$3d_{3/2}$ (binding energy 793.67 eV) arising from spin splitting [272] [Figure 5.12]. The spin-orbit coupling energy of $3d_{5/2}$ and $3d_{3/2}$ is around 15.31 eV. Each spin-orbit splitting peak is deconvoluted into two peaks, one main peak and one shoulder peak. The presence of these two peaks indicates the presence of two chemical states for the Ba atom [278]. The main peak corresponds to the Ba^{2+} state in the perovskite BTO [279].

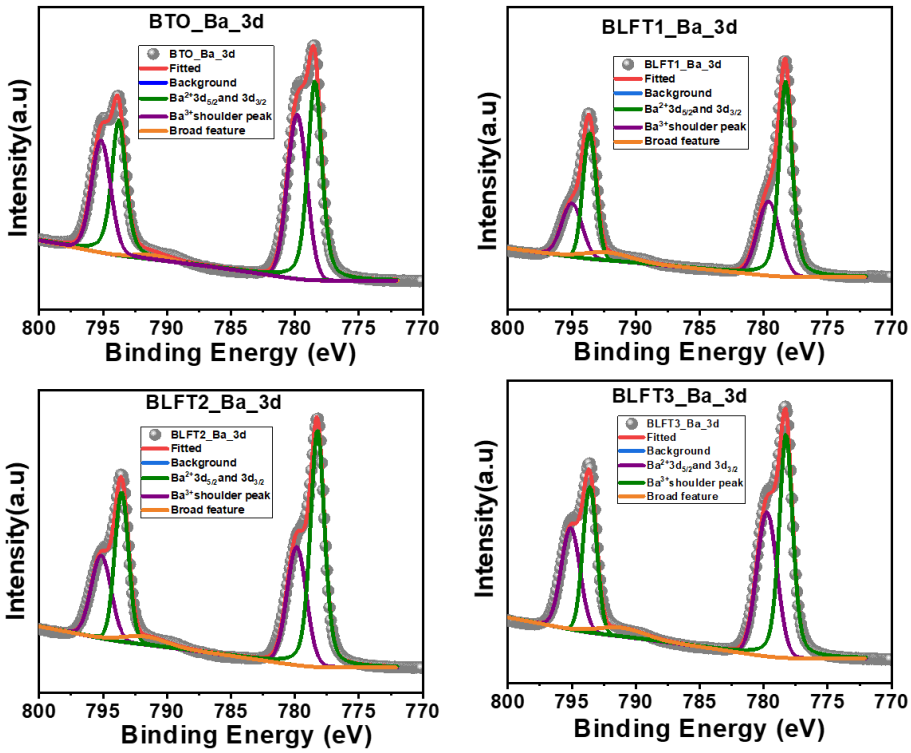

Figure 5.11: *Ba 3d core level XPS spectra of all samples*

The pair of shoulder peaks observed at higher energies of the main peak is frequently reported for the BTO samples. Some possible reasons for the occurrence of these peaks, as reported in many reports, can be attributed to the Ba vacancy [279], [280], surface $BaCO_3$ contamination [153], [281]

near-surface phase related to a relaxation of residual strain[154]. Surface grinding produces a preferred orientation of their domains with their c axis perpendicular to the surface in polycrystalline BTO. S. Kumar *et al.* [154] claimed the main peak contribution at lower B.E. is related to the domains with their `a′ axes aligned along the surface normal, and the shoulder peak at higher B.E. is related to the domains with their `c′ axis aligned along the surface normal. In our Ca/Mn modified $BaTiO_3$, after etching, this shoulder peak is completely removed, indicating merely a surface contribution of this peak.

Extra hump-like features are observed around ~791 eV, which are not mentioned clearly in the literature. One report claims the possibility of the Ba loss attributed to this feature [282]. Baniecki *et al.* [283] studied the angle-resolved X-ray photoelectron spectroscopy in which this loss feature is highest at 90° and lowest at 0° take-off angle. The weak presence of this peak at 0° takeoff angle indicates that these features do not correspond to surface impurities, and it is related to the lattice features. Miot *et al.* [152] have studied the ageing of BTO ceramics with XPS studies. In their work, they have shown a reduction of this feature with ageing (from immediately after sintering, one month, and six months). In the same work, they have done etching studies, and they have found that with etching, the presence of this broad feature increases. These studies prove that these features are not related to surface carbonates or impurities but are most probably related to bulk perovskite BTO. Possible reasons for the occurrence of this peak in all these samples are probably attributed to loss features in the BTO lattice: mostly Ba loss. Since with etching, the prominence observed for this loss feature in the previous reports supports the possibility of Ba loss in all these samples. Further studies are needed to get a clear picture of the origin of this broad feature observed in all these samples.

O1s core level spectra

The literature is rich with defining different types of oxygen species

related to the different structure correlated properties that are exhibited by oxide materials. In BTO, the O1s XPS spectra can be deconvoluted to three peaks corresponding to the B.E. of lattice oxygen (O_I) at ~529.5 eV, second feature (O_{II}) claimed as O_v and OH^- at ~ 531 eV, and adsorbed oxygen (O_{III}) at ~ 532.4 eV, respectively [276]. In BTO, these peaks are observed at 529.25 eV, 530.80 eV, and 532.28 eV. O_{III} corresponds to the adsorbed chemical species present on the BTO surface [276], which is present only on the surface, and depending on the external parameters, its dynamical entity varies. Hence, only O_I and O_{II} will contribute to the lattice dynamics. From our etching studies of Ca/Mn modified $BaTiO_3$, we have confirmed a lattice origin of the O_{II} peak, which can be correlated with O_v.

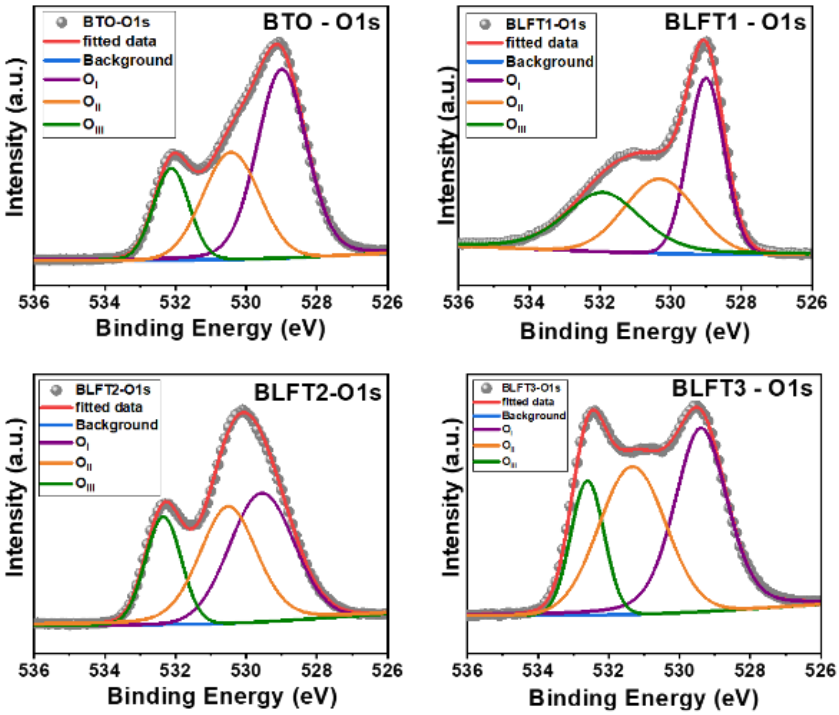

***Figure 5.12**: O 1s core level XPS spectra of all samples*

A numerical estimation of the amount of O_I and O_{II} was performed by deconvoluting the O1s XPS spectrum [Figure 5.13]. The fraction of O_{II} content can be calculated from the ratio $f_{OII}= [O_{II}]/([O_I]+[O_{II}])$. Hence, $[O_{II}]$ and $[O_I]$ can be considered as the concentrations of O_V and O_L. The fraction f_{Ov} value for BTO was ~0.29, which gradually increased with increasing

substitution, to 0.493 (BLFT1), 0.513 (BLFT2), 0.525 (BLFT3).

In search of the reasons for O_V, one can observe two potent sources of generation. The existence of Ti^{3+}, i.e., a lower valence state ion as compared to the majority expected Ti^{4+} ions in the lattice, demands anionic loss. Also, the presence of Ba_{loss} broad peaks can be correlated with anionic loss, i.e., O_V. Hence, the finite values of the fraction f_{Ti3+} in BTO may be the prime reason for O_V in the sample. However, it is not so certain whether it is due to the loss of Ba and the conversion of the Ti^{4+} to a Ti^{3+} that one expects O_V, or it is the generation of O_V due to the annealing process at high temperatures that leads to Ba loss and simultaneous production of Ti^{4+} to Ti^{3+} conversion. However, one important observation is the fact that these three parameters, along with the Fe^{3+} to Fe^{2+} conversion, are all coexistent. Hence, the XPS studies lay the foundation for the structural studies and enable us to understand the underlying parameters that control structure and thereby the functionalities of the material.

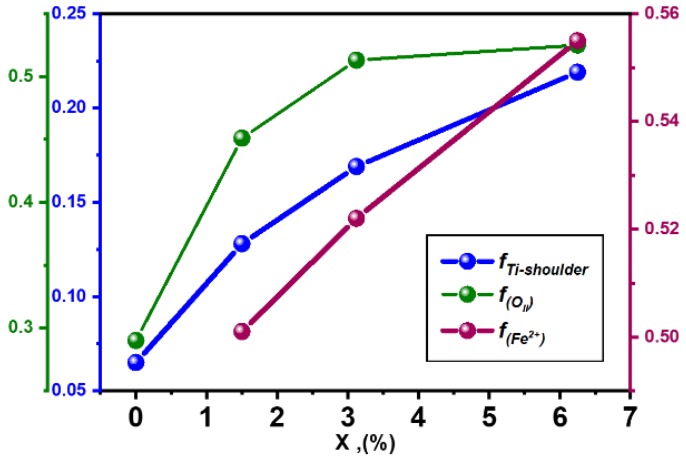

***Figure 5.12**: Variation of area fraction of $f_{Ti\text{- }shoulder}$, f_{Fe2+}, f_{OII} with substitution.*

5.2.5 Electron Spin Resonance spectroscopy

ESR is particularly useful for detecting the unpaired electrons. O_v represents donor-type defects that can bind one or two electrons, giving rise to singly charged, F^+ centers (vacancy traps 1 electron → EPR active) or to neutral O_vs, F^0 centers (vacancy traps 2 electrons → EPR silent). Previous

studies of such defects in BTO have shown that, in the case of the F^+ center, a trapped electron is located at $Ti^{3+}e_g$ $d_{3z^2-r^2}$ orbital forming a Ti^{3+}-O_v paramagnetic complex. In undoped BTO, there is no aliovalent dopant to demand charge compensation, so that O_vs may remain in the F^+ or F^0 [284]. Lande g factor can be calculated from the formula; $g = \frac{h\nu}{\nu_B B}$, where, ν is the frequency of the EM signal, ν_B Bohr magneton, B is the magnetic field, h is Planck's constant. The value of the g factor allows for the prediction of the Zeeman splitting and aids in characterising the electron configurations and local environments in materials.

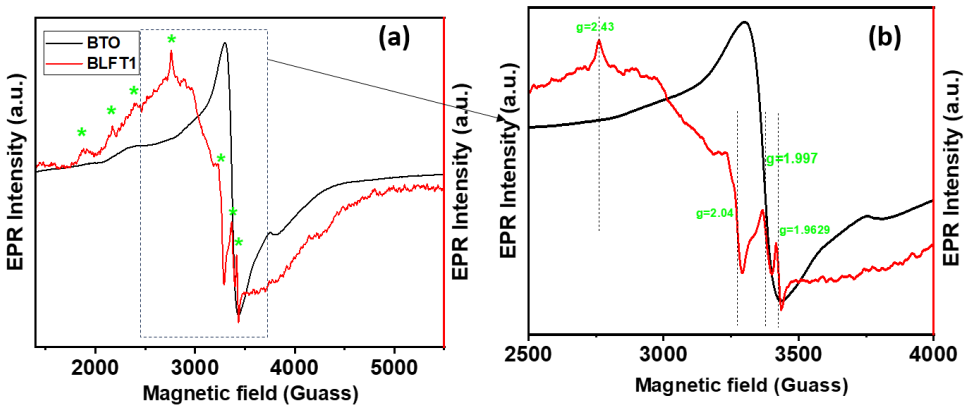

Figure 5.15: *EPR signals of (a) BTO, (b)BLFT1, the derivative of the EPR signal (c) BTO, (d) BLFT1.*

Figure 5.15 shows the EPR scan of BTO and BLFT1 at RT. A sharp and steep signal at g = 1.997 is obtained for the pure BTO as evidence for the F^+ center, corresponding to Ti^{3+} $-O_v$ complex formed due to an electron trapped in O_v [285]. The shape and symmetry of the line are more consistent with an electron trapped in an O_v, rather than a Ti^{3+} signal, which often exhibits more anisotropy and a g value of around 1.94-1.98. A single peak like this usually corresponds to a system with one unpaired electron and no hyperfine coupling. Several EPR measurements assigned their signals to a paramagnetic center, Ti^{3+} $-O_v^{2+}$, composed of O_v^{2+} with the nearest Ti^{4+} ion trapping one electron. Considering its total charge, this paramagnetic center corresponds to O_v^+ [286].

In BLFT, ESR spectra contain a broad signal with multiple splittings. Characteristic spectra of Fe^{3+} in octahedral environment, Fe^{3+}-O_v, Ti^{3+}-O_v, and Ti^{3+}-La^{3+} were observed with g factors g=2.05 (Fe^{3+}), g=1.997 (Ti^{3+}-O_v), and 1.9629 (Ti^{3+}-La^{3+}) [287]. There are a lot of additional peaks (shown as green asterisks in Figure 5.15) that can be correlated to the distortions and vacancy interactions, suggesting interaction with nearby magnetic nuclei. The signal at ~g=2.04 can correspond to Fe^{3+} in the distorted octahedral environment. Fe doping introduces new paramagnetic centres and can influence conductivity. The peak intensity relates to the concentration of paramagnetic Fe^{3+} centres. Strong intensity means more Fe ions contributing to the EPR signal, or a higher concentration of O_vs that stabilise Fe^{3+} centres [288]. Absence of resolved hyperfine splitting suggests strong broadening or weak nuclear interactions. The O_vs modulate the local environment and are responsible for the broadening and peak characteristics. EPR reveals Fe^{3+}– O_v complexes. This indicates that O_vs act as charge compensators and are stabilised by Fe doping. The EPR signal near $g \approx 1.963$ was assigned to the complex center Ti^{3+}–La^{3+}, where La^{3+} is substituted for Ba^{2+}. The appearance of Ti^{3+}–La^{3+} centers would be a necessity of charge compensation for the rare-earth ion. BTO shows negligible EPR activity, indicating low intrinsic O_v concentration. BLFT1 exhibits strong EPR signals, confirming the presence of Fe^{3+} ions and O_v, which likely form Fe–O_v defect complexes. Thus, La and Fe doping increase O_v concentration, which is directly evidenced by the appearance of paramagnetic signals in the EPR spectrum [289].

5.2.6 Ferroelectric properties

The RT electric field-dependent polarisation was measured and shown as the P-E hysteresis loop [Figure 5.14 (a)-(e)]. The test frequency of the P-E loop will depend on the polarisation and coercive field. Two factors are limiting the measurement frequency for the hysteresis loop. The first is the existence of a finite relaxation time for the domain switching process. If the electric field changes too fast, the domain switching process

cannot be completed, which leads to partial polarisation reversal, and the hysteresis loop becomes distorted. The second is the heat generation during the hysteresis measurement at high frequencies, which will cause a change of polarisation and the coercive field. In our case, the measurement was done with a frequency of 20 Hz, which gives proper FE P-E hysteresis loops [290].

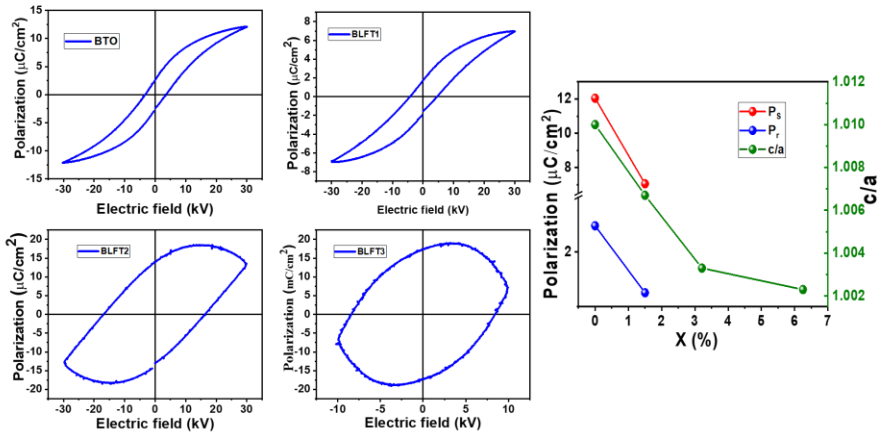

Figure 5.14: *P-E loop of the samples at 30 kV and Variation of P_r and P_s with composition and correlation of variation of P_r and P_s with c/a ratio.*

A conventional nonlinear P-E hysteresis non-lossy loop was observed for BTO, BLFT1, suggesting the presence of FE in these samples. This was also confirmed from dielectric studies, where the FE→PE transition was observed above room temperature for BTO and BLFT1. The saturation polarisation is observed to slightly decrease from BTO to BLFT1. This is likely to be correlated with the decrease in the tetragonality with La and Fe incorporation. The tetragonality factor, c/a ratio, P_s, and P_r seem to follow a similar trend of decrement with substitution [Figure 5.14 (f)]. Hence, P_s and P_r seem to be correlated with the changes in structure that modify the tetragonality of the phase. The loss increases with further substitution. Hence, extremely lossy loops, due to conduction losses, were obtained for the BLFT2 and BLFT3 samples, suggesting lossy improper FE-type behaviour in these materials. With higher substitution, the O_V has increased, and so has the loss of materials. Conduction loss is an extremely

important component in the case of FE polarisation. One of the important observations is that along with the reduction of tetragonality, the amount of loss component increases, a combination of which may be the reason behind the decrease of P_r and P_s with the increase of substitution.

In FE materials, O_v are prominent structural defects that assemble near the domain walls. O_v arrests the motion of domain walls, a phenomenon widely known as pinning of the domain wall. The amount of O_v is critical to understanding the motion of domain walls. From these observations, it seems that degradation of FE is associated with the pinning of domain wall motion by O_v. Excessive presence of O_v restricts the motion of domain walls, a phenomenon widely known as pinning of the domain wall, thereby immobilising the FE domains. Apart from that, capacitive charging effects, ionic migration, space charges, or charge trapping at interfaces can also produce a round or loop-like lossy behaviour, particularly when measured at low frequencies. Grain size of the samples also has a dependence on the FE properties exhibited by these ceramics, where the point defects contribution is not dominant, the maximum and remnant polarisation decrease with decreasing grain size [173]. From the SEM data, the grain size is found to decrease from BTO to BLFT3; hence, in the FE loop, P_r and P_s decrease with the decrease in grain size. The high number of defects and the lossy P-E loops hint at a high conduction loss in the BLFT2 and BLFT3 samples. Due to the high loss of the BLFT3 sample, the electric field can provide up to 10 kV.

5.2.7 Magnetic studies

The field-dependent magnetic studies were performed in the range -60 kOe to + 60 kOe at room temperature for all the samples [Figure 5.16 (a)]. The BTO sample exhibits a dominant diamagnetic nature, whereas the introduction of La and Fe results in samples with a dominant paramagnetic behaviour. However, upon detailed inspection, there is evidence of a very weak FM when zoomed in at the zero field conditions [Figure 5.16(a)

inset]. This is consistent with other reports on BTO with surface oxygen or O_V or other defects in the lattice [291].

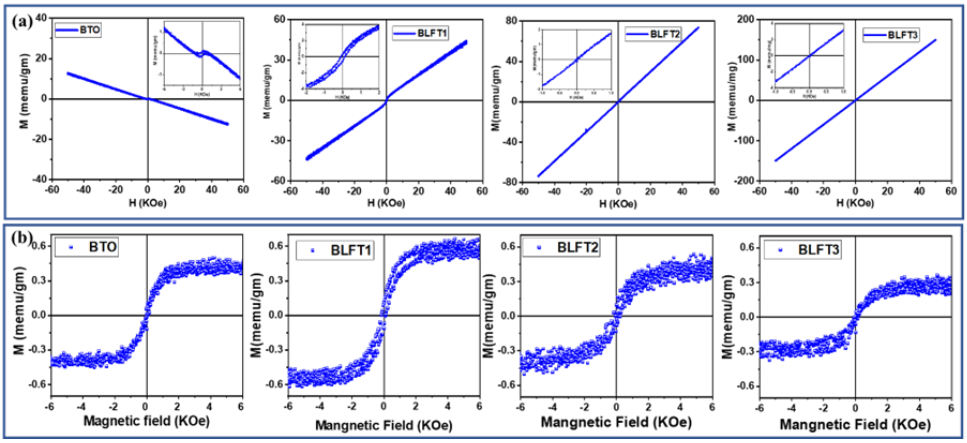

Figure 5.16: *(a) M-H loop of the samples at 60 kOe [Inset: Zoomed M-H loop at 6 kOe shows small opening] (b)Diamagnetic and paramagnetic subtracted M-H loop.*

Various correlated parameters influence the magnetism in these materials, including the grain size effect [292], the different valence states of Fe and Ti ions [293], and lattice disorder [294]. The overall magnetism has contributions from all these effects. The permeability of the material has been influenced by the grain size, distribution of grain size, the amount of pore, domain wall contribution, etc. However, detailed studies are required to understand the different contributions of these parameters to magnetic properties. For analysing the magnetic ordering of these samples, the paramagnetic or diamagnetic background was subtracted from the data, and the weak ferromagnetic saturated M-H loop was evident for all samples [Figure 5.16(b)].

Diamagnetism in BTO arises due to the Ti^{4+} cations, which have empty orbitals. FM can originate in such samples from conventional superexchange or double exchange interactions that can produce long-range magnetic order of magnetic cations. However, at lower concentrations of magnetic cations, such interactions are not possible [295]. Hence, ideally, Ti^{4+} being nonmagnetic, FM in BTO cannot be expected. In search of the origin of FM in BTO, one can relate to the presence of Ti^{3+} ions in these

materials. The origin of room temperature ferromagnetism in undoped BTO can be correlated to O_V. There can be several types of O_V, such as singly ionised ($O^{\bullet}$), doubly ionised ($O^{\bullet\bullet}$), and neutral (O_v). When interacting with Ti^{3+} ions, $O^{\bullet}$ and $O^{\bullet\bullet}$ can produce magnetism. O_v on the surface of BTO can trap the electrons locally and create an F center. The magnetism due to the F-center exchange mechanism arises in the $O^{\bullet}$- Ti^{3+} networks. An electron in either the Ti^{3+} ($3d^1$) ion or $O^{\bullet}$ effectively behaves like a localised electron. The spin polarisation of the 3*d* electron happens when an electron at the $O^{\bullet}$ sites bind with the localised 3*d* electron. The electrons in the $O^{\bullet}$ and Ti^{3+} ions exhibiting parallel spins lead to ferromagnetic exchange interaction and result in the formation of bound magnetic polarons (BMP) [Figure 5.17]. Similarly, when $O^{\bullet\bullet}$ is in the two nearest neighbouring Ti^{3+} ions, BMP is formed due to the exchange interaction of two electrons. Hence, the RTFM in BTO is the result of exchange interaction in BMPs. A schematic of the formation of BMPs is shown in Figure 5.17. These charged defect complexes can lead to weak FM in the pure BTO. With La and Fe addition, the BLFT samples show a dominant paramagnetism. The diamagnetism to Para magnetism conversion may be only justified due to the presence of Fe ions. As the Fe^{3+} ion concentration is extremely low, these are isolated and cannot interact with each other. Hence, they contribute to Pauli Paramagnetism. In addition to the paramagnetism, there is a very weak ferromagnetism. The small value of M_S in the BLFT samples can be correlated to two reasons: The La and Fe substitution in BTO increases f_{Ov}, which acts as an electron trap center, and increases the BMP [296]. Here, Ti^{3+}- $O^{\bullet}$, Fe^{3+}-$O^{\bullet}$, Ti^{3+}-$O^{\bullet\bullet}$ -Ti^{3+} charge defect complexes are created. The increase of Fe^{2+}/Fe^{3+} magnetic ions in the BTO lattice, which will also lead to an increase in BMP.

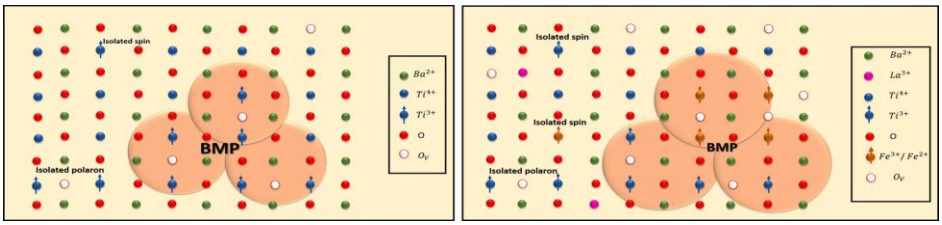

Figure 5.17: *(a)Schematic of the BMP in BTO (b) Schematic of BMP in BLFT.*

The saturation magnetization, M_s, and the remnant magnetization, M_r, increase from BTO to BLFT1. Thereafter, these values decrease for BLFT2 and further for BLFT3 [Figure 5.18].

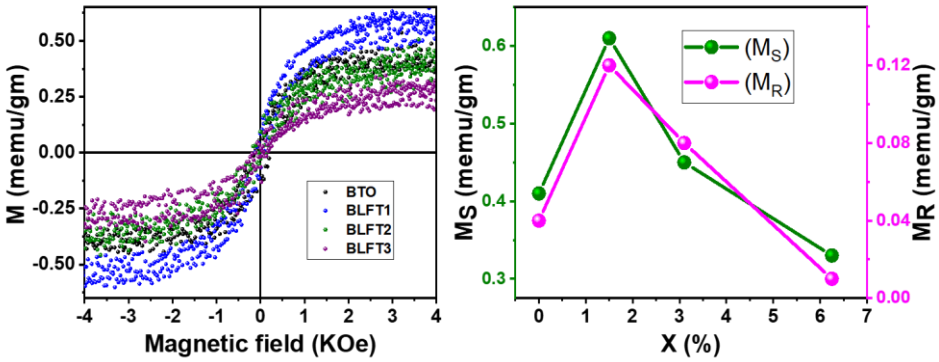

Figure 5.18: *(a) Comparison of M-H curve of all the samples together (b)Variation in the M_s and M_R value with composition, (c) Variation of Ti-O-Ti bond angle with composition.*

The increase in the values of M_s and M_r can be correlated to the increase in BMP due to an increase in O_v and, thereby, the charge defect complexes. However, for BLFT2 and BLFT3, the structural modifications reduce the amount of these charge defect complexes and which leads to the deterioration of BMP; thereby, ferromagnetism will reduce. For lower-doped samples, the defect concentrations are below the critical values that allow double exchange to be mitigated through O_v. This will result in a magnetic ordering as discussed in dilute Fe-doped $BaTiO_3$ [297]. But such conditions are violated for higher substitutions, thereby losing the ferromagnetism.

5.2.8 Multiferroicity and magnetodielectric studies

The BTO, BLFT1 samples exhibit simultaneous existence of FM and FE and hence possess multiferroicity at RT. However, the existence of multiferroicity in a single phase does not confirm the coupling of these two ferroic orders. A direct MEC measurement of these samples did not give a proper P-H loop due to the high level of noise in the measurement data. This indicates the very low value of the MEC coefficient that cannot be extracted from the noise level, or may be the absence of MEC in the material.

A magneto-dielectric (MD) measurement [298] is performed for analysing the capacitance variation with the application of a magnetic field. Magnetic modification of the dielectric permittivity can be an indirect indication of a possible MEC. Since the magnetic field affects magnetic ordering, the field indirectly alters the dielectric constant of magnetoelectric multiferroics. This is the so-called magnetodielectric effect (MDE) or magnetocapacitance effect (MCE). However, MEC is not the only way to produce MC: magneto-resistive artifacts can also give rise to MDE. Thus, while multiferroicity may imply MC, the converse is not true [299]. Hence, MDE is an indirect way to study the MEC.

Room temperature MDE in the La/Fe modified BTO compositions has been investigated with a frequency-dependent dielectric measurement at various magnetic fields. The dielectric spectra were observed to vary with an increase in the applied magnetic field for all the compositions. The MC between electric and magnetic dipoles was evaluated by measuring the change of the dielectric constant ($\Delta\varepsilon_r$) with the applied magnetic field (H) at room temperature. The magneto-capacitance can be expressed as:

$$MC = \frac{\varepsilon(H) - \varepsilon(0)}{\varepsilon(0)}$$

where ε(H), ε(0) denote the dielectric constants in the presence and absence of magnetic field H, respectively.

Figure 5.19 shows the variation of permittivity with frequency for different magnetic fields from 0 T to 1 T. The Inset of each figure shows the variation with magnetic field for a small range of frequency 1kHz–10kHz. The results show that there is significant variation in the dielectric properties of the samples with magnetic fields. MC has been reported in literature to be both positive and negative. In these samples, ε_r decreases with the increase of the applied magnetic field, which signifies a negative coupling coefficient [300]. The sign of the MDE depends on the product of the spin pair correlation of the neighbouring spins and the coupling constant [301], [302].

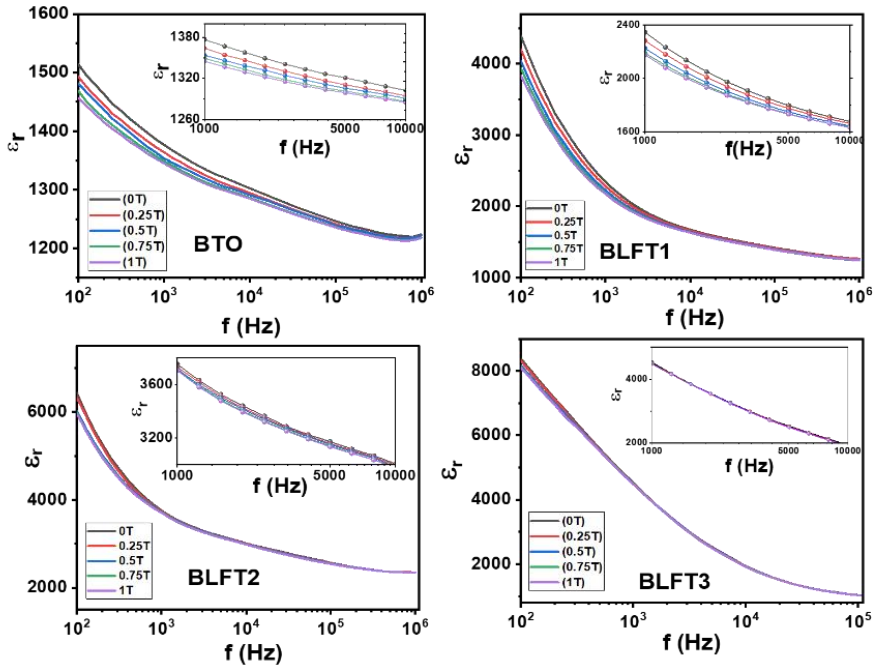

Figure 5.19: *Variation of ε_r with frequency for all the samples under different magnetic field from 0 T to 1 T.*

Figure 5.20 [a-d] shows the variation of MC with magnetic field for different frequencies, 1 kHz, 10 kHz, 100 kHz, for the increase in magnetic field from 0 to 1 T. The absolute value of MC increases with an increase in La/Fe content up to BLFT1; after that, the value decreases for BLFT2 and BLFT3. Dielectric constant decreases with the increase in the applied magnetic field in the investigated frequency range. The applied magnetic

field induces strain in the multiferroic material. The strain induces stress on the piezoelectric, since all ferroelectrics are piezoelectric, which generates the electric field. The orientation of the ferroelectric domains due to this generated electric field leads to a change in polarization value. Eventually, a change in dielectric permittivity occurs with the application of a magnetic field [303], [304]. The MC decreases with an increase in frequency.

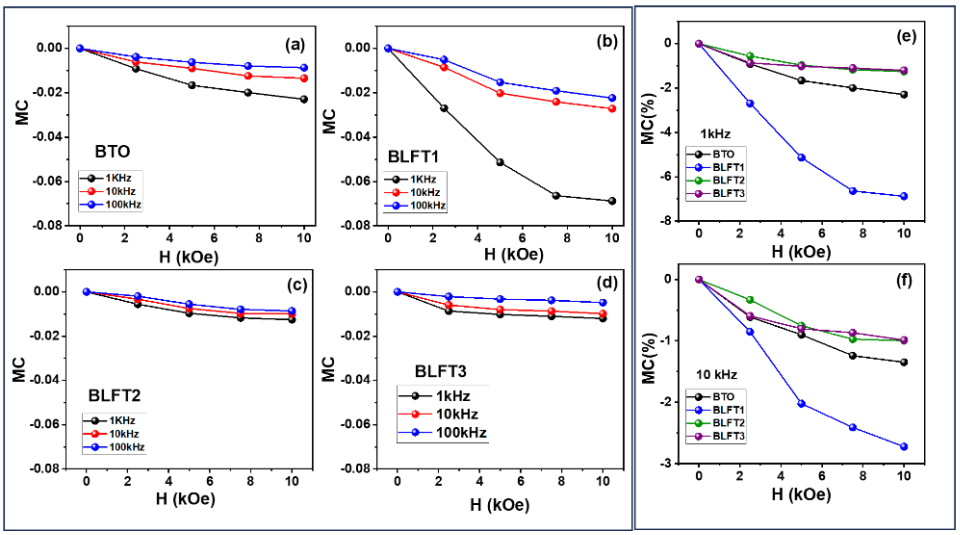

Figure 5.20: *Variation of MC% of all samples with magnetic field at (a)-(e) 1kHZ,10kHZ, 100 kHz, (f) Comparison of MC% for all the samples at 1 kHz.*

Figure 5.20 [e,f] shows the MC% of different samples at 1kHz and 10kHz for a magnetic field of 1T. At lower frequencies, the contribution of space charges also comes into the picture, and that also contributes to the MC, while at higher frequencies, the relaxation of the space charges and the contribution to the space charge polarization will be less and lead to a decrease in the MC%. This plot reveals that the MC% is highest for the BLFT1 sample compared to all other samples. The existence of magnetic and ferroelectric ordering in these samples leads to the electric dipoles aligning in a certain orientation and induces polarization with the application of a magnetic field.

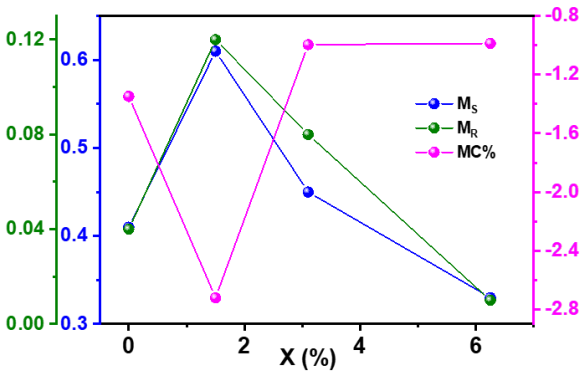

Figure 5.21: *Variation of M_r, M_s, and MC% at a magnetic field of 1 T and a n electric field of 10 kHz for all compositions.*

Figure 5.21 shows the variation of MC% for 10 kHz and M_s and M_r values with composition. The MC% increases from BTO to BLFT1, then decreases afterwards. The decrease of M_s and M_r with composition in the M-H loop and the increase in the lossy nature of the P-E loop can be correlated to the decrease in the MD effect after BLFT1. The highest MC% value of BLFT1 indirectly indicates the MEC shown by these materials.

Table 5.2: Maximum magnetocapacitance (%) values were collected from literature data and compared with the present system.

No	System	MC%	Frequency	Magnetic field	Ref.
1	(0.7) $BiFeO_3$– (0.3) $BaTiO_3$	-0.23	1	0.9	[305]
2	0.6(0.3$CoFe_2O_4$–0.7$BiFeO_3$)– (0.4) $BaTiO_3$	-3.2	1	0.9	[306]
3	(0.5) $MgFe_2O_4$– (0.5) $BaTiO_3$	-0.4	10	0.7	[307]
4	$BaT_{0.95}Fe_{0.05}O_{3-\delta}$	-3.7	10	1	[308]
5	$BaTiO_3$- $CoFe_2O_4$	-4.5	1	2.1	[309]
6	(0.94) $BaTiO_3$-(0.6) $CoFe_2O_4$	-9	1	0.26	[310]
7	(0.94) $BaTiO_3$-(0.6) $ZnFe_2O_3$	-7	1	0.26	[310]
8	(0.99) $BaTiO_3$-(0.01) $LaFeO_3$	-2.7	10	1	Present work

Hence, the coexistence of FE and magnetic ordering in BLFT1 leads to enhanced MD effect. In some of the composites of $BaTiO_3$ with magnetic materials with different phases, the reported MC% value is greater than the

MC% value obtained for the BLFT1 sample [310], [311]. Whereas this MC% value ~ - 7.8 at 1 kHz and ~ - 2.7 at 10 kHz obtained for BLFT1 is the highest value reported in a solid solution with single-phase material [312] [Table 5.2].

5.3 Conclusions

Sol-gel prepared $Ba_{(1-x)}La_{(x)}Ti_{(1-y)}Fe_{(y)}O_3$ revealed a pure tetragonal *P4mm* phase for x = 0 and 0.01, while a mixed tetragonal and cubic *Pm-3 m* phase for 0.03 and 0.06. The modifications were confirmed by XRD and Raman studies. From XPS and ESR measurement shows the presence of O_V, Ti^{3+}, and Fe^{2+} with substitution. The presence of these ions and vacancies can form defect complexes suitable to exchange interaction of of spins.

The grain size was observed to decrease from 2.89 μm to 1.38 μm from FESEM studies. Ferroelectricity was observed in the single-phase samples up to x = 0.01. For x >0.01, the samples become improper ferroelectrics due to the high conduction losses, and the multiferroicity is lost. Along with the ferroelectric ordering, a ferromagnetic component was also observed in the single-phase samples. The ferromagnetism arises from the F center exchange mediated by Bound Magnetic Polarons. However, for the higher substitution (x>0.01), both orderings are compromised and lose the multiferroicity. The coupling of the ferroelectric and ferromagnetic orders was revealed from magnetodielectric property measurements. The magnetocapacitance percentage value 2.7 at 10 kHz is highest for x = 0.01 at 1 T. This is an indication of MEC, and can be correlated with the structural variations and associated ferroelectric and magnetic properties.

CHAPTER 6

Defects induced band gap modification, polaron formation, and dielectric properties of La and Fe-doped $BaTiO_3$ $Ba_{(1-x)}La_{(x)}Ti_{(1-y)}Fe_{(y)}O_3$ (x=y=0, 0.01, 0.03, 0.06)

This chapter details the optical band gap modification of La/Fe-modified $BaTiO_3$. Theoretical DOS and ELF calculations predict the defect state formation and lattice distortions. Dielectric properties and ac conductivity studies explore the polaron formation and changes in the conduction mechanisms.

6.1 Introduction

Transition metal-based oxide perovskites are widely used in optoelectronic devices due to their electronic structure, charge transport mechanisms, and defect states [313], [314]. The optical properties and electrical conduction mechanisms are correlated in optoelectronic materials [315], [316]. Optical memories, electro-optic devices, actuators, sensors, photovoltaics, photocatalysis, etc., are applications where bandgap tuning and associated changes in electrical and optical properties are essential to be explored in materials where there is the flexibility of modifications using various probes, including chemical modifications [317], [318].

$BaTiO_3$ (BTO) is a wide bandgap semiconductor and a well-known dielectric material with an optical bandgap of ~3.2 eV [319]. The bandgap can be tuned depending on the crystal structure and defects. The tetragonal structure of BTO has a higher bandgap than the cubic structure [320]. This variation of hybridisation of orbitals in the crystal structure is an important factor [321]. Experimentally and theoretically, Fe-doped BTO [322] and La-doped BTO [323] were found to have a reduced bandgap. However, there needs to be more explanation of band structures. While some describe Fe-doped BTO as leading to the modification of the Ti orbitals [324], others refer to the formation of Fe defect bands near the valence band [325], [326].

In the previous chapter, we studied the structure-correlated multiferroic and magnetodielectric applications of La and Fe-doped BTO. A mixed valence state of TM ions was observed in these samples. O_v increased with doping. For $x > 0.01$, an increase in the lossy nature of the samples was observed, hinting at a better transport property of these materials [150]. Hence, a study of the electronic, dielectric properties of the doped materials becomes important. In this chapter, we have taken four samples of La and Fe doped series named as BTO (x=0), BLFT1 (x=0.01), BLFT2(x=0.03), and BLFT3(x=0.06). Knowing that these properties are correlated to the modifications in the electronic density of states (DOS), orbital shapes, etc., an attempt to correlate the theoretical and experimental

results is of prime interest. The introduction of lattice disorder/ distortions by introducing foreign elements and O_v may lead to such modifications in the DOS and orbital shapes and formation of polarons, thereby making this solid solution interesting. The structural changes leading to changes in the electronic properties of these materials provide an ideal opportunity to investigate such possibilities [327]. In this work, an attempt has been made to justify the theoretical and experimental observations of defects, correlated band gap, and dielectric properties.

6.2 RESULTS AND DISCUSSION

6.2.1 Optical band gap studies UV-DRS absorption spectroscopy

The optical bandgap energy, E_g, was measured using the UV-visible DRS absorption spectrum. The optical bandgap was estimated by fitting the absorption coefficient in Tauc's relation given by $(\alpha h\nu)^n = C(h\nu - E_g)$ [328], where C is the proportionality constant, h is the Planck constant, E_g is the optical bandgap, and n is 2 for the direct bandgap [329]. Tauc's plot of all the samples is given in Figure 6.1. The extrapolation of the straight portion of the curve to the energy axis will give the bandgap. The structural disorder and the defects in the lattice are associated with the E_U [330]. The spectral dependence of the absorption coefficient α in the spectral region corresponding to transitions involving the tails of the electronic density of states is described by the Urbach equation,

$$\alpha = \alpha_0 exp\left(\frac{h\upsilon - E_g}{E_U}\right),$$

where α_0 is a constant, E_U is the energy that reflects structural disorder and defects of a semiconductor.

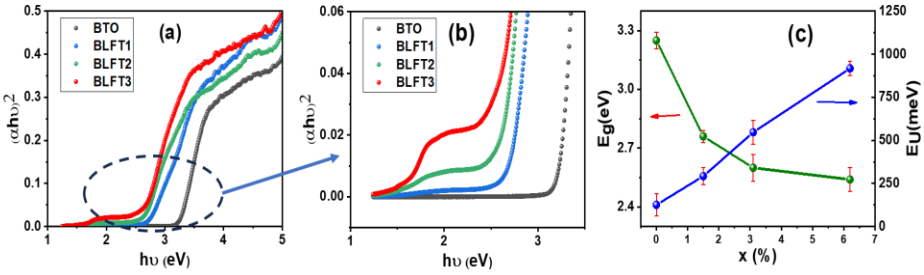

***Figure 6.1**: (a) UV-visible tauc plot of the samples, (b) enlarged view of the pre absorption edge (c) Variation of E_g and E_U with composition.*

E_g, constantly decreased from the UV region ~3.25 eV (BTO) to the visible region ~2.6 eV (BLFT3) (Figure 6.1). The band structure of BTO is formed mainly due to the Ti3d (CB) and O2p (VB) orbitals [331]. Changes in the overlapping pattern of the Ti and O orbitals can also lead to modifications in the energy gap. Modifications of electronic hybridisation ultimately redefine the energy gap. The shift of Ti^{4+} ions with doping leads to distortion of the TiO_6 octahedra, which results in changes in the strength of hybridisation in the Ti–O bond through crystal field splitting [332]. Panchal *et al.* [333], with the help of X-ray absorption, studied the difference in the strength of Ti–O hybridisation in tetragonal and cubic phases. The enhanced extent of hybridisation of e_g and t_{2g} orbitals and a smaller crystal field due to the reduction in tetragonal distortion and lifting of the TiO_6 octahedral symmetry led to a reduction in the effective bandgap. E_U increases from 126 meV for pure BTO to 917 meV for BLFT3 as shown in Figure 6.1. This increase confirms the structural disorder in BTO with La and Fe substitution.

In BTO, doping causes structural asymmetry due to the displacement of Ba and Ti atoms. This introduces atomic orbital destabilisation and causes pseudo-Jahn–Teller (PJT) effect [334]. In pure BTO, Ti is supposed to be in the Ti^{4+} state. This Ti^{4+} ion does not have a d-electron and hence cannot participate in a PJT. On the other hand, Ti^{3+} has one 3d-electron, which can participate in PJT. In the BLFT samples, Ti^{3+} and Fe^{2+} ions can induce PJT. Displacements in Ti–O/Fe–O and Ba–O/La–

O bonds for the BLFT samples [150] ensure the PJT effect. These distortions modify the energy and the splitting. Hence, a lowering of the bandgap is observed along with the reduction of the energies of the band edges. There can also be an increase in intermediate states in the bandgap [335]. It has been observed that Fe generates defect states near E_F [336] and inside the CB. It was observed through XPS and EPR studies that dopant cations and O_v can form defect clusters in doped lattices. These defect clusters can influence the ac conductivity through charge transfer [337]. This inhomogeneous charge distribution allows the trapping of electrons. Hence, an increase in carrier concentration can be expected. For the states near E_F, one can also expect an increase in conduction mediated through these defect states. Such defects can also contribute to localised electronic states inside the gap. Electrons can be trapped in these states, thereby increasing the carrier concentration.

For the BTO, the absorption edge is sharp [Figure 6.1(a)], which shows the negligible presence of defect states in the lattice and a very low value of E_U. In the case of doped samples, there is a gradual reduction in the sharpness of the absorption edge from BLFT1 to BLFT3. Such a reduction in the sharpness indicates the presence of band tails due to strain from structural deformation, increasing in E_U. However, one should not rule out the presence of dopant-initiated states very close to the conduction band maximum (CBM) and valence band minimum (VBM). A theoretical assessment has been performed using DOS analysis in the next section to verify such effects.

A hump-like broad pre-absorption peak is observed for BLFT samples [Figure 6.1(b)]. These absorption edges correspond to the absorption due to intermediate states or d-d transitions. As the defect states increase, doping leads to an increase in the intensity of this pre-absorption edge at a lower energy than the bandgap energy. DOS analysis is essential to understand such states responsible for the pre-edge absorption.

6.2.2 Density of states analysis

To investigate experimentally obtained reduction in bandgap and additional absorption pre-edge, electronic total density of states (TDOS) and partial density of states (PDOS) in BTO and BLFT3 have been performed using the fully relaxed crystal structure, as shown in Figure 6.2. For simplicity, E_F is shifted in both compounds to 0 eV. The electronic density of states shown is mainly dominated by Ba 5p, Ti 3d, O 2p, Fe 3d, and La 5d states. The partial density of states of Ba 5p orbitals near the Fermi level indicates Ba has a small electronic contribution to the conduction band; it acts as a charge balancer to balance the system charge [338]. The contribution from La is not significant in BLFT3 compared to Ba in the electronic DOS.

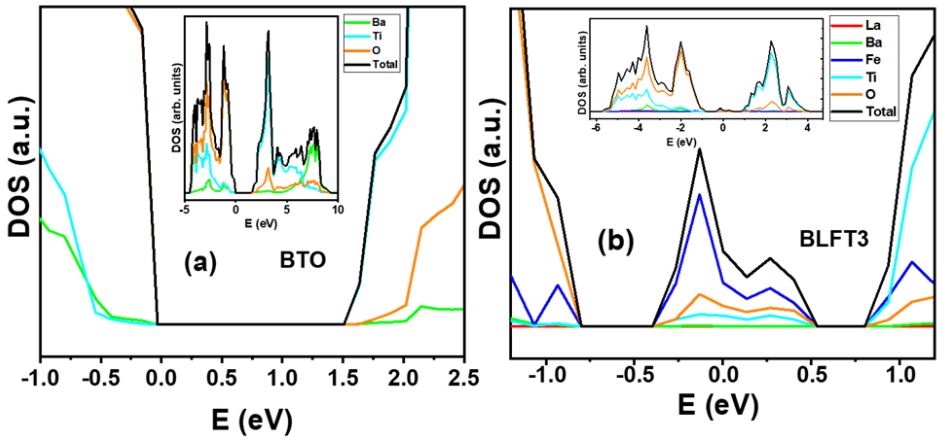

***Figure 6.2**: DOS of Ba 5p states, La 5d states, Ti 3d states, Fe 3d states, O 2p states. (a) BTO and (b) BLFT3.*

In the case of BTO, the VBM and CBM near E_F show a large density of states and sharp edges compared to BLFT3. This correlates with the sharp absorption edge experimentally obtained in the UV–visible absorption spectra of BTO, revealing lower E_U, but a tailing absorption edge for doped BLFT samples, revealing higher E_U. The bandgap of both samples was found to be of the order of ~1.6 eV. The VBM of BTO was observed at 0.031 eV lower than E_F, while that of the BLFT3 was observed at 0.799 eV

lower than E_F, a shift to a lower energy by 0.768 eV. On the other hand, the CBM of BTO was observed at 1.507 eV above E_F, while that of the BLFT3 was observed at 0.803 eV above E_F, a shift to a lower energy by 0.704 eV. Hence, both VBM and CBM display a shift toward lower energies for the BLFT3 sample as compared to BTO. This change in the shift of CBM and VBM leads to moving E_F closer to the CBM. A point to observe is that in the BTO, E_F is close to the VBM while it moves toward the middle of the gap with doping. The closeness of E_F to the VBM in the case of BTO is indicative of a p-type nature of the sample. On the other hand, the Fermi level rises with doping for BLFT3, indicating an increase in the negative carriers and a decrease in the positive carriers.

In the case of BTO, the CBM is contributed mainly by the Ti states, while the VBM is contributed by the O states. Hence, the bandgap is mainly associated with the hybridisation of Ti–O bonds. In the BLFT3 sample, apart from the O states, the Fe states also contribute to VBM. On the other hand, the CBM is a contribution of not only the Ti-states but also the Fe-states. Hence, Fe seems to affect both the VBM and CBM. Hence, the presence of Fe in the lattice modifies the electronic charge distribution in such a manner that shifts the Fermi level to a higher position in the bandgap.

It is notable that in BTO, there are no defect states inside the bandgap. However, with the advent of La and Fe in the lattice, a considerable amount of defect states is observed near E_F of the BLFT3 sample. These states are contributed mainly by Fe, followed by O and nominally by Ti. In a p-type semiconductor, E_F is generally shifted toward the VBM due to the acceptor level near the VBM, while in an n-type semiconductor, E_F is generally shifted toward the CBM due to the donor level being near the CBM. Hence, the shift of E_F toward the middle of the gap may be a consequence of the presence of these defect states at the middle of the band in the BLTF3. O_V was also found to increase, which changes the density of states. Such changes in the cationic valence state and

oxygen content are expected to generate changes in the DOS. Such changes are hereby observed in terms of the new states inside the bandgap. Thus, the lowering of the CBM and VBM concerning E_F is correlated with the changes in the cationic valence states.

The pre-edge absorption found experimentally from absorption spectroscopy [Figure 6.1(b)] is a consequence of the mid-band defect states. Photo-excited electrons from the O-states in the VB to Ti-states in the CB will be significantly affected by the changes in the effective charge of the Ti atoms and the absence or presence of the O atoms. Such changes, along with the introduction of the Fe-states at both the VBM and CBM, are also partially contributors to the shifting of the E_F. Such effects may also be responsible for the loss of sharpness of the VBM and CBM edges. The observed defect states within the bandgap can trap the electrons and act as localised distortions or polarons in the lattice [339]. These polaron formations and how the electron charge distribution between Ti and O varies with doping can be analysed with the electron localisation function calculation detailed in the section on "Electron localisation function."

6.2.3 Electron localisation function calculation

It is necessary to understand how the doping of La and Fe affects the BTO lattice in terms of electronic charge distribution, in other words, the hybridisation of the atoms. A theoretical estimation can be obtained by comparing the electron localisation plots of a pure and doped sample. In this study, such a comparison is made between the pure BTO and the maximum doped BLFT3 samples. We have shown electron density distribution in ab-planes, separately for the Ba–O planes [Figure 6.3(a) and 6.3(b)] and the Ti–O planes [Figure 6.3(c) and 6.3(d)]. The warmer red colour depicts the high electronic charge density, and the colder blue colour represents the absence of electrons. The covalent nature of the bonds is revealed from the contours of charge density. For the Ti–O planes, as expected, the charge distribution around each Ti and O atom in BTO is identical. However, with

doping, a distortion in charge density distribution appears in the vicinity of the dopant atom and modifies the surrounding lattice to some extent. As a result of doping, the continuity of the redness between two oxygen atoms is reduced in the doped lattice. This hints at the localisation of electrons or the formation of polarons in the lattice due to La and Fe doping. Similarly, in the Ba–O planes, variations are observed around the La sites. A lattice contraction is observed with La and Fe substitution surrounding the dopants.

From the localisation of electrons, it seems that a stronger hybridisation between the Ti and O atoms is present in the BTO lattice than in the BLFT3 lattice. Similarly, the same can be inferred for the hybridisation between the Ba and O atoms. This means that the bond strength of both the Ti–O and Ba–O bonds weakens with doping.

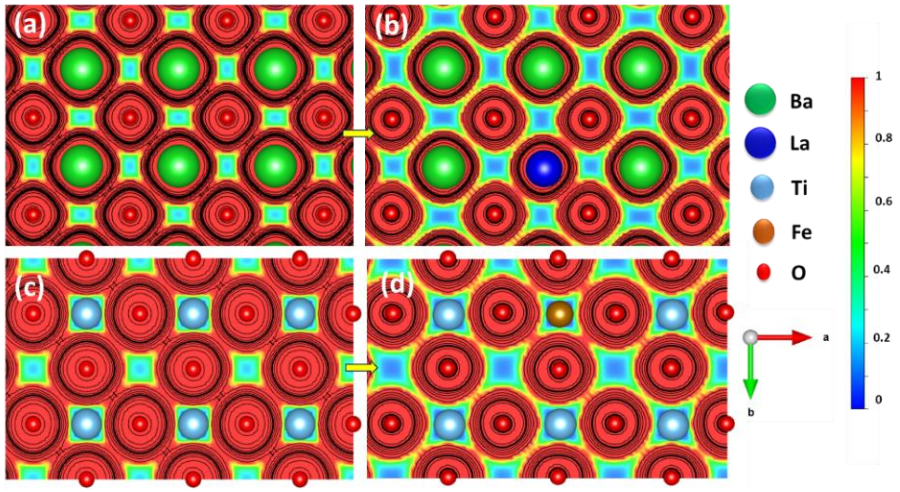

Figure 6.3: *Schematic of the electron density plots of the (a) Ba-O layer in the a–b plane of BTO. (b) Ba-O layer in the a–b plane for La atoms doped in the Ba site. (c) Ti-O layer in the a–b plane of BTO. (d) Ti-O layer in the a–b plane of Fe atoms doped in the Ti site.*

The band gap in $BaTiO_3$ is formed by Ti 3d (conduction band) and O 2p (valence band) orbitals. DFT calculations on BLFT3 reveal that the band gap is due to the separation of the same Ti 3d and O 2p orbitals.

However, the relative position of the Fermi energy concerning the valence band and the conduction band was found to be modified. To add to these changes the E-k diagram reveals modifications in the Ti 3d and O 2p orbitals. Such changes are due to the presence of La and Fe in the lattice. A more visible effect is observed from the ELF studies. It was observed that the electron density is modified around the Ti and O sites. Further, a structural disorder in the lattice can also be observed from the modification of electron density near Ba and Ti ions. Hence, the lattice gets disordered due to the incorporation of La and Fe.

6.2.4 Dielectric properties

Room temperature frequency-dependent dielectric constant (ε_r) [Figure 6.4 (a)] and loss factor ($\tan\delta$) [Figure 6.4 (b)] was studied in detail. At lower frequencies, ε_r is high and drops significantly with the increase of frequency. At very high frequencies, ~1 kHz, ε_r becomes almost invariant for BTO. This frequency increases with increasing substitution. On the other hand, the change in ε_r is larger in higher-doped samples than the lower-doped samples. Space charge polarisation can be responsible for such a fast variation at lower frequencies [173]. The higher value of dielectric constant at lower frequencies is explained by the Maxwell–Wagner interfacial polarisation model. According to this model, the dielectric constant has contributions from interfacial, hopping, dipolar, ionic, and electronic polarisations, leading to its higher value. As the frequency increases, the ε_r decreases due to space charge relaxation [340], [341]. In addition, in the Maxwell-Wagner model, the high dielectric constant value at the lower frequency region has more contribution from the conducting grain boundaries. The characteristic relaxation frequencies of the dipolar, hopping, and interfacial polarisations are prominent in the ranges ~ $10^6 - 10^{10}$ Hz, 10^2-10^5 Hz, and $1 - 10^3$ Hz, respectively [291].

In this sample, the sharp drop of ε_r is mostly within 1 kHz. Hence, it is likely that interfacial polarisation plays an active role in these materials. Interfacial polarisation arises from the separation of charge carriers accumulated at the grain boundary. From FESEM studies, the grain size was observed to be reduced with increasing substitution. A reduction of grain size implies an increase in the volume of grain boundaries. This, in turn, provides more charge carriers to be accumulated in these grain boundaries. On the other hand, the increasing presence of multivalent cations, as in Fe^{2+}/Fe^{3+} and Ti^{3+}/Ti^{4+}, enables more charge carriers to be freely available. Hence, the increase of multiple oxidation states in place of Ti^{4+} and O_v are strong source of argument towards increasing carrier concentration at the grain boundaries. Such a bi-fold source of enhancement of probable contributors to interfacial polarisations is indeed a strong proof of such a drastic increase of ε_r with increasing substitution.

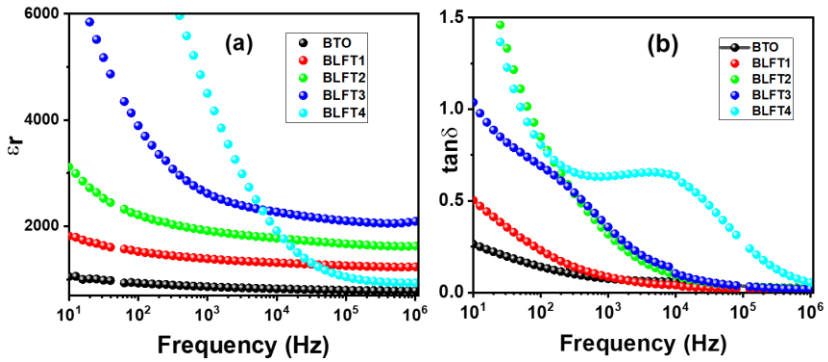

Figure 6.4: *Room temperature (a) dielectric permittivity and (b) loss tangent with frequency.*

For higher substitutions, the reduction happens in the range 1–10^5 Hz, which may also involve the participation of hopping polarisation. Hopping polarisation happens due to the hopping of electrons between Ti^{4+}/Ti^{3+}, Fe^{2+}/Fe^{3+} ions in the lattice. This leads to changes in the charge separation and related polarisation. With doping, the Fe^{2+}, $Ti^{3+,}$ and Ov increase. Such changes in the grain offer higher hopping polarisation contributions. Hence, for the higher substituted samples, one can observe a delay reduction with frequency. The value of tanδ is high for lower

frequencies and low for higher frequencies. At very high frequencies, ~1 MHz, the value of tanδ reduces to negligible values. Hence, at such high frequencies, all samples are less lossy. However, at lower frequencies, the loss of the doped samples is extremely high compared to the BTO sample. The loss increases with doping, with increasing substitution for all frequencies. The increment in the value of tanδ is related to the increase in the conductivity or energy loss of the materials. In oxide materials, an increase in conductivity can be related to O_V, cationic vacancies, or polaron hopping. Note that there are no volatile elements in the samples. Also, the sintering temperature, heating process, and environment were unaltered. Hence, the chance for the cationic vacancy is negligible [292]. The f_{OV} was found to increase from BTO to BLFT3 from XPS studies. Also, the increase of multiple oxidation states in the BLFT samples can lead to an increased polaron hopping mechanism. A broad hump-like feature is observed in the tanδ value of BLFT3 near 10 kHz. This could be attributed to non-Debye type relaxations, which might arise due to space charge conduction [293]. The hopping motion of doubly ionised O_V could also play a role in causing such a type of relaxation [294]. A minor hump-like feature is present in BLFT2, too. The ferroelectric loops of these samples also appear lossy.

Temperature-dependent dielectric property analysis is an effective method to understand the behaviour of phase transitions. A dielectric constant anomaly at a temperature, T_c, is indicated by a phase transition at which ε is the maximum (ε_m). At this temperature, a phase transition from the noncentrosymmetric strained *P4mm* tetragonal ferroelectric to a noncentrosymmetric *Pm-3 m* cubic paraelectric phase happens [295]. The temperature-dependent dielectric spectra show a ferroelectric to paraelectric phase transition at T_c. For the BLFT samples, T_c was observed in the 50–140 ºC temperature range [Figure 6.5]. For the BTO sample, T_c ~137 °C, but T_c reduces to 90 °C for BLFT1. With increasing substitution, the tetragonal strain decreases, which reduces T_c. Such a reduction of

tetragonality was also observed from XRD analysis. From dielectric properties measurement, which was limited to 50 °C, the phase transition was evident even for BLFT2, for which T_c *is at* ~room temperature. From structural studies, for BLFT2, $c/a \rightarrow 1$, but it was not equal to 1. This agrees with the dielectric property observations. However, for BLFT3, the transition shifted to lower temperatures and was not visible within the scope of the experiment. The shift of T_c towards room temperature with doping results in an increase in the ε_r value for doped samples at RT.

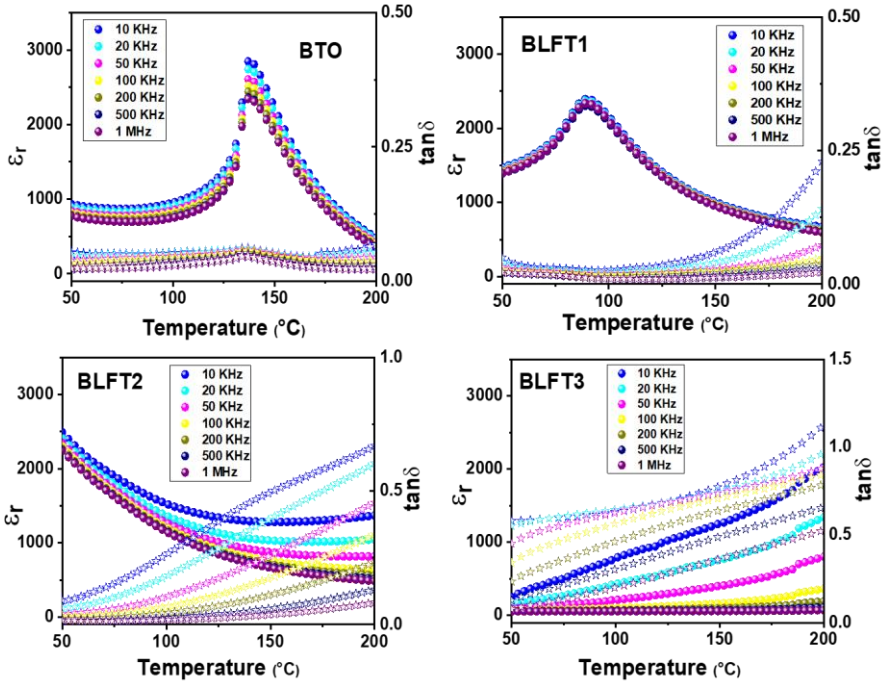

Figure 6.5: *Variation of dielectric permittivity with temperature and tanδ in the temperature range 50 ^{0}C to 200 ^{0}C. [Solid circles represent permittivity and a hollow star indicates tanδ].*

The BO_6 octahedral distortion decreases continuously from BTO to BLFT3. The average Ba-O bond and average Ti-O bond length decrease. Also, the c/a ratio decreases. On the other hand, the phase transition temperature reduces accordingly. Hence, a direct correlation between these two can be justified. For the BLFT2 and BLFT3 samples, the non-existence of the T_c can be justified from the presence of mixed *P4mm*

and *Pm-3 m* from the XRD analysis. The incorporation of La and Fe in the BTO sample reduces the tetragonality, enabling the ferroelectric to paraelectric transition at a lower temperature. In the case of BLFT3, the phase transition is not observed in the temperature-dependent dielectric since the cubic phase was more prominent in the XRD studies.

6.2.5 AC conductivity studies

AC conductivity (σ_{ac}) can be obtained from the formula $\sigma_{ac} = 2\pi f \varepsilon_0 \varepsilon''$, where f is the frequency (Hz), ε_0 is the permittivity of vacuum, and ε'' is the imaginary part of dielectric permittivity. Frequency-dependent σ_{ac} (10Hz–1MHz) was estimated in the temperature range of 323–563K [Figure 6.6] to understand the conduction mechanism of the BLFT samples. Three distinct regions appear in three different frequency ranges of the σ_{ac} data:

(6) a low frequency regime ($f \sim 10^4$ Hz).

(ii) an intermediate frequency regime ($f \sim 10^3$–10^4 Hz)

(iii) a higher frequency regime ($f > 10^4$ Hz).

The low-frequency regime reveals a plateau region and generally corresponds to the total DC conductivity of the grain and grain boundary [342]. The intermediate frequency regime reveals the first dispersion region and is generally a characteristic of localised charges in the grains and trapped charges in the grain boundaries [343]. The higher frequency regime reveals a second dispersion region and is representative of the presence of an increased mobility of the charge carriers. This change in the conductivity with frequency is correlated to the jump relaxation model proposed by Funke [344]. It depicts a transition from long-range hopping to short-range motion due to the short time available for carrier movement at higher frequencies. The successful hopping of charged species to nearby available sites contribute to the frequency-independent plateau at low frequencies. At

high frequencies, conductivity is the result of two processes. (i) the correlated forward and backward motion of charge carriers, which results in unsuccessful hopping, and (ii) the motion of charge carriers to the new sites, leading to a relaxation process and thereby a successful hopping. The more dispersive nature at higher frequencies is due to the higher rate of successful to unsuccessful hopping [343]. Hence, conductivity at different frequencies is explained using the model Jonscher's double power law: $\sigma_{ac} = \sigma_{dc} + A\omega^n + B\omega^m$, where A, B are constants, n and m are frequency exponents. Long-range translational motion of charge carriers contributes to the dc conductivity σ_{dc}. Short-range translational motion contributes to the low-frequency dispersion region $A\omega^n$ where $0<n< 1$. Re-orientational motion at high frequencies contributes to the third term, $B\omega^m$, where $0 < m<2$ [344], [345]. Figure 6.6 shows the fitting of the ac conductivity plot with Jonscher's double power law.

Depending on the variation of n with T, different conduction mechanisms can be explained. Four models can define the conduction mechanism in this material [346].

(a) Quantum Mechanical Tunnelling (QMT),

(b) Correlated Barrier Hopping (CBH),

(c) Non-overlapping Small Polaron Hopping (NSPH),

(d) Overlapping Large Polaron Tunnelling (OLPT).

A T-independent "n" corresponds to QMT. On the other hand, n increases with T for an NSPH model while it decreases with T for a CBH model. If n decreases with T, attains a minimum, and thereafter increases, then an OLPT model can be justified. Variation of the exponent n with T is plotted in Figure 6.7.

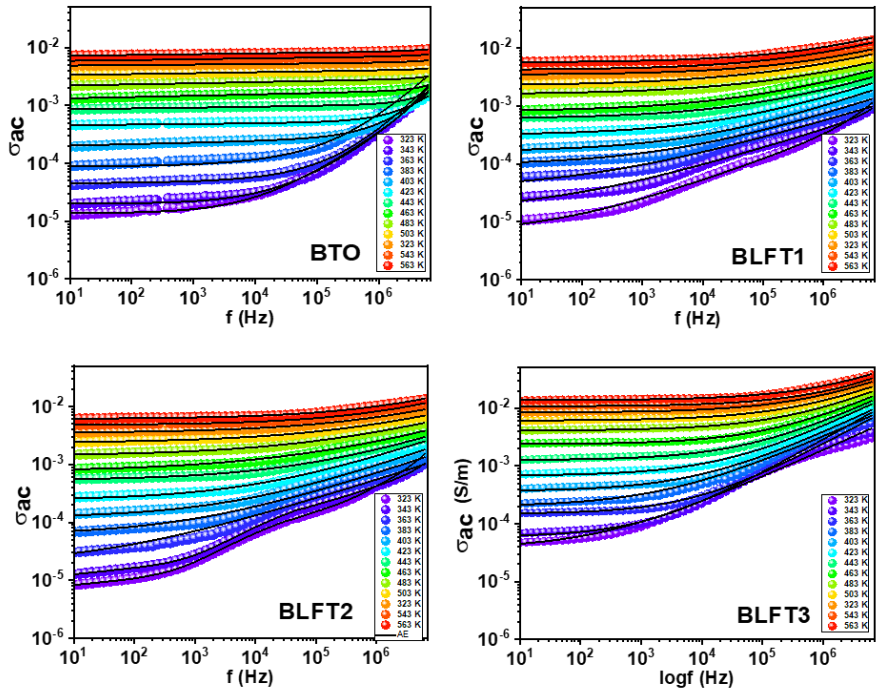

Fig 6.6: *Fitted AC conductivity plots with Johnscher's double power law.*

For the CBH model, ac conductivity is represented by

$$\sigma_{ac}(\omega) = \frac{\pi^3 n' \varepsilon_r \varepsilon_0 \{N(E_F)\}^2 \omega R_\omega^6}{24} \quad \text{and,} \quad n = 1 - \frac{6k_BT}{W_H + k_BT ln\,(\omega\tau_0)}.$$

In the above equations, n is 2 for bipolaron and 1 for single polaron hopping mechanism, N is the density of the localised states, R_ω is the hopping distance, τ_0 is the characteristic relaxation time, and W_H is the barrier height of the energy band needed to hop from one site to another.

For the NSPH model,

$$\sigma_{ac} = \frac{\pi^4 e^2 k_BT \{N(E_F)\}^2 \omega R_\omega^4}{24\alpha} \quad \text{and,} \quad n = 1 + \frac{4k_BT}{W_H - k_BT ln(\omega\tau_0)}$$

In the OLPT model, the polaron is expected to tunnel with an energy W_H called the polaron tunnelling energy, given by $W_H = W_{HO}\left(1 - \frac{r_P}{R_\omega}\right)$, where the activation energy, $W_{HO} = \frac{e^2}{4\varepsilon_P r_P}$, where r_p is the polaron radius,

and ε_P is the effective dielectric constant. W_{HO} is associated with charge transfer between the overlapping sites. The tunnelling process takes place when the polaron is incapable of hopping over the potential barrier, W_H. The AC conductivity can be defined as

$$\sigma_{ac}(\omega) = \left[\frac{\pi^4 e^2 (k_B T)^2 \{N(E_F)\}^2}{12}\right] \times \frac{\omega R_\omega^4}{2\alpha k_B T + \frac{W_{HO} r_P}{R_\omega^2}} \quad \text{and}$$

$$n = 1 - \frac{8\alpha R_\omega + (\frac{6W_{HO} r_p}{R_\omega k_B T})}{\{2\alpha R_\omega + (\frac{W_{HO} r_P}{R_\omega k_B T})\}^2} \qquad \text{(eq-1)}$$

where $N(E_F)$ is the density of states at the Fermi level, α is the decay parameter for the localised wave function. It is the spatial decay parameter for the s-like wave function assumed to describe the localised state at each site [346].

To fit the OLPT model, equation 1 is redefined according to the relation:

$$\frac{1}{1-n} = \frac{\left\{2\alpha R_\omega + \left(\frac{W_{HO} r_P}{R_\omega k_B T}\right)\right\}^2}{8\alpha R_\omega + \left(\frac{6W_{HO} r_p}{R_\omega k_B T}\right)} \qquad \text{(eq-2)}$$

considering $2\alpha R_\omega = R'_\omega$, $2\alpha r_p = r'_p$, and $\frac{1}{k_B T} = \beta$ The eq-2 was further modified as:

$$\frac{4}{1-n} = \frac{R_\omega' \left\{1 + \left(\frac{\beta W_{HO} r_P'}{(R_\omega')2}\right)\right\}^2}{1 + \left(\frac{3\beta W_{HO} r_P'}{2(R_\omega')2}\right)} \qquad \text{(eq-3).}$$

By replacing $\frac{\beta W_{HO} r_P'}{(R_\omega')2} = z$. The eq-3 can be simplified as: $\frac{6}{1-n} = \frac{z R_\omega' \left\{1 + \left(\frac{1}{z}\right)\right\}^2}{1 + \left(\frac{2}{3z}\right)}$; Assuming $\frac{2}{3z} < 1$ The equation can be approximated up to the first order of β and hence can be written as:

$$\frac{6}{1-n} = \frac{4}{3} R'_\omega + \frac{\beta W_{HO} r_P'}{R_\omega'} + \frac{(R_\omega')^3}{9\beta W_{HO} r_P'} + C \qquad \text{(eq-4).}$$

CBH, NSPH, and OLPT models are considered to fit $\frac{6}{1-n}$ vs T for uniformity.

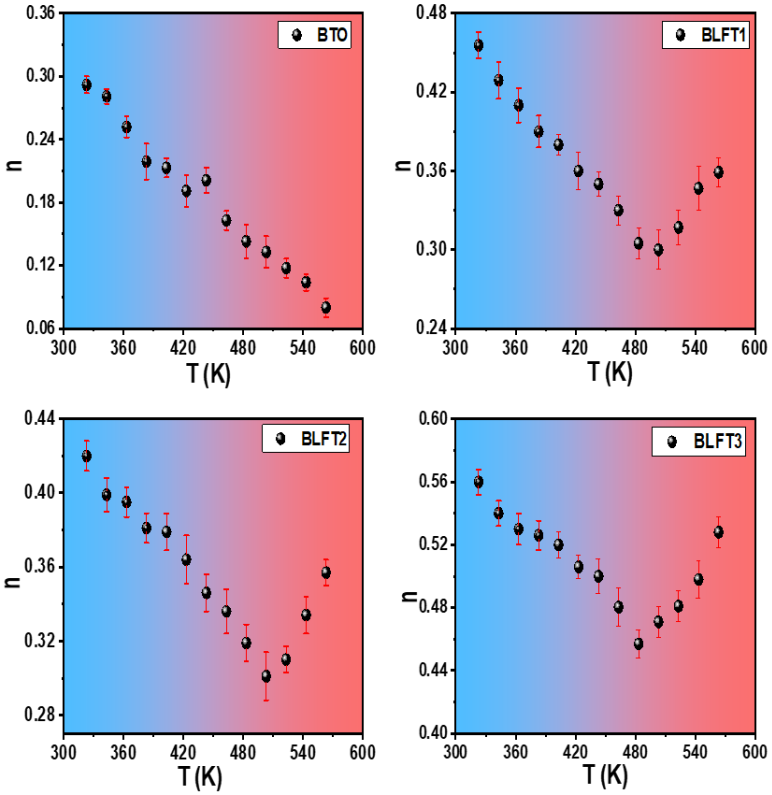

Figure 6.7: *n−T plots of all samples.*

In the OLPT model, at low temperatures, n decreases from unity as the temperature increases. However, at high temperatures, the variation of n with temperature depends on the polaron radius. For large values of r_p, n continues to decrease with increasing temperature, eventually tending to the QMT model of non-polaron-forming carriers. On the other hand, for small values of r_p it exhibits a minimum value at a certain temperature. Subsequently, it increases with increasing temperature in a similar fashion to the case of NSPH [347], [348].

In BTO, the exponent n decreases with temperature [Figure 6.7] throughout the temperature range, revealing a CBH model. Moreover, the chances of polaron formation will be negligible in BTO, according to the above discussions related to defect formation and electron localisation studies. In BLFT samples, the exponent n decreases with T at low

temperature and attains a minimum, and afterwards increases with temperature. This trend is the case for the OLPT model with small values of r_p [347], [349]. However, fitting the whole range with a single OLPT model was not possible, and hence we have fitted the whole range with an OLPT model in the low temperature region and an NSPH model in the higher temperature region separately [Figure 6.8] [350].

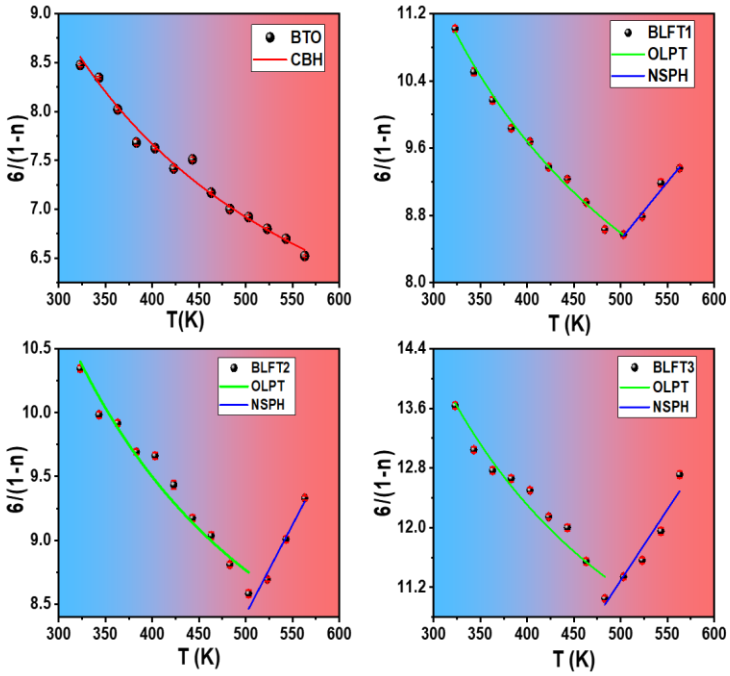

Figure 6.8: *Fitting of the 6/(1-n) v/s T with different models*

Fitted values of 6/(1-n) v/s T plots with OLPT and CBH model for the low temperature region and with NSPH model for the high temperature region are tabulated in Table 6.1. There is a gradual evolution of the BTO lattice with La and Fe addition that modifies the bonding orbitals of Ba, Ti, and O. This indicates the deformation of the lattice wave functions such that the potential wells were highly modified, and polarons are formed. Such modifications not only modified the experimental and theoretical band gap but also influenced the transportation of the carriers. The defects thus formed will overlap the potential wells and lead to the tunnelling process to take part in the short-range conduction process in doped samples.

Table 6.1: Fitted values with the different models of the 6/(1-n) v/s T plot								
	CBH		OLPT				NSPH	
	W_H (eV)	$\omega\tau_0$	R'_ω	r'_p	W_{HO} (eV)	W_H (eV)	W_H (eV)	$\omega\tau_0$
BTO	0.1285	0.051	2.01	0.447	0.212	0.1648	-	-
BLFT1	0.1875	0.068	2.2669	0.7234	0.432	0.2941	0.0211	1.0432
BLFT2	0.1277	0.032	3.1684	0.7284	0.366	0.2818	0.0220	1.0269
BLFT3	0.1045	0.077	3.8274	1.3052	0.386	0.2543	0.0156	1.0272

6.2.6 Impedance and modulus analysis

The dielectric data can also be represented in the form of complex impedance Z^* and complex modulus M^*. Z^* is related to complex permittivity ε^* by the equation: $\varepsilon^* = 1/i\omega c_0 Z^*$ where C_0 is the empty cell capacitance and ω is the angular frequency. The complex number Z^* can be expressed as $Z^* = Z' + iZ''$, where Z' and Z'' are the real numbers belonging to the real and imaginary components of Z^*. These are calculated from the capacitance (C) and resistance (R) of the material and can be defined by: $Z' = R/[1+(\omega RC)^2]$ and $Z'' = \omega R^2 C/[1+(\omega RC)^2]$. On the other hand, the electrical modulus, M^*, is related to ε^* as $M^* = 1/\varepsilon^*$. Like Z^*, the complex quantity M^* can be expressed as $M^* = M' + iM'' = i\omega C_0 Z^*$. Hence, $M' = \omega C_0 Z''$ and $M'' = \omega C_0 Z'$. Impedance formalism indicates the electric resistance of the sample and is used to evaluate the frequency of relaxation of the most resistive component of the sample [351]. Compared to impedance, the modulus formalism [352] helps to interpret the dielectric relaxation mechanism, since it neglects the contribution from the interfacial effects and capacitance due to the electrode interface [353]. Also, it highlights whether a process is a short-range charge displacement or can be attributed to long-range charge transport.

The imaginary component of impedance, Z′, plotted against frequency provides valuable insights into charge carrier dynamics. A pronounced decrease in the real part of impedance (Z′) at intermediate frequencies, accompanied by saturation at low and high frequencies, is indicative of localized charge carrier motion, with AC resistivity dominating the mid-frequency regime [Figure 6.9]. Conversely, at low frequencies, DC resistivity and long-range charge transport mechanisms prevail. A peak observed in the Z″ spectrum corresponds to a relaxation process, and the characteristics of these peaks can help elucidate the nature of charge carrier movement. For instance. The imaginary impedance is also closely related to the resistive component and consistently exhibits a relaxation peak across all temperatures. Notably, this peak broadens with increasing temperature, implying the involvement of multiple overlapping relaxation processes.

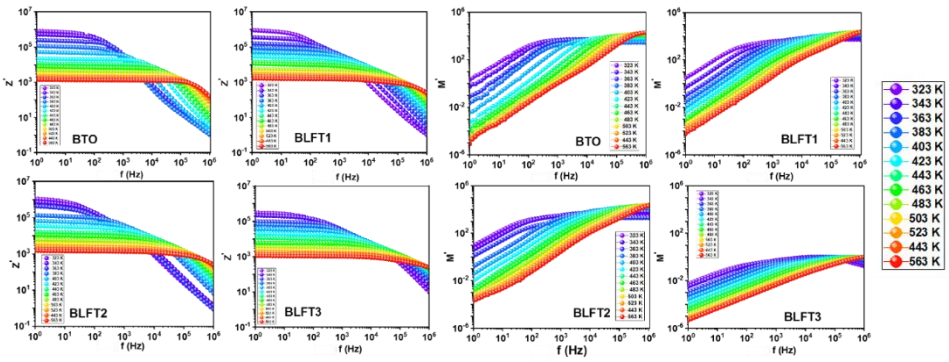

Figure 6.9: *Plots of Z' and M' with frequency*

Electric modulus is used to study charge transport processes related to the mobility of charge carriers. The modulus behaviour, specifically the imaginary part of the modulus (M″), indicates the presence of correlation between the motions of mobile charge carriers. When relaxation peaks are observed in the M″ versus frequency plots, a shift towards higher frequencies or a decrease in intensity and broadening with increasing temperature can suggest temperature-dependent relaxation processes and short-range mobility. Peaks in the high-frequency range generally signify short-term mobility of charge carriers, while those in the low-frequency

range indicate long-term mobility. A decline in the real part of the modulus, M′, with increasing temperature can also be explained by the short-range migration of charge carriers [Figure 6.9].

The comparison of the imaginary part of impedance and modulus is used to find out whether the conduction mechanism is long-range transport or short-range transport. The permittivity for a pure dielectric Debye response is described by the following equation [328]: $\varepsilon^* = 1/(j\omega\varepsilon_0 Z^*).d/a = \varepsilon_\infty + (\varepsilon_S - \varepsilon_\infty)/(1 + j\omega\tau) = \varepsilon_\infty[1+(r-1)/(1 + j\omega\tau)$ where the high frequency limit of permittivity is denoted by ε_∞ , and the low frequency permittivity is denoted by ε_S and $r = \varepsilon_s /\varepsilon_\infty$.

Figure 6.10 shows the imaginary part (Z″) of the impedance and modulus (M″) of the material in a temperature range of 323~563K. The frequency dependence of Z″ and M″ reveals a maximum at a particular frequency. This maximum corresponds to the most probable relaxation mechanism happening within the material and is generally found to spread over a region due to imperfections in the lattice. In BLFT samples, more than one relaxation peaks are observed for Z″ and M″, which becomes more evident at higher temperatures. Note that for the BTO sample, only a single relaxation peak can be observed for all temperatures. The multiple peaks in Z″ and M″ correspond to the different relaxation mechanisms associated with differences in capacitance and resistance values in the grain and grain boundary. It has already been discussed that the capacitance and resistance values from the grain and grain boundaries are different with composition and temperature, which can further lead to different relaxation mechanisms at different frequencies and hence result in multiple relaxation peaks in Z″ and M″ plots.

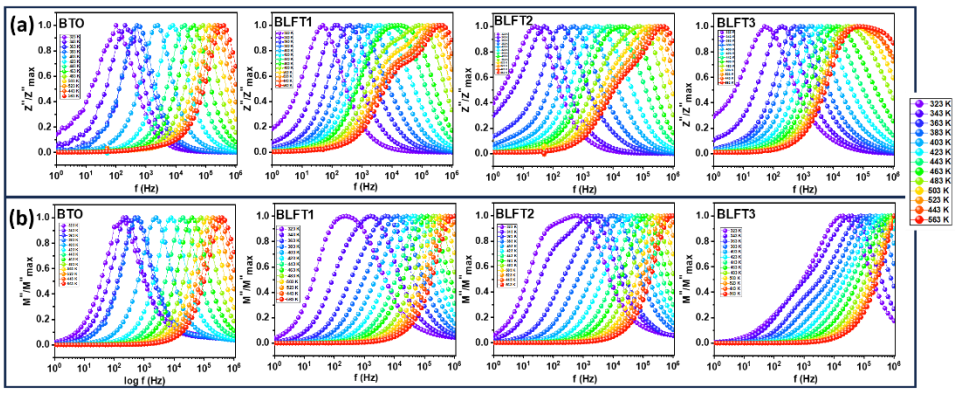

Figure 6.10: *(a) Variation of Z" with frequency (b) Variation of M" with frequency*

Depending on r in the Debye response equation, the imaginary parts for the different physical quantities (ε″, Z″, M″) may differ significantly. As the value of r increases, the separation between the maxima of Z″ and M″ peaks increases, indicating a non-Debye type relaxation. Whereas, for r =1, the curve converges and corresponds to a Debye-type relaxation. A non-Debye type relaxation is generally associated with a short-range motion of charge carriers confined to nearby potential wells [354]. On the other hand, the Debye type relaxation corresponds to the long-range motion of charge carriers. Note that for the BTO sample [Figure 6.11], the low temperature data reveal a small disparity in the overlap of the *Z″* and *M"* peaks, indicating the possibility of nominally non-Debye type relaxation. However, at higher temperatures, the overlap is more prominent, indicating a better Debye-type relaxation. This indicates a transition from a shorter long-range motion to a longer long-range motion. However, for the doped BLFT samples, the non-overlapping *Z″* and *M"* peaks indicate short-range motion of the carriers.

With an increase in temperature, the frequency of the Z''_{max}, M''_{max} shifts towards a higher frequency [Figure 6.11]. Hence, the relaxation process is thermally activated. A shift of the maxima towards higher frequencies at higher temperatures corresponds to lower time constants and, therefore, faster relaxation processes. Note that the separation between the

Z″ and *M''* peaks increase with doping. This indicates a shorter short-range motion of charge carriers with doping. Hence, a transition from the long-range to short-range mobility has been observed with doping [352]. The above observations are exactly in line with the information on distortions, defects, and polaron formation obtained in the experimental and theoretical studies and the changes in the conduction phenomena.

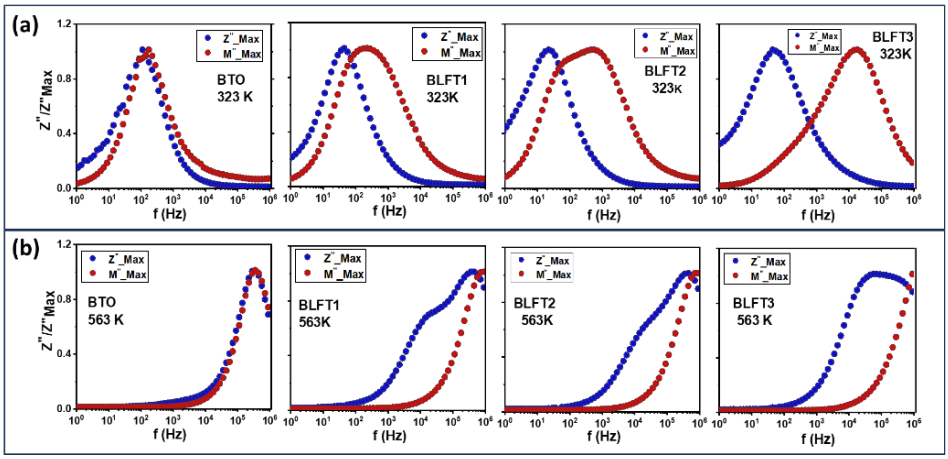

Figure 6.11: *Combined plots of the imaginary part of impedance Z″ and the imaginary part of modulus M″*

6.3 Conclusion

$Ba_{(1-x)}La_{(x)}Ti_{(1-y)}Fe_{(y)}O_3$ (x=y=0, 0.01, 0.03, 0.06) series of samples revealed band gap tuning from the UV region (3.25 eV in BTO) to the visible region (2.54 eV in BLFT3) with La/Fe doping, which can be correlated to an increase of lattice distortion and disorder from a previous study on these samples. Theoretical calculations reveal shifts in the valence band maxima and conduction band minima, along with the formation of defect states inside the bandgap with La/Fe doping. The electronic states are modified due to such defect states and correlated structural distortions/disorders, which increase the E_U. Such electronic modifications were justified by transportation measurement using dielectric properties, AC conductivity, and impedance spectroscopy. A theoretical assessment of the modifications was estimated using electron localisation function

calculations, revealing a more distorted lattice for the doped samples, suggesting localisation of the electrons. An experimental verification of the localisation was estimated using different transportation models, which revealed the presence of large polaron tunnelling for La/Fe-modified BLFT samples. For the less distorted pure BTO lattice, a hopping of charge carriers was found to be a justified transportation method. With doping, the local structural deformations and the polaron formations lead to the transportation towards a polaron tunnelling process. The defects induce band gap tuning, and the associated polaron-induced conduction mechanism makes these samples suitable for optoelectronic applications.

CHAPTER 7

Conclusions and Future Scopes

In this chapter, overall conclusions obtained from this thesis work are highlighted. The future scope of this work to be carried out for further development in this field is also detailed.

In this thesis, a comprehensive study of structural, electronic, magnetic, dielectric, and multiferroic properties of A-site and B-site modified $BaTiO_3$ has been performed.

Chapters 3 and 4 focused on investigating Ca/Mn-doped $BaTiO_3$. Room temperature ME coupling obtained in the $Ba_{0.97}Ca_{0.03}Ti_{0.97}Mn_{0.03}O_3$ sample is correlated with the structural modifications and valence state of different ions in Chapter 3. Chapter 4 studies the hexagonal polymorphism and the modification of the electronic band gap through UV-DRS, PES, and theoretical calculations. A detailed dielectric study is also included in this chapter.

Chapters 5 and 6 focused on investigating La and Fe-doped $BaTiO_3$. The structural changes and oxidation state modifications are correlated with ferroelectric and magnetic properties in Chapter 5. Magneto dielectric measurements have also been performed in Chapter 5 as indirect evidence for MEC. Chapter 6 includes the optical band gap modification, dielectric properties, and ac conductivity studies of La/Fe-doped $BaTiO_3$. A theoretical calculation of the density of states and the Electron localisation function calculation is also included in Chapter 6.

The main observations, along with the key finding of the thesis, are summarised below. In the end, a brief outlook on the possible future scope of the work in this field is presented.

1. Conclusions

- **Structural properties:**
    - La/Fe-doped BTO revealed a pure tetragonal *P4mm* phase for x = 0 and 0.015, while a mixed tetragonal and cubic *Pm-3 m* phase for 0.032, and 0.0625. XRD and Raman studies show the transformation to a more centrosymmetric structure with doping. Doping of Fe

will induce a hexagonal structure in BTO; however, the simultaneous doping of La at the A site prevents the hexagonal formation and pulls the structure to a more centrosymmetric cubic phase.

  - Ca/Mn doped BTO revealed pure tetragonal phase for x=0 and have a mixed phase tetragonal *P4mm* and hexagonal $P6_3/mmc$ structure of $BaTiO_3$ for x=0.03, 0.06 and 0.09. Mn doping at the B site triggers the hexagonal formation; however, the simultaneous doping of Ca at the A site slows down this phase transformation and retains tetragonality even for the x=0.09 sample.

- **Valence state**
  - Fe is observed in Fe^{2+} and Fe^{3+} states, and Ti is in Ti^{4+} states with the presence of Ti^{3+} in La/Fe-doped BTO. The percentage of Fe^{2+} and Ti^{3+} increases with doping, indicating an increase of O_v in this material.
  - In Ca/Mn doped BTO, Mn^{3+} and Mn^{4+} state are present along with Ti^{3+} and Ti^{4+}. Mn^{3+} area fraction is higher in the x=0.03 sample and then decreases with an increase in doping, while Ti^{3+} increases from pure to x=0.03, then remains the same with doping. Hence, the amount of O_v will be more in the x=0.03 sample compared to pure and other doped samples. EXAFS measurement also shows the mixed valence state of Mn and the modification of the local environment with doping.
  - Pure $BaTiO_3$, depending on the sintering conditions, the valence state of Ti can be varied.
- **Electronic band gap**
  - Both La/Fe doping and Ca/Mn doping decrease the optical band gap of the material decrease from the UV to the Visible region. There is defect states formed due to

Fe, Mn, Ti, and O within the band gap, which leads to a reduction of the band gap and an increase of Urbach tails. Theoretical calculation shows an insulator tetragonal BTO and metallic nature Hexagonal BTO, hence the presence of these two in the Ca/Mn doped sample makes it semiconducting and reduces of band gap. Substitution of Fe in Ti induces pre-absorption edges in the UV-Visible DRS corresponding to d-d transitions.

- **Dielectric properties**
    - Room temperature dielectric permittivity of La/Fe-doped BTO increases with doping, due to the decrease of T_c towards the room temperature. No proper ferroelectric transition is observed above ~50°C for x=0.03 and 0.06. For Ca/Mn doped BTO, there slight decrease in the T_c value, but it is above room temperature (~99°C). Room temperature permittivity decreases with the increase of Ca and Mn doping, corresponding to the decrease of tetragonality and hexagonal phase formation. The phase transition has transformed into a diffuse behaviour with doping. AC conductivity studies of La/Fe-doped BTO indicate polaron tunnelling and localised relaxation processes in the material.
    - Not only can the doping of the sintering conditions affect the Curie temperature.
- **Ferroelectric properties**
    - Ferroelectricity was observed in the single-phase La/Fe BTO samples up to x = 0.01. For x >0.01, the samples show lossy P-E loops corresponding to the high conduction losses. For Ca/Mn-doped BTO, all doped samples show an unsaturated P-E loop corresponding to the improper ferroelectric nature. PUND measurement

of BCTMO samples shows that there is still proper ferroelectric components persist in those materials.

- **Magnetic properties**
  - Weak Magnetism observed in La/Fe-doped BTO materials can be explained merely in terms of Bound magnetic Polarons. However, in Ca/Mn-doped BTO, for x=0.03 enhanced magnetic moment observed corresponds to Bound magnetic polarons and the increase in magnetic exchange interactions.
- **Magnetoelectric properties**
  - Though La/Fe-doped BTO shows magnetodielectric coupling, it fails to give ME voltage at room temperature. The magnetodielectric coupling shown by the material can correspond to the extrinsic effect due to magnetoresistance, not correlated to intrinsic MEC. However, Ca/Mn-doped BTO produces magnetoelectric voltage of 0.704 $meVcm^{-1}Oe^{-1}$ at room temperature, indicating a direct coupling of the ferroic orders.

2. Contributions of the Thesis

The notable contribution of the thesis in understanding the structure, local structure, electronic, dielectric, magnetic, and multiferroic properties of La/Fe-doped $BaTiO_3$ and Ca/Mn-doped $BaTiO_3$ samples is given below:

- Room temperature ME coupling is obtained from bulk material through Ca and Mn modification of $BaTiO_3$.
- Optimization of the doping percentage is necessary to include both ferroelectric and ferromagnetic contributions. An increase or decrease of optimum doping can vanish the multiferroic nature.

- Substitution of Ca in the Ba site can stabilise the tetragonal structure of BTO and slow down the hexagonal transformation with TM doping at the B site.
- Aliovalent La substitution at the Ba site prevents the transformation of BTO to a hexagonal structure by Fe doping at the B site and converts it to a cubic structure. La fails to stabilise the tetragonal structure of BTO
- Magneto dielectric coupling does not guarantee the direct ME coupling in a material.
- The band gap can be tuned by doping at the B site of BTO as per the requirement.
- Decrease of Curie temperature by doping at the B site can be tuned by suitable A site substitution in BTO.

3. Future Scope

The present work focused on examining the structure-correlated multiferroic properties of modified $BaTiO_3$. The research outcome of the thesis can be expanded to the next level.

- Complex magnetic interactions in this series need to be further investigated with temperature-dependent X-ray and neutron diffraction studies.
- There are a lot of scopes to investigate the magneto-transport and magnetocaloric properties of these materials.
- Thin film preparation of this bulk material can be further investigated for better physical properties.
- Thin film fabrication of FE and FM material can enhance the interface-induced MEC
- Dielectric Resonator Antenna application of this magnetoelectric material can form a multifunctional device for fabrication.

APPENDIX

Appendix A

Magnetoelectric Ca/Mn modified $BaTiO_3$ for Dielectric Resonator Antenna Application

Introduction

Dielectric materials play a pivotal role in modern technology, enabling the efficient and reliable operation of a wide range of devices and systems. Their unique insulating properties, ability to store and manage energy, and influence on signal transmission make them indispensable in electronics, telecommunications, energy storage, and numerous other fields [355]. Oxide multiferroics are promising materials for a broad range of interesting applications in spintronics, information storage, and sensing devices [356], due to their unique properties resulting from the coupling between ferromagnetic and ferroelectric character in a specific temperature range. Due to the possibility of engineering both permittivity and permeability by microstructures and by electric and magnetic field inputs, an interesting and less-exploited potential application of magnetoelectric is for miniaturised antennas.

In this work, the magnetoelectric samples studied in the thesis work have been used to study the potential use in applications, as miniaturised dielectric resonator antennas were explored.

Experimental methods

The magnetoelectric $Ba_{0.97}Ca_{0.03}Ti_{0.97}Mn_{0.03}O_3$ (BCTMO1) sample is used for the DRA fabrication. The radius and height of the pellets are determined from the empirical formula for the resonance frequency of the hybrid $HEM_{11\delta}$ mode is given by [357]:

$$f = \frac{6.324c}{2\Pi r\sqrt{(\varepsilon r+2)}}[0.27 + 0.36\,(\frac{r}{2h}) + 0.002\,(\frac{r}{2h})^2] \quad (1)$$

This formula is known to be accurate in the range $0.4 < a/h < 6$. Here, r, h, $\varepsilon_{r,}$ and c represent radius, height, ε_r of the DRA, and the velocity of the light in free space, respectively. The sintered pellets of required dimension are placed on a Microstrip line fed to a Sub-Miniature A-type (SMA) connector. An EM-wave in the frequency range 1GHz- 10GHz was fed to the SMA connector from a Vector Network Analyser (VNA) (Anritsu S820E). Then, by using the measured S_{11} parameter (which shows a distinguishing dip at some frequency where most of the source energy gets transmitted and ultimately radiated via the DR), the resonance frequency is recognised. As the resonating frequency is dependent on the ε_r of the material [equation 1], the selection of the frequency range will lead to the fixing of ε_r range for which the DRA will work. Here, the selected range is 1GHz to 10 GHz, so the ε_r range will be ~15-80. The MSL design is made according to those specifications.

The antenna design was simulated and verified using ANSYS High Frequency Structure Simulator (HFSS) software. HFSS uses the Finite Element Method (FEM) to solve electromagnetic equations for 3D structures working at high-frequency ranges (micrometre or millimetre wavelength). The signal was fed to the DR placed on a 50 Ω MSL fabricated on a Fibre glass-Reinforced epoxy-laminated sheet substrate (FR4, with ε_{subs}=4.4) with dimensions of 60 mm (length) × 60 mm (breadth) × 1.6mm (thickness) [Table 1]. The input impedance of 50Ω of the MSL was achieved with a 35 mm (length) × 3 mm (width) MSL on the FR4 substrate. The MSL was experimentally fabricated with the help of a 3D printer (LPKF Protomat-S104) on one side of the FR4 substrate, while the opposite conducting side was retained as the ground plate with the same length × breadth as that of the substrate. Input impedance matching is crucial in determining the best energy coupling criteria [358]. Hence, the DR, MSL, and FR4 substrate dimensions were optimised using HFSS. One of the necessary conditions to achieve efficient coupling between the MSL and DR is $\varepsilon_{subs} << \varepsilon_{DRA}$ [359] is also taken care of while designing the DRA. In

the simulation, a radiation box of air with a size of 120mm × 120mm × 50 mm is used to calculate the far-field parameters. The dimension considers that all the box surfaces are at least $\lambda_o/4$ away from the radiating body (λ_o is the wavelength corresponding to the resonance frequency) [360]. The values of radius and height of DR are initially optimised in HFSS to simulate the required design of the proposed DRA.

Results and Discussion

The radius and height of the DRA calculated from the empirical formula (1) are 5.5 mm and 2.25 mm, height. MSL length, width, and substrate dimensions obtained from HFSS simulation software are tabulated in Table 1.

Table 1: Optimised design parameters (in mm)			
DRA radius (r)	5.77	MSL width	3
DRA height (h)	5.75	Substrate thickness	1.6
MSL length	35	Substrate length × width	60 × 60

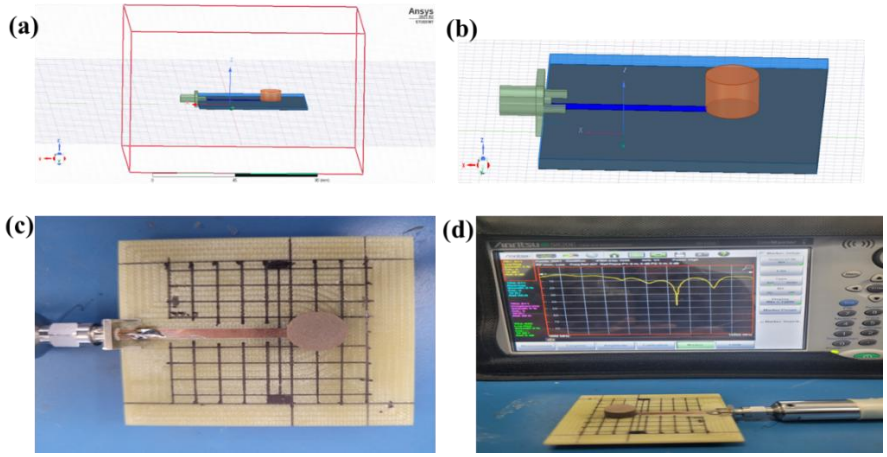

Figure 1:(a) Simulated CDRA with radiation box, (b) Simulated DRA on microstrip line, (c) Fabricated DRA on microstrip line, (d) measurement of S_{11} with VNA.

The S_{11} parameter of the fabricated MSL (without DR) was measured and simulated to verify the authenticity of the design. The simulated and experimental values of the S_{11} parameter show a similar

trend. This can be considered as a perfect verification of the fabricated design. Figure 1 (a) and (b) show the simulated DRA design, and (c) and (d) show the fabricated DRA design.

A Cylindrical Dielectric Resonator (CDR) offers three fundamental modes, $HEM_{11\delta}$, $TM_{01\delta,}$ and $TE_{01\delta}$ [361]. Here, the first index denotes the number of full-period field variations in the azimuthal direction, the second one represents the no. of radial variations, and the third index represents the variation in the z-direction [361]. From the multipole analysis of the radiation pattern, it can be shown that the most prominent contribution comes from the lower order terms, e.g., electric dipole or magnetic dipole (oriented in different directions), along with less weightage from the other higher order terms (i.e., quadrupole, octupole). The $HEM_{11\delta}$ mode is generated due to a magnetic dipole placed in the equatorial plane of the DR. The feeding mechanism using this MSL and ε_r of the DR, ranging between ~15-80, yields a prominent $HEM_{11\delta}$ mode in the frequency range 1GHz to 10GHz.

A CDR, when positioned near the MSL, effectively couples the magnetic field lines associated with it. The key to successful coupling lies in the critical positioning of the CDR on the MSL. The length of the open end of the MSL under the DRA, known as the overlapping distance (l_o). Optimal coupling is achieved when l_o equals 2.5 mm. Figure 2 shows the simulated radiation pattern on MSL and DRA after proper placement of the DRA on MSL. However, along with the $HEM_{11\delta}$ mode, some other higher-order modes may also resonate in the given frequency interval. In other words, properly detecting the $HEM_{11\delta}$ mode is essential in this technique. The $HEM_{11\delta}$ mode is verified by simulating the E-field and H-field distribution within the DRA. The pattern of E-field and H-field confirms that the $HEM_{11\ \delta}$ mode has been excited. Confirmation of the mode using field distribution and the radiation pattern enables the correct detection of the resonant frequency of the $HEM_{11\delta}$ mode.

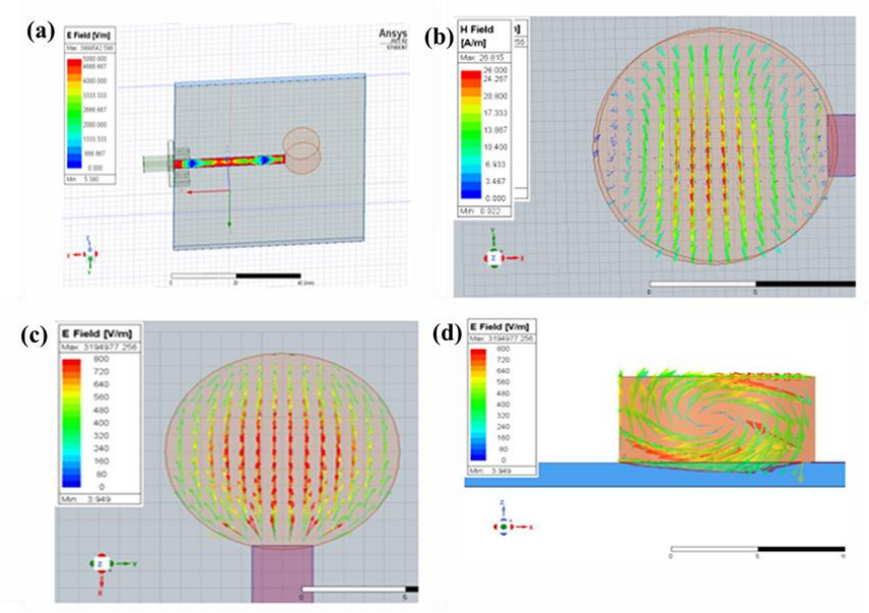

Figure 2: *(a) simulated radiation pattern on microstrip line, (b) H field pattern IN DRA along z direction, (c)E field pattern in DRA along z direction, E-field pattern in DRA along y direction.*

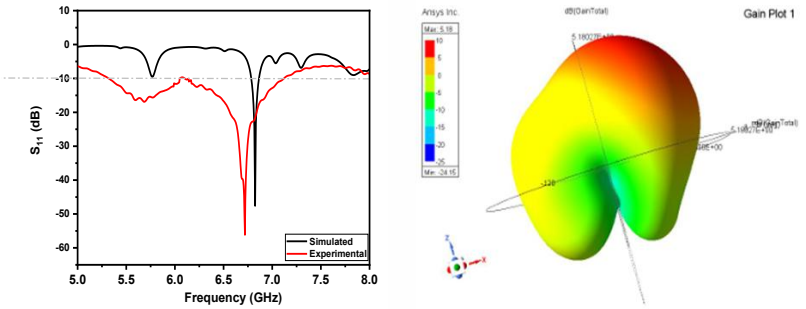

Figure 3: *Experimental and simulated S_{11} parameter and Gain plot*

Figure 3 shows the reflection coefficient S_{11} parameter measured experimentally and theoretically. The $HEM_{11\delta}$ is obtained at 6.62GHz experimentally and 6.72GHz theoretically. The broadside radiation gain pattern is also proof of the same mode. The experimental and theoretical output parameters obtained are tabulated in Table 2.

Table 2: Obtained output parameters		
Design parts	**Experimental**	**Simulated**
Resonant frequency	6.62 GHz	6.72 GHz
Frequency band	6.12-7.12 GHz	6.78-6.87GHz
Mode	$HEM_{11\delta}$	$HEM_{11\delta}$
Impedance matching	48.3 Ω	49.7 Ω
S11 (dB)	-58 dB	-52 dB

Conclusions:

A magnetoelectric BCTMO sample is fabricated as DRA, with resonant frequency 6.62GHz. The radiation pattern needs to be experimentally verified with an anechoic chamber for further conclusions and proceedings of the project.

Appendix B

$BaTiO_3$ and $CaMnO_3$ epitaxial film by Pulsed Laser Deposition

Introduction

Heterostructure of epitaxial ferroelectric thin film and ferromagnetic/antiferromagnetic thin films can produce interface strain-induced magnetoelectric coupling. $BaTiO_3$ (BTO) thin films are an excellent choice for the ferroelectric part, and the $CaMnO_3$ (CMO) film can be chosen as a magnetic film. The heterostructure formation of these two films may induce strain in the interface due to lattice mismatch, and that can be useful for the coupling of the electric and magnetic ordering in these materials. As a preliminary step for this project, BTO and CMO films are deposited through Pulsed Laser Deposition (PLD).

Experimental methods

The Pulsed Laser deposition technique is used to deposit the thin film samples [Figure 1].

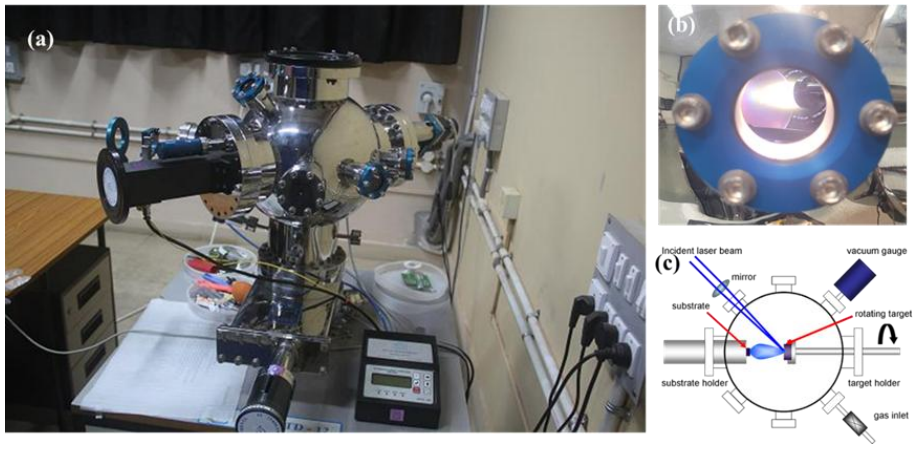

Figure 1: *(a) PLD unit, (b) Plasma formed during the deposition of CMO film, (c) Schematic of the PLD unit.*

$BaTiO_3$ and $CaMnO_3$ target materials are prepared through sol sol-gel method and made into 16mm pellets. Hard pellets were formed after

sintering at 1350 °C for $BaTiO_3$ and 1300°C for $CaMnO_3$. PLD unit is shown in Figure 1, and the Deposition conditions are tabulated in Table 1.

Table 1: PLD deposition conditions	
Parameter	**Value**
Laser energy	310 mJ
Target to substrate distance	4.5 cm
Base pressure	10^{-4} Pa
O_2 Partial pressure	40 Pa
Substrate temp.	720° C
No. of laser shots	1050 (BTO), 2100 (CMO)
Repetition Rate	4 Hz
Annealing time	3 min.
Annealing Pressure	1000 Pa (O_2 gas)

Results and Discussion

XRD data of BTO thin films for 15nm and 30 nm indicate the peaks corresponding to the (100), (200), (300) (Figure 1(a)). All the peaks are at a lower 2θ angle than the corresponding STO peaks, indicating a compressive strain in the BTO lattice deposited on the STO substrate. A shift of this peak towards higher 2θ values with increasing thickness indicates a more strained film at 15nm compared to 30 nm [Figure 1(b), (c)].

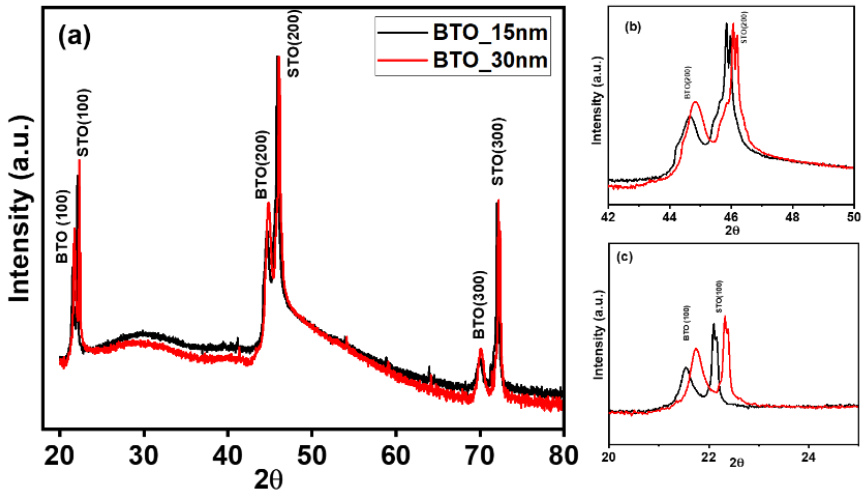

Figure 2: *(a) XRD data of $BaTiO_3$ thin films, (b)zoomed image of the (200) peak, (c) zoomed image of the (100) peak.*

XRD data of CMO thin films for 15 nm and 30 nm indicate the peaks corresponding to (100) and (200) [Figure 2(a)]. Peaks of CMO are observed at a higher 2θ angle of the corresponding STO peaks, indicating a tensile strain in the film due to the lattice mismatch between STO and CMO [Figure 1(b),(c)].

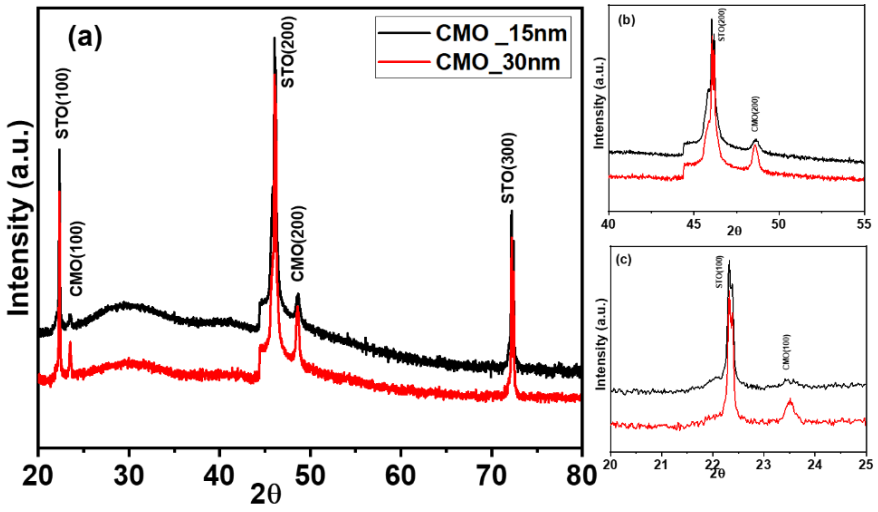

Figure 3: *(a) XRD data of $CaMnO_3$ thin films, (b)zoomed image of the (200) peak, (c) zoomed image of the (100) peak.*

AFM image of the BTO films [Figure 4] indicates epitaxial growth of the film on the STO substrate. The height obtained from the AFM image is nearly equal to the predicted 15nm and 30nm. Uniform grain size distribution is observed in both BTO films.

AFM image of the CMO films [Figure 5] does not show epitaxial growth; instead, island kind of formation is observed for both thicknesses. The non-uniform growth indicates the Vomer-Weber growth (Island growth) [362]. This is due to the strong adatom interaction rather than the adatom-substrate interactions. Since STO is an insulator and CMO is metallic, stable clusters nucleate initially and then grow in 3 dimensions to form islands. In such materials, there will be a critical thickness (Tc) below which the epitaxial growth can be possible above which the island formation. For growth situations with a very small Schwoebel–Ehrlich barrier (SE), the diminished

island size is no advantage; on the contrary, it enhances second-layer nucleation [363].

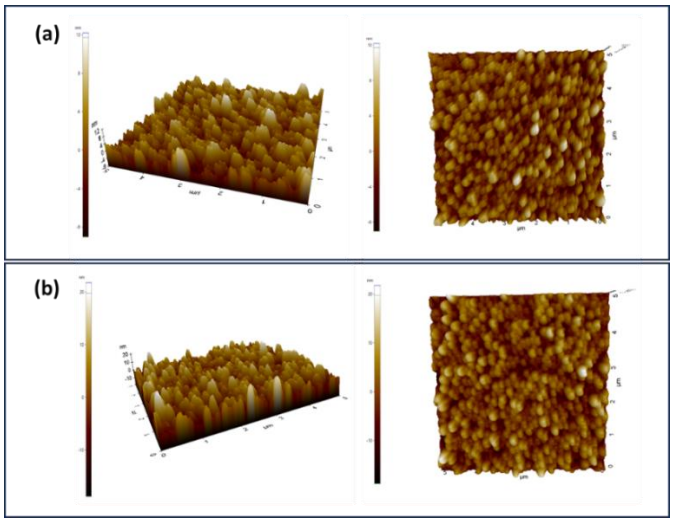

Figure 4: *(a) AFM image of the BTO 15nm film, (b) BTO 30nm film*

The SE barrier refers to the case when an adatom diffuses down an island of multiple layers during thin-film deposition. A high SE barrier means that atoms deposited on the islands can leave them with a higher probability before another atom nucleates on them. If the CMO S-E barrier is lower and the intensity of the laser beam is higher, it leads to the growth of islands instead of layer-by-layer growth.

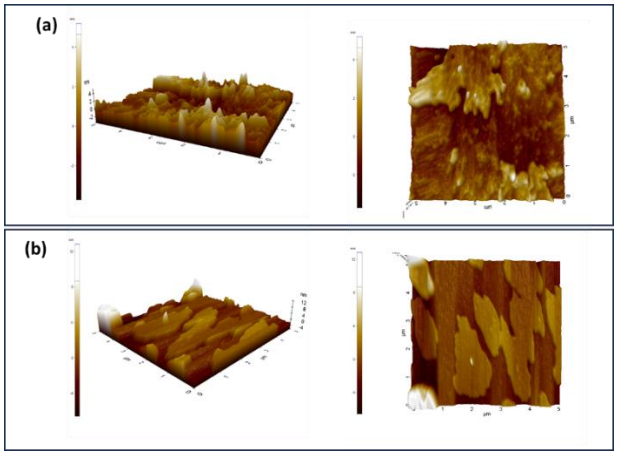

Figure 5: *(a) AFM image of the CMO 15nm film, (b) CMO 30nm film*

Magnetic measurement of the CMO 30 nm film shows a ferromagnetic M-H loop at 5K after diamagnetic subtraction [Figure 6].

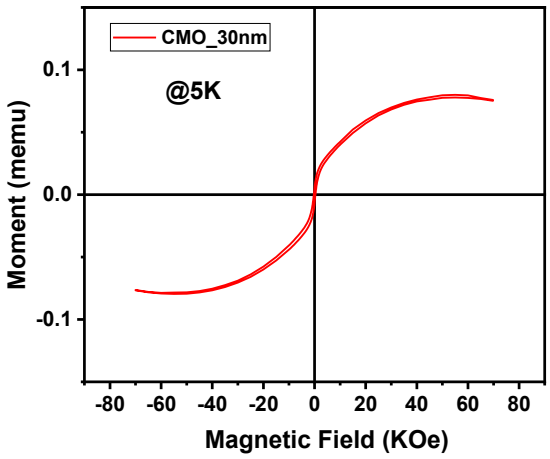

Figure 6: *M-H loop of CMO 15 nm film at 5K*

Conclusions

$BaTiO_3$ epitaxial films are formed with uniform grain growth for the preferred growth conditions on $SrTiO_3$ substrate. $CaMnO_3$ growth on $SrTiO_3$ substrate leads to island growth formation under the given growth conditions. The PLD growth conditions need to be modified for the epitaxial growth of $CaMnO_3$ thin films on $SrTiO_3$.

REFERENCES

[1] D. Fu, M. Itoh, D. Fu, and M. Itoh, “Role of Ca off-Centering in Tuning Ferroelectric Phase Transitions in Ba(Zr,Ti)O3System,” in *Ferroelectric Materials - Synthesis and Characterization*, IntechOpen, 2015. doi: 10.5772/61017.

[2] “High dielectric constant ceramics | Industrial & Engineering Chemistry.” Accessed: May 20, 2025. [Online]. Available: https://pubs.acs.org/doi/10.1021/ie50443a009

[3] B. M. Wul and I. M. Goldman, “Dielectric constant of barium titanate as a function of strength of an alternating field,” *Compt Rend Acad Sci URSS*, vol. 46, pp. 154–57, 1945.

[4] “Changes in Polycrystalline Barium-Strontium Titanate at its Transition Temperature | Nature.” Accessed: May 20, 2025. [Online]. Available: https://www.nature.com/articles/157020a0

[5] H. F. Kay and P. and Vousden, “XCV. Symmetry changes in barium titanate at low temperatures and their relation to its ferroelectric properties,” *The London, Edinburgh, and Dublin Philosophical Magazine and Journal of Science*, vol. 40, no. 309, pp. 1019–1040, Oct. 1949, doi: 10.1080/14786444908561371.

[6] S. Miyake and R. Ueda, “On polymorphic change of BaTiO3,” *Journal of the Physical Society of Japan*, vol. 1, no. 1, pp. 32–33, 1932.

[7] R. B. Gray, “Transducer and method of making the same,” Nov. 01, 1949 Accessed: May 20, 2025. [Online]. Available: https://patents.google.com/patent/US2486560A/en

[8] P. W. Forsbergh, “Domain Structures and Phase Transitions in Barium Titanate,” *Phys. Rev.*, vol. 76, no. 8, pp. 1187–1201, Oct. 1949, doi: 10.1103/PhysRev.76.1187.

[9] W. L. Cherry and R. Adler, “Piezoelectric Effect in Polycrystalline Barium Titanate,” *Phys. Rev.*, vol. 72, no. 10, pp. 981–982, Nov. 1947, doi: 10.1103/PhysRev.72.981.

[10] “A stand out family | Nature Materials.” Accessed: May 20, 2025. [Online]. Available: https://www.nature.com/articles/s41563-021-01127-8

[11] M. Mohan, N. P. Shetti, and T. M. Aminabhavi, “Perovskites: A new generation electrode materials for storage applications,” *Journal of Power Sources*, vol. 574, p. 233166, Aug. 2023, doi: 10.1016/j.jpowsour.2023.233166.

[12] P. Maneesha, S. Chandra Baral, E. G. Rini, and S. Sen, “An overview of the recent developments in the structural correlation of magnetic and electrical properties of *Pr*2*NiMnO*6 double perovskite,” *Progress in Solid State Chemistry*, vol. 70, p. 100402, June 2023, doi: 10.1016/j.progsolidstchem.2023.100402.

[13] C. Autieri, M. Cuoco, and C. Noce, “Structural and electronic properties of ${\mathrm{Sr}}_{2}$${\mathrm{RuO}}_{4}$${\mathrm{/Sr}}_{3}$${\mathrm{Ru}}_{2}$${\mathrm{O}}_{7}$ heterostructures,” *Phys. Rev. B*, vol. 89, no. 7, p. 075102, Feb. 2014, doi: 10.1103/PhysRevB.89.075102.

[14] S. C. Baral, P. Maneesha, E. G. Rini, and S. Sen, “Recent advances in *La2NiMnO6* double perovskites for various applications; challenges and opportunities,” *Progress in Solid State Chemistry*, vol. 72, p. 100429, Dec. 2023, doi: 10.1016/j.progsolidstchem.2023.100429.
[15] V. M. Goldschmidt, “Geochemische verteilungsgesetze der elemente, I Mater,” *Naturvid. Kl*, no. 2, 1926.
[16] G. George, S. R. Ede, and Z. Luo, *Fundamentals of Perovskite Oxides: Synthesis, Structure, Properties and Applications*. Boca Raton: CRC Press, 2020. doi: 10.1201/9780429351419.
[17] J. A. Alonso, M. J. Martínez-Lope, M. T. Casais, and M. T. Fernández-Díaz, “Evolution of the Jahn−Teller Distortion of MnO6 Octahedra in RMnO3 Perovskites (R = Pr, Nd, Dy, Tb, Ho, Er, Y): A Neutron Diffraction Study,” *Inorg. Chem.*, vol. 39, no. 5, pp. 917–923, Mar. 2000, doi: 10.1021/ic990921e.
[18] I. B. Bersuker, “Jahn–Teller and Pseudo-Jahn–Teller Effects: From Particular Features to General Tools in Exploring Molecular and Solid State Properties,” *Chem. Rev.*, vol. 121, no. 3, pp. 1463–1512, Feb. 2021, doi: 10.1021/acs.chemrev.0c00718.
[19] I. B. Bersuker, “A Local Approach to Solid State Problems: Pseudo Jahn-Teller origin of Ferroelectricity and Multiferroicity,” *J. Phys.: Conf. Ser.*, vol. 428, no. 1, p. 012028, Apr. 2013, doi: 10.1088/1742-6596/428/1/012028.
[20] H. P. Paudel, S. R. Acharya, E. J. Popczun, J. W. Lekse, and Y. Duan, “Vacancy-Dependent Diffusion Mechanism in Oxygen-Defective SrFeO3 Perovskite Materials: First-Principles Density Functional Theory and Experimental Approach,” *J. Phys. Chem. C*, vol. 129, no. 14, pp. 6574–6583, Apr. 2025, doi: 10.1021/acs.jpcc.4c08288.
[21] C. A. Stanciu, M. Cernea, E. C. Secu, G. Aldica, P. Ganea, and R. Trusca, “Lanthanum influence on the structure, dielectric properties and luminescence of BaTiO3 ceramics processed by spark plasma sintering technique,” *Journal of Alloys and Compounds*, vol. 706, pp. 538–545, June 2017, doi: 10.1016/j.jallcom.2017.02.258.
[22] P. Pal *et al.*, “Origin and tuning of room-temperature multiferroicity in Fe-doped ${\mathrm{BaTiO}}_{3}$,” *Phys. Rev. B*, vol. 101, no. 6, p. 064409, Feb. 2020, doi: 10.1103/PhysRevB.101.064409.
[23] S. K. Nayak, H. T. Langhammer, W. A. Adeagbo, W. Hergert, T. Müller, and R. Böttcher, “Chromium point defects in hexagonal ${\mathrm{BaTiO}}_{3}$: A comparative study of first-principles calculations and experiments,” *Phys. Rev. B*, vol. 91, no. 15, p. 155105, Apr. 2015, doi: 10.1103/PhysRevB.91.155105.
[24] A. M. Mendes and A. E. Martinelli, “Morphological mapping of high-pressure solvothermal synthesis of BaTiO3 particles,” *Materials Letters*, vol. 256, p. 126597, Dec. 2019, doi: 10.1016/j.matlet.2019.126597.
[25] J. Harada, J. D. Axe, and G. Shirane, “Neutron-Scattering Study of Soft Modes in Cubic BaTi O 3,” *Phys. Rev. B*, vol. 4, no. 1, pp. 155–162, July 1971, doi: 10.1103/PhysRevB.4.155.
[26] M. Paściak, T. R. Welberry, J. Kulda, S. Leoni, and J. Hlinka, “Dynamic Displacement Disorder of Cubic ${\mathrm{BaTiO}}_{3}$,” *Phys. Rev. Lett.*, vol. 120, no. 16, p. 167601, Apr. 2018, doi: 10.1103/PhysRevLett.120.167601.

[27] “NMR study of disorder in and | Phys. Rev. B.” Accessed: May 21, 2025. [Online]. Available: https://journals.aps.org/prb/abstract/10.1103/PhysRevB.71.064107
[28] D. Damjanovic, “Ferroelectric, dielectric and piezoelectric properties of ferroelectric thin films and ceramics,” *Rep. Prog. Phys.*, vol. 61, no. 9, p. 1267, Sept. 1998, doi: 10.1088/0034-4885/61/9/002.
[29] C. Tarantini *et al.*, “Significant enhancement of upper critical fields by doping and strain in iron-based superconductors,” *Phys. Rev. B*, vol. 84, no. 18, p. 184522, Nov. 2011, doi: 10.1103/PhysRevB.84.184522.
[30] “The Theory of Phase Transitions | Nature.” Accessed: Aug. 12, 2025. [Online]. Available: https://www.nature.com/articles/138840a0
[31] A. F. Devonshire, “Theory of ferroelectrics,” *Advances in Physics*, vol. 3, no. 10, pp. 85–130, Apr. 1954, doi: 10.1080/00018735400101173.
[32] E. K. Akdogğan and A. Safari, “Thermodynamics of Ferroelectricity,” in *Piezoelectric and Acoustic Materials for Transducer Applications*, A. Safari and E. K. Akdoğan, Eds., Boston, MA: Springer US, 2008, pp. 3–16. doi: 10.1007/978-0-387-76540-2_1.
[33] J. Akimoto, Y. Gotoh, and Y. Oosawa, “Refinement of hexagonal BaTiO3,” *Acta Cryst C*, vol. 50, no. 2, pp. 160–161, Feb. 1994, doi: 10.1107/S0108270193008637.
[34] “Origin of ferroelectricity in perovskite oxides | Nature.” Accessed: May 21, 2025. [Online]. Available: https://www.nature.com/articles/358136a0
[35] “Nanostructured Ferroelectrics: Fabrication and Structure–Property Relations - Han - 2011 - Advanced Materials - Wiley Online Library.” Accessed: May 21, 2025. [Online]. Available: https://advanced.onlinelibrary.wiley.com/doi/full/10.1002/adma.201102249
[36] M. Acosta *et al.*, “BaTiO3-based piezoelectrics: Fundamentals, current status, and perspectives,” *Applied Physics Reviews*, vol. 4, no. 4, p. 041305, Dec. 2017, doi: 10.1063/1.4990046.
[37] “Applications of Modern Ferroelectrics | Science.” Accessed: May 21, 2025. [Online]. Available: https://www.science.org/doi/10.1126/science.1129564
[38] I. A. Santos and J. A. Eiras, “Phenomenological description of the diffuse phase transition in ferroelectrics,” *J. Phys.: Condens. Matter*, vol. 13, no. 50, pp. 11733–11740, Dec. 2001, doi: 10.1088/0953-8984/13/50/333.
[39] V. Polinger and I. B. Bersuker, “Origin of polar nanoregions and relaxor properties of ferroelectrics,” *Phys. Rev. B*, vol. 98, no. 21, p. 214102, Dec. 2018, doi: 10.1103/PhysRevB.98.214102.
[40] H. Chen, C. Yang, J. Zhang, B. Wang, and H. Ji, “Electrical behavior of BaZr0.1Ti0.9O3 and BaZr0.2Ti0.8O3 thin films,” *Applied Surface Science*, vol. 255, no. 8, pp. 4585–4589, Feb. 2009, doi: 10.1016/j.apsusc.2008.12.003.
[41] K. Funke, “Jump relaxation in solid electrolytes,” *Progress in Solid State Chemistry*, vol. 22, no. 2, pp. 111–195, Jan. 1993, doi: 10.1016/0079-6786(93)90002-9.
[42] A. Ghosh, “Frequency-dependent conductivity in bismuth-vanadate glassy semiconductors,” *Phys. Rev. B*, vol. 41, no. 3, pp. 1479–1488, Jan. 1990, doi: 10.1103/PhysRevB.41.1479.
[43] M. A. Rahman and A. K. M. A. Hossain, “Relaxation mechanism of (x)Mn0.45Ni0.05Zn0.50Fe2O4 + (1 − x)BaZr0.52Ti0.48O3 multiferroic

materials," *Phys. Scr.*, vol. 89, no. 11, p. 115811, Oct. 2014, doi: 10.1088/0031-8949/89/11/115811.
[44] "Microstructures and Electrical Conduction Behaviors of Gd/Cr Codoped Bi3TiNbO9 Aurivillius Phase Ceramic." Accessed: May 19, 2025. [Online]. Available: https://www.mdpi.com/1996-1944/14/19/5598
[45] "Optimization of Pb content in enhancing ferroelectricity and shifting the Tc of BaTiO3 to a higher temperature | Journal of Applied Physics | AIP Publishing." Accessed: May 22, 2025. [Online]. Available: https://pubs.aip.org/aip/jap/article/126/17/174105/595138
[46] "Influence of Ca doping in structural, electronic, optical and mechanical properties of Ba1−xCaxTiO3 perovskite from first-principles investigation | Scientific Reports." Accessed: May 22, 2025. [Online]. Available: https://www.nature.com/articles/s41598-023-36719-8
[47] S. M. Yakout, "Influence of Na and Na/Fe doping on the dielectric constant, ferromagnetic and sunlight photocatalytic properties of BaTiO3 perovskite," *Journal of Solid State Chemistry*, vol. 290, p. 121517, Oct. 2020, doi: 10.1016/j.jssc.2020.121517.
[48] "Preparation and Characterization of Ag-Doped BaTiO3 Conductive Powders - Hao - 2011 - International Journal of Inorganic Chemistry - Wiley Online Library." Accessed: May 22, 2025. [Online]. Available: https://onlinelibrary.wiley.com/doi/10.1155/2011/837091
[49] "Recent Progress on Barium Titanate-Based Ferroelectrics for Sensor Applications - Deng - 2024 - Advanced Sensor Research - Wiley Online Library." Accessed: May 19, 2025. [Online]. Available: https://advanced.onlinelibrary.wiley.com/doi/10.1002/adsr.202300168
[50] S. K. Upadhyay, V. R. Reddy, P. Bag, R. Rawat, S. M. Gupta, and A. Gupta, "Electro-caloric effect in lead-free Sn doped BaTiO3 ceramics at room temperature and low applied fields," *Applied Physics Letters*, vol. 105, no. 11, p. 112907, Sept. 2014, doi: 10.1063/1.4896044.
[51] X. Tong, Y.-H. Lin, S. Zhang, Y. Wang, and C.-W. Nan, "Preparation of Mn-doped BaTiO3 nanoparticles and their magnetic properties," *Journal of Applied Physics*, vol. 104, no. 6, p. 066108, Sept. 2008, doi: 10.1063/1.2973202.
[52] "Enhanced Piezocatalytic Performance of Li-doped BaTiO3 Through a Facile Sonication-Assisted Precipitation Approach - Dong - 2024 - ChemSusChem - Wiley Online Library." Accessed: May 22, 2025. [Online]. Available: https://chemistry-europe.onlinelibrary.wiley.com/doi/full/10.1002/cssc.202400796
[53] "Staruch et al. - 2020 - Magnetic and multiferroic properties of dilute Fe-.pdf." Accessed: May 22, 2025. [Online]. Available: https://watermark.silverchair.com/031109_1_online.pdf?token=AQECAHi208BE49Ooan9kkhW_Ercy7Dm3ZL_9Cf3qfKAc485ysgAAB4swggeHBgkqhkiG9w0BBwagggd4MIIHdAIBADCCB20GCSqGSIb3DQEHATAeBglghkgBZQMEAS4wEQQMlV7H6V1TpjOy5TQXAgEQgIIHPsPQFz8Yy4r_ruIk89VMoBXLydmUqCniwbQxLQLa0gVrVxQkbablgDuYEEbeWNwz8FPGdE2eTN_1RKgR5glWvC7OJQPDv-QF2PuDJmTzdXjOirpaOr5Z-XabCCKrbiPhB7Pd0m-ixBxKKZU3Jrvo7DBVwsPyCLIzEKnYjvRd_rSkIrVwzRE821h5PdAWzt8JCNsFSq40bc529Uyc_49f3F5tFUP7VnBIb9RFEEGQhmfTzKA04SUgZcGJYv1Ys5B4Tt2kEpj7lSMqdzwQ3REMULxKGh6j3ZLSaz-fjgEo8qOuDYiRa-oRxpqdrPQwqIvL6XjXLdTg-

ML07xQcFd4TOcMoDPMbIYRFDUM4rPl7AZDyZxOZFZRSw0Qj1DKiTWpHXLID
U8CAI37V2Yuz6-
ira8hzHm3Ha9lcZfUa7rWZ7fsL__X_PAbZycKN5AjoIoTOQpPPzFf9LmrmHN1q
DP1TrCw1hH6PddQUM0xz7loo80uo4Q7rFnrvqc35mcxFGKdjYWmIFWHBnRI
5SxopyIu-yxVK8C6XZwamL2a56g7g81Mz6HEsoFMUdvpWC-chh35aCMeW-
dWjjqNAC89U4UTmi5RgWdNV1qJwe0dsDFOaioSagylhEA1z6q4g-
XbYbmSpH_x0u4zrJECnWCKxGsuFiE2kKDI8_xN0oa7Dm92EfdCU6XQW3YA7d
dM0H3d6hGxBXencjjz5zEFAO1gj8wYE_ZPnhx0TOdRYYwhbE3_uXUWvyoaN2
QGicRhKnr4m8NvjVp7YD2QFnqgLr-pOfU4Xx-
orwAne4x5MdgdJ8MOYLRcGEPcMLzenhY_yh98k_Egy0HVrGk0V6JmBvjBPxO
NaqS5271vPNowiPJ1FLfeVY-
4w_45QRgvd2JOnsLfHv8Ek5BfvtAAWvhtDWfTyoltI2Q2Xt-
oRTxG420PrZXcQCZ-
mipoXCQ4EwYyLMOyQxeJoCzRQqXcY9SAmZVie31r1ktNi-
IjkrGNZBM65t8ngXklFIUWj2ilnDKsd2lTsDBJU8zpMCe-tN0J7XyqG-
d8SbLGmcCzK3pZPyXGjq-10eaoymacC3XnbgSNjZ9NhvMSBsElSkJ_rxB-
ENIUDQjEtlNZ8S1aE3SNWcRcls_VETZnwmUjccImpswHxm55fR6wm-
4LKW81sDtSyHsm-
k676e64wtn2BohjprJ6Aeo2SXTGBnT6rHXennCqpNRDWIz0KwhxiJpBdT-
jN9AiO_2kt8okebGu8hQF__qFFmCh2ULV7-
DvPnbJyCJi20xsNLZfSWwF6_nMakSF-
9tZ57CFPnWMPcNlxrqyQGQs2HdbVXCWmEnTMNgom53SSKnFzBlnq1oVkKci
0zRtqcMXy72qu82TLPMATNu2bHP1exKqq59HgGbYKVFEUWhgG_EOYgs-
WlE1oh79YVpRDvSnkCLFLHvsZqfd0vTT-
cMtYoNY_7BrXaqiJFvCtHJDT6Cjk9PIj3ATI8I68HH99MuVA0aq-
mYEn2LUUP4J8Qoy9gkQ5Zu8BBb62Lu8gXlUwXJ7qE3BYbAWdvAQoFlu_KuM
LkO9szyifdOr240Z_GhZHXVcZj4bU3hXlMWN3_Go4TfrRX47LKG7Ub4tNTYqq
G_Oq8qSPAu8XHdwkdDGx-xYSvfMMlFGHww0YoAW0jbFF8D-
Gjr1GRzYvsDI7f_JWkzX9x9UTtPMDcDIzVhTyXozeoVJxVfvauRXM2ORNQM9F
20dk6aAL1JPOc6Y5ZUCWMrrMZEZu1STLZRHlQijoBJQsEV2RVvIjB60TQbovQtl
uXg6aRo9k2C5dNcGuuVq-
3wOoQA1Ba8lOpjLWZbOF2OS4ksmsOMwtqfAmdcOCBG0ICSQ0Bh-
F6uHSxPDgkAWmk64rEMWhZG_ra7rWAiaFEaqHPLRFYGf5pRIEr6BhIsFPn0b8
m_8RL8iit6DapYoLU2mnstz3Hsi4mh7F9LWUKm427ftpsE4dAPNgRbtoPyJvTB
yNrVg5ZTDBe6OPlpnAYwMlE5vu6IcIgzwmhBQLqtD-
W803U0egh9AAMEPuJfE-
ql6Fk5jp2UgzhsyrmiFKrN4XXtmfrUNQZtJDaVSpcpEjYxfVIz8X9NNSNn73OKIpg
tOBpocjYDpHYmfQN0EWaIgoPXBRE2Jz-
VCERXB_1v_Apu15JsmQAgHXKxZN1B8cHjsAbKkHDPk0Cp7-
7WCYDpRj57tcEpJMTNxBDNHp7THKQankSA6UT_vx_3JVIsYOABAfsvkwxnSlK
zRSJXqHNbeZAtl3935L1SC4UrPfHHQ525EWhKQxO_a5O6-Rwg-
eWlkqOFghcQaZTbv_szgRYuC8uriyqSTp4G4Yu1YLI8yWjXubv8Ifzy2zVn__eZ2
s--
lIv2k805BCYmQleVSVdcNw5HN0HJO9dOXEpPxRRLC4elcjZ0LqyhdehaigLGYU
22uq83b7ICmmezrlLYzGPR6yv3Qwwvkf7rJrSufF12BVqqCIJg

[54] U. Younas *et al.*, “Fabrication of La 3+ doped Ba 1−x La x TiO 3 ceramics with improved dielectric and ferroelectric properties using a composite-hydroxide-mediated method,” *RSC Advances*, vol. 13, no. 8, pp. 5293–5306, 2023, doi: 10.1039/D2RA06640H.

[55] V. Buscaglia, M. T. Buscaglia, and G. Canu, “BaTiO3-Based Ceramics: Fundamentals, Properties and Applications,” in *Encyclopedia of Materials: Technical Ceramics and Glasses*, M. Pomeroy, Ed., Oxford: Elsevier, 2021, pp. 311–344. doi: 10.1016/B978-0-12-803581-8.12132-0.

[56] R. Machado, A. Di Loreto, A. Frattini, M. Sepliarsky, and M. G. Stachiotti, “Site occupancy effects of Mg impurities in BaTiO3,” *Journal of Alloys and Compounds*, vol. 809, p. 151847, Nov. 2019, doi: 10.1016/j.jallcom.2019.151847.

[57] Z. Hanani *et al.*, “Thermally-stable high energy storage performances and large electrocaloric effect over a broad temperature span in lead-free BCZT ceramic,” *RSC Advances*, vol. 10, no. 51, pp. 30746–30755, 2020, doi: 10.1039/D0RA06116F.

[58] M. Mahesh Kumar, M. B. Suresh, and S. V. Suryanarayana, “Electrical and dielectric properties in double doped BaTiO3 showing relaxor behavior,” *Journal of Applied Physics*, vol. 86, no. 3, pp. 1634–1637, Aug. 1999, doi: 10.1063/1.370939.

[59] “Ferromagnetism in Fe-doped BaTiO3 Ceramics | Journal of Superconductivity and Novel Magnetism.” Accessed: May 22, 2025. [Online]. Available: https://link.springer.com/article/10.1007/s10948-017-4321-0

[60] S. K. Das, B. K. Roul, V. Mohanta, S. K. Behera, and M. Sahu, “Defect mediated magnetism in CO based BaTiO3 ferroelectric,” *Physica B: Condensed Matter*, vol. 465, pp. 38–44, May 2015, doi: 10.1016/j.physb.2015.03.010.

[61] N. Dang, T. Thanh, L. Hong, V. Lam, and T. Phan, “Structural, Optical and Magnetic Properties of Polycrystalline BaTi1−xFexO3 Ceramics,” *Journal of Applied Physics*, vol. 110, pp. 043914–043914, Aug. 2011, doi: 10.1063/1.3625235.

[62] R. Amin, K. Samantaray, S. Ayaz, S. N. Sarangi, I. Bhaumik, and S. Sen, “Room temperature multiferroicity with enhanced ferroelectric and ferromagnetic properties in Ba0.75Pb0.25Ti1-xFexO3,” *Journal of Alloys and Compounds*, vol. 897, p. 162734, Mar. 2022, doi: 10.1016/j.jallcom.2021.162734.

[63] “Origin of ferromagnetism in transition metal doped BaTiO3 | Journal of Applied Physics | AIP Publishing.” Accessed: May 22, 2025. [Online]. Available: https://pubs.aip.org/aip/jap/article/113/20/203904/991534/Origin-of-ferromagnetism-in-transition-metal-doped

[64] “A review on current status and mechanisms of room-temperature magnetoelectric coupling in multiferroics for device applications | Journal of Materials Science.” Accessed: Aug. 12, 2025. [Online]. Available: https://link.springer.com/article/10.1007/s10853-022-07377-4

[65] P. Senthilkumar, S. Dhanuskodi, J. Karthikeyan, and P. Murugan, “dz2 orbital-mediated bound magnetic polarons in ferromagnetic Ce-doped BaTiO3 nanoparticles and their enriched two-photon absorption cross-section,” *Phys. Chem. Chem. Phys.*, vol. 21, no. 7, pp. 4032–4045, Feb. 2019, doi: 10.1039/C8CP06055J.

[66] N. V. Dang, T.-L. Phan, T. D. Thanh, V. D. Lam, and L. V. Hong, “Structural phase separation and optical and magnetic properties of BaTi1−xMnxO3 multiferroics,” *Journal of Applied Physics*, vol. 111, no. 11, p. 113913, June 2012, doi: 10.1063/1.4725195.

[67] P. Pal *et al.*, “Engineering room-temperature multiferroicity in Bi and Fe codoped BaTiO3,” *Applied Physics Letters*, vol. 117, no. 1, p. 012901, July 2020, doi: 10.1063/5.0004785.
[68] J. Shah and R. K. Kotnala, “Induced magnetism and magnetoelectric coupling in ferroelectric BaTiO3 by Cr-doping synthesized by a facile chemical route,” *J. Mater. Chem. A*, vol. 1, no. 30, pp. 8601–8608, July 2013, doi: 10.1039/C3TA11845B.
[69] K. C. Verma and R. K. Kotnala, “Multiferroic approach for Cr,Mn,Fe,Co,Ni,Cu substituted BaTiO3 nanoparticles,” *Mater. Res. Express*, vol. 3, no. 5, p. 055006, May 2016, doi: 10.1088/2053-1591/3/5/055006.
[70] R. Sharma *et al.*, “Doping stimulated ferromagnetic ordering and tailoring of the dielectric properties of Ba 1−x Ce x TiO 3,” *Materials Advances*, vol. 5, no. 21, pp. 8638–8651, 2024, doi: 10.1039/D4MA00593G.
[71] J. Nie, G. Xu, Y. Yang, and C. Cheng, “Strong magnetoelectric coupling in CoFe2O4–BaTiO3 composites prepared by molten-salt synthesis method,” *Materials Chemistry and Physics*, vol. 115, no. 1, pp. 400–403, May 2009, doi: 10.1016/j.matchemphys.2008.12.011.
[72] Z. Shi, J. Zhang, D. Gao, Z. Zhu, Z. Yang, and Z. Zhang, “Giant magnetoelectric coupling observed at high frequency in $NiFe_2O_4$ –$BaTiO_3$ particulate composite,” *RSC Adv.*, vol. 10, no. 45, pp. 27242–27248, 2020, doi: 10.1039/D0RA05782G.
[73] D. V. Karpinsky, R. C. Pullar, Y. K. Fetisov, K. E. Kamentsev, and A. L. Kholkin, “Local probing of magnetoelectric coupling in multiferroic composites of BaFe12O19–BaTiO3,” *J. Appl. Phys.*, vol. 108, no. 4, Aug. 2010, doi: 10.1063/1.3474967.
[74] G. Dong *et al.*, “Strain-Induced Magnetoelectric Coupling in Fe3O4/BaTiO3 Nanopillar Composites,” *ACS Appl. Mater. Interfaces*, vol. 14, no. 11, pp. 13925–13931, Mar. 2022, doi: 10.1021/acsami.2c00058.
[75] T. Buttlar, T. Walther, K. Dörr, and S. G. Ebbinghaus, “Preparation and Magnetoelectric Behavior of Ni/BaTiO3 Heterostructures with 0-3 Connectivity,” *physica status solidi (b)*, vol. 257, no. 7, p. 1900622, 2020, doi: 10.1002/pssb.201900622.
[76] H.-I. Hsiang, Y.-H. Yang, C.-Y. Huang, and K.-H. Yang, “Dielectric properties of BaTiO3 and Ba0.95Ca0.05TiO3 sintered in a reducing atmosphere,” *Ceramics International*, vol. 49, no. 17, Part B, pp. 28751–28757, Sept. 2023, doi: 10.1016/j.ceramint.2023.06.134.
[77] Z. Yao *et al.*, “Structure and dielectric behavior of Nd-doped BaTiO3 perovskites,” *Materials Chemistry and Physics*, vol. 109, no. 2, pp. 475–481, June 2008, doi: 10.1016/j.matchemphys.2007.12.019.
[78] M. Ganguly *et al.*, “Characterization and Rietveld Refinement of A-site deficient Lanthanum doped Barium Titanate,” *Journal of Alloys and Compounds*, vol. 579, pp. 473–484, Dec. 2013, doi: 10.1016/j.jallcom.2013.06.104.
[79] Z. Li, J. Yu, S. Hao, and P.-E. Janolin, “Enhancing properties of lead-free ferroelectric BaTiO3 through doping,” *Journal of the European Ceramic Society*, vol. 42, no. 12, pp. 4693–4701, Sept. 2022, doi: 10.1016/j.jeurceramsoc.2022.05.023.
[80] F. Yang *et al.*, “Tailoring Bandgap of Perovskite BaTiO3 by Transition Metals Co-Doping for Visible-Light Photoelectrical Applications: A First-Principles

Study," *Nanomaterials (Basel)*, vol. 8, no. 7, p. 455, June 2018, doi: 10.3390/nano8070455.
[81] P. M. K., B. B., V. T.p., R. M. T.v., and V. G. B. M., "Experimental and first-principles investigation of structural, electronic, optical, elastic and ferroelectric properties of BaTiO3<math><msub is="true"><mrow is="true"></mrow><mrow is="true"><mn is="true">3</mn></mrow></msub></math>," *Physica B: Condensed Matter*, vol. 674, p. 415548, Feb. 2024, doi: 10.1016/j.physb.2023.415548.
[82] "Optical investigation and computational modelling of BaTiO3 for optoelectronic devices applications | Scientific Reports." Accessed: May 22, 2025. [Online]. Available: https://www.nature.com/articles/s41598-023-31652-2
[83] A. Boubaia, A. Assali, S. Berrah, H. Bennacer, I. Zerifi, and A. Boukortt, "Band gap and emission wavelength tuning of Sr-doped BaTiO3 (BST) perovskites for high-efficiency visible-light emitters and solar cells," *Materials Science in Semiconductor Processing*, vol. 130, p. 105837, Aug. 2021, doi: 10.1016/j.mssp.2021.105837.
[84] M. Rizwan, Hajra, I. Zeba, M. Shakil, S. S. A. Gillani, and Z. Usman, "Electronic, structural and optical properties of BaTiO3 doped with lanthanum (La): Insight from DFT calculation," *Optik*, vol. 211, p. 164611, June 2020, doi: 10.1016/j.ijleo.2020.164611.
[85] Md. A. Islam, Md. A. Momin, and M. Nesa, "Effect of Fe doping on the structural, optical and electronic properties of BaTiO3: DFT based calculation," *Chinese Journal of Physics*, vol. 60, pp. 731–738, Aug. 2019, doi: 10.1016/j.cjph.2019.06.013.
[86] A. D. Becke and K. E. Edgecombe, "A simple measure of electron localization in atomic and molecular systems," *J. Chem. Phys.*, vol. 92, no. 9, pp. 5397–5403, May 1990, doi: 10.1063/1.458517.
[87] "Giant Electric Field Tuning of Magnetic Properties in Multiferroic Ferrite/Ferroelectric Heterostructures - Liu - 2009 - Advanced Functional Materials - Wiley Online Library." Accessed: Aug. 12, 2025. [Online]. Available: https://advanced.onlinelibrary.wiley.com/doi/10.1002/adfm.200801907
[88] "B.D. Cullity, S.R. Stock - Elements of X-Ray Diffraction-Pearson Education Limited (2014).pdf." Accessed: June 02, 2025. [Online]. Available: https://www.eng.uc.edu/~beaucag/Classes/AdvancedMaterialsThermodynamics/Books/B.D.%20Cullity,%20S.R.%20Stock%20-%20Elements%20of%20X-Ray%20Diffraction-Pearson%20Education%20Limited%20(2014).pdf
[89] L. Brügemann and E. K. E. Gerndt, "Detectors for X-ray diffraction and scattering: a user's overview," *Nuclear Instruments and Methods in Physics Research Section A: Accelerators, Spectrometers, Detectors and Associated Equipment*, vol. 531, no. 1, pp. 292–301, Sept. 2004, doi: 10.1016/j.nima.2004.06.019.
[90] S. A. Hassanzadeh-Tabrizi, "Precise calculation of crystallite size of nanomaterials: A review," *Journal of Alloys and Compounds*, vol. 968, p. 171914, Dec. 2023, doi: 10.1016/j.jallcom.2023.171914.
[91] Z. Yang, Y. Lu, X. Liu, F. Li, and J. Chen, "Application of high energy X-ray diffraction and Rietveld refinement in layered lithium transition metal oxide cathode materials," *Nano Research*, vol. 16, no. 7, pp. 9954–9967, July 2023, doi: 10.1007/s12274-023-5630-1.

[92] C. V. Raman and K. S. Krishnan, “A New Type of Secondary Radiation,” *Nature*, vol. 121, no. 3048, pp. 501–502, Mar. 1928, doi: 10.1038/121501c0.
[93] “Instrument Presentation.” Accessed: June 03, 2025. [Online]. Available: https://www.horiba.com/ind/scientific/technologies/raman-imaging-and-spectroscopy/raman-spectrometer-presentation/
[94] J. Tauc, R. Grigorovici, and A. Vancu, “Optical Properties and Electronic Structure of Amorphous Germanium,” *Physica Status Solidi (b)*, vol. 15, no. 2, pp. 627–637, Jan. 1966, doi: 10.1002/pssb.19660150224.
[95] “Investigating the correlation between the Urbach energy and asymmetry parameter of the Raman mode in semiconductors | Phys. Rev. B.” Accessed: May 20, 2025. [Online]. Available: https://journals.aps.org/prb/abstract/10.1103/PhysRevB.104.245205
[96] S. Hofmann, “Qualitative Analysis (Principle and Spectral Interpretation),” in *Auger- and X-Ray Photoelectron Spectroscopy in Materials Science*, vol. 49, in Springer Series in Surface Sciences, vol. 49. , Berlin, Heidelberg: Springer Berlin Heidelberg, 2013, pp. 43–76. doi: 10.1007/978-3-642-27381-0_3.
[97] F. A. Stevie and C. L. Donley, “Introduction to x-ray photoelectron spectroscopy,” *Journal of Vacuum Science & Technology A*, vol. 38, no. 6, p. 063204, Dec. 2020, doi: 10.1116/6.0000412.
[98] J. F. Watts and J. Wolstenholme, *An introduction to surface analysis by XPS and AES*, Repr. New York Weinheim: Wiley, 2008.
[99] D. Briggs, “Handbook of X-ray Photoelectron Spectroscopy C. D. Wanger, W. M. Riggs, L. E. Davis, J. F. Moulder and G. E.Muilenberg Perkin-Elmer Corp., Physical Electronics Division, Eden Prairie, Minnesota, USA, 1979. 190 pp. $195,” *Surface and Interface Analysis*, vol. 3, no. 4, pp. v–v, 1981, doi: 10.1002/sia.740030412.
[100] J. D. Andrade, “X-ray Photoelectron Spectroscopy (XPS),” in *Surface and Interfacial Aspects of Biomedical Polymers: Volume 1 Surface Chemistry and Physics*, J. D. Andrade, Ed., Boston, MA: Springer US, 1985, pp. 105–195. doi: 10.1007/978-1-4684-8610-0_5.
[101] “X-ray Photoelectron Spectroscopy,” Methods. Accessed: June 04, 2025. [Online]. Available: https://serc.carleton.edu/msu_nanotech/methods/xps.html
[102] “Indus 2. RRCAT.” [Online]. Available: https://www.rrcat.gov.in/technology/accel/srul/beamlines/exafsscan.html
[103] “XANES: X-ray Absorption Near Edge Structure - - Diamond Light Source.” Accessed: June 04, 2025. [Online]. Available: https://www.diamond.ac.uk/Instruments/Techniques/Spectroscopy/XANES.html
[104] B. Ravel and M. Newville, “ATHENA, ARTEMIS, HEPHAESTUS: data analysis for X-ray absorption spectroscopy using IFEFFIT,” *J Synchrotron Radiat*, vol. 12, no. Pt 4, pp. 537–541, July 2005, doi: 10.1107/S0909049505012719.
[105] “1585214437_PHY(H)-VI-NANO_MATERIAL-11-AJAYPRATAP.pdf.” Accessed: June 05, 2025. [Online]. Available: https://www.deshbandhucollege.ac.in/pdf/resources/1585214437_PHY(H)-VI-NANO_MATERIAL-11-AJAYPRATAP.pdf
[106] “JEM-F200 Multi-purpose Electron Microscope | Products | JEOL Ltd.,” JEM-F200 Multi-purpose Electron Microscope | Products | JEOL Ltd. Accessed: Aug. 05, 2025. [Online]. Available: https://www.jeol.com/

[107] P. January 31 and 2014, “Advanced Electron Paramagnetic Resonance Spectroscopy for the Identification of Irradiated Food.” Accessed: Aug. 18, 2025. [Online]. Available: https://www.americanlaboratory.com/914-Application-Notes/154111-Advanced-Electron-Paramagnetic-Resonance-Spectroscopy-for-the-Identification-of-Irradiated-Food/
[108] M. M. Roessler and E. Salvadori, “Principles and applications of EPR spectroscopy in the chemical sciences,” *Chem. Soc. Rev.*, vol. 47, no. 8, pp. 2534–2553, 2018, doi: 10.1039/C6CS00565A.
[109] M. Choi, F. Oba, and I. Tanaka, “Electronic and structural properties of the oxygen vacancy in BaTiO3,” *Applied Physics Letters*, vol. 98, no. 17, p. 172901, Apr. 2011, doi: 10.1063/1.3583460.
[110] “Measurement of polarisation.” Accessed: June 05, 2025. [Online]. Available: https://www.doitpoms.ac.uk/tlplib/ferroelectrics/measuring_pol.php
[111] “1307-010.pdf.” Accessed: June 06, 2025. [Online]. Available: https://qdusa.com/siteDocs/productBrochures/1307-010.pdf
[112] “main-vision-manual-ii-precision-testers-and-accessories.pdf.” Accessed: Aug. 11, 2025. [Online]. Available: https://www.ferrodevices.com/download/5891/main-vision-manual-ii-precision-testers-and-accessories.pdf
[113] G. Kresse and J. Hafner, “Ab initio molecular dynamics for liquid metals,” *Phys. Rev. B*, vol. 47, no. 1, pp. 558–561, Jan. 1993, doi: 10.1103/PhysRevB.47.558.
[114] G. Kresse and J. Furthmüller, “Efficient iterative schemes for ab initio total-energy calculations using a plane-wave basis set,” *Phys. Rev. B*, vol. 54, no. 16, pp. 11169–11186, Oct. 1996, doi: 10.1103/PhysRevB.54.11169.
[115] G. Kresse and D. Joubert, “From ultrasoft pseudopotentials to the projector augmented-wave method,” *Phys. Rev. B*, vol. 59, no. 3, pp. 1758–1775, Jan. 1999, doi: 10.1103/PhysRevB.59.1758.
[116] G. Kresse and J. Hafner, “Ab initio molecular dynamics for liquid metals,” *Phys. Rev. B*, vol. 47, no. 1, pp. 558–561, Jan. 1993, doi: 10.1103/PhysRevB.47.558.
[117] G. Kresse and D. Joubert, “From ultrasoft pseudopotentials to the projector augmented-wave method,” *Phys. Rev. B*, vol. 59, no. 3, pp. 1758–1775, Jan. 1999, doi: 10.1103/PhysRevB.59.1758.
[118] J. P. Perdew, K. Burke, and M. Ernzerhof, “Generalized Gradient Approximation Made Simple,” *Phys. Rev. Lett.*, vol. 77, no. 18, pp. 3865–3868, Oct. 1996, doi: 10.1103/PhysRevLett.77.3865.
[119] H. J. Monkhorst and J. D. Pack, “Special points for Brillouin-zone integrations,” *Phys. Rev. B*, vol. 13, no. 12, pp. 5188–5192, June 1976, doi: 10.1103/PhysRevB.13.5188.
[120] S.-W. Cheong and M. Mostovoy, “Multiferroics: a magnetic twist for ferroelectricity,” *Nature Mater*, vol. 6, no. 1, pp. 13–20, Jan. 2007, doi: 10.1038/nmat1804.
[121] “Magnetoelectrics: Three Centuries of Research Heading Towards the 4.0 Industrial Revolution.” Accessed: Aug. 21, 2025. [Online]. Available: https://www.mdpi.com/1996-1944/13/18/4033
[122] “A review on current status and mechanisms of room-temperature magnetoelectric coupling in multiferroics for device applications | Journal of Materials Science.” Accessed: Aug. 21, 2025. [Online]. Available: https://link.springer.com/article/10.1007/s10853-022-07377-4

[123] A. C. Lima, N. Pereira, P. Martins, and S. Lanceros-Mendez, “Chapter 2 - Magnetic materials for magnetoelectric coupling: An unexpected journey,” in *Handbook of Magnetic Materials*, vol. 29, E. Brück, Ed., Elsevier, 2020, pp. 57–110. doi: 10.1016/bs.hmm.2020.09.002.
[124] A. Raeliarijaona, “Ferromagnetism in ferroelectric <math xmlns="http://www.w3.org/1998/Math/MathML"><msub><mi>BaTiO</mi><mn>3</mn></msub></math> induced by vacancies: Sensitive dependence on charge state, origin of magnetism, and temperature range of existence,” *Phys. Rev. B*, vol. 96, no. 14, 2017, doi: 10.1103/PhysRevB.96.144431.
[125] T. Costanzo, J. McCracken, A. Rotaru, and G. Caruntu, “Quasi-Monodisperse Transition-Metal-Doped BaTiO3 (M = Cr, Mn, Fe, Co) Colloidal Nanocrystals with Multiferroic Properties,” *ACS Applied Nano Materials*, Sept. 2018, doi: 10.1021/acsanm.8b01036.
[126] Y.-H. Lin *et al.*, “Multiferroic behavior observed in highly orientated Mn-doped BaTiO3 thin films,” *Appl. Phys. Lett.*, vol. 95, no. 3, July 2009, doi: 10.1063/1.3182793.
[127] “Room-temperature magnetoelectric coupling in single-phase BaTiO3-BiFeO3 system | Journal of Applied Physics | AIP Publishing.” Accessed: Aug. 21, 2025. [Online]. Available: https://pubs.aip.org/aip/jap/article/113/14/144101/689252/Room-temperature-magnetoelectric-coupling-in
[128] S. Sahoo, S. Das, P. K. Mahapatra, and R. N. P. Choudhary, “Fabrication and characterization of LaFeO3-BaTiO3 electroceramics,” *Materials Chemistry and Physics*, vol. 216, pp. 158–169, Sept. 2018, doi: 10.1016/j.matchemphys.2018.05.032.
[129] “Large magneto-electric effects in hexagonal La0.7Ba0.3MnO3-BaTiO3 solid solutions and magneto-electric coupling mechanism discussion | Journal of Applied Physics | AIP Publishing.” Accessed: Aug. 21, 2025. [Online]. Available: https://pubs.aip.org/aip/jap/article/116/13/134103/857504/Large-magneto-electric-effects-in-hexagonal-La0
[130] S. Dabas, M. Kumar, P. Chaudhary, and O. P. Thakur, “Enhanced magneto-electric coupling and energy storage analysis in Mn-modified lead free BiFeO3-BaTiO3 solid solutions,” *J. Appl. Phys.*, vol. 126, no. 13, Oct. 2019, doi: 10.1063/1.5119291.
[131] M. M. Niu, J. Liu, T. L. Sun, R. Z. Jiang, D. H. Hou, and D. Xu, “Effect of transition metal element substitution on magnetoelectric properties of BiFeO3-BaTiO3 ceramics,” *Journal of Alloys and Compounds*, vol. 859, p. 158224, Apr. 2021, doi: 10.1016/j.jallcom.2020.158224.
[132] “A new (Ba, Ca) (Ti, Zr)O3 based multiferroic composite with large magnetoelectric effect | Scientific Reports.” Accessed: Aug. 21, 2025. [Online]. Available: https://www.nature.com/articles/srep32164
[133] “Multiple magnetoelectric coupling effect in BaTiO3/Sr2CoMoO6 heterostructures | Scientific Reports.” Accessed: Aug. 21, 2025. [Online]. Available: https://www.nature.com/articles/s41598-017-03876-6
[134] “Nanoparticle-Based Magnetoelectric BaTiO3–CoFe2O4 Thin Film Heterostructures for Voltage Control of Magnetism | ACS Nano.” Accessed:

Aug. 21, 2025. [Online]. Available: https://pubs.acs.org/doi/full/10.1021/acsnano.6b05469
[135] “Advances in magnetoelectric multiferroics | Nature Materials.” Accessed: Aug. 21, 2025. [Online]. Available: https://www.nature.com/articles/s41563-018-0275-2
[136] “Enhancement of tetragonal anisotropy and stabilisation of the tetragonal phase by Bi/Mn-double-doping in BaTiO3 ferroelectric ceramics | Scientific Reports.” Accessed: Aug. 21, 2025. [Online]. Available: https://www.nature.com/articles/srep45842
[137] “Structural, spectroscopic and dielectric properties of Ca-doped BaTiO3 | Applied Physics A.” Accessed: Aug. 21, 2025. [Online]. Available: https://link.springer.com/article/10.1007/s00339-019-2487-y
[138] “Influence of Ca doping in structural, electronic, optical and mechanical properties of Ba1−xCaxTiO3 perovskite from first-principles investigation | Scientific Reports.” Accessed: Aug. 21, 2025. [Online]. Available: https://www.nature.com/articles/s41598-023-36719-8
[139] “Preparation of Mn-doped BaTiO3 nanoparticles and their magnetic properties | Journal of Applied Physics | AIP Publishing.” Accessed: Aug. 21, 2025. [Online]. Available: https://pubs.aip.org/aip/jap/article/104/6/066108/344220/Preparation-of-Mn-doped-BaTiO3-nanoparticles-and
[140] S. K. Nayak, “Chromium point defects in hexagonal <math xmlns="http://www.w3.org/1998/Math/MathML"><msub><mi>BaTiO</mi><mn>3</mn></msub></math>: A comparative study of first-principles calculations and experiments,” *Phys. Rev. B*, vol. 91, no. 15, 2015, doi: 10.1103/PhysRevB.91.155105.
[141] “Structural Polymorphism of Mn-Doped BaTiO3 | Journal of Electronic Materials.” Accessed: Aug. 21, 2025. [Online]. Available: https://link.springer.com/article/10.1007/s11664-016-4382-z
[142] “Origin and tuning of room-temperature multiferroicity in Fe-doped | Phys. Rev. B.” Accessed: Aug. 20, 2025. [Online]. Available: https://journals.aps.org/prb/abstract/10.1103/PhysRevB.101.064409
[143] P. Pal, “Origin and tuning of room-temperature multiferroicity in Fe-doped <math xmlns="http://www.w3.org/1998/Math/MathML"><msub><mi>BaTiO</mi><mn>3</mn></msub></math>,” *Phys. Rev. B*, vol. 101, no. 6, 2020, doi: 10.1103/PhysRevB.101.064409.
[144] “Engineering room-temperature multiferroicity in Bi and Fe codoped BaTiO3 | Applied Physics Letters | AIP Publishing.” Accessed: Aug. 20, 2025. [Online]. Available: https://pubs.aip.org/aip/apl/article/117/1/012901/39002/Engineering-room-temperature-multiferroicity-in-Bi
[145] “Modified Phase Diagram for the Barium Oxide–Titanium Dioxide System for the Ferroelectric Barium Titanate - Lee - 2007 - Journal of the American Ceramic Society - Wiley Online Library.” Accessed: Aug. 21, 2025. [Online]. Available: https://ceramics.onlinelibrary.wiley.com/doi/full/10.1111/j.1551-2916.2007.01794.x
[146] J. L. Clabel H *et al.*, “Insights on the mechanism of solid state reaction between TiO2 and BaCO3 to produce BaTiO3 powders: The role of

calcination, milling, and mixing solvent," *Ceramics International*, vol. 46, no. 3, pp. 2987–3001, Feb. 2020, doi: 10.1016/j.ceramint.2019.09.296.
[147] "Materials Data on BaMnO3 by Materials Project," LBNL Materials Project; Lawrence Berkeley National Laboratory (LBNL), Berkeley, CA (United States), mp-1016852, July 2020. doi: 10.17188/1349494.
[148] "Materials Data on CaMnO3 by Materials Project," LBNL Materials Project; Lawrence Berkeley National Laboratory (LBNL), Berkeley, CA (United States), mp-19201, July 2020. doi: 10.17188/1194051.
[149] "Shannon Radii." Accessed: Aug. 21, 2025. [Online]. Available: http://abulafia.mt.ic.ac.uk/shannon/ptable.php
[150] P. Maneesha *et al.*, "Effect of oxygen vacancies and cationic valence state on multiferroicity and magnetodielectric coupling in (1-x)BaTiO3.(x)LaFeO3 solid solution," *Journal of Alloys and Compounds*, vol. 971, p. 172587, Jan. 2024, doi: 10.1016/j.jallcom.2023.172587.
[151] Y. Hirotaka, U. Hiromoto, S. Tunetaro, and S. Etsuro, "Raman-Scattering Study of the Soft Phonon Modes in Hexagonal Barium Titanate," *Journal of the Physical Society of Japan*, Nov. 2013, doi: 10.1143/JPSJ.56.589.
[152] C. Miot, E. Husson, C. Proust, R. Erre, and J. P. Coutures, "X-ray photoelectron spectroscopy characterization of barium titanate ceramics prepared by the citric route. Residual carbon study," *Journal of Materials Research*, vol. 12, no. 9, pp. 2388–2392, Sept. 1997, doi: 10.1557/JMR.1997.0316.
[153] K. Siemek, A. Olejniczak, L. N. Korotkov, P. Konieczny, and A. V. Belushkin, "Investigation of surface defects in BaTiO3 nanopowders studied by XPS and positron annihilation lifetime spectroscopy," *Applied Surface Science*, vol. 578, p. 151807, Mar. 2022, doi: 10.1016/j.apsusc.2021.151807.
[154] S. Kumar, V. S. Raju, and T. R. N. Kutty, "Investigations on the chemical states of sintered barium titanate by X-ray photoelectron spectroscopy," *Applied Surface Science*, vol. 206, no. 1, pp. 250–261, Feb. 2003, doi: 10.1016/S0169-4332(02)01223-0.
[155] "XPS Analysis of Submicrometer Barium Titanate Powder - Wegmann - 2004 - Journal of the American Ceramic Society - Wiley Online Library." Accessed: Aug. 21, 2025. [Online]. Available: https://ceramics.onlinelibrary.wiley.com/doi/10.1111/j.1551-2916.2004.00371.x
[156] "A Facile In Situ Hydrothermal Etching Method to CaTiO3/TiO2 Heterostructure for Efficient Photocatalytic N2 Reduction | Catalysis Letters." Accessed: Aug. 21, 2025. [Online]. Available: https://link.springer.com/article/10.1007/s10562-021-03813-3
[157] "One-step epitaxy of high-mobility La-doped BaSnO3 films by high-pressure magnetron sputtering | APL Materials | AIP Publishing." Accessed: Aug. 21, 2025. [Online]. Available: https://pubs.aip.org/aip/apm/article/9/6/061103/123107/One-step-epitaxy-of-high-mobility-La-doped-BaSnO3
[158] H. Idriss, "On the wrong assignment of the XPS O1s signal at 531–532 eV attributed to oxygen vacancies in photo- and electro-catalysts for water splitting and other materials applications," *Surface Science*, vol. 712, p. 121894, Oct. 2021, doi: 10.1016/j.susc.2021.121894.
[159] "Photoelectron spectroscopy of ceria: Reduction, quantification and the myth of the vacancy peak in XPS analysis - Morgan - 2023 - Surface and

Interface Analysis - Wiley Online Library." Accessed: Aug. 21, 2025. [Online]. Available: https://analyticalsciencejournals.onlinelibrary.wiley.com/doi/full/10.1002/sia.7254
[160] "Role of oxygen vacancy in metal oxide based photoelectrochemical water splitting - Wang - 2021 - EcoMat - Wiley Online Library." Accessed: Aug. 21, 2025. [Online]. Available: https://onlinelibrary.wiley.com/doi/full/10.1002/eom2.12075
[161] "Formation, Detection, and Function of Oxygen Vacancy in Metal Oxides for Solar Energy Conversion - Wang - 2022 - Advanced Functional Materials - Wiley Online Library." Accessed: Aug. 21, 2025. [Online]. Available: https://advanced.onlinelibrary.wiley.com/doi/full/10.1002/adfm.202109503
[162] Z. Wang *et al.*, "Understanding the Roles of Oxygen Vacancies in Hematite-Based Photoelectrochemical Processes", doi: 10.1002/anie.201810583.
[163] "Constructing a pathway for mixed ion and electron transfer reactions for O2 incorporation in Pr0.1Ce0.9O2−x | Nature Catalysis." Accessed: Aug. 21, 2025. [Online]. Available: https://www.nature.com/articles/s41929-019-0401-9
[164] "Self-reduction of the native TiO2 (110) surface during cooling after thermal annealing – in-operando investigations | Scientific Reports." Accessed: Aug. 21, 2025. [Online]. Available: https://www.nature.com/articles/s41598-019-48837-3
[165] A. Posada-Borbón, N. Bosio, and H. Grönbeck, "On the signatures of oxygen vacancies in O1s core level shifts," *Surface Science*, vol. 705, p. 121761, Mar. 2021, doi: 10.1016/j.susc.2020.121761.
[166] R. Nawaz *et al.*, "Manipulation of the Ti3+/Ti4+ ratio in colored titanium dioxide and its role in photocatalytic degradation of environmental pollutants," *Surfaces and Interfaces*, vol. 32, p. 102146, Aug. 2022, doi: 10.1016/j.surfin.2022.102146.
[167] G. Greczynski and L. Hultman, "Towards reliable X-ray photoelectron spectroscopy: Sputter-damage effects in transition metal borides, carbides, nitrides, and oxides," *Applied Surface Science*, vol. 542, p. 148599, Mar. 2021, doi: 10.1016/j.apsusc.2020.148599.
[168] J. F. Moulder and J. Chastain, Eds., *Handbook of X-ray photoelectron spectroscopy: a reference book of standard spectra for identification and interpretation of XPS data*, Update. Eden Prairie, Minn: Perkin-Elmer Corporation, 1992.
[169] "Structural phase separation and optical and magnetic properties of BaTi1−xMnxO3 multiferroics | Journal of Applied Physics | AIP Publishing." Accessed: Aug. 21, 2025. [Online]. Available: https://pubs.aip.org/aip/jap/article/111/11/113913/898378/Structural-phase-separation-and-optical-and
[170] B. Deka, "Ferromagnetism in Fe-doped BaTiO3 Ceramics," *Journal of Superconductivity and Novel Magnetism*, vol. 31, pp. 1–7, May 2018, doi: 10.1007/s10948-017-4321-0.
[171] "dz2 orbital-mediated bound magnetic polarons in ferromagnetic Ce-doped BaTiO3 nanoparticles and their enriched two-photon absorption cross-section - Physical Chemistry Chemical Physics (RSC Publishing)." Accessed: Aug. 21, 2025. [Online]. Available: https://pubs.rsc.org/en/content/articlelanding/2019/cp/c8cp06055j

[172] S. Martin, N. Baboux, D. Albertini, and B. Gautier, “A new technique based on current measurement for nanoscale ferroelectricity assessment: Nano-positive up negative down,” *Rev. Sci. Instrum.*, vol. 88, no. 2, Feb. 2017, doi: 10.1063/1.4974953.
[173] Y. Tan *et al.*, “Unfolding grain size effects in barium titanate ferroelectric ceramics,” *Sci Rep*, vol. 5, no. 1, p. 9953, May 2015, doi: 10.1038/srep09953.
[174] Y. Yu *et al.*, “Room temperature ferroelectricity in donor-acceptor co-doped TiO2 ceramics using doping-engineering,” *Acta Materialia*, vol. 150, pp. 173–181, May 2018, doi: 10.1016/j.actamat.2018.03.016.
[175] Z.-H. Zhao, Y. Dai, and F. Huang, “The formation and effect of defect dipoles in lead-free piezoelectric ceramics: A review,” *Sustainable Materials and Technologies*, vol. 20, p. e00092, July 2019, doi: 10.1016/j.susmat.2019.e00092.
[176] “Biasing Effects in Ferroic Materials | IntechOpen.” Accessed: Aug. 21, 2025. [Online]. Available: https://www.intechopen.com/chapters/48734
[177] “The Defect Chemistry of Metal Oxides,” ResearchGate. Accessed: Aug. 21, 2025. [Online]. Available: https://www.researchgate.net/publication/234551055_The_Defect_Chemistry_of_Metal_Oxides
[178] Z. Li, J. Yu, S. Hao, and P.-E. Janolin, “Enhancing properties of lead-free ferroelectric BaTiO3 through doping,” *Journal of the European Ceramic Society*, vol. 42, no. 12, pp. 4693–4701, Sept. 2022, doi: 10.1016/j.jeurceramsoc.2022.05.023.
[179] Y. A. Genenko, J. Glaum, M. J. Hoffmann, and K. Albe, “Mechanisms of aging and fatigue in ferroelectrics,” *Materials Science and Engineering: B*, vol. 192, pp. 52–82, Feb. 2015, doi: 10.1016/j.mseb.2014.10.003.
[180] “Large electric-field-induced strain in ferroelectric crystals by point-defect-mediated reversible domain switching | Nature Materials.” Accessed: Aug. 21, 2025. [Online]. Available: https://www.nature.com/articles/nmat1051
[181] S. Li, D. Zhou, Z. Shi, M. Hoffmann, T. Mikolajick, and U. Schroeder, “Involvement of Unsaturated Switching in the Endurance Cycling of Si-doped HfO2 Ferroelectric Thin Films,” *Advanced Electronic Materials*, vol. 6, no. 8, p. 2000264, 2020, doi: 10.1002/aelm.202000264.
[182] “Direct observation of nanoscale dynamics of ferroelectric degradation | Nature Communications.” Accessed: Nov. 24, 2025. [Online]. Available: https://www.nature.com/articles/s41467-021-22355-1
[183] “Measurement Techniques of the Magneto-Electric Coupling in Multiferroics.” Accessed: Aug. 21, 2025. [Online]. Available: https://www.mdpi.com/1996-1944/10/8/963
[184] D. K. Pradhan *et al.*, “Exploring the Magnetoelectric Coupling at the Composite Interfaces of FE/FM/FE Heterostructures,” *Sci Rep*, vol. 8, no. 1, p. 17381, Nov. 2018, doi: 10.1038/s41598-018-35648-1.
[185] S. Sahoo, S. Das, P. K. Mahapatra, and R. N. P. Choudhary, “Fabrication and characterization of LaFeO3-BaTiO3 electroceramics,” *Materials Chemistry and Physics*, vol. 216, pp. 158–169, Sept. 2018, doi: 10.1016/j.matchemphys.2018.05.032.
[186] S.-C. Yang, A. Kumar, V. Petkov, and S. Priya, “Room-temperature magnetoelectric coupling in single-phase BaTiO3-BiFeO3 system,” *Journal of Applied Physics*, vol. 113, no. 14, p. 144101, Apr. 2013, doi: 10.1063/1.4799591.

[187] K. C. Verma, V. Gupta, J. Kaur, and R. K. Kotnala, “Raman spectra, photoluminescence, magnetism and magnetoelectric coupling in pure and Fe doped BaTiO3 nanostructures,” *Journal of Alloys and Compounds*, vol. 578, pp. 5–11, Nov. 2013, doi: 10.1016/j.jallcom.2013.05.025.
[188] J. Shah and R. K. Kotnala, “Induced magnetism and magnetoelectric coupling in ferroelectric BaTiO3 by Cr-doping synthesized by a facile chemical route,” *J. Mater. Chem. A*, vol. 1, no. 30, p. 8601, 2013, doi: 10.1039/c3ta11845b.
[189] J. W. Liang *et al.*, “Magnetoelectric coupling in Sm substituted 0.67BiFeO3-0.33BaTiO3 ceramics,” *Journal of Alloys and Compounds*, vol. 901, p. 163681, Apr. 2022, doi: 10.1016/j.jallcom.2022.163681.
[190] S. Divya Lakshmi and I. B. Shameem Banu, “Tailoring the multiferroic properties of BiFeO3 by co-doping Er at Bi site with aliovalent Nb, Mn and Mo at Fe site,” *International Journal of Applied Ceramic Technology*, vol. 16, no. 4, pp. 1622–1631, 2019, doi: 10.1111/ijac.13201.
[191] J. R. D. E., R. A. U. Rahman, S. B., and M. Ramaswamy, “Room temperature multiferroicity and magnetoelectric coupling in Na-deficient sodium bismuth titanate,” *Applied Physics Letters*, vol. 114, no. 6, p. 062902, Feb. 2019, doi: 10.1063/1.5078575.
[192] J. Paul, S. Bhardwaj, K. K. Sharma, R. K. Kotnala, and R. Kumar, “Room temperature multiferroic behaviour and magnetoelectric coupling in Sm/Fe modified Bi4Ti3O12 ceramics synthesized by solid state reaction method,” *Journal of Alloys and Compounds*, vol. 634, pp. 58–64, June 2015, doi: 10.1016/j.jallcom.2015.01.259.
[193] S. D. Lakshmi and I. B. S. Banu, “Multiferroism and magnetoelectric coupling in single-phase Yb and X (X = Nb, Mn, Mo) co-doped BiFeO3 ceramics,” *J Sol-Gel Sci Technol*, vol. 89, no. 3, pp. 713–721, Mar. 2019, doi: 10.1007/s10971-018-4901-x.
[194] “Optical investigation and computational modelling of BaTiO3 for optoelectronic devices applications | Scientific Reports.” Accessed: Aug. 21, 2025. [Online]. Available: https://www.nature.com/articles/s41598-023-31652-2
[195] M. A. Rahman, “Understanding of doping sites and versatile applications of heteroatom modified $BaTiO_3$ ceramic,” *Journal of Asian Ceramic Societies*, vol. 11, no. 2, pp. 215–224, Apr. 2023, doi: 10.1080/21870764.2023.2203635.
[196] V. B. Parmar, D. Raval, S. K. Gupta, P. N. Gajjar, and A. M. Vora, “BaTiO3 perovskite for optoelectronics application: A DFT study,” *Materials Today: Proceedings*, Feb. 2023, doi: 10.1016/j.matpr.2023.01.410.
[197] “Structural phase transition driven dielectric and optical properties with reduction in band gap in Sr2+ modified BaTiO3 ceramics | Semantic Scholar.” Accessed: Aug. 21, 2025. [Online]. Available: https://www.semanticscholar.org/paper/Structural-phase-transition-driven-dielectric-and-Mallick-Kumar/d7f471c19271a35e1f537bd5b7a4bfa5bb5c30a6
[198] X. Zhu, S. Li, and Y. Li, “Distinct Effects of Selective Sn Doping at A or B Sites in $BaTiO_3$,” *Physica Status Solidi (a)*, vol. 222, no. 9, p. 2400822, May 2025, doi: 10.1002/pssa.202400822.
[199] “Energy storage enhancement and bandgap narrowing of lanthanum and sodium co-substituted BaTiO3 ceramics | Semantic Scholar.” Accessed: Aug. 21, 2025. [Online]. Available:

https://www.semanticscholar.org/paper/Energy-storage-enhancement-and-bandgap-narrowing-of-Alkathy-Eiras/0c5cf40f95d4869accb47c4444a711733cb5fdad
[200] “Ferroelectric properties of BaTiO3 thin films co-doped with Mn and Nb | AIP Advances | AIP Publishing.” Accessed: Aug. 21, 2025. [Online]. Available: https://pubs.aip.org/aip/adv/article/9/9/095207/1076239/Ferroelectric-properties-of-BaTiO3-thin-films-co
[201] A. Semenov *et al.*, “Mn-Doped BaTiO3 Ceramics: Thermal and Electrical Properties for Multicaloric Applications,” *Materials*, vol. 12, no. 21, p. 3592, Jan. 2019, doi: 10.3390/ma12213592.
[202] “Structure and Dielectric Behavior of La-Doped BaTiO3 Ceramics | Semantic Scholar.” Accessed: Aug. 21, 2025. [Online]. Available: https://www.semanticscholar.org/paper/Structure-and-Dielectric-Behavior-of-La-Doped-Li-Xu/8f50de70a0ce17c73b1e896c871d5e8e174f4860
[203] D. Pandey, V. S. Tiwari, T. B. Singh, L. Pandey, O. Parkash, and P. Ramachandrarao, “Diffuse phase transition in (Ba, Ca) TiO3 ceramics,” *Phase Transitions: A Multinational Journal*, Jan. 1987, doi: 10.1080/01411598708241332.
[204] B. Ravel and M. Newville, “ATHENA, ARTEMIS, HEPHAESTUS: data analysis for X-ray absorption spectroscopy using IFEFFIT,” *J Synchrotron Radiat*, vol. 12, no. Pt 4, pp. 537–541, July 2005, doi: 10.1107/S0909049505012719.
[205] S. Kato *et al.*, “Dielectric response of BaTiO3<math><msub is="true"><mrow is="true"></mrow><mn is="true">3</mn></msub></math> electronic states under AC fields via microsecond time-resolved X-ray absorption spectroscopy,” *Acta Materialia*, vol. 207, p. 116681, Apr. 2021, doi: 10.1016/j.actamat.2021.116681.
[206] R. V. Vedrinskii, V. L. Kraizman, A. A. Novakovich, P. V. Demekhin, and S. V. Urazhdin, “Pre-edge fine structure of the 3d atom K x-ray absorption spectra and quantitative atomic structure determinations for ferroelectric perovskite structure crystals,” *J. Phys.: Condens. Matter*, vol. 10, no. 42, pp. 9561–9580, Oct. 1998, doi: 10.1088/0953-8984/10/42/021.
[207] V. Krayzman, I. Levin, J. C. Woicik, F. Bridges, E. J. Nelson, and D. C. Sinclair, “Ca K-edge X-ray absorption fine structure in BaTiO3-CaTiO3 solid solutions,” *Journal of Applied Physics*, vol. 113, no. 4, p. 044106, Jan. 2013, doi: 10.1063/1.4784226.
[208] T. Chakraborty, C. Meneghini, G. Aquilanti, and S. Ray, “Microscopic distribution of metal dopants and anion vacancies in Fe-doped BaTiO3−δ single crystals,” *J. Phys.: Condens. Matter*, vol. 25, no. 23, p. 236002, May 2013, doi: 10.1088/0953-8984/25/23/236002.
[209] S. Mukherjee *et al.*, “Structure and Electronic Effects from Mn and Nb Co-doping for Low Band Gap BaTiO3 Ferroelectrics,” *J. Phys. Chem. C*, vol. 125, no. 27, pp. 14910–14923, July 2021, doi: 10.1021/acs.jpcc.1c02539.
[210] Y. Imanaka, H. Amada, F. Kumasaka, N. Awaji, and A. Kumamoto, “Nanoparticulate BaTiO3 film produced by aerosol-type nanoparticle deposition,” *J Nanopart Res*, vol. 18, no. 4, p. 102, Apr. 2016, doi: 10.1007/s11051-016-3407-0.
[211] Ph. Ghosez, X. Gonze, Ph. Lambin, and J.-P. Michenaud, “Born effective charges of barium titanate: Band-by-band decomposition and sensitivity to structural features,” *Phys. Rev. B*, vol. 51, no. 10, pp. 6765–6768, Mar. 1995, doi: 10.1103/PhysRevB.51.6765.

[212] "(PDF) A Pre-Edge Analysis of Mn K-edge XANES Spectra to determine Speciation of Manganese in Minerals and Glasses," ResearchGate. Accessed: Aug. 21, 2025. [Online]. Available: https://www.researchgate.net/publication/225399141_A_Pre-Edge_Analysis_of_Mn_K-edge_XANES_Spectra_to_determine_Speciation_of_Manganese_in_Minerals_and_Glasses

[213] V. Celorrio *et al.*, "Relationship between Mn Oxidation State Changes and Oxygen Reduction Activity in (La,Ca)MnO3 as Probed by In Situ XAS and XES," *ACS Catal.*, vol. 11, no. 11, pp. 6431–6439, June 2021, doi: 10.1021/acscatal.1c00997.

[214] I. Fongkaew, J. T-Thienprasert, and S. Limpijumnong, "Identification of Mn site in Mn-doped SrTiO3: First principles study," *Ceramics International*, vol. 43, pp. S381–S385, Aug. 2017, doi: 10.1016/j.ceramint.2017.05.258.

[215] S. Limpijumnong, S. Rujirawat, A. Boonchun, M. Smith, and B. Cherdhirunkorn, "Identification of Mn site in Pb(Zr,Ti)O-3 by synchrotron X-ray absorption near-edge structure: Theory and experiment," *Applied Physics Letters*, vol. 90, pp. 103113–103113, Mar. 2007, doi: 10.1063/1.2711200.

[216] "Room temperature multiferroicity and magnetoelectric coupling in Ca/Mn-modified BaTiO3 - Journal of Materials Chemistry C (RSC Publishing)." Accessed: July 22, 2025. [Online]. Available: https://pubs.rsc.org/en/content/articlelanding/2025/tc/d5tc00873e

[217] T. Kanazawa *et al.*, "Influence of the Hydride Content on the Local Structure of a Perovskite Oxyhydride $BaTiO_{3-x}H_x$," *J. Phys. Chem. C*, vol. 127, no. 15, pp. 7546–7551, Apr. 2023, doi: 10.1021/acs.jpcc.3c00915.

[218] S. Mukherjee *et al.*, "Structure and Electronic Effects from Mn and Nb Co-doping for Low Band Gap BaTiO3 Ferroelectrics," *J. Phys. Chem. C*, vol. 125, no. 27, pp. 14910–14923, July 2021, doi: 10.1021/acs.jpcc.1c02539.

[219] V. Celorrio *et al.*, "Relationship between Mn Oxidation State Changes and Oxygen Reduction Activity in (La,Ca)MnO3 as Probed by In Situ XAS and XES," *ACS Catal.*, vol. 11, no. 11, pp. 6431–6439, June 2021, doi: 10.1021/acscatal.1c00997.

[220] "Evaluation of the Tauc method for optical absorption edge determination: ZnO thin films as a model system - Viezbicke - 2015 - physica status solidi (b) - Wiley Online Library." Accessed: Aug. 21, 2025. [Online]. Available: https://onlinelibrary.wiley.com/doi/10.1002/pssb.201552007

[221] C. Rodenbücher, G. Bihlmayer, C. Korte, D. Rytz, J. Szade, and K. Szot, "An Operando Study of the Thermal Reduction of BaTiO3 Crystals: The Nature of the Insulator–Metal Transition of the Surface Layer," *Crystals*, vol. 13, no. 8, Art. no. 8, Aug. 2023, doi: 10.3390/cryst13081278.

[222] L. T. Hudson, R. L. Kurtz, S. W. Robey, D. Temple, and R. L. Stockbauer, "Photoelectron spectroscopic study of the valence and core-level electronic structure of ${\mathrm{BaTiO}}_{3}$," *Phys. Rev. B*, vol. 47, no. 3, pp. 1174–1180, Jan. 1993, doi: 10.1103/PhysRevB.47.1174.

[223] D. Phuyal *et al.*, "Ferroelectric properties of BaTiO3 thin films co-doped with Mn and Nb," *AIP Advances*, vol. 9, no. 9, p. 095207, Sept. 2019, doi: 10.1063/1.5118869.

[224] M.-Q. Cai, Y.-J. Zhang, Z. Yin, and M.-S. Zhang, "First-principles study of structural and electronic properties of

$\mathrm{Ba}\mathrm{Ti}{\mathrm{O}}_{3}(001)$ oxygen-vacancy surfaces," *Phys. Rev. B*, vol. 72, no. 7, p. 075406, Aug. 2005, doi: 10.1103/PhysRevB.72.075406.

[225] L. T. Hudson, R. L. Kurtz, S. W. Robey, D. Temple, and R. L. Stockbauer, "Surface core-level shifts of barium observed in photoemission of vacuum-fractured ${\mathrm{BaTiO}}_{3}$(100)," *Phys. Rev. B*, vol. 47, no. 16, pp. 10832–10838, Apr. 1993, doi: 10.1103/PhysRevB.47.10832.

[226] "Ultraviolet Photoelectron Spectroscopy (UPS) and LEED Studies of BaTiO3 (001) and SrTiO3 (100) Surfaces - Courths - 1980 - physica status solidi (b) - Wiley Online Library." Accessed: July 19, 2025. [Online]. Available: https://onlinelibrary.wiley.com/doi/abs/10.1002/pssb.2221000114

[227] A. Sharma, P. Yadav, R. Bhatt, S. Banik, G. Singh, and I. Bhaumik, "Effect of Nb substitution on the electronic property of lead-free piezoelectric (Na0.41K0.09Bi0.50)TiO3 single crystal: Optical absorption and photoelectron study," *Journal of Applied Physics*, vol. 132, no. 20, p. 205103, Nov. 2022, doi: 10.1063/5.0124508.

[228] G. H. Jonker, "On the dielectric curie-weiss law and diffuse phase transition in ferroelectrics," *Materials Research Bulletin*, vol. 18, no. 3, pp. 301–308, Mar. 1983, doi: 10.1016/0025-5408(83)90117-4.

[229] V. Risinggård, I. Kulagina, and J. Linder, "Electric field control of magnon-induced magnetization dynamics in multiferroics," *Sci Rep*, vol. 6, no. 1, p. 31800, Aug. 2016, doi: 10.1038/srep31800.

[230] "Solutions for maximum coupling in multiferroic magnetoelectric composites by material design | Scientific Reports." Accessed: Aug. 20, 2025. [Online]. Available: https://www.nature.com/articles/s41598-018-22964-9

[231] N. A. Spaldin, "Multiferroics beyond electric-field control of magnetism," *Proc Math Phys Eng Sci*, vol. 476, no. 2233, p. 20190542, Jan. 2020, doi: 10.1098/rspa.2019.0542.

[232] "Scalable energy-efficient magnetoelectric spin–orbit logic | Nature." Accessed: Aug. 20, 2025. [Online]. Available: https://www.nature.com/articles/s41586-018-0770-2

[233] "Physics and Applications of Bismuth Ferrite - Catalan - 2009 - Advanced Materials - Wiley Online Library." Accessed: Aug. 20, 2025. [Online]. Available: https://advanced.onlinelibrary.wiley.com/doi/abs/10.1002/adma.200802849

[234] "Magnetoelectric Composites: Applications, Coupling Mechanisms, and Future Directions." Accessed: Aug. 20, 2025. [Online]. Available: https://www.mdpi.com/2079-4991/10/10/2072

[235] H. Wu *et al.*, "Significantly enhanced hybrid improper ferroelectricity of Ca3Ti2O7 ceramics by the oxygen vacancy engineering," *Materials Today Chemistry*, vol. 26, p. 101226, Dec. 2022, doi: 10.1016/j.mtchem.2022.101226.

[236] S. C. Baral *et al.*, "Rare Earth Manganites and Related Multiferroicity," in *Emerging Applications of Low Dimensional Magnets*, CRC Press, 2022.

[237] T. Zhong, X. Li, M. Wu, and J.-M. Liu, "Room-temperature multiferroicity and diversified magnetoelectric couplings in 2D materials," *Natl Sci Rev*, vol. 7, no. 2, pp. 373–380, Feb. 2020, doi: 10.1093/nsr/nwz169.

[238] D. M. Evans *et al.*, “The nature of magnetoelectric coupling in Pb(Zr,Ti)O3 - Pb(Fe,Ta)O3,” *Adv Mater*, vol. 27, no. 39, pp. 6068–6073, Oct. 2015, doi: 10.1002/adma.201501749.
[239] R. Gao *et al.*, “Electric Field–Induced Magnetization Rotation in Magnetoelectric Multiferroic Fluids,” *Advanced Electronic Materials*, vol. 4, no. 6, p. 1800030, 2018, doi: 10.1002/aelm.201800030.
[240] “Experimental and theoretical studies on induced ferromagnetism of new (1 − x)Na0.5Bi0.5TiO3 + xBaFeO3−δ solid solution | Scientific Reports.” Accessed: Aug. 20, 2025. [Online]. Available: https://www.nature.com/articles/s41598-021-88377-3
[241] R. Gao, Z. Wang, G. Chen, X. Deng, W. Cai, and C. Fu, “Influence of core size on the multiferroic properties of CoFe2O4@BaTiO3 core shell structured composites,” *Ceramics International*, vol. 44, pp. S84–S87, Nov. 2018, doi: 10.1016/j.ceramint.2018.08.234.
[242] A. S. Gaikwad *et al.*, “Magneto-electric coupling and improved dielectric constant of BaTiO3 and Fe-rich (Co0.7Fe2.3O4) ferrite nano-composites,” *Journal of Magnetism and Magnetic Materials*, vol. 465, pp. 508–514, Nov. 2018, doi: 10.1016/j.jmmm.2018.06.036.
[243] P. Esther Rubavathi, D. Dhayanithi, N. V. Giridharan, M. T. Rahul, N. Kalarikkal, and B. Sundarakannan, “Origin of magnetic, magnetoelectric effect and the influence of reentrant ferroelectric phase on the structural and multiferroic properties of Dy3+-Fe3+ co-substituted BaTiO3 ceramics,” *Journal of Magnetism and Magnetic Materials*, vol. 538, p. 168260, Nov. 2021, doi: 10.1016/j.jmmm.2021.168260.
[244] X. Qi *et al.*, “Compositional dependence of ferromagnetic and magnetoelectric effect properties in BaTiO3–BiFeO3–LaFeO3 solid solutions,” *RSC Adv.*, vol. 7, no. 82, pp. 51801–51806, Nov. 2017, doi: 10.1039/C7RA10563K.
[245] M. M. Kumar, A. Srinivas, G. S. Kumar, and S. V. Suryanarayana, “Investigation of the magnetoelectric effect in BiFeO3-BaTiO3 solid solutions,” *J. Phys.: Condens. Matter*, vol. 11, no. 41, p. 8131, Oct. 1999, doi: 10.1088/0953-8984/11/41/315.
[246] “Room-temperature multiferroic magnetoelectrics | NPG Asia Materials.” Accessed: Aug. 20, 2025. [Online]. Available: https://www.nature.com/articles/am201358
[247] R. V. K. Mangalam, N. Ray, U. V. Waghmare, A. Sundaresan, and C. N. R. Rao, “Multiferroic properties of nanocrystalline BaTiO3,” *Solid State Communications*, vol. 149, no. 1, pp. 1–5, Jan. 2009, doi: 10.1016/j.ssc.2008.10.023.
[248] R. Gao *et al.*, “Strong magnetoelectric coupling effect in BaTiO3@CoFe2O4 magnetoelectric multiferroic fluids,” *Nanoscale*, vol. 10, no. 25, pp. 11750–11759, July 2018, doi: 10.1039/C8NR02368A.
[249] R. Gao *et al.*, “Enhancement of magnetoelectric properties of (1-x)Mn0.5Zn0.5Fe2O4-xBa0.85Sr0.15Ti0.9Hf0.1O3 composite ceramics,” *Journal of Alloys and Compounds*, vol. 795, May 2019, doi: 10.1016/j.jallcom.2019.05.013.
[250] “Anomalous properties in ferroelectrics induced by atomic ordering | Nature.” Accessed: Aug. 20, 2025. [Online]. Available: https://www.nature.com/articles/35092530

[251] I. N. Apostolova, A. T. Apostolov, S. Golrokh Bahoosh, and J. M. Wesselinowa, “Origin of ferromagnetism in transition metal doped BaTiO3,” *J. Appl. Phys.*, vol. 113, no. 20, p. 203904, May 2013, doi: 10.1063/1.4807412.
[252] S. Ray *et al.*, “High temperature ferromagnetism in single crystalline dilute Fe-doped $\mathrm{Ba}\mathrm{Ti}{\mathrm{O}}_{3}$,” *Phys. Rev. B*, vol. 77, no. 10, p. 104416, Mar. 2008, doi: 10.1103/PhysRevB.77.104416.
[253] T. Chakraborty, S. Ray, and M. Itoh, “Defect-induced magnetism: Test of dilute magnetism in Fe-doped hexagonal BaTiO${}_{3}$ single crystals,” *Phys. Rev. B*, vol. 83, no. 14, p. 144407, Apr. 2011, doi: 10.1103/PhysRevB.83.144407.
[254] X. K. Wei *et al.*, “Origin of ferromagnetism and oxygen-vacancy ordering induced cross-controlled magnetoelectric effects at room temperature,” *J. Appl. Phys.*, vol. 111, no. 7, p. 073904, Apr. 2012, doi: 10.1063/1.3696979.
[255] A. Sagdeo *et al.*, “Disappearance of dielectric anomaly in spite of presence of structural phase transition in reduced BaTiO3: Effect of defect states within the bandgap,” *J. Appl. Phys.*, vol. 123, no. 16, p. 161424, Apr. 2018, doi: 10.1063/1.5010870.
[256] S. Acharya, J. Mondal, S. Ghosh, S. K. Roy, and P. K. Chakrabarti, “Multiferroic behavior of lanthanum orthoferrite (LaFeO3),” *Materials Letters*, vol. 64, no. 3, pp. 415–418, Feb. 2010, doi: 10.1016/j.matlet.2009.11.037.
[257] K. Lee, S. Hajra, M. Sahu, and H. J. Kim, “Colossal dielectric response, multiferroic properties, and gas sensing characteristics of the rare earth orthoferrite LaFeO3 ceramics,” *Journal of Alloys and Compounds*, vol. 882, p. 160634, Nov. 2021, doi: 10.1016/j.jallcom.2021.160634.
[258] N. Kim *et al.*, “Magnetodielectric effect in BaTiO3−LaMnO3 composites,” *Journal of Applied Physics*, vol. 102, pp. 014107–014107, July 2007, doi: 10.1063/1.2752798.
[259] “FullProf Suite Homepage.” Accessed: Aug. 21, 2025. [Online]. Available: https://www.ill.eu/sites/fullprof/
[260] V. Dwij *et al.*, “Revisiting eigen displacements of tetragonal BaTiO3: Combined first principle and experimental investigation,” *Physica B: Condensed Matter*, vol. 624, p. 413381, Jan. 2022, doi: 10.1016/j.physb.2021.413381.
[261] “Effect of structural disorder on the electronic and phononic properties of Hf doped BaTiO3 | Journal of Materials Science: Materials in Electronics.” Accessed: Aug. 21, 2025. [Online]. Available: https://link.springer.com/article/10.1007/s10854-019-01281-5
[262] J. D. Freire and R. S. Katiyar, “Lattice dynamics of crystals with tetragonal ${\mathrm{BaTiO}}_{3}$ structure,” *Phys. Rev. B*, vol. 37, no. 4, pp. 2074–2085, Feb. 1988, doi: 10.1103/PhysRevB.37.2074.
[263] “Ferroelectric domain wall motion induced by polarized light | Nature Communications.” Accessed: Aug. 21, 2025. [Online]. Available: https://www.nature.com/articles/ncomms7594
[264] U. D. Venkateswaran, V. M. Naik, and R. Naik, “High-pressure Raman studies of polycrystalline ${\mathrm{BaTiO}}_{3}$,” *Phys. Rev. B*, vol. 58, no. 21, pp. 14256–14260, Dec. 1998, doi: 10.1103/PhysRevB.58.14256.
[265] N. Baskaran, A. Ghule, C. Bhongale, R. Murugan, and H. Chang, “Phase transformation studies of ceramic BaTiO3 using thermo-Raman and

dielectric constant measurements," *J. Appl. Phys.*, vol. 91, no. 12, pp. 10038–10043, June 2002, doi: 10.1063/1.1481771.
[266] M. DiDomenico, S. H. Wemple, S. P. S. Porto, and R. P. Bauman, "Raman Spectrum of Single-Domain BaTi${\mathrm{O}}_{3}$," *Phys. Rev.*, vol. 174, no. 2, pp. 522–530, Oct. 1968, doi: 10.1103/PhysRev.174.522.
[267] V. K. Veerapandiyan *et al.*, "B-site vacancy induced Raman scattering in BaTiO3-based ferroelectric ceramics," *Journal of the European Ceramic Society*, vol. 40, no. 13, pp. 4684–4688, Oct. 2020, doi: 10.1016/j.jeurceramsoc.2020.05.051.
[268] "B. E. Warren, 'X-Ray diffraction,' Addison Wesley, Reading, MA, 1969. - References - Scientific Research Publishing." Accessed: Aug. 21, 2025. [Online]. Available: https://www.scirp.org/reference/referencespapers?referenceid=29114
[269] E. G. Rini, M. K. Gupta, R. Mittal, A. Mekki, M. H. Al Saeed, and S. Sen, "Structural change from *Pbnm* to *R3̄c* phase with varying Fe/Mn content in *(1-x)* LaFeO3.*x*LaMnO3 solid solution leading to modifications in octahedral tilt and valence states," *Journal of Alloys and Compounds*, vol. 883, p. 160761, Nov. 2021, doi: 10.1016/j.jallcom.2021.160761.
[270] M. Uma *et al.*, "Structural, Chemical and Electrical Properties of Au/La2O3/n-GaN MIS Junction with a High-k Lanthanum Oxide Insulating Layer," *J. Electron. Mater.*, vol. 48, no. 7, pp. 4217–4225, July 2019, doi: 10.1007/s11664-019-07193-8.
[271] S.-J. Oh, G.-H. Kim, G. A. Sawatzky, and H. T. Jonkman, "Effect of hole-induced shakedown in the Auger spectrum of lanthanum," *Phys. Rev. B*, vol. 37, no. 11, pp. 6145–6152, Apr. 1988, doi: 10.1103/PhysRevB.37.6145.
[272] S. Sarkar *et al.*, "X-ray photoelectron spectroscopy study of a layered tri-chalcogenide system LaTe3," *AIP Conf. Proc.*, vol. 2220, no. 1, p. 100005, May 2020, doi: 10.1063/5.0001764.
[273] A. S. Medina, N. A. Wall, C. F. Ivory, S. B. Clark, and H. Beyenal, "Preconcentration mechanism of trivalent lanthanum on eQCM electrodes in the presence of α-hydroxy isobutyric acid," *J Electroanal Chem (Lausanne)*, vol. 857, p. 113731, Jan. 2020, doi: 10.1016/j.jelechem.2019.113731.
[274] "Dissolution and oriented aggregation: transformation from lepidorocite to goethite by the catalysis of aqueous Fe(ii) - RSC Advances (RSC Publishing)." Accessed: Aug. 21, 2025. [Online]. Available: https://pubs.rsc.org/en/content/articlelanding/2015/ra/c5ra19787b
[275] T. Yamashita and P. Hayes, "Analysis of XPS spectra of Fe2+ and Fe3+ ions in oxide materials," *Applied Surface Science*, vol. 254, no. 8, pp. 2441–2449, Feb. 2008, doi: 10.1016/j.apsusc.2007.09.063.
[276] "Negative voltage modulated multi-level resistive switching by using a Cr/BaTiOx/TiN structure and quantum conductance through evidence of H2O2 sensing mechanism | Scientific Reports." Accessed: Aug. 21, 2025. [Online]. Available: https://www.nature.com/articles/s41598-017-05059-9
[277] "Formation of oxygen vacancies and Ti3+ state in TiO2 thin film and enhanced optical properties by air plasma treatment | Scientific Reports." Accessed: Aug. 21, 2025. [Online]. Available: https://www.nature.com/articles/srep32355
[278] A. Rodrigues, S. Bauer, and T. Baumbach, "Effect of post-annealing on the chemical state and crystalline structure of PLD Ba0.5Sr0.5TiO3 films analyzed by combined synchrotron X-ray diffraction and X-ray photoelectron

spectroscopy," *Ceramics International*, vol. 44, no. 13, pp. 16017–16024, Sept. 2018, doi: 10.1016/j.ceramint.2018.06.038.
[279] "Crystalline Structure, Defect Chemistry and Room Temperature Colossal Permittivity of Nd-doped Barium Titanate | Scientific Reports." Accessed: Aug. 21, 2025. [Online]. Available: https://www.nature.com/articles/srep42274
[280] "Characterization of hollow BaTiO3 nanofibers and intense visible photoluminescence | Journal of Applied Physics | AIP Publishing." Accessed: Aug. 21, 2025. [Online]. Available: https://pubs.aip.org/aip/jap/article/114/13/134303/901840/Characterization-of-hollow-BaTiO3-nanofibers-and
[281] G. Chen, X. Chang, J. Chen, W. Zhao, and J. Peng, "Investigation of BaCO3 Powders Synthesized by Microwave Homogeneous Precipitation," *High Temperature Materials and Processes*, vol. 34, no. 8, pp. 757–764, Dec. 2015, doi: 10.1515/htmp-2014-0153.
[282] K. S. Samantaray, R. Amin, M. P, I. Bhaumik, and S. Sen, "Effect of electrical poling on the structural, vibrational, and electrical properties of 0.94(Na0.5Bi0.5TiO3) -(0.06-x) CaTiO3-x (BaTiO3) lead-free ceramics," *Ceramics International*, vol. 49, no. 9, Part A, pp. 14310–14326, May 2023, doi: 10.1016/j.ceramint.2023.01.018.
[283] J. D. Baniecki, M. Ishii, T. Shioga, K. Kurihara, and S. Miyahara, "Surface core-level shifts of strontium observed in photoemission of barium strontium titanate thin films," *Appl. Phys. Lett.*, vol. 89, no. 16, p. 162908, Oct. 2006, doi: 10.1063/1.2357880.
[284] J. Gil-Londoño *et al.*, "Unraveling the Role of F-Type Color Centers on the Optical and Electrical Properties of Al2W3O12 Nanoparticles with Different Content of Oxygen Vacancies," *J. Phys. Chem. C*, vol. 129, no. 5, pp. 2649–2662, Feb. 2025, doi: 10.1021/acs.jpcc.4c06098.
[285] D. Lu, Y. Zheng, and L. Yuan, "Electron Paramagnetic Resonance Study on Oxygen Vacancies and Site Occupations in Mg-Doped BaTiO3 Ceramics," *Materials*, vol. 12, no. 9, p. 1525, Jan. 2019, doi: 10.3390/ma12091525.
[286] M. Choi, F. Oba, and I. Tanaka, "Electronic and structural properties of the oxygen vacancy in BaTiO3," *Appl. Phys. Lett.*, vol. 98, no. 17, p. 172901, Apr. 2011, doi: 10.1063/1.3583460.
[287] M. D. Glinchuk *et al.*, "Influence of impurities on the properties of rare-earth-doped barium-titanate ceramics," *J. Mater. Chem.*, vol. 10, no. 4, pp. 941–947, Jan. 2000, doi: 10.1039/A909647G.
[288] T.-L. Phan, P. Zhang, D. S. Yang, T. D. Thanh, D. A. Tuan, and S. C. Yu, "Origin of ferromagnetism in BaTiO3 nanoparticles prepared by mechanical milling," *J. Appl. Phys.*, vol. 113, no. 17, p. 17E305, Apr. 2013, doi: 10.1063/1.4799473.
[289] E. Possenriede, P. Jacobs, and O. F. Schirmer, "Paramagnetic defects in BaTiO3 and their role in light-induced charge transport. I. ESR studies," *J. Phys.: Condens. Matter*, vol. 4, no. 19, p. 4719, May 1992, doi: 10.1088/0953-8984/4/19/013.
[290] Z. Chen, Y. Zhang, S. Li, X.-M. Lu, and W. Cao, "Frequency dependence of the coercive field of 0.71Pb(Mg1/3Nb2/3)O3-0.29PbTiO3 single crystal from 0.01 Hz to 5 MHz," *Appl Phys Lett*, vol. 110, no. 20, p. 202904, May 2017, doi: 10.1063/1.4983712.

[291] W. Li *et al.*, “Oxygen-Vacancy-Induced Antiferromagnetism to Ferromagnetism Transformation in Eu0.5Ba0.5TiO3−δ Multiferroic Thin Films,” *Sci Rep*, vol. 3, no. 1, p. 2618, Sept. 2013, doi: 10.1038/srep02618.
[292] K. Kawano, M. Hachiya, Y. Iijima, N. Sato, and Y. Mizuno, “The grain size effect on the magnetic properties in NiZn ferrite and the quality factor of the inductor,” *Journal of Magnetism and Magnetic Materials*, vol. 321, no. 16, pp. 2488–2493, Aug. 2009, doi: 10.1016/j.jmmm.2009.03.015.
[293] A. T. Kozakov *et al.*, “Bi1-xCaxFeO3-δ (0 ≤ *x* ≤ 1) ceramics: Crystal structure, phase and elemental composition, and chemical bonding from X-ray diffraction, Raman scattering, Mössbauer, and X-ray photoelectron spectra,” *Journal of Alloys and Compounds*, vol. 664, pp. 392–405, Apr. 2016, doi: 10.1016/j.jallcom.2015.12.241.
[294] H. Xian, L. Tang, Z. Mao, J. Zhang, and X. Chen, “Bounded magnetic polarons induced enhanced magnetism in Ca-doped BiFeO3,” *Solid State Communications*, vol. 287, pp. 54–58, Jan. 2019, doi: 10.1016/j.ssc.2018.09.009.
[295] J. M. D. Coey, M. Venkatesan, and C. B. Fitzgerald, “Donor impurity band exchange in dilute ferromagnetic oxides,” *Nat Mater*, vol. 4, no. 2, pp. 173–179, Feb. 2005, doi: 10.1038/nmat1310.
[296] T. Dietl and J. Spałek, “Effect of Fluctuations of Magnetization on the Bound Magnetic Polaron: Comparison with Experiment,” *Phys. Rev. Lett.*, vol. 48, no. 5, pp. 355–358, Feb. 1982, doi: 10.1103/PhysRevLett.48.355.
[297] “Magnetic and multiferroic properties of dilute Fe-doped BaTiO3 crystals | APL Materials | AIP Publishing.” Accessed: Aug. 21, 2025. [Online]. Available: https://pubs.aip.org/aip/apm/article/8/3/031109/594629/Magnetic-and-multiferroic-properties-of-dilute-Fe
[298] M. Arora *et al.*, “Evidence of Finite Magneto-electric Coupling in SmFeO3 – PbTiO3 Solid Solutions,” July 15, 2021, *Research Square*. doi: 10.21203/rs.3.rs-703464/v1.
[299] G. Catalan, “Magnetocapacitance without magnetoelectric coupling,” *Appl. Phys. Lett.*, vol. 88, no. 10, p. 102902, Mar. 2006, doi: 10.1063/1.2177543.
[300] D. K. Pradhan, V. S. Puli, S. Narayan Tripathy, D. K. Pradhan, J. F. Scott, and R. S. Katiyar, “Room temperature multiferroic properties of Pb(Fe0.5Nb0.5)O3–Co0.65Zn0.35Fe2O4 composites,” *J. Appl. Phys.*, vol. 114, no. 23, p. 234106, Dec. 2013, doi: 10.1063/1.4847595.
[301] T. Katsufuji and H. Takagi, “Coupling between magnetism and dielectric properties in quantum paraelectric ${\mathrm{EuTiO}}_{3}$,” *Phys. Rev. B*, vol. 64, no. 5, p. 054415, July 2001, doi: 10.1103/PhysRevB.64.054415.
[302] T. Katsufuji and H. Takagi, “Magnetocapacitance and spin fluctuations in the geometrically frustrated magnets ${R}_{2}{\mathrm{Ti}}_{2}{\mathrm{O}}_{7}$ $(R=\mathrm{rare}\mathrm{}\mathrm{earth})$,” *Phys. Rev. B*, vol. 69, no. 6, p. 064422, Feb. 2004, doi: 10.1103/PhysRevB.69.064422.
[303] “Multiferroicity in polarized single-phase Bi0.875Sm0.125FeO3 ceramics | Journal of Applied Physics | AIP Publishing.” Accessed: Aug. 21, 2025. [Online]. Available: https://pubs.aip.org/aip/jap/article/100/2/024109/145493/Multiferroicity-in-polarized-single-phase-Bi0
[304] V. R. Palkar, D. C. Kundaliya, S. K. Malik, and S. Bhattacharya, “Magnetoelectricity at room temperature in the

${\mathrm{Bi}}_{0.9\ensuremath{-
}x}{\mathrm{Tb}}_{x}{\mathrm{La}}_{0.1}{\mathrm{FeO}}_{3}$ system," *Phys. Rev. B*, vol. 69, no. 21, p. 212102, June 2004, doi: 10.1103/PhysRevB.69.212102.

[305] H. Singh, A. Kumar, and K. L. Yadav, "Structural, dielectric, magnetic, magnetodielectric and impedance spectroscopic studies of multiferroic BiFeO 3–BaTiO 3 ceramics," *Materials Science and Engineering B-advanced Functional Solid-state Materials*, vol. 176, pp. 540–547, Apr. 2011, doi: 10.1016/j.mseb.2011.01.010.

[306] N. Adhlakha, K. L. Yadav, and R. Singh, "Effect of BaTiO3 addition on structural, multiferroic and magneto-dielectric properties of 0.3CoFe2O4–0.7BiFeO3 ceramics," *Smart Materials and Structures*, vol. 23, p. 105024, Sept. 2014, doi: 10.1088/0964-1726/23/10/105024.

[307] S. Tan, S. Shannigrahi, S. Tan, and F. Tay, "Synthesis and characterization of composite MgFe(2)O(4)-BaTiO(3) multiferroic system," *Journal of Applied Physics*, vol. 103, May 2008, doi: 10.1063/1.2917394.

[308] "Structure, morphology and magnetodielectric investigations of BaTi1−xFexO3−δ ceramics | Journal of Materials Science: Materials in Electronics." Accessed: Aug. 21, 2025. [Online]. Available: https://link.springer.com/article/10.1007/s10854-019-00864-6

[309] "Multiferroic and magnetoelectric properties of core-shell CoFe2O4@BaTiO3 nanocomposites | Applied Physics Letters | AIP Publishing." Accessed: Aug. 21, 2025. [Online]. Available: https://pubs.aip.org/aip/apl/article/97/6/062904/339965/Multiferroic-and-magnetoelectric-properties-of

[310] S. Pachari, S. K. Pratihar, and B. B. Nayak, "Enhanced magneto-capacitance response in BaTiO3–ferrite composite systems," *RSC Adv.*, vol. 5, no. 128, pp. 105609–105617, Dec. 2015, doi: 10.1039/C5RA16742F.

[311] M. ud D. Rather, R. Samad, and B. Want, "Improved magnetoelectric effect in ytterbium doped BaTiO3 –CoFe2O4 particulate multiferroic composites," *Journal of Alloys and Compounds*, vol. 755, pp. 89–99, July 2018, doi: 10.1016/j.jallcom.2018.04.289.

[312] "Investigation of electrical, magneto-dielectric and transport properties of multiferroic (1 − x) BiFeO3–(x) BaSr0.7Ti0.3O3 solid solutions | Journal of Materials Science: Materials in Electronics." Accessed: Aug. 21, 2025. [Online]. Available: https://link.springer.com/article/10.1007/s10854-019-01058-w

[313] X. Yu, T. J. Marks, and A. Facchetti, "Metal oxides for optoelectronic applications," *Nature materials*, vol. 15, no. 4, pp. 383–396, Mar. 2016, doi: 10.1038/nmat4599.

[314] V. Pustovalov, "Thermo-Optical Properties of Metal Oxide Nanoparticles and Their Applications," 2023, pp. 487–512. doi: 10.1007/978-981-99-5640-1_16.

[315] H. Gouadria *et al.*, "Spectroscopic properties, conduction processes and the Summerfield scaling of barium titanate ceramics based on Bi and Fe," *Inorganic Chemistry Communications*, vol. 157, p. 111417, Nov. 2023, doi: 10.1016/j.inoche.2023.111417.

[316] "Nanomagnetic Materials | 11 | Structural and Magnetic Properties | P." Accessed: Aug. 21, 2025. [Online]. Available: https://www.taylorfrancis.com/chapters/edit/10.1201/9781003197492-

11/nanomagnetic-materials-maneesha-suresh-chandra-baral-rini-somaditya-sen
[317] P. Maneesha, S. Chandra Baral, E. G. Rini, and S. Sen, “An overview of the recent developments in the structural correlation of magnetic and electrical properties of *Pr*2*NiMnO*6 double perovskite,” *Progress in Solid State Chemistry*, vol. 70, p. 100402, June 2023, doi: 10.1016/j.progsolidstchem.2023.100402.
[318] S. C. Baral *et al.*, “Enhanced photocatalytic degradation of organic pollutants in water using copper oxide (CuO) nanosheets for environmental application,” *JCIS Open*, vol. 13, p. 100102, Apr. 2024, doi: 10.1016/j.jciso.2024.100102.
[319] M. Elmahgary, A. Mahran, M. Ganoub, and S. Abdellatif, “Optical investigation and computational modelling of BaTiO3 for optoelectronic devices applications,” *Scientific Reports*, vol. 13, Mar. 2023, doi: 10.1038/s41598-023-31652-2.
[320] I. Derkaoui, M. Achehboune, I. Boukhoubza, Z. El Adnani, and A. Rezzouk, “Improved first-principles electronic band structure for cubic (Pm 3¯<math><mover accent="true" is="true"><mrow is="true"><mn is="true">3</mn></mrow><mrow is="true"><mo stretchy="false" is="true">¯</mo></mrow></mover></math> m) and tetragonal (P4mm, P4/mmm) phases of BaTiO3 using the Hubbard U correction,” *Computational Materials Science*, vol. 217, p. 111913, Jan. 2023, doi: 10.1016/j.commatsci.2022.111913.
[321] H. Gao, J. Cao, L. Liu, and Y. Yang, “Theoretical investigation on the structure and electronic properties of barium titanate,” *Journal of Molecular Structure*, vol. 1003, no. 1, pp. 75–81, Sept. 2011, doi: 10.1016/j.molstruc.2011.07.024.
[322] F. D. Cortés-Vega, C. Montero-Tavera, and J. M. Yañez-Limón, “Influence of diluted Fe3+ doping on the physical properties of BaTiO3,” *Journal of Alloys and Compounds*, vol. 847, p. 156513, Dec. 2020, doi: 10.1016/j.jallcom.2020.156513.
[323] M. Rizwan, Hajra, I. Zeba, M. Shakil, S. S. A. Gillani, and Z. Usman, “Electronic, structural and optical properties of BaTiO3 doped with lanthanum (La): Insight from DFT calculation,” *Optik*, vol. 211, p. 164611, June 2020, doi: 10.1016/j.ijleo.2020.164611.
[324] M. Tihtih, J. E. F. M. Ibrahim, M. A. Basyooni, R. En-nadir, I. Hussainova, and I. Kocserha, “Functionality and Activity of Sol–Gel-Prepared Co and Fe co-Doped Lead-Free BTO for Thermo-Optical Applications,” *ACS Omega*, vol. 8, no. 5, pp. 5003–5016, Feb. 2023, doi: 10.1021/acsomega.2c07660.
[325] Md. A. Islam, Md. A. Momin, and M. Nesa, “Effect of Fe doping on the structural, optical and electronic properties of BaTiO3: DFT based calculation,” *Chinese Journal of Physics*, vol. 60, pp. 731–738, Aug. 2019, doi: 10.1016/j.cjph.2019.06.013.
[326] “Successive redox-mediated visible-light ferrophotovoltaics | Nature Communications.” Accessed: Aug. 21, 2025. [Online]. Available: https://www.nature.com/articles/s41467-020-14763-6
[327] “Atomic insight to lattice distortions caused by carrier self-trapping in oxide materials | Scientific Reports.” Accessed: Aug. 21, 2025. [Online]. Available: https://www.nature.com/articles/srep36929
[328] “Optical Properties and Electronic Structure of Amorphous Germanium - Tauc - 1966 - physica status solidi (b) - Wiley Online Library.” Accessed: Aug.

21, 2025. [Online]. Available: https://onlinelibrary.wiley.com/doi/10.1002/pssb.19660150224
[329] "J. I. Pankove, 'Optical Processes in Semiconductors,' Dover Publications, Inc., New York, 1975. (Unabridged republication of the work originally published by Prentice-Hall, Inc., 1971). - References - Scientific Research Publishing." Accessed: Aug. 21, 2025. [Online]. Available: https://www.scirp.org/reference/referencespapers?referenceid=844645
[330] O. V. Rambadey, A. Kumar, and P. R. Sagdeo, "Investigating the correlation between the Urbach energy and asymmetry parameter of the Raman mode in semiconductors," *Phys. Rev. B*, vol. 104, no. 24, p. 245205, Dec. 2021, doi: 10.1103/PhysRevB.104.245205.
[331] F. Yang *et al.*, "Tailoring Bandgap of Perovskite BaTiO3 by Transition Metals Co-Doping for Visible-Light Photoelectrical Applications: A First-Principles Study," *Nanomaterials*, vol. 8, no. 7, p. 455, July 2018, doi: 10.3390/nano8070455.
[332] F. Wang, I. Grinberg, and A. M. Rappe, "Band gap engineering strategy via polarization rotation in perovskite ferroelectrics," *Appl. Phys. Lett.*, vol. 104, no. 15, p. 152903, Apr. 2014, doi: 10.1063/1.4871707.
[333] G. Panchal, R. J. Choudhary, S. Yadav, and D. M. Phase, "Probing the effect of ferroelectric to paraelectric phase transition on the Ti-3d and O-2p hybridization in BaTiO3," *J. Appl. Phys.*, vol. 125, no. 21, p. 214102, June 2019, doi: 10.1063/1.5089731.
[334] E. Orhan, F. Pontes, E. Leite, P. Pizani, J. Varela, and E. Longo, "Experimental and Theoretical Investigation of the Room-Temperature Photoluminescence of Amorphized Pb(Zr,Ti)O3," *Chemphyschem : a European journal of chemical physics and physical chemistry*, vol. 6, pp. 1530–6, Aug. 2005, doi: 10.1002/cphc.200500030.
[335] "Photoluminescence of Barium Titanate and Barium Zirconate in Multilayer Disordered Thin Films at Room temperature | The Journal of Physical Chemistry A." Accessed: Aug. 21, 2025. [Online]. Available: https://pubs.acs.org/doi/10.1021/jp801610y
[336] I. Suzuki, L. Gura, and A. Klein, "The energy level of the Fe2+/3+-transition in BaTiO3 and SrTiO3 single crystals," *Phys. Chem. Chem. Phys.*, vol. 21, no. 11, pp. 6238–6246, Mar. 2019, doi: 10.1039/C8CP07872F.
[337] M. Ganguly *et al.*, "Characterization and Rietveld Refinement of A-site deficient Lanthanum doped Barium Titanate," *Journal of Alloys and Compounds*, vol. 579, pp. 473–484, Dec. 2013, doi: 10.1016/j.jallcom.2013.06.104.
[338] "First-Principle Study on Correlate Structural, Electronic and Optical Properties of Ce-Doped BaTiO3." Accessed: Aug. 21, 2025. [Online]. Available: https://www.mdpi.com/2073-4352/13/2/255
[339] H. Jin *et al.*, "It's a trap! On the nature of localised states and charge trapping in lead halide perovskites," Feb. 2020, doi: 10.1039/C9MH00500E.
[340] Z. Chen, Y. Zhang, S. Li, X.-M. Lu, and W. Cao, "Frequency dependence of the coercive field of 0.71Pb(Mg1/3Nb2/3)O3-0.29PbTiO3 single crystal from 0.01 Hz to 5 MHz," *Appl Phys Lett*, vol. 110, no. 20, p. 202904, May 2017, doi: 10.1063/1.4983712.
[341] "Unfolding grain size effects in barium titanate ferroelectric ceramics | Scientific Reports." Accessed: Aug. 21, 2025. [Online]. Available: https://www.nature.com/articles/srep09953

[342] R. Amin, K. Samantaray, E. G. Rini, I. Bhaumik, and S. Sen, “Grain and grain boundary contributions to AC conductivity in ferroelectric Ba0.75Pb0.25Ti1-xZrxO3 ceramics,” *Ceramics International*, vol. 47, no. 9, pp. 13118–13128, May 2021, doi: 10.1016/j.ceramint.2021.01.176.
[343] L. T. H. Phong *et al.*, “Structural, optical and conductivity properties in tetragonal BaTi1−xCoxO3 (0≤ x ≤0.1),” *RSC Adv.*, vol. 12, no. 25, pp. 16119–16130, May 2022, doi: 10.1039/D2RA01411D.
[344] K. Funke, “Jump relaxation in solid electrolytes,” *Progress in Solid State Chemistry*, vol. 22, no. 2, pp. 111–195, Jan. 1993, doi: 10.1016/0079-6786(93)90002-9.
[345] H. Chen, C. Yang, J. Zhang, B. Wang, and H. Ji, “Electrical behavior of BaZr0.1Ti0.9O3 and BaZr0.2Ti0.8O3 thin films,” *Applied Surface Science*, vol. 255, no. 8, pp. 4585–4589, Feb. 2009, doi: 10.1016/j.apsusc.2008.12.003.
[346] A. Ghosh, “Frequency-dependent conductivity in bismuth-vanadate glassy semiconductors,” *Phys. Rev. B*, vol. 41, no. 3, pp. 1479–1488, Jan. 1990, doi: 10.1103/PhysRevB.41.1479.
[347] L. Essaleh, S. Amhil, S. M. Wasim, G. Marín, E. Choukri, and L. Hajji, “Theoretical and experimental study of AC electrical conduction mechanism in the low temperature range of *p*-CuIn3Se5,” *Physica E: Low-dimensional Systems and Nanostructures*, vol. 99, pp. 37–42, May 2018, doi: 10.1016/j.physe.2018.01.012.
[348] “AC conductivity evolution in bulk and grain boundary response of sodium tungstate Na2WO4 | Ionics.” Accessed: Aug. 21, 2025. [Online]. Available: https://link.springer.com/article/10.1007/s11581-017-2193-8
[349] A. K. Tammam, D. Gawad, and M. F. Mostafa, “Crossover from overlap large polaron to small polaron tunneling: A study of conduction mechanisms and phase transitions in a new long chain organic inorganic hybrid,” *Journal of Physics and Chemistry of Solids*, vol. 149, p. 109787, Feb. 2021, doi: 10.1016/j.jpcs.2020.109787.
[350] “The influence of frequency and temperature on the AC-conductivity in $$\text {TlInTe}_2$$ semiconductor single crystal | Scientific Reports.” Accessed: Aug. 21, 2025. [Online]. Available: https://www.nature.com/articles/s41598-025-87788-w
[351] “The ‘universal’ dielectric response | Nature.” Accessed: Aug. 21, 2025. [Online]. Available: https://www.nature.com/articles/267673a0
[352] “The role of ionic diffusion in polarisation in vitreous ionic conductors,” SciSpace - Paper. Accessed: Aug. 21, 2025. [Online]. Available: https://scispace.com/papers/the-role-of-ionic-diffusion-in-polarisation-in-vitreous-1pgde1z1by
[353] “Impedance and modulus studies of magnetic ceramic oxide Ba2Co2Fe12O22 (Co2Y) doped with Bi2O3 | Journal of Applied Physics | AIP Publishing.” Accessed: Aug. 21, 2025. [Online]. Available: https://pubs.aip.org/aip/jap/article/110/3/034107/977487/Impedance-and-modulus-studies-of-magnetic-ceramic
[354] F. B. L. B. Siqueira and D. C. Campos, “Application of impedance spectroscopy to analyze the electrical properties of cobalt doped SrTiO3,” *Solid State Ionics*, vol. 391, p. 116140, Mar. 2023, doi: 10.1016/j.ssi.2022.116140.
[355] “(PDF) Dielectric materials for wireless communication,” ResearchGate. Accessed: Aug. 21, 2025. [Online]. Available:

https://www.researchgate.net/publication/280836553_Dielectric_materials_for_wireless_communication
[356] N. A. Spaldin, S.-W. Cheong, and R. Ramesh, “Multiferroics: Past, present, and future,” *Physics Today*, vol. 63, no. 10, pp. 38–43, Oct. 2010, doi: 10.1063/1.3502547.
[357] B.-T. Lim, “Dielectric Resonator Antennas : theory and design,” Thesis, Massachusetts Institute of Technology, 1999. Accessed: Aug. 21, 2025. [Online]. Available: https://dspace.mit.edu/handle/1721.1/36782
[358] “On the Matching of Microstrip-Fed Dielectric Resonator Antennas | Request PDF,” ResearchGate. Accessed: Aug. 21, 2025. [Online]. Available: https://www.researchgate.net/publication/258509348_On_the_Matching_of_Microstrip-Fed_Dielectric_Resonator_Antennas
[359] A. V. P. Kumar, V. Hamsakutty, J. Yohannan, and K. T. Mathew, “MICROSTRIPLINE FED CYLINDRICAL DIELECTRIC RESONATOR ANTENNA WITH A COPLANAR PARASITIC STRIP,” *PIER*, vol. 60, pp. 143–152, 2006, doi: 10.2528/PIER05121301.
[360] “HFSSintro.pdf.” Accessed: Aug. 21, 2025. [Online]. Available: https://athena.ecs.csus.edu/~milica/EEE212/HAND/HFSSintro.pdf
[361] “Dielectric resonator antennas—a review and general design relations for resonant frequency and bandwidth - Mongia - 1994 - International Journal of Microwave and Millimeter-Wave Computer-Aided Engineering - Wiley Online Library.” Accessed: Aug. 21, 2025. [Online]. Available: https://onlinelibrary.wiley.com/doi/abs/10.1002/mmce.4570040304
[362] “Monte Carlo Simulation of Epitaxial Growth | IntechOpen.” Accessed: Aug. 21, 2025. [Online]. Available: https://www.intechopen.com/chapters/56552
[363] M. A. Chabowska, “Step meandering: Balance between the potential well and the Ehrlich-Schwoebel barrier,” *Phys. Rev. B*, vol. 111, no. 15, 2025, doi: 10.1103/PhysRevB.111.155401.